Plasma out of thermodynamical equilibrium : influence of the plasma environment on atomic structure and collisional cross sections

Madeny Belkhiri

UNIVERSITÉ PARIS SUD

Comprendre le monde, construire l'avenir®

EDOM

Ecole Doctorale Ondes et Matière

UNIVERSITÉ PARIS-SUD XI

ÉCOLE DOCTORALE 288 :
ONDES ET MATIÈRE

Laboratoire : Interactions dynamique et lasers

THÈSE DE DOCTORAT

PHYSIQUE

par

Madeny Belkhiri

Plasma out of thermodynamical equilibrium : influence of the plasma environment on atomic structure and collisional cross sections

Date de soutenance : Le 3 Novembre 2014

Composition du jury :

Directeur de thèse :	Michel Poirier	Chercheur C.E.A Saclay
Rapporteurs :	Christophe Blancard	Ingénieur-chercheur C.E.A Bruyères–le-châtel
	Olivier Peyrusse	Ingénieur-chercheur CELIA
Examinateurs :	Guy Bonnaud	Professeur INSTN
	Djamel Benredjem	Professeur Paris XI Sud
	Jean-Marcel Rax	Professeur Paris XI Sud

" Si la théorie s'est fourvoyée, c'est parce que très peu de théoriciens avaient vu la guerre"

Maréchal Ferdinand Foch.

Des principes de la guerre -1903-

Abstract

In hot dense plasmas, the interaction of an ion with other ions and free electrons may strongly affect the atomic structure. To account for such effects we have implemented a potential correction based on the uniform electron gas model and on a Thomas-Fermi Approach in the Flexible Atomic Code (FAC). This code has been applied to obtain energies, wave-functions and radiative rates modified by the plasma environment. In hydrogen-like ions, these numerical results have been successfully compared to an analytical calculation based on first-order perturbation theory. In the case of multi-electron ions, we observe level crossings in agreement with another recent model calculation. Various methods for the collision cross-section calculations are reviewed. The influence of plasma environment on these cross-sections is analyzed in detail. Some analytical expressions are proposed for hydrogen-like ions in the limit where Born or Lotz approximations apply and are compared to the numerical results from the FAC code. Finally, we study the influence of the plasma environment by including it in a new collisional-radiative model named -Foch-. Because of this environment, the mean charge state of the ions increases. The line shift is observed on the bound-bound emission spectra. A good agreement is found between our work and experimental data on a Titanium plasma.

Keywords : Collisional-radiative model, Ion sphere, Plasma potential, Flexible Atomic Code, Collisional cross sections

Aknowledgement

En tout premier lieu je tiens à remercier mon directeur de thèse Michel Poirier qui a été présent durant ces trois années. Je tiens à souligner son implication, sa rigueur, son sérieux ainsi que son opiniâtreté dans ce travail. Il n'a jamais laissé une de mes questions sans réponse. Je le remercie pour ses lectures attentives de ce manuscrit, ainsi que pour ses nombreuses recommandations.

Je n'oublie pas et je n'oublierai pas mon camarade de thèse Clément Caizergues devenu ami. Il a été le premier à m'aider dans les difficultés du quotidien. Il a toujours fait preuve d'un bon esprit critique de mon travail. Je le remercie pour sa lecture pertinente de ce manuscrit. Ces trois années n'auraient pas été les mêmes sans lui.

Je remercie Christopher Fontes qui a apporté une contribution importante à ma compréhension des problèmes de diffusion, ainsi que de la physique atomique. Je le remercie pour le temps qu'il a pris pour répondre à mes nombreux e-mails ; pour les références qu'il m'a fournies ; et pour ses conseils.

Un merci appuyé à ma femme Anna-Liisa Ikart, pour son soutien moral, ses idées sur mon travail et sa correction de l'anglais.

Dans l'équipe MHDE, je remercie Frédéric Thais pour sa disponibilité, sa bonne humeur et son aide pour les problèmes informatique. Mais également Thomas Blenski, le chef de l'équipe MHDE pour ses connaissances de la physique des plasmas et sa grande disponibilité.

Un grand merci à l'ensemble du corps professoral du master des sciences de la Fusion pour la qualité de leur enseignement. Plus particulièrement Guy Bonnaud, Frank Rosmej et bien sûr Jean Marcel Rax.

Un merci à mes camarades/amis de promotions Clément Dutreix et Aurélien Colladant pour avoir relu certaine parties de ce manuscrit. Ainsi qu'à ma soeur Sofia pour son soutien moral.

Je remercie l'école doctorale ondes et matières de m'avoir autorisé à écrire ce manuscrit en anglais, notamment le conseiller aux thèses Djamel Benredjem.

Pour finir, j'exprime ma gratitude à Christophe Blancard et Olivier Peyrusse, qui ont accepté d'être les rapporteurs de cette thèse.

Contents

Chapitre 1

Introduction

1.1 Context and motivations

This work tries to give a contribution to a better understanding of the fundamental nature of plasma matter. Plasmas constitute the fourth state of matter in addition to the solid, liquid and gas states. Few natural plasmas can be found on Earth, the most known being the lightning and the auroras. The most interesting and studied plasmas remain in space, the closest non-terrestrial plasma being the Sun. Stars make an excellent sample of plasma diversity. Indeed, from the core of Sun to the corona, the temperature and density are completely different. Three zones may be distinguished: the core, the radiative zone and the convective zone. In the sun interior the density overcomes the solid state density, with 10^{24}-10^{26}electron/cm^3. Meanwhile, at the most external layer the density is very low, around 10^{16}electron/cm^3. This diversity gives rise to different fields of plasma physics. The plasma conditions related to our work are those prevailing from the core to the radiative zone. The phenomenon which focuses the attention of an important part of the plasma community takes place in the core of the Sun: the thermonuclear fusion reactions.

Gravitational fusion

The core of a star is governed by the equilibrium between two mechanisms, the radiation pressure and the gravitational effect. The radiation pressure is the result of the emission of photon stemming from the fusion reaction. At the beginning of their cycle stars are made of light elements such as hydrogen and helium. Under the effect of the gravitation, the density and the temperature ($\sim 10^7 K$) reach a critical value which initiate the first reactions of fusion. Once stars run out of light combustible elements, the radiation cannot counterbalance the gravitation. As a consequence, the star is compressed under its own mass leading to an increase of temperature and density which makes possible the thermonuclear reactions of heavier elements. This cycle is repeated until the star runs out of combustible elements leading to its end. Of course, depending on the mass of the star the scenarios of its death differ. The fusion is possible in stars because of their mass and a

long time confinement of the combustible elements.

Fusion for energy

The objective of a part of the plasma community is to be able to reproduce the conditions occurring in the core of stars, in order to achieve the fusion reaction. In the stars, several fusion reactions take place, mostly the proton-proton fusion. The most common reaction that the plasma community intends to reproduce is the reaction of two hydrogen isotopes, the deuterium (D) and the tritium (T), following the process

$$ {}^{2}_{1}D^{+} + {}^{3}_{1}T^{+} \rightarrow {}^{4}_{2}He^{2+} + n \ . \tag{1.1.1} $$

Many reasons justify the interest for this reaction. Both elements are light elements, therefore the energy required to permit the reaction is sustainable. Other reactions involving light elements exist, however, the cross section of the D-T reaction is the highest, and possible at reasonable temperatures in the range $10^7 - 10^8$K. Furthermore, the deuterium can be extracted from the oceans, which represent an inexhaustible supply, the tritium, in quantities too small in nature, has to be produced artificially in the cover of a reactor using a neutron flux on lithium, which is also abundant in the earth's crust. The Lawson criterion gives the condition to obtain a profitable energy (twice the invested energy)

$$ N_e \tau > 10^{14} \mathrm{cm}^{-3}\mathrm{s}, \tag{1.1.2} $$

where N_e represents the electronic density and τ the time of confinement. On Earth, two approaches have been retained to achieve this reaction of fusion, the magnetic and inertial fusion.

Magnetic fusion [1]

This approach consists of confining the plasma for a long period of time (about seconds), the plasma density is low around 10^{14}electron/cm^3. In order to confine the plasma, magnetic field is used. Different configurations or geometries can be used for that purpose. The most famous and simple is the tokamak designed by the Russian physicists I.Tamm and A.Sakharov. A tokamak has a shape of a torus and two magnetic fields are generated to confine the plasma. One toroidal made by exterior coil which induced an helicoidal trajectory of the plasma particles. To correct the transverse drift induces by the first field, a poloidal field is added. This field is made by the toroidal current generated inside the plasma. Other geometries exists such as the stellerators, in that case the magnetic fields are both made by exterior coils. The community of magnetic fusion faces various problems to achieve the project: plasma instabilities (link to the competition between the magnetic field and the plasma drift), the plasma-wall interaction and turbulences (edge and H mode).

Inertial fusion [2]

For this approach, the plasma confinement time is very short $\sim 10^{-12}\text{s}^{-1}$ and the densities are very high $10^{24} - 10^{26}\text{electron/cm}^3$. The idea is to encapsulate in a nanometric pellet a gas of deuterium and tritium. Then high power lasers are used to compress the pellet in order to reach the requested densities. To compress the capsule, different schemes exist: direct irradiation, indirect irradiation with the support or not the so-called method fast ignition. The direct irradiation is a direct compression of the capsule by the lasers. A good efficiency of this method requests an uniform compression. In the indirect scheme, the capsule is set in a cavity made of a high Z element, usually gold. In that scenario the cavity targeted by the laser beams re-emits of X-ray radiation leading to the capsule heating. The higher is the atomic number, the more important is X-ray conversion and then the heating efficiency. The efficiency of the energy conversion from the cavity to the capsule constitutes the weakness of that approach. The plasma generated by the process described above, presents the same diversity as the stellar plasmas. Indeed, three domains can be distinguished, each one of them being characterized by a different range of temperature and density. These are:

- Shock zone: The plasma is highly compressed leading to a density higher than the solid state but the temperature is quite low ∼eV.
- Conduction zone: In that region the density is between the solid state density and the critical density. This latter density is defined by $N_c(\text{cm}^{-3}) \simeq 10^{21}/\lambda^2$, where λ is the laser wave-length in μm. When this density is reached the laser cannot propagate any futher. For a laser with a wavelength $\lambda = 0.1\mu\text{m}$, $N_c = 10^{23}\text{electron/cm}^3$. The temperature increases due to the heating of the target by the X-rays, its order of magnitude being between 10 eV to 1 keV.
- Corona: The density of that region is below the critical density and the temperature rises to one keV or more.

In order to make these technological innovations possible, the physicists have to be able to predict and diagnose the evolution of the plasma. This present work mainly finds its application in the inertial fusion and astrophysical plasmas such as stellar interiors. However, this work may also be applicable to the analysis of radiative losses in the divertor zone, and can be extended to industrial applications like nano-lithography, or X-ray and XUV sources. To illustrate the diversity of plasma, we have set the diagram

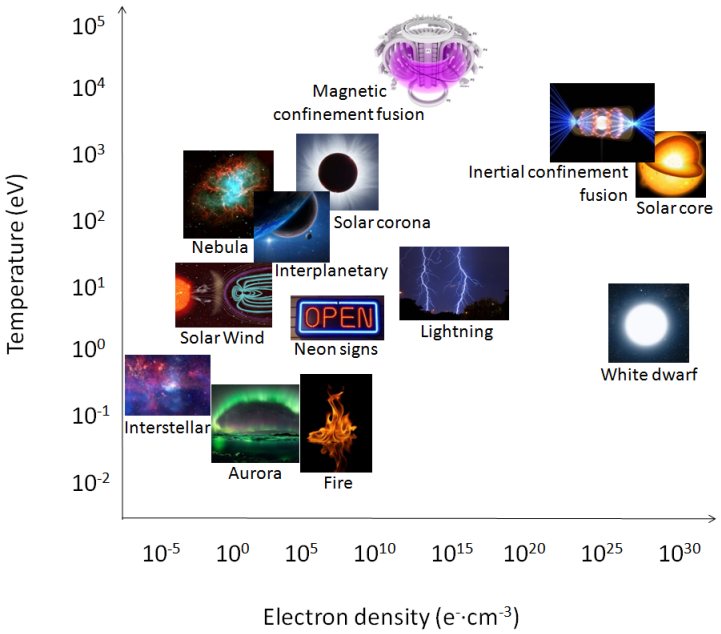

FIGURE 1.1.1 : Temperature-density phase diagram of plasmas

1.2 Plasma parameters

Several dimensionless parameters characterize the properties of plasmas under investigation. The density of the electrons N_e and the ions N_i are linked by the neutrality condition

$$N_e = Z^* N_i \tag{1.2.1}$$

Z^*being to the mean charge of the plasma, starting from here the density is expressed in cm^{-3} instead of electron/cm^3. Even though our study is out of thermodynamical equilibrium, we assume here that free electrons are thermalized, and therefore can be described by a temperature kT_e. The parameter k is the Boltzmann constant and T_e the electron temperature, however for convenience kT_e is used as the temperature. Two mechanisms compete in plasmas: the thermal motion and the Coulombic interaction between electrons. This competition is measured by the coupling parameter Γ. This quantity is defined [3] by

$$\Gamma = \frac{Z^{*2}}{R_0 kT_e} \tag{1.2.2}$$

with the temperature and radius in atomic unit, where R_0 is defined in this work by the neutrality condition

$$R_0^3 = \frac{3Z^*}{4\pi N_e}. \tag{1.2.3}$$

In the case of an important thermal motion $\Gamma \ll 1$, the plasma is weakly correlated (ideal plasmas), disorder dominates. Such plasmas are found in magnetic fusion or stellar corona. On the other hand if $\Gamma \gg 1$, the plasma is strongly correlated, the structure of

the plasma is organized and close to a fluid. Stellar interior plasmas are a good example of plasmas dominated by the Coulombic force.

The second parameter γ determines whether if the free electrons have to be described by a classical or a quantum approach. Defining the thermal de Broglie wave-length as $\lambda_{th} = h/(2\pi mkT_e)^{1/2}$, where h is the Planck constant and m the electron mass. We express γ by

$$\gamma = N_e \lambda_{th}^3 \tag{1.2.4}$$

If $\gamma \ll 1$, a Maxwell-Boltzmann statistic is relevant to describe the free electrons but if $\gamma \gg 1$ a Fermi-Dirac statistic has to be used.

The present work focus on dense plasmas with densities from 10^{15}cm^{-3} to 10^{25}cm^{-3}, i.e which can be as high as solid density. Concerning the temperature we investigate plasma above the eV, however, we will not study relativistic plasmas for which $kT_e \geq mc^2$. Therefore, the plasmas considered in this work are moderately to strongly correlated $10 > \Gamma > 10^{-2}$, and usually non-degenerate $\gamma < 1$.

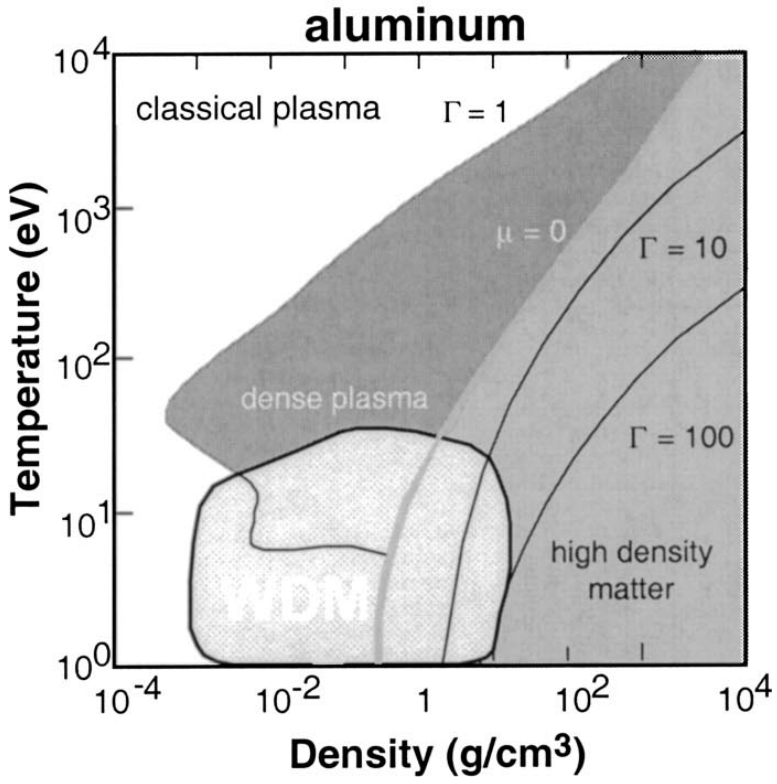

FIGURE 1.2.1 : Temperature-density phase diagram for aluminium. The relevant regimes are noted, as are the various values of the coupling parameter Γ.[4]

1.3 État de l'art

The main information that physicists have access to in hot and dense plasmas, is the radiation emitted by the plasma. The goal of the theoretician is to build a theory able to

retrieve or predict this information. The photons emitted by the plasma are the result of transitions from one atomic state to another. Therefore, to describe the spectral properties (emissivity, absorption), it is necessary to determine the atomic energy levels and their occupations. It is a complex task to model such a problem because plasma is a N-body problem. To circumvent this issue, two theoretical approaches have to be combined, the statistical and the atomic approach. Atomic stucture theory is used to calculate energies and wave-functions, while statistical physics characterizes the thermodynamics of the plasma and obtain the atomic populations.

We focus our attention on two approaches to draw a picture of our theoretical field. The first one involves the plasma environment and thermodynamics in a consistent way and is classified under the generic term of average atom model. By environment we mean the effect of the free electrons and neighbouring ions of the central ion. The second approach solves the atomic structure and then obtains the level populations from statistics or kinetic equations. These theories belong to what is called here the chemical picture.

Average atom models

Those models mostly rely on Density Functional Theory (DFT), founded by Hohenberg [5] and Kohn [6]. In the DFT theory, the N-body problem is reduced to the determination of a spatially dependent charge density. Instead of obtaining the N-electron wave function of the system, the effort is made on the electronic density. In the AA model, the idea is to model the plasma by a fictitious atom. This model allows to calculate an average electronic structure. We may distinguish two groups of average-atom models depending on the way they model the plasma environment.

In the first group, the plasma is divided into neutral cells named Weigner-Seitz cells; each cell is centred around a nucleus of charge Z. Each cell also contains the exact number of electrons to ensure the neutrality of the sphere. The first average-atom model with a quantum treatment was proposed by Rozsnyai [7, 8]. In the original version of Rozsnyai the Weigner-Seitz cell is spherical and periodic conditions are imposed on the sphere. The boundary condition requires that the wave functions and their derivatives cancel on the sphere. The last hypothesis is relevant in the case of condensed matter but not of plasmas. In his work, the bound electrons are treated by the theories of bands, while the free electrons are treated via the Fermi-Dirac statistics. In the INFERNO model of Liberman [9], the bound and free electrons are treated via quantum mechanics. The condition of periodicity [7] is replaced by a uniform density of electron gas (also named jellium) beyond the ion sphere. This requires that the derivative of the potential to be zero outside the Weigner-Seitz sphere but not that the wave functions are zero on the sphere.

The second group of models is based on the atom in the jellium developed by Perrot [10] and completed by Blenski and Piron [11, 12]. In their work, the atom is set in a jellium as in the INFERNO model, but the condition of neutrality of the sphere is replaced by a

global neutrality with the jellium. In that model [11] all electrons are treated via quantum mechanics.

The strength of the average-atom theory lies in its description of the plasma environment. This environment plays a significant role for strongly correlated plasmas. This type of approach is mainly used when plasma is in thermodynamical equilibrium. Therefore, the atomic populations are determined by statistical laws (Saha-Boltzmann and Boltzmann statistics). However, the weakness of the average-atom model lies in the description of the spectral properties. Indeed, the levels of the AA model are calculated without taking into account explicitly the electrostatic interaction between electrons. Indeed, most of the time in the AA model the problem is not purely described by a DFT approach. The exchange-correlation potential is modeled by a local density approximation (LDA); this type of approach is called DFT-LDA.

Chemical picture

In the following, approaches starting with isolated ion are classified under the generic term of "chemical picture" though this term roughly regroups the corresponding theories. In this type of approach, the plasma effects (statistics and plasma environment) are included in a subsequent step. The objective of this approach is to provide the wave functions and energies of all ions present in the plasma. To obtain those quantities, we have to solve the Schrödinger or the Dirac[13] equations of each present charge state. In order to obtain this atomic structure for isolated ions, many atomic codes have been developed over the past decades such as the non-relativistic Cowan code [14] and SUPERSTRUCTURE [15], relativistic codes such as HULLAC [16], MCDF [17], RATS [18], GRASP [19] and the Flexible Atomic Code (FAC) [20]. The difference between these codes is mainly in the potential used. The Chapter 2 will provide more details on the atomic structure calculation.

This theory and codes can be called detailed because atomic states are calculated. Such an approach prevails in the case of low Z elements and therefore provides accurate and detailed atomic spectra. However, in the case of intermediate to high Z element, such a method represents a prohibitive task due to the high number of levels and possible transitions (in principle infinite but in practice limited to the computing capacities). To circumvent this problem, an idea is to regroup the electronic levels into configurations [21] or to regroup them into super-configurations[22]. This regrouping is relevant when energies of levels are close enough (compared to temperature kT_e) to be at thermal equilibrium. Furthermore, in the case of high Z plasma, meaning a high number of bound states, the atomic spectra of a detailed calculation are characterized by complex structures due to the overlap of many lines. The approach proposed by C. Bauche-Arnoult *et al.* [23] reduces that problem; this method is called Unresolved Transition Array (UTA) for intermediate Z and Spin-Orbit-Split-Array (SOSA) for high Z values. They suggested to treat statistically those unresolved transitions by representing them as a continuous envelope. UTAs or

SOSAs are usually modeled by one or many Gaussian(s) whose amplitude and width are evaluated through the moments of the energy distribution of the lines.

An other kind of approximation that we classify in this group (for conveniency), is the screened-hydrogenic model [24]. This type of approach is used in the FLYCHK code [25], in the work of Scott et al. [26] and in the reference of Faussurier et al. [27].

The main weakness of the detailed calculation compared to the average-atom approach is the fact that the ions are considered to be isolated. When the density can be considered low, the plasma is weakly coupled and the effect of the plasma environment on the ion can be disregarded. However, in the dense to highly dense regime, the presence of free electrons and neighbouring ions break the picture of an isolated ion. An important objective of this thesis is the inclusion of the plasma environment in the atomic structure code. In the chapter 5 we will discuss the several approaches to model the plasma environment in detail.

1.4 Objectives

As mentioned before, in thermodynamical equilibrium the atomic populations are determined by the Saha-Boltzmann equations and Boltzmann statistic. Out of local thermodynamical equilibrium regime, each atomic population depends on all atomic processes which populate and depopulate the atomic level to the others. These atomic processes are divided into two categories, collisional and radiative processes. To calculate these quantities, atomic and scattering physics have to be considered. Therefore, to obtain the atomic populations, kinetic equations have to be solved. Such approach leads to build the so-called collisional-radiative models which amounts to solve a large set of kinetic equations. The Chapter 3 is devoted to the kinetic equations in plasmas, and in the chapter 4 a non-exhaustive review of atomic-process calculation is made.

The goal of the present thesis is to provide a detailed description of the plasma mostly out of thermodynamical equilibrium. To achieve this task, a "Chemical picture" approach based on the FAC code [20] was chosen to provide the atomic structure and the collisional cross sections. An important effort was the inclusion of the plasma environment via an ion sphere model. This approach led us to modify the physical and numerical content of FAC. A collisional-radiative code named Foch has been developed to obtain the atomic populations, the plasma emissivity and other plasma properties. This code is able to carry out both detailed and UTA calculations. Our research had three objectives:

- Build a new kinetic code using the data from FAC in order to obtain the atomic populations and emission spectra.
- Take into account the plasma environment while keeping an accurate atomic description.

- Investigate into details cross sections calculations. This point was motivated by the inclusion of the plasma environment, but also by the need to reduce the calculations time.

1.5 Organization of the manuscript

The manuscript is built in six parts to answer to those objectives. In the second chapter, we describe the atomic physic used for plasmas. The aim of this chapter is to provide basic knowledge of atomic physics and to introduce the necessary formalism for the study of the plasma influence on the atomic structure (chapter 5 and 6) and the collisional processes (chapter 4 and 6). The third chapter is dedicated to the general theory of thermodynamical regime of plasma. Its interest is to set the collisional radiative model and to give the main formulas relevant for the present work. In the fourth chapter, a review of the method to calculate collisional cross section is done. While the main goal of this thesis is to include density effects in plasma modeling, it was unclear for the present author how the electron impact calculations should be considered in plasma modeling. Therefore, we choose to do some investigation of electron impact excitation in order to better understand the validity of the basic atomic theory as it applies to collisional-radiative modeling. Furthermore, this part is necessary for understanding the influence of the plasma environment on the collisional cross sections. The central part of this work is the chapter 5 which is devoted to the model of the plasma environment. It presents the existing ways to model the plasma environment; a review and discussion of the ion sphere model is made. We explain our choice of plasma potential and the domain of validity of our approach. An extensive investigation of the ion sphere plasma potential is done via the development of analytical formulas for hydrogen-like ions. The latter developments support the numerical results in the next chapter. After presenting the theory under our plasma potential, we show in the chapter 6 the influence of the plasma environment on the atomic parameters such as energies, wave functions and on cross sections. The chapters 5 and 6 follow closely two articles; one is published [28] and the other is submitted [29]. In the chapter 7, we analyze how the influence of the plasma environment affect the collisional rates; and more generally the population kinetics. The different results of this chapter are obtained through our new kinetic code Foch. In this part we will first validate the kinetic code without plasma effect by comparing numerical results with an experiment at low density on the krypton. Next, we investigate the density effect on an aluminium plasma. To conclude this chapter, a comparison with a recently published experiment on titanium which highlights the effect of the plasma environment, is shown. We end this manuscript by summarizing results obtained and describe the perspectives of this work.

Chapter 2

Atomic Structure

2.1 Introduction

To accurately model the kinetics or radiative transfer in a plasma, we need a reliable atomic structure model. When dealing with highly ionized plasmas, it may be preferable to use a fully relativistic theory, i.e Dirac equation instead of Schrödinger equation. A wide variety of codes is available in the literature, based on Hartree-Fock or parametric potential formalism [14, 17, 16, 15].To provide these atomic data, we have chosen the Flexible Atomic Code [20]. This fully relativistic code is widely used by the plasma NLTE community. FAC has the advantage to be available without explicit restrictions of use. FAC also allows to calculate the collisional cross section needed for the resolution of the collisional-radiative model.

In this part we first present the Schrödinger and Dirac equations for one particle in a central field. Some analytical formulas noted here for hydrogen-like ions will be confronted to FAC results in the analysis of plasmas environment effects (chapter 5). Then, we discuss how to describe multi-electron ion. A short review of different average potential is done. This chapter ends with models which account for the thermodynamics of the plasma. Atomic units are used throughout this chapter.

2.2 Schrödinger equation

The Hamiltonian for a single particle in a spherical potential $V(r)$ field writes [30]

$$H_S = \frac{p^2}{2} + V(r), \tag{2.2.1}$$

where p is the kinetic momentum of the particle. From the Hamiltonian (2.2.1), we can write the Schrödinger equation

$$\left[\Delta + 2\left(E - V(r)\right)\right]\Psi(r,\theta,\varphi) = 0, \tag{2.2.2}$$

where Ψ is the wave-function of the particle which respects the normalization condition, for bound states $\langle\Psi|\Psi\rangle = 1$, E is the energy associated to that wave-function and Δ is the Laplacian operator. The system (2.2.1) possesses three degrees of freedom (r, θ, φ). It requires three observables which commute to characterize the eigenfunctions. The above Hamiltonian commutes with the z component of the orbital angular moment operator $\boldsymbol{L}$. This operator is defined by

$$\mathbf{L} = \boldsymbol{r} \wedge \boldsymbol{p}, \tag{2.2.3}$$

where $\boldsymbol{r}$ is the position and $\boldsymbol{p}$ the momentum of the particle. The square of this operator $\boldsymbol{L}^2$ and its z component $\boldsymbol{L}_z$ commutes with the Hamiltonian H_S. We obtain from these observables the eigenvalues called quantum numbers which characterize the system. Operators $\boldsymbol{L}^2$ and $\boldsymbol{L}_z$ only depend of the coordinates θ and φ, therefore their eigenfunctions only depend on θ and φ. Their eigenfunctions $Y_{l,m}(\theta, \varphi)$ are the spherical harmonics with eigenvalues $l(l+1)$ and m for $\boldsymbol{L^2}$ and $\boldsymbol{L_z}$ respectively; l corresponds to the orbital quantum number and m to the magnetic quantum number. The structure of the Hamiltonian suggests to decompose the wave-function in a product of a radial and spherical function $\Psi_{n,l,m}(r, \theta\varphi) = \frac{1}{r} R_{n,l}(r) Y_{l,m}(\theta, \varphi)$, where n is the principal quantum number. By replacing the wave-function with this product, we obtain for the radial equation

$$\frac{\partial^2 R_{n,l}}{\partial^2 r} + 2\left(E - V(r) - \frac{l(l+1)}{2r^2}\right) R_{n,l} = 0. \tag{2.2.4}$$

The radial function $R_{n,l}$ has to respect the boundary condition $R_{n,l}(0) = 0$ and $R_{n,l}(\infty) = 0$ because Ψ has to be finite everywhere. We point out that in the case of fermions as in our concern we have to take into account the spin of the particle. Taking into account the electron spin, the wave-function Ψ includes a Pauli spinor i.e

$$\Psi_{n,l,m,m_s} = \frac{1}{r} R_{n,l}(r) Y_{l,m}(\theta, \varphi)\, \chi_{m_s}(s_z), \tag{2.2.5}$$

where $\chi_{m_s}(s_z)$ is the spin eigenfunction , s_z is the component of the spin operator $\boldsymbol{S}$ and m_z the spin quantum number. At the non-relativistic approximation the Hamiltonian does not depend on the spin of the particle. When dealing with relativistic effect at first perturbation order additional terms are added to the Hamiltonian:

$$H_S = \frac{p^2}{2} + V(r) - \frac{\alpha^2}{4}\left[(E-V)^2 + \frac{dV}{dr}\frac{\partial}{\partial r} - \frac{2}{r}\frac{dV}{dr}\boldsymbol{L}\cdot\boldsymbol{S}\right]. \tag{2.2.6}$$

where α is the fine structure constant. In equation (2.2.6) in order of appearance, the corrections are the mass-velocity effect, the Darwin term and the spin-orbit interaction. These terms are derived from the Dirac equation that we will see in the next section (2.3).

Hydrogen-like ions

The radial equation (2.2.4) can be solved analytically in a Coulomb field, which corresponds to the case of hydrogen-like ions. The bound energies are

$$E = -Z^2/2n^2 \tag{2.2.7}$$

The corresponding radial wave-functions are

$$R_{n,l}(r) = \frac{Z^{1/2}}{n}\sqrt{\frac{(n-l-1)!}{(n+l)!}}\rho^{l+1}e^{-\rho/2}F_{n-l-1}^{2l+1}(\rho)\,., \tag{2.2.8}$$

where$\rho = 2Zr/n$ and $F_{n-l-1}^{2l+1}(\rho)$ stands for the Laguerre polynomials,

$$F_{n-l-1}^{2l+1}(\rho) = \sum_{m=0}^{n-l-1}\frac{(-1)^m}{m!}\frac{(n+l)!}{(2l+1+m)!\,(n-l-1-m)!}\rho^m. \tag{2.2.9}$$

These results will be used in the analytical developments of the chapter 5.

2.3 Dirac equation

The detailed theory for relativistic atoms may be found in the books of Johnson [31] and Grant [32].The Dirac Hamiltonian for a single particle in a central field $V(r)$ writes

$$h_D(r) = c\boldsymbol{\alpha}\cdot\boldsymbol{p} + c^2\beta + V(r)\,, \tag{2.3.1}$$

where c is the speed of light, $\boldsymbol{p}$ the impulsion vector of the particle, $\boldsymbol{\alpha}$ and $\boldsymbol{\beta}$ are Dirac matrices of dimension 4×4. They are defined by

$$\boldsymbol{\alpha} = \begin{pmatrix} 0 & \boldsymbol{\sigma} \\ \boldsymbol{\sigma} & 0 \end{pmatrix} \qquad \boldsymbol{\beta} = \begin{pmatrix} I & 0 \\ 0 & -I \end{pmatrix}, \tag{2.3.2}$$

where I is the identity matrix and $\boldsymbol{\sigma} = (\sigma_x, \sigma_y, \sigma_z)$ is the Pauli matrix of dimension 2×2. The Pauli matrix is linked to the spin angular momentum operator $\boldsymbol{S}$ by

$$\boldsymbol{S} = \frac{1}{2}\boldsymbol{\sigma}. \tag{2.3.3}$$

The system possesses four degrees of freedom, three of space (r,θ,φ) and one for the spin. We need four quantum numbers to fully describe the system. Contrary to the non-relativistic case, the Hamiltonian h_D does not commute with the orbital angular momentum $\boldsymbol{L}$ but with the total angular momentum $\mathbf{J}$, defined as follows:

$$\mathbf{J} = \mathbf{L} + \mathbf{S}. \tag{2.3.4}$$

The eigenvalues of the operator $\boldsymbol{J^2}$ are $j\,(j+1)$, with $|l-s| \leq j \leq |l+s|$, where $l\,(l+1)$ and $s\,(s+1)$ are the eigenvalues of the operator $\mathbf{L}^2$ and $\mathbf{S}^2$, respectively. For electrons the spin value is $s = \pm 1/2$ meaning $j = l \pm 1/2$. As mentioned before the Hamiltonian does not commute either with $\boldsymbol{L}$ or with $\boldsymbol{S}$. Thus, the spherical harmonics $Y_{lm}\,(\theta, \varphi)$ and the two-component spinor χ_μ (μ stands for the spin up or down) are no more eigenstates of the system (2.3.1). However, by combining them we obtain the eigenstates of the Dirac Hamiltonian, which are commonly named spherical spinors $\Omega_{jlm}\,(\theta, \varphi)$. The spherical Pauli spinors write

$$\Omega_{jlm}\,(\theta, \varphi) = \sum_{\mu} C\,(l, 1/2, j, m-\mu, \mu, m)\, Y_{lm-\mu}\,(\theta, \varphi)\, \chi_\mu, \tag{2.3.5}$$

where $C\,(l, 1/2, j, m-\mu, \mu, m)$ is a Clebsch-Gordan coefficient [31], $\mu = \pm 1/2$ due to the spin value of electrons. The two component spinor χ_μ, for electrons is

$$\chi_{1/2} = \begin{pmatrix} 1 \\ 0 \end{pmatrix} \qquad \chi_{-1/2} = \begin{pmatrix} 0 \\ 1 \end{pmatrix}. \tag{2.3.6}$$

Spherical spinors are eigenfunctions of $\boldsymbol{\sigma} \cdot \boldsymbol{L}$. We define the operator $K = -1 - \boldsymbol{\sigma} \cdot \boldsymbol{L}$ for which eigenvalues are

$$K\Omega_{jlm}\,(\theta, \varphi) = \kappa \Omega_{jlm}\,(\theta, \varphi)\,, \tag{2.3.7}$$

where κ is the quantum relativistic angular number, defined by

$$\kappa = \begin{cases} l & \text{if } j = l - \frac{1}{2} \\ -l-1 & \text{if } j = l + \frac{1}{2} \end{cases}. \tag{2.3.8}$$

For the total angular momentum eigenvalues are

$$\boldsymbol{J^2}\Omega_{jlm}\,(\theta, \varphi) = j\,(j+1)\,\Omega_{jlm}\,(\theta, \varphi) \tag{2.3.9}$$

and

$$\boldsymbol{J_z}\Omega_{jlm}\,(\theta, \varphi) = m\Omega_{jlm}\,(\theta, \varphi)\,. \tag{2.3.10}$$

Through the new quantum number κ we can write that $\Omega_{jlm}\,(\theta, \varphi) = \Omega_{\kappa m}\,(\theta, \varphi)$. Including the explicit value of the Clebsch-Gordan coefficients, one has the spherical spinors

$$\Omega_{-l-1,m}\,(\theta, \varphi) = \begin{pmatrix} \sqrt{\frac{l+m+1/2}{2l+1}} Y_{l,m-1/2}\,(\theta, \varphi) \\ \sqrt{\frac{l-m+1/2}{2l+1}} Y_{l,m+1/2}\,(\theta, \varphi) \end{pmatrix} \tag{2.3.11}$$

$$\Omega_{l,m}\,(\theta, \varphi) = \begin{pmatrix} -\sqrt{\frac{l-m+1/2}{2l+1}} Y_{l,m-1/2}\,(\theta, \varphi) \\ \sqrt{\frac{l+m+1/2}{2l+1}} Y_{l,m+1/2}\,(\theta, \varphi) \end{pmatrix} \tag{2.3.12}$$

An important property of the spherical spinors is that they fulfill the orthonormal condition as the spherical harmonics do for the Schrödinger equation.

To summarize, the system (2.3.1) is determined by four quantum numbers: the principal quantum number n, the total angular momentum j, the relativistic quantum number κ and the magnetic quantum number m. We solve now explicitly the Dirac equation with a spherical potential

$$h_D \Psi_{n,\kappa,m} = E_{n,\kappa,m} \Psi_{n,\kappa,m}, \tag{2.3.13}$$

where $\Psi_{n,\kappa,m}$ is the wave-function of the system associated to the energy $E_{n,\kappa,m} \equiv E$. We try to find wave-functions under a factorized form in radial and angular parts

$$\Psi_{n,\kappa,m} = \frac{1}{r} \begin{pmatrix} P_{n,\kappa}(r)\Omega_{\kappa,m}(\theta,\varphi) \\ iQ_{n,\kappa}(r)\Omega_{-\kappa,m}(\theta,\varphi) \end{pmatrix}. \tag{2.3.14}$$

The radial parts $P_{n,\kappa}$ and $Q_{n,\kappa}$ are called large and small wave-function component, respectively. Before applying the operator h_D on the wave-function we have to express the term $\boldsymbol{\sigma} \cdot \boldsymbol{p} = -i\sigma_r \left(\partial_r + \frac{K+1}{r}\right)$[32],

$$h_D \Psi_{n,\kappa,m} = \begin{pmatrix} \frac{1}{\alpha^2} + V(r) & -\frac{i}{\alpha}\sigma_r \left(\partial_r + \frac{K+1}{r}\right) \\ -\frac{i}{\alpha}\sigma_r \left(\partial_r + \frac{K+1}{r}\right) & -\frac{1}{\alpha^2} + V(r) \end{pmatrix} \begin{pmatrix} \frac{P_{n,\kappa}(r)}{r}\Omega_{\kappa,m}(\theta,\varphi) \\ i\frac{Q_{n,\kappa}(r)}{r}\Omega_{-\kappa,m}(\theta,\varphi) \end{pmatrix}, \tag{2.3.15}$$

where α is the fine structure constant. We then obtain a system of two coupled equations for the radial part

$$\left[\frac{d}{dr} + \frac{\kappa}{r}\right] P_{n,\kappa}(r) = \alpha \left[E - V(r) + \frac{2}{\alpha^2}\right] Q_{n,\kappa}(r) \tag{2.3.16}$$

and

$$\left[\frac{d}{dr} - \frac{\kappa}{r}\right] Q_{n,\kappa}(r) = \alpha \left[V(r) - E\right] P_{n,\kappa}(r). \tag{2.3.17}$$

We have also set a variable change $E = E - 1/\alpha^2$.The normalization condition writes

$$\int_0^\infty \left[P_{n,\kappa}^2(r) + Q_{n,\kappa}^2(r)\right] dr = 1. \tag{2.3.18}$$

For convenience, we rewrite those first order differential coupled equations in a single second order differential equation, also known as Schrödinger-like form. We first define

$$A(r) = \sqrt{\left[E - V(r) + \frac{2}{\alpha^2}\right]} \tag{2.3.19}$$

and in order to cancel the first order derivative in equation (2.3.16) and (2.3.17) , we set

$$P_{n,\kappa}(r) = F_{n,\kappa}(r)A(r), \tag{2.3.20}$$

from (2.3.16) we can express the $Q_{n,\kappa}(r)$ in relation with $F_{n,\kappa}(r)$

$$Q_{n,\kappa}(r) = \frac{1}{A\left(r\right)}\left[\frac{d}{dr} + \frac{\kappa}{r}\right] F_{n,\kappa}\left(r\right). \tag{2.3.21}$$

Then by introducing (2.3.19),(2.3.20) and (2.3.21) in equation (2.3.17), we obtain the Schrödinger-like form

$$F_{n,\kappa}^{"}\left(r\right) + F_{n,\kappa}\left(r\right)\left\{2E - 2V\left(r\right) - \frac{\kappa\left(\kappa+1\right)}{r^2} + \alpha^2 W\left(r\right)\right\} = 0, \tag{2.3.22}$$

with

$$W\left(r\right) = \left(E - V\left(r\right)\right)^2 - \frac{1}{2A(r)^2}\left[V'' - \frac{3\alpha^2 V^{'2}}{A\left(r\right)^2} + \frac{\kappa V^{'}}{r}\right]. \tag{2.3.23}$$

In the literature, we often find the equation (2.3.22) rewritten with an effective potential labeled $U(r)$

$$F_{n,\kappa}^{"}\left(r\right) + F_{n,\kappa}\left(r\right)\left[2\left(E - U\left(r\right)\right) - \frac{\kappa\left(\kappa+1\right)}{r^2}\right] = 0, \tag{2.3.24}$$

where $U(r) = V(r) - \alpha^2 W(r)$. This equation is similar to the Schrödinger equation with an additional term $\alpha^2 W(r)$ which represents the relativistic effects valid even in the case where these are not perturbative terms. This equation (2.3.24) can be analytically solved in the case of an hydrogen-like ion, i.e for a potential $V(r) = -Z/r$. The procedure to find the wave-functions and energies is the same as for the Schrödinger equation. The solution for energies [31] is

$$E_{n,\kappa} = \frac{1}{\alpha^2\sqrt{1 + \left[\frac{\alpha Z}{(\kappa^2 - \alpha^2 Z^2 + n - |\kappa|)}\right]^2}}. \tag{2.3.25}$$

If we expand this energy in powers of αZ we find

$$E_{n,\kappa} = \frac{1}{\alpha^2} - \frac{Z^2}{2n^2} - \frac{\alpha^2 Z^4}{2n^3}\left(\frac{1}{|\kappa|} - \frac{3}{4n}\right). \tag{2.3.26}$$

We obtain in order of appearance the energy at rest of electron, the non-relativistic energy of the Schrödinger equation and the first order of relativistic corrections.

2.4 Spectroscopic notations

In a multi-electronic ion, we intend to build the global wave-function by adding products of independent electron wave-functions. Each electron is assumed to be described by the quantum numbers n, j, l, m. The quantum number n is a strictly positive integer which identifies the shell of an electron. The orbital quantum number l is also an integer and it is related to n as follows: $n \geq l + 1$, this number identifies sub-shells named orbitals. It

is the Pauli principle which determines the number of electrons that a shell and sub-shell can contain. For a shell we have $2n^2$ electrons and for a sub-shell $4l + 2$ electrons. Shells and sub-shells are identified by letters, some examples are given in the Table 2.1.

Table 2.1 : Spectroscopic notation for shells and sub-shells

Shell					
n	1	2	3	4	5
Notation	K	L	M	N	O

Sub-shell					
l	0	1	2	3	4
Notation	s	p	d	f	g

When all electrons of an atom or ion are defined by their sub-shells, they form a non-relativistic electron configuration. As an example the ground state of the helium is $1s^2$ and for the krypton the configuration is $1s^2 2s^2 2p^6 3s^2 3p^6 4s^2 3d^{10} 4p^4$. To each configuration correspond several atomic micro-states (i.e., with a given magnetic quantum number). The number of such states is called the degeneracy of a configuration. From the Pauli principle, the calculation of the degeneracy G of a configuration is the product of the degeneracies y_i of sub-shells:

$$G = \prod_i y_i = \prod_i \frac{(2l+1)!}{x_i!\,((2l+1)-x_i)!}, \tag{2.4.1}$$

where x_i corresponds to the number of electrons in the sub-shell i. If a sub-shell is full, its degeneracy is equal to one. On Table 2.2, we show an example of an excited state of a boron-like ion.

Table 2.2 : Example of degeneracy calculation on a boron-like ion

Configuration $1s^2 2s^1 2p^2$	
Sub-shell	Degeneracy
$1s^2$	1
$2s^1$	2
$2p^2$	15
G	30

In order to identify energy levels, spectral terms are used. Assuming L and S are approximate good quantum numbers which occurs when relativistic effect are small (low Z atoms), an ionic state is written ${}^{2S+1}L_J$. For an example, the ground state of carbon $1s^2 2s^2 2p^2$ is represented by the spectral term ${}^3P_0$.

The degree of ionization of an atom is labelled d with $d = Z - N$, where Z is the charge of the nucleus and N is the number of bound electrons. An lithium-like aluminium ion, can be identify by Al XI or Al^{10+}.

2.5 N electron ions

Until now, we have considered the Dirac and Schrödinger equations for one particle in a spherical field. However, our interest concerns multi-charged ions, with N bound electrons. In this section, we show how to obtain eigenvalues and eigenfunctions for such an ion. The Dirac or Schrödinger equation writes

$$H_{ion}\Psi_k = E_k\Psi_k, \tag{2.5.1}$$

where E_k is the energy of the state k associated to the wave-function Ψ_k. H_{ion} represents the Hamiltonian of the system (nucleus+bound electrons), it includes the following terms:

- Kinetic energies of electrons and nucleus
- The attractive potential of the nucleus on bound electrons
- The repulsive potential between bound electrons
- Relativistic corrections (spin orbit, Darwin, mass velocity), the Dirac equation intrinsically accounts for such terms.
- Quantum electrodynamics corrections (Breit interaction, vacuum polarization, Lamb shift) and the finite nuclear size; a subsection is dedicated to these corrections.

Considering the four first terms of the list, the relativistic Hamiltonian $H_{rel,ion}$ writes

$$H_{rel,ion} = \sum_{i=1}^{N} h_D(r_i) - \sum_{i=1}^{N}\frac{Z}{r_i} + \sum_{i<j}\frac{1}{r_{ij}}, \tag{2.5.2}$$

where $h_D(r_i)$ is the single-electron Dirac Hamiltonian with no potential, the second term corresponds to the attractive field between nucleus and bound electrons and the last term is for the electrostatic repulsion between bound electrons.

In the non-relativistic case, the Hamiltonian expresses

$$H_{non-rel,ion} = -\frac{1}{2}\sum_{i=1}^{N}\boldsymbol{\nabla}_i^2 - \sum_{i=1}^{N}\frac{Z}{r_i} + \sum_{i<j}\frac{1}{r_{ij}}. \tag{2.5.3}$$

For $N \geq 2$ such an Hamiltonian is not separable and therefore no analytical solution is possible. The only problem we can solve is that of a central field potential analyzed in section 2.2 and 2.3. In that case the total energy of the ion is simply the sum of the energies of all individual states. The main idea for solving the N electron ion problem is to reduce the real potential to a central average potential and treat the difference with the real one perturbatively.

2.5.1 Average central field

To obtain the eigenvalues of equation (2.5.1), we replace the nucleus potential and electron-electron interactions by an average central potential $U(r)$ and take into account perturbatively the difference between the average potential and the real potential. The Hamiltonian $H_{rel,ion}$ is split into two parts

$$H_{rel,ion} = H_0 + H_1, \tag{2.5.4}$$

where H_0 stands for the zero order relativistic Hamiltonian and is defined as follows:

$$H_0 = \sum_{i=1}^{N} \left[h_D(r_i) + U(r_i) \right]. \tag{2.5.5}$$

U is the average spherical potential replacing $-Z/r_i + 1/r_{ij}$. The second part of the Hamiltonian H_1 is

$$H_1 = \sum_{i=1}^{N} \left[-\frac{Z}{r_i} - U(r_i) \right] + \sum_{i<j} \frac{1}{r_{ij}}, \tag{2.5.6}$$

where H_1 is considered as a perturbation with respect to H_0, therefore $H_1 \ll H_0$. If we use a non-relativistic approach we have to add relativistic corrections (the spin-orbit interaction, mass, Darwin term) as an additional term H_2. Indeed, for elements with high Z the spin-orbit interaction is stronger than the electrostatic repulsion. In this non-fully relativistic approach, we write the Hamiltonian as

$$H_{non-rel,ion} = \underbrace{\sum_{i=1}^{N} \left[-\frac{1}{2}\boldsymbol{\nabla}_i^2 + U(r_i) \right]}_{H_0} + \underbrace{\sum_{i=1}^{N} \left[-\frac{Z}{r_i} - U(r_i) \right] + \sum_{i<j} \frac{1}{r_{ij}}}_{H_1} + \underbrace{\frac{\alpha^2}{2} \sum_{i=1}^{N} \frac{1}{r_i} U'(r_i) \boldsymbol{l_i} \cdot \boldsymbol{s_i}}_{H_2}. \tag{2.5.7}$$

We have ignored here relativistic corrections other than spin-orbit. This Hamiltonian can be divided into three parts H_0, H_1 and H_2; the last two are considered as small perturbation compared to H_0. Depending on the importance of the H_1 and H_2, two coupling can be defined:

- In the **LS coupling** we consider that $H_1 \gg H_2$, so we first add perturbatively H_1 to H_0 and then we apply H_2 as a perturbation of $H_0 + H_1$. This approximation is usually appropriate for low Z elements and also for weakly excited states of weakly ionized high Z .

- In the **jj coupling** we consider that $H_2 \gg H_1$, thus we first add perturbatively H_2 to H_0 and then we apply H_1 as a perturbation of $H_0 + H_2$. This approximation is appropriate for high Z elements highly ionized.

An example in Table 2.3 illustrates the level structure for these two coupling. The jj scheme is used with the Dirac equation because the individual electron wave-function are constructed by coupling their orbital and spin momentum l and s first.

Table 2.3 : Comparison of construction of levels with LS and jj coupling for a configuration $ns - mp$

LS coupling

H_0	H_1			H_2		
$ns - mp$	S	L	degeneracy	J	Level	degeneracy
$l_1 = 0$ and $l_2 = 1$	0	1	3	1	$^1P_1$	3
	1	1	9	0	$^3P_0$	1
				1	$^3P_1$	3
				2	$^3P_2$	5

jj coupling

H_0	H_2			H_1		
$ns - mp$	j_1	j_2	degeneracy	J	Level	degeneracy
$l_1 = 0$ and $l_2 = 1$	1/2	1/2	4	1	$^1P_1$	3
				0	$^3P_0$	1
	1/2	3/2	8	1	$^3P_1$	3
				2	$^3P_2$	5

2.5.1.1 Choice of local potential

Many methods exist to model the real potential $-Z/r_i + 1/r_{ij}$ with an average field $U(r)$ among which the Hartree-Fock-Slater method [33], the Dirac-Fock-Slater and the parametric potential [34, 35]. All these potentials have to fulfill two boundary conditions. Close to the nucleus the active electron has to see only the charge of the nucleus and at large distances the charge of the nucleus is screened by the $N - 1$ electrons. These conditions write

$$U(r) = \begin{cases} -\frac{Z}{r} & r \to 0 \\ -\frac{Z-N+1}{r} & r \to \infty \end{cases}. \tag{2.5.8}$$

Hartree-Fock-Slater

The potential is modelled by three terms in this approach. The first is the potential of the nucleus $-Z/r$. The second term labelled here V_c, accounts for the potential generated by the $N - 1$ electrons. This potential is calculated by the Poisson equation, where the density distribution of an electron in a sub-shell nl is defined by

$$\rho_{nl}(r) = \frac{R_{nl}^2(r)}{4\pi r^2}, \tag{2.5.9}$$

where R_{nl} is the non-relativistic wave-function of the active electron. By using the Poisson equation the potential is deduced

$$V_c(r) = \sum_{nl} w_{nl} \int_0^\infty \frac{r^{'2}}{r>} R_{nl}^2(r^{'}) dr^{'}. \tag{2.5.10}$$

where $w_{n,l}$ is the occupation number of the sub-shell nl.This potential is directly obtained through the Hartree-Fock equation and is called the classical potential. In the relativistic version, the term $R^2_{nl}(r')$ has to be replaced by $P^2_{n\kappa}(r') + Q^2_{n\kappa}(r')$.

The third term is the exchange interaction labelled $V_{ex}(r)$

$$V_{ex}(r) = -\left[\frac{24}{\pi}\rho(r)\right]^{1/3}. \tag{2.5.11}$$

For the coefficient of this potential we use the Kohn-Sham [6] value. This term is deduced from the hypothesis of a free electron gas (see for instance[14]). Finally the average potential used (for one electron) in the Hartree-Fock-Slater approach is

$$U(r) = -\frac{Z}{r} + V_c(r) + V_{ex}(r) \tag{2.5.12}$$

Parametric potential

An analytical expression is assumed for the parametric potential. The potential is usually taken as

$$U(r) = \frac{Z}{r}\sum_{n=0}^{m} a_n r^n e^{-b_n r}, \tag{2.5.13}$$

where m is an integer , a_n and b_n are parametric numbers which have to be optimized. These parameters may be determined by two ways: comparison with experimental data or variational principle. In practice such parametric potential codes try to find the parameters which minimize the average energy (Hartree-Fock criteria) of a configuration, thus the method is iterative. It is worth noting that this approach takes into account the exchange correlation term. Therefore, it is not necessary to add an extra term contrary to the previous methods. In the Flexible Atomic Code this type of potential is used, under the following form

$$U_{FAC}(r) = -\frac{Z}{r} + \frac{N-1}{r}\left(1 - \frac{e^{-\lambda r}}{1+ar}\right), \tag{2.5.14}$$

where λ and a are parameters to be determined. The first term stands for the nuclear potential and the second term for the electrostatic interaction. These parameters are determined via the energy minimization of a mean configuration specified by the user.

2.5.2 Average energy of a configuration

Independantly of any central potential used, we can evaluate the energy contribution of the different terms of Hamiltonian $H_{rel,ion}$ to a configuration C. Through the perturbation theory the average energy E_{avg} of the configuration C is determined by $\left\langle \Psi_k^{(0)} \left| H_{rel,ion} \right| \Psi_k^{(0)} \right\rangle$, where $\Psi_k^{(0)}$ are the zero order wave-functions of the Hamiltonian H_0. Using fully anti-symmetrized N mono-electronic wave-functions as required by the Pauli principle, we

obtain [31, 32]

$$E_{avg} = \sum_i^N \left\langle \gamma_i \left| \frac{1}{\alpha} \boldsymbol{\alpha} \cdot \boldsymbol{p} + \frac{\beta}{\alpha^2} \right| \gamma_i \right\rangle + \sum_i^N \left\langle \gamma_i \left| -\frac{Z}{r} \right| \gamma_i \right\rangle + \sum_{i<j} \left[\left\langle \gamma_i \gamma_j \left| \frac{1}{r_{ij}} \right| \gamma_i \gamma_j \right\rangle - \left\langle \gamma_i \gamma_j \left| \frac{1}{r_{ij}} \right| \gamma_j \gamma_i \right\rangle \right], \tag{2.5.15}$$

where i and j stand for electrons in the configuration C and γ represents any quantum number which characterize the state. We recognize the single particle Dirac Hamiltonian in the two first terms. These terms arise from the separable (one-electron) part of the Hamiltonian. The radial contribution for these two terms is directly obtained:

$$\begin{aligned} E^i_{avg,single} = \int_0^\infty \Big\{ & \frac{1}{\alpha^2} \left[P^2_{n,\kappa}(r) + Q^2_{n,\kappa}(r) \right] \\ & + \frac{1}{\alpha} \left[P_{n,\kappa}(r) \left(\frac{d}{dr} - \frac{\kappa}{r} \right) Q_{n,\kappa}(r) - Q_{n,\kappa}(r) \left(\frac{d}{dr} + \frac{\kappa}{r} \right) P_{n,\kappa}(r) \right] \\ & - \frac{Z}{r} \left[P^2_{n,\kappa}(r) + Q^2_{n,\kappa}(r) \right] \Big\} dr. \end{aligned} \tag{2.5.16}$$

The quantum numbers are noted as n, κ for simplicity but depend on the electron i.The last two terms of equation (2.5.15) correspond to the *electron-electron* interaction, they are a two electrons operator. It is more complicated to calculate due to its dependency on r_i and r_j. This term has to be rewritten through the Al-Kashi theorem $r_{12}^2 = r_1^2 + r_2^2 - 2r_1 r_2 \cos\theta$, and when using the Taylor series expansion and the Legendre polynomials it comes

$$\frac{1}{r_{12}} = \sum_{n=0}^{\infty} \frac{r_<^n}{r_>^{n+1}} P_n(\cos\theta). \tag{2.5.17}$$

Developing this term is too long and not of interest in the context of the present work, especially the angular contribution. The radial contribution of the electrostatic term is made of two integrals

$$F^n(12,12) = \int_0^\infty \int_0^\infty \left[P^2_{n,\kappa}(r_1) + Q^2_{n,\kappa}(r_1) \right] \frac{r_<^n}{r_>^{n+1}} \left[P^2_{n',\kappa'}(r_2) + Q^2_{n'\kappa',}(r_2) \right] dr_1 dr_2 \tag{2.5.18}$$

$$\begin{aligned} G^n(12,21) = \int_0^\infty \int_0^\infty & \left[P_{n,\kappa}(r_1) P_{n',\kappa'}(r_1) + Q_{n,\kappa}(r_1) Q_{n',\kappa'}(r_1) \right] \frac{r_<^n}{r_>^{n+1}} \\ & \times \left[P_{n',\kappa'}(r_2) P_{n,\kappa}(r_2) + Q_{n,'\kappa'}(r_2) Q_{n,\kappa}(r_2) \right] dr_1 dr_2 \end{aligned} \tag{2.5.19}$$

where n, κ (resp n', κ') are the quantum numbers of electron 1 and 2. The first integral is called direct integral, it corresponds to the field generated by the $N-1$ particles on the active electron. Contrary to the nucleus attraction, it contributes positively to the energy. The second integral is called exchange integral: it corresponds to the exchange interaction between electrons which is a consequence of the Pauli principle. The contribution of this term is negative.

2.5.3 Resolution of the N electron problem

Indenpendent particle solution

Once the average potential is chosen, we can start the resolution of the N electron problem. At zero order, we only have to consider the Hamiltonian H_0. We solve N independent Hamiltonians with a selected average potential. The resolved system of a mono-electron state i is

$$H_0\varphi_i^{(0)} = E_i^{(0)}\varphi_i^{(0)}. \tag{2.5.20}$$

Through this resolution we obtain the uncorrelated energies and wave-functions of N electrons forming a configuration C. The total energy of a level k in the configuration C is the sum of energies of N electrons

$$E_{k,C}^{(0)} = \sum_{i=1}^{N} E_i^{(0)} \tag{2.5.21}$$

and the total wave-function $\Psi_{k,C}$ is the product of N electrons wave-functions labeled $(\varphi_1, ..., \varphi_N)$. We also have to take into account the Pauli principle, which requests that the wave-function is antisymmetric. Therefore the zero order wave-function writes

$$\Psi_{k,C}^{(0)} = A\prod_{i=1}^{N}\varphi_{n,l,j,m}^{(0)}(r_i), \tag{2.5.22}$$

where A is the antisymmetric operator defined as

$$A = \frac{1}{\sqrt{N!}}\sum_{P}(-1)^{\chi(P)}\,P \tag{2.5.23}$$

where $\chi(P)$ is the parity of the permutation and P is any permutation of electrons.

Matrix elements of the non-central interaction

Once the uncorrelated wave-functions $\Psi_{k,C}^{(0)}$ are obtained, we have to correct the results accounting for H_1, whose matrix elements in this basis are

$$\left\langle \Psi_{k,C}^{(0)} \left| H_1 \right| \Psi_{k',C'}^{(0)} \right\rangle = \left\langle \Psi_{k,C}^{(0)} \left| \sum_{i=1}^{N} -\frac{Z}{r_i} \right| \Psi_{k',C'}^{(0)} \right\rangle - \left\langle \Psi_{k,C}^{(0)} \left| \sum_{i=1}^{N} U(r_i) \right| \Psi_{k',C'}^{(0)} \right\rangle + \left\langle \Psi_{k,C}^{(0)} \left| \sum_{i<j} \frac{1}{r_{ij}} \right| \Psi_{k',C'}^{(0)} \right\rangle. \tag{2.5.24}$$

The computation of the two first terms of the equation above is not difficult because $\Psi_{k,C}^{(0)}$ involves an antisymmetrized product of one electron wave-functions. However, the last term as we have seen before, has to be rewritten because it is a two-electron operator. To obtain the wave-function Ψ fully accounting for dielectronic interaction, we have to

diagonalize the full Hamiltonian $H_0 + H_1$

$$\Psi = \sum_{k,C=1} b_k \Psi^{(0)}_{k,C}, \tag{2.5.25}$$

where b_k are the mixing coefficients determined by the diagonalization of the total Hamiltonian. The number of configuration N_c plays an important role in the quality of the atomic data, because it allows to take into account the interaction of configuration. There is no clear criteria to choose the set of relevant configurations. This set may be defined by examining the convergence of the level energies when the number of configurations is increased.

Diagonalizion of the full Hamiltonian

To illustrate the general procedure, we conisder the case where only two configurations are included. The Hamiltonian which account for two configurations C_1 and C_2 has the general form

Configuration C_1	Configuration C_2
$E^{(0)}_{i,C_1}\delta_{ij} + \langle C_1 i \,\vert H_1 \vert\, C_1 j\rangle$	$\langle C_1 i \,\vert H_1 \vert\, C_2 j\rangle$
$\langle C_2 i \,\vert H_1 \vert\, C_1 j\rangle$	$E^{(0)}_{i,C_2}\delta_{ij} + \langle C_2 i \,\vert H_1 \vert\, C_2 j\rangle$

On the block diagonal we find the Hamiltonian matrix of a single configuration. On these blocks we identify on the diagonal the average energy with the correction due to the direct contribution of the Hamiltonian H_1 mentioned before. The off diagonal contributions come from the electronic coupling between electrons i.e LS coupling and the electrostatic interaction. The two non-diagonal blocks of the diagram correspond to the interaction of configuration ($H^{inte}_{C_1-C_2}$). This term is calculated in the same way as the matrix element of a single configuration. Finally, from the diagonalization of this matrix, in the given set of configurations we obtain energies and wave-functions of the considered ion.

2.5.4 Quantum electrodynamic and nucleus size effects

In the Flexible Atomic Code and in many relativistic codes, quantum electrodynamic (QED) corrections are added to the relativistic Hamiltonian. Some of these effects are important enough to modify the order of energy levels. In the resolution of the N-electron Hamiltonian, these effects are usually a second order effect.

Generalized Breit interaction

The Breit interaction is the most important QED correction for high Z elements. The first effect corresponds to the exchange of a virtual photon between two electrons. The second

effect is the retardation effect due to the interaction of a moving electron in a magnetic field generated by another electron. The general Breit interaction writes [36]

$$B(i,j) = -2(\boldsymbol{\alpha_i} \cdot \boldsymbol{\alpha_j})\frac{e^{i\omega r_{ij}}}{r_{ij}} + 2\left(\boldsymbol{\alpha_i} \cdot \boldsymbol{\nabla_i}\right)\left(\boldsymbol{\alpha_j} \cdot \boldsymbol{\nabla_j}\right)\frac{e^{i\omega r_{ij}} - 1}{\omega^2 r_{ij}}, \tag{2.5.26}$$

where ω is wave number of the exchanged virtual photon and $\boldsymbol{\alpha_i}$ is the Dirac matrix.

Lamb shift

This effect regroups two phenomena, the self-energy and the vacuum polarization. The self-energy corresponds to the emission of an electron by a photon or an electron/positron pair which is then reabsorbed. According to the QED, in the vacuum there is a constant creation and annihilation of electron/positron pairs, which is considered as a vacuum fluctuation. At the vicinity of an electron this pair is polarized leading to a small decrease of the effective charge of this electron. The Lamb shift notably explains the energy difference between levels $2s_{1/2}$ and $2p_{1/2}$ of H-like ions.

Nuclear finite size

This effect has an order of magnitude close to (but usually smaller than) the above discussed corrections.

The nucleus of ions possesses a finite size. To model this fact it is supposed that the charge of the nucleus is uniformly distributed in a sphere with a radius R_{nuc}. The potential is deduced from the Poisson equation

$$V_{nuclear}(r) = \begin{cases} -\frac{Z}{R_{nuc}}\left(\frac{3}{2} - \frac{r^2}{2R_{nuc}^2}\right) & \text{for } r \leq R_{nuc} \\ \frac{-Z}{r} & \text{for } r \geq R_{nuc} \end{cases}. \tag{2.5.27}$$

In FAC, the radius of the nucleus is determined by the empirical formula $R_{nuc} = 2.2677 \times 10^{-5} A^{1/3}$ in atomic units, where A is the atomic mass. Orbitals which are mostly affected by this effect are the ones with a significant density probability close to the nucleus.

An example of the energy contribution of the QED correction is given in Table 2.4. This data come from the article of Desiderio and Johnson [37].

2.6 Atomic models accounting for thermodynamics

The above discussion concerns an isolated ion, in this section we briefly present models which account for thermodynamics.

Table 2.4 : Contribution of the quantum electrodynamic term to the binding energy of a K electron shell with $Z = 74$

Terms	Energy contribution in Ry unit
Electrostatic energy	-5135.99
Breit (magnetic)	18.53
Lamb shift (self-energy)	10.96
Lamb shift (vacuum polarization)	-2.23
Breit (retardation)	-1.39
Total	5110.02

2.6.1 Thomas-Fermi approach

In this approach, the treatment of electron lies on a semi-classical treatment. We suppose in this model that bound and free electrons are classical particles. The electrons are described by a charge density $n_e(r)$ and not by their wave-function. It is assumed that, at a given position the density $n_e(r)$ is the one corresponding to a free electron gas obeying to the Fermi-Dirac statistics at the temperature kT_e with a kinetic energy

$$\frac{p^2}{2} = E - U\left(r\right) \tag{2.6.1}$$

where E is the ion total energy which is chosen to be zero. The charge density is supposed to be spherically symmetric

$$n_e(r) = \frac{\sqrt{2}}{\pi^2} k T_e^{3/2} F_{1/2}\left(\frac{U\left(r\right) - \mu}{kT_e}\right), \tag{2.6.2}$$

where μ is chemical potential and $F_{1/2}$ is the Fermi integral of order 1/2 defined by

$$F_n(x) = \int_0^\infty \frac{y^n}{1 + e^{y-x}} dy. \tag{2.6.3}$$

The potential is obtained by using the Poisson equation with the density (2.6.2)

$$U(r) = \int_0^\infty 4\pi \frac{r'^2}{r_>} n_e(r') dr', \tag{2.6.4}$$

where $r_> = max(r, r')$. The main problem of the Thomas-Fermi model is that the exchange correlation term is neglected in the e-e interaction. This term is only present through the Pauli principle in the Fermi distribution. An improvement of this model is made by the Thomas-Fermi-Dirac model which takes into account this missing term.

2.6.2 Average Atom model

We present here a basic average atom model inspired by the work of Blenski et al.[38] in a non-relativistic frame. This approach tries to model the plasma via an average cell

named Wigner-Seitz cell. In that cell the nucleus, the bound and the free electrons are present. On this sphere a neutrality condition is imposed. Under the hypothesis of an average field, each electron satisfies a self-consistent Schrödinger or Dirac equation

$$\frac{\partial^2 R_{n,l}}{\partial^2 r} + 2\left(E_{n,l} - V(r) - \frac{l\,(l+1)}{2r^2}\right) R_{n,l} = 0, \tag{2.6.5}$$

The difference with the previous models is that now $V\,(r)$ is a function of temperature. The same equation is solved for the free electrons. The average potential $V\,(r)$ is divided in two parts a direct and exchange term.

$$V = V_{dir} + V_{exc}. \tag{2.6.6}$$

The exchange term is simply derived from a local density approximation (see equation (2.5.11)).The direct term is calculated via the Poisson equation

$$\triangle V_{dir} = 4\pi\left(-\rho\,(r) + Z\delta\,(r)\right) \tag{2.6.7}$$

$\rho\,(r)$ is the electron density,$\rho\,(r) = \rho_{bound}\,(r) + \rho_{free}\,(r)$. The densities of bound electron is evaluated by

$$\rho_{bound} = \frac{1}{4\pi r^2}\sum_{n,l} 2\,(2l+1)\,F\,(E_{n,l},\mu)\,R_{n,l}\,(r)^2 \tag{2.6.8}$$

where $F\,(E_{n,l},\mu)$is the Fermi distribution

$$F\,(E_{nl},\mu) = \frac{1}{1+\exp\left[\left(E_{n,l}-\mu\right)/kT_e\right]}. \tag{2.6.9}$$

The free electrons density obeys to a similar equation as (2.6.8) by replacing n, l by ϵ, l. Finally, the chemical potential μ is obtained through the neutrality condition of the Wigner-Seitz cell. In the case of a spherical sphere of radius R_0, it comes

$$Z = 4\pi\int_0^{R_0} \rho\,(r)\,r^2 dr. \tag{2.6.10}$$

2.7 Summary

We have discussed the "Hartree-Fock type" approach to calculate the atomic structure of an isolated ion. In the FAC code, the average potential is used under the form of a parametric potential. The theoretical description of the ion is made via the Dirac equation with quantum electrodynamic corrections. As we may notice such description does not account for the free electrons. In the following chapter we show how in a subsequent step we account for the thermodynamic of plasmas.

Chapter 3

Basic properties of plasmas: kinetics and spectroscopy

3.1 Introduction

In this chapter we detail how to obtain the atomic populations and radiative properties of a plasma. We note that we only consider uniform plasmas. Three types of particles are present in the plasmas: ions, free electrons and photons. Therefore, it is more accurate to distinguish three temperatures, kT_e as the temperature of free electrons, kT_i as the ionic temperature and kT_r as the temperature of photons. Depending of the regime of study, those quantities can be equal or different. Futhermore, one may find situations where one or several types of particles are not thermalized. For instance, distribution with suprathermal electrons may deserve some attention.

The thermodynamical regime of the plasma depends on the competition between collisions and radiative processes. At least three regimes can be distinguished: non-local thermodynamical equilibrium (NLTE), local thermodynamical equilibrium (LTE) and the corona regime. First, in this chapter we define the elementary processes considered. Then the basic equations to obtain the atomic populations for NLTE, LTE and corona regime are given. A discussion of their domain of validity is made through semi-empirical formulas. This chapter ends with the calculation of atomic spectra and the line broadening.

3.2 Elementary processes

The elementary processes represent the interaction of ions with free electrons or photons leading to a change in the ionic structure. This change may be an excitation or deexcitation or a modification of the charge state of ions (ionization or recombination). We distinguish two categories of processes: collision and radiative processes. For the collisional processes, we only consider impact between an ion and a free electron, collisions between ions is disregarded due to their strong inertia.

Every elementary process corresponds to its inverse process. The relation between the direct and the inverse process rate is obtained from the micro-reversibility or detailed balance principle. We neglect elastic processes, which do not change the dynamics (rates) but may be included in line profile analysis.

In what follows, the symbol X represents some atomic element of charge Z, * corresponds to an excited state, e stands for an electron and $h\nu$ for a photon.

- **Collisional excitation and deexcitation;**

$$X(Z) + e \rightleftharpoons X^*(Z) + e. \tag{3.2.1}$$

- **Collisional ionization and three-body recombination.** Because the recombination involves two free electrons, it will be important at high densities. Its density dependence is in N_e^2;

$$X(Z) + e \rightleftharpoons X(Z+1) + 2e. \tag{3.2.2}$$

- **Auto-ionization (or Auger effect) and dielectronic capture;**

$$X^{**}(Z) \rightleftharpoons X(Z+1) + e. \tag{3.2.3}$$

- **Photo-ionization and radiative recombination;**

$$X(Z) + h\nu \rightleftharpoons X(Z+1) + e. \tag{3.2.4}$$

- **Spontaneous emission and photo-absorption**. We can add to the spontaneous emission the induced emission due to an external field;

$$X^*(Z) \rightleftharpoons X(Z) + h\nu. \tag{3.2.5}$$

The probability with which all those processes happen in the plasma determine the atomic and thermodynamical properties. These probabilities are defined by rates which describe the number of processes per unit of time

$$\text{rate} = \frac{\text{number of processes}}{\text{time}}. \tag{3.2.6}$$

For collisional processes involving electrons as projectiles, the rate R_{ij} from a level i to a level j writes

$$R_{ij} = N_e \langle v\sigma_{ij}(E) \rangle , \tag{3.2.7}$$

where $\sigma_{ij}(E)$ is the cross section of the considered process, N_e is the density of free electrons and v their velocity. Nv represents the number of particles hitting a unit of surface during a unit of time. Assuming that free electrons speed obeys a statistical

distribution $f(v)$, one has

$$R_{ij} = N_e \int_{v_{ij}}^{\infty} v f(v) \sigma_{ij}(v) dv, \tag{3.2.8}$$

where v_{ij} is the speed corresponding to the transition energy. The normalization is defined by

$$\int_0^{\infty} f(v) dv = 1. \tag{3.2.9}$$

The calculations of cross sections of elementary processes is a complex task, the chapter 4 is dedicated to that duty. Thanks to the detailed balance, we only have to calculate one process to obtain its inverse process. The detailed balance equation writes:

$$n_i R_{ij} = n_j R_{ji}, \tag{3.2.10}$$

where n_i and n_j are the populations of level i and j at local thermodynamical equilibrium. In the case of suprathermal electron, this relation does not hold.

3.3 Non-local thermodynamical equilibrium (NLTE)

We consider here a regime where the free electron collisions do not ensure the thermalization of the ionic level because the radiative processes are too important. We have

$$N_e \sum_{\substack{j \\ j<i}} C_{ij} \sim \sum_{\substack{j \\ j<i}} A_{ij}, \tag{3.3.1}$$

where C_{ij} is the rate coefficient of collisional excitation and A_{ij} is the radiative rate. Under this condition, the Boltzmann law is not verified, and neither the Saha-Boltzmann equations (cf equation (3.4.5)). However, we consider that free electrons are thermalized and, therefore follow the Maxwell distribution. This assumption does not hold in case of supra-thermal electrons. In the NLTE regime, we have to take into account all the elementary processes. To obtain the atomic population, we have to write a kinetic equation. We illustrate that purpose on figure (3.3.1) with a two-level ion;

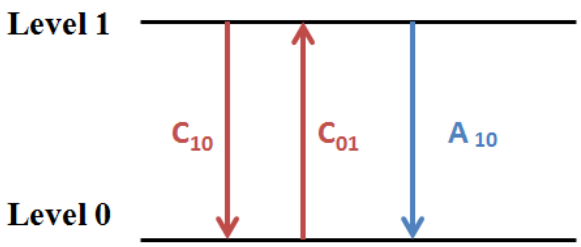

Figure 3.3.1 : Elementary processes considered in a two-level ion

The evolution of the population n_1 of level 1 depends on the population n_0 of level 0

and on the different process between them. We can write the equation

$$\frac{dn_1}{dt} = n_0 N_e C_{01} - n_1 \left(N_e C_{10} + A_{10}\right). \tag{3.3.2}$$

The generalization of this equation to all levels and ions present in the plasma, is called kinetic equation or rate equation and is written

$$\frac{dn_j(z)}{dt} = \sum_{z'} \sum_{k} n_k(z) W_{kj}^{z'z} - n_j(z) \sum_{z'} \sum_{i} W_{ji}^{zz'}, \tag{3.3.3}$$

where $W_{ji}^{zz'}$ is the matrix containing all the elementary process rates which contribute to the depopulation of level j of the ion z to level i of an ion z'. On the other hand, $W_{kj}^{z'z}$ corresponds to all elementary processes populating the level j of the ion z through level k of ion z'. The atomic populations are constrained by the condition

$$\sum_{z'} \sum_{j} n_j(z') = 1. \tag{3.3.4}$$

The rate equation is difficult to solve for many reasons. First, to describe accurately an ion, we have to deal with a large number of states (many millions in practical cases) and also deal with many ions. Then we have to take into account all the possible transitions between all those ion states which easily reach millions of transitions. To circumvent those difficulties, assumptions are made; the most commonly used is the hypothesis of stationarity $\frac{dn_j(z)}{dt} = 0$. This assumption holds when the macroscopic parameters such as the temperature and density vary more slowly than the microscopic parameters (collisional rates). Even in the stationary case, solving the kinetic system (3.3.3) is a difficult task. Moreover, the computation of millions (or billions) of rates is very demanding. The stationary assumption finds its application for the plasma-laser interaction, where the interaction is of the order of the nanosecond.

Another assumption used to simplify equation (3.3.3) is to suppose that the plasma is optically thin. It means that all emitted photons are supposed to escape from the plasma without being absorbed. Therefore, the photo-ionization process is discarded as well as the photo-absorption and the induced emission.

We point out that at a given temperature when the density increases, the collisional-radiative model converges to the LTE regime and when the density decreases, it converges to the corona regime.

3.4 Local thermodynamical equilibrium (LTE)

In the LTE regime, the collisions dominate the radiative processes, resulting in a thermalization of ions by the free electrons. The condition for a collisional LTE regime writes

$$N_e \sum_{\substack{j \\ j<i}} C_{ij} \gg \sum_{\substack{j \\ j<i}} A_{ij}. \tag{3.4.1}$$

We have the equality between the temperature of ions and free electrons $kT_e = kT_i$, because the micro-reversibility is ensured for collisional processes which are much more probable than the (unbalanced) radiative processes. A LTE regime can also be reached with a strong radiative field, this situation is named a LTE radiative regime. The thermodynamical equilibrium of an isolated system is defined by the maximum of entropy S such as

$$\Delta S = \Delta \left(k \ln P \left(n_1, n_2, ..., n_N \right) \right) = 0, \tag{3.4.2}$$

where P is the probability to distribute N particles with the respective populations $n_1, n_2, .., n_N$. From equation (3.4.2), we can obtain the four statistical laws which completely describe the plasma.

The free electrons velocity v distribution follows the Maxwell law

$$f(v) = \left(\frac{m}{2\pi k T_e} \right)^{3/2} v \mathrm{e}^{-mv^2/2kT_e}. \tag{3.4.3}$$

Conversely, if the free electrons are considered degenerate, they follow the Fermi-Dirac distribution.

The populations of levels i and j from the same ion labelled n_i and n_j, respectively, are distributed according to the Boltzmann law

$$\frac{n_j}{n_i} = \frac{g_j}{g_i} e^{-\Delta E_{ji}/kT_e}, \tag{3.4.4}$$

where $\Delta E_{ij} = E_j - E_i$ is the transition energy between level i and j, g_i and g_j are the statistical weights of level i and j, respectively.

The atomic population of levels of different ions obeys the Saha-Boltzmann equations

$$\frac{n_i^{Z+1}}{n_j^Z} N_e = 2 \frac{g_i^{Z+1}}{g_j^Z} \frac{\left(2\pi m k T_e\right)^{3/2}}{h^3} e^{-\Delta E_{ji}^{Z,Z+1}/kT_e}, \tag{3.4.5}$$

where $\Delta E_{ij}^{Z,Z+1}$ is the transition energy between level i of the charge state $Z+1$ and j of the charge state Z, g_i^{Z+1} and g_j^Z are their statistical weights.

Assuming a Planckian (thermal) radiation field at temperature kT_r, the photon distri-

bution is given by

$$\rho(\nu) = \frac{8\pi h\nu^3}{c^3}\frac{1}{e^{\frac{h\nu}{kT_r}} - 1}. \tag{3.4.6}$$

However, we have to point out that if the equilibrium is only local, photons will not follow the Planck law. This occurs because photons easily escape from a particular zone of the plasma, contrary to ions and electrons. This case concerns the optically thin plasma. The difference between a Global and a Local equilibrium is due to the presence of gradients of temperature and density. We remark, that to be at LTE, the stationarity is a necessary but not sufficient condition.

3.5 Corona regime

In the corona regime, the collisions are dominated by the radiative processes;

$$N_e \sum_{\substack{j \\ j<i}} C_{ij} \ll \sum_{\substack{j \\ j<i}} A_{ij}. \tag{3.5.1}$$

This regime concerns low density plasmas. Under this condition, we still have to solve a kinetic equation similar to equation (3.3.3). The atomic populations mainly remain in the ion ground state, meanwhile, the excited states have a population lower than the one obtained at LTE. Many atomic processes can be neglected, such as the three-body recombination which varies with the electron density as N_e^2. For the ground state, the atomic processes which dominate, are the radiative recombination R and the collisional ionization I. From this we can write for a ground state g

$$\frac{dn_g}{dt} = \sum_j \left(n_j R_{j,g}^{Z+1,Z} + n_j I_{j,g}^{Z-1,Z} - n_g I_{g,j}^{Z,Z+1} - n_g R_{g,j}^{Z,Z-1} \right). \tag{3.5.2}$$

We can also neglect all processes originating from an excited state. The excited states are mostly populated by collisional excitation originating from the ground state and depopulated by radiative decay. Usually excited states may also be populated by radiative decay from higher auto-ionization states but such process is only important for heavy ions [39]. The kinetic equation for an excited state i is as follows:

$$n_i^Z = n_g^Z N_e \frac{C_{g,i}}{A_{ig}}. \tag{3.5.3}$$

3.6 Validity of regime

To ensure the LTE regime, we have to justify the three statistical distributions for free electrons, ions and levels in an ion described above.

The Maxwell distribution of free electrons is the easiest to justify. To obtain this

distribution, free electrons need to thermalize. To estimate the equipartition time (unit is in seconds) which ensures the thermalization, Spitzer [40] has proposed

$$t_c = 3.3 \times 10^{-13} \left(\frac{kT_e}{100} \right) \frac{10^{21}}{N_i \log \Lambda}, \tag{3.6.1}$$

where kT_e is the temperature in eV, N_i is the ionic density in $\mathrm{cm}^{-3}$and $\log \Lambda$ is the Coulomb logarithm defined by

$$\Lambda = \frac{3}{2Z^{*2}} \left(\frac{(kT_e)^3}{\pi e^6 N_e} \right)^{1/2}. \tag{3.6.2}$$

One has $10 < \Lambda < 20$ for plasma with a temperature higher than10 eV. The characteristic time of thermalization is almost always less than the evolution time of the plasma. A numerical application for a neon plasma with $kT_e = 100$ eV and $N_e = 10^{18}\mathrm{cm}^{-3}$ with $Z^* \sim 9.8$, gives $t_c \approx 10^{-10}$s. However, in the case of femtosecond laser this assumption breaks.

For the Saha-Boltzmann equations, two mechanisms compete: the three-body recombination which drives the system to equilibrium and the radiative recombination which drives the system to NLTE. Salzmann [41] set the following criteria to ensure the validity of Saha-Boltzmann equations:

$$N_e \gg \frac{R_{rr}}{R_{r3b}} \equiv N_{Saha}, \tag{3.6.3}$$

where $N_e R_{rr}$ is the radiative recombination rate and $N_e^2 R_{r3b}$ is the three-body recombination rate. It is possible to give an analytical expression of those rates via empirical formulas. The Lotz formula (6.3.8) and Ref. [42] is used to calculate the ionization rates and R_{r3b} is determined by microreversibily. The radiative rate $N_e R_{rr}$ is derived from the Kramers formula (equation (6.3.12) and Ref.[43]). From these calculations, it comes

$$N_e \gg N_{Saha} = 10^{13}\mathrm{cm}^{-3}\mathrm{eV}^{-3} \left(kT_e\right)^3 \left(\frac{\Delta E_{ij}^{Z,Z+1}}{kT_e} \right)^{5/2}. \tag{3.6.4}$$

A numerical application gives a density of $N_{Saha} = 1.3 \times 10^{24}\mathrm{cm}^{-3}$ for the ionization of $1s$ of the H-like aluminium at $kT_e = 500$ eV. Griem [44, 45] has estimated that the density N_e has to be higher by a factor 10 from N_{Saha} to deviate from NLTE of 10%. The formulas used in equation (3.6.4) to determine the rates are not the most accurate and have to be used in particular conditions (cf chapter4). Especially the Kramers formula can only be used for hydrogen-like ions. Hence, we only consider the criteria (3.6.4) for hydrogen-like ions.

The last law to verify is the Boltzmann distribution which stands for the states in an

ion, where

$$N_e \gg \frac{A_{ij}}{C_{ij}}. \tag{3.6.5}$$

This law is the most difficult to justify because no accurate analytical formula for excitation cross section exists. However, using the Van Regemorter formula for the expression of the deexcitation rate, which is again valid under particular condition (cf chapter4), Mc Whirter[46] has proposed the condition

$$N_e \geq 1.8 \times 10^{14} k T_e^{1/2} \Delta E_{ij}^3 \tag{3.6.6}$$

in cm^{-3} and with kT_e and ΔE_{ij} in eV. Unfortunately, formula (3.6.6) is too strict condition and this formula has only proved their utility for hydrogen-like ions. Due to the difficulty to obtain an accurate analytical formula for the collisional excitation rate, we are not able to give a clear limit between LTE and NLTE regimes.

3.7 Radiative spectra

Once the atomic populations of the different species present in the plasma are obtained, the emission spectra of the plasma can be calculated. In validating theoretical models, emission and absorption spectra are one of the most important sources of information about the plasma status. Three different processes are considered: bound-bound, bound-free and free-free. Historically, the free-free and bound-free processes were the first to be considered for evaluating opacity in stellar atmospheres, notably by Eddington [47] who based his research on the work of Kramers [43] on photo-absorption cross sections.

3.7.1 Free-free spectrum

The electric field of ions can decelerate a free electron, as a consequence the electron loses energy and emits a photon. This phenomenon is called bremsstrahlung. The emissivity (energy per unit of time, volume and per energy of photon) may be evaluated from the semi-classical Kramers formula [40]

$$j_{ff}(E) = \frac{32\sqrt{6}}{9}\pi^{3/2}\frac{e^6}{m^{3/2}hc^3}\frac{Z^{*2}N_iN_e}{\sqrt{kT_e}}\exp\left(-\frac{E}{kT_e}\right)g_{ff}, \tag{3.7.1}$$

where g_{ff} is a corrective Gaunt factor, E is the photon energy and Z^* the ionization degree of the plasma. This radiation is important for fully ionized light elements. In most cases its contribution decreases with energy and is a continuous background.

3.7.2 Bound-free spectrum

This radiation originates from the recombination of free electrons with ions. Therefore, the radiation depends on the photo-ionization cross section. This process also supposes that the photon possesses an energy equal or superior to the ionization energy, otherwise the radiation is zero. The bound-free emission (energy radiated per unit of time, per energy of photon per ion) is given by

$$j_{bf}(E) = \begin{cases} \frac{4\pi}{h^3c^2}\lambda_{th}^3 n_j^{z+1}\frac{g_i}{g_j}N_e N_i E^3 \exp\left(-\frac{(E-\Delta E_{ij})}{kT_e}\right)\sigma_{ij}^{photo}(E)g_{bf} & \text{if } E \geq \Delta E_{ij} \\ 0 & \text{if } E < \Delta E_{ij} \end{cases}, \quad (3.7.2)$$

where $\Delta E_{ij} = E_j - E_i$ is the transition energy, g_{bf} is a corrective Gaunt factor which is equal to 1 if a quantum calculation is done for the photo-ionization cross section,λ_{th} is the electron thermal wavelength defined by

$$\lambda_{th} = \left(\frac{h^2}{2\pi m k T_e}\right)^{1/2} \quad (3.7.3)$$

and σ_{ij}^{photo} is the photo-ionization cross section. The main difficulty lies in the evaluation of the cross section because of its dependence on the photon energy. Obtaining cross section on the all relevant range of energy is possible but the calculation is very cumbersome, especially with the FAC suite that has been used in this work. To circumvent that problem, interpolations can be done on the "exact" quantum cross sections or by using a semi-empirical expression such as the Kramers formula [43] with a corrective Gaunt factor:

$$\sigma_{ij}^{photo}(E) = \frac{64}{3\sqrt{3}}\frac{\sqrt{R_y}}{Z}\frac{(\Delta E_{ij})^{5/2}}{E^3}a_0^2, \quad (3.7.4)$$

where R_y is the Rydberg constant and a_0 the Bohr radius. The Gaunt factor can be obtained trhought the ratio between the photo-ionization rate of an accurate method and the photo-ionization rate calulated by the Kramers formula.

This radiation is important for intermediate temperatures, mostly for highly ionized ions such as hydrogen-like, helium-like and lithium-like ions.

3.7.3 Bound-bound spectrum

The last radiation process is the most important for moderate and high Z elements which are not fully ionized. The radiation originates from the spontaneous emission. The emissivity per ion (energy radiated per unit of time, photon energy) of all excited levels present in the plasma is

$$j_{bb}(E) = \sum_i \sum_j \Delta E_{ij} n_j A_{ji} \varphi_{ij}(E), \quad (3.7.5)$$

where A_{ji} is the radiative rate from level j to i and $\varphi_{ij}(E)$ is the spectral profile, discussed in the next section.

3.7.4 Line broadening

The spectral profile $\varphi_{ij}(E)$ originates from various physical processes.

Natural broadening

The natural broadening is the consequence of the Heisenberg principle and is present whatever the plasma condition. Therefore, the excited states have a finite lifetime. The profile corresponding to this broadening is a Lorentz function

$$\varphi_{ij}(E) = \frac{\Gamma_{nat}}{2\pi} \frac{1}{\left(E - \Delta E_{ij}\right)^2 + \left(\Gamma_{nat}/2\right)^2}, \tag{3.7.6}$$

where Γ_{nat} is the width of the Lorentzian defined by

$$\Gamma_{nat} = \hbar \left(\sum_m A_{im} + \sum_i A_{jn} \right), \tag{3.7.7}$$

where A_{ij} stands for the radiative decay. This natural broadening is the weaker broadening in plasmas. Furthermore, it is almost impossible to measure this broadening. We may include the auto-ionization to the natural broadening. In the case of auto-ionizing states, the natural broadening may be of the same order of magnitude as the Stark broadening.

Doppler

Due to the motion of the ions in the plasma, the frequency of the emitted photon is shifted. The emission profile associated to this process follows a Gaussian distribution

$$\varphi_{ij}(E) = \frac{1}{\sqrt{\pi}\sigma_d} \exp\left[- \left(\frac{E - \Delta E_{ij}}{\sigma_d} \right)^2 \right], \tag{3.7.8}$$

where σ_d is the variance of the Gaussian. For the Doppler effect, the variance writes

$$\sigma_d = \Delta E_{ij} \sqrt{\frac{2kT_i}{Mc^2}}, \tag{3.7.9}$$

where M is the mass of the ion, kT_i is the temperature of the ion related to its motion of translation. We may write $kT_i = kT_e$, if we assume a thermalization of ions by the free electrons. This process is important for small Z and high temperature.

Stark effect

The Stark effect is a consequence of the interaction of local electric field with the emitter ion. The local electric field is generated by electrons and ions. Due to the difference of mobility of those particles, the Stark effet is in the standard approach decomposed into two parts: the electron impact broadening and the quasi-static Stark effect. An accurate description of this phenomenon is difficult and constitute a physics topic in itself. In order to describe that effect, we use semi-empirical formulas. For more details on line broadening topics we recommend the article of Baranger [48] and the book of Griem [49].

- **The electron impact broadening**

As its name indicates, this effect is induced by the collisions of free electrons which perturb the radiation by shortening the lifetime of excited states. It is generally assumed that the spectral profile is Lorentzian with a line width defined by [48], i.e equal to the collision rate of electrons and ions

$$\Gamma_c = N_e \langle \sigma v_e \rangle \,, \tag{3.7.10}$$

where σ stands for the total elastic and inelastic cross sections and v_e for the speed of free electrons. A rough estimation of the electron impact broadening gives $\Gamma_c \sim N_e/kT_e^{1/2}$. A semi-empirical formula of Dimitrijévic *et al.* [50] can also be used to evaluate the line width such as the

$$\hbar\Gamma_c = \frac{4\pi}{3}\sqrt{\frac{2\pi}{3}}\frac{\hbar^3}{m^{3/2}\left(kT_e\right)^{1/2}} N_e \left(0.9 - \frac{1.1}{Z^*}\right) \sum_{k=i,f} \frac{3n_k}{2Z^*}\left(n_k^2 - l_k^2 - l_k - 1\right), \tag{3.7.11}$$

where n_i (resp n_f) is the principal quantum number of the initial state (resp final state) and $Z^*$the effective charge of the considered ion, the summation being done on the initial and final state of the transition. Notice that such an expression lies on the hypothesis that only one electron is involved in the transition.

- **The quasi-static effect**

It concerns the micro-field generated by neighbouring ions. This effect is named quasi-static because the ions are supposed slow compare to the emission of radiation, thus the generated electric field is almost static. In that case the interaction time between the neighbouring ions and the emitter ion is longer than the time between two collisions. The micro-field is in the simplest case calculated via the Holstmark theory [51].

Depending on the density and temperature of the plasma, one broadening can dominate or two of them coexist. For low density plasma ($N_e \lesssim 10^{15} cm^{-3}$), the Doppler effect and the natural line broadening dominate. For moderately dense plasmas, the Doppler effect is the most important. For highly ionized plasma, the Stark effect dominates. We illustrate our purpose on the table 3.1

$kT_e = 500$ eV $N_e = 5 \times 10^{23}$ cm^{-3}

Transitions	ΔE (eV)	Natural (eV)	Doppler (eV)	Stark (eV)
1s-2p$_{1/2}$	1727.7	0.0118	0.573	0.537

$kT_e = 250$ eV $N_e = 10^{24}$ cm^{-3}

Transitions	ΔE (eV)	Natural (eV)	Doppler (eV)	Stark (eV)
1s-2p$_{1/2}$	1727.7	0.0118	0.406	1.518

Table 3.1 : Example of line broadening for Aluminium XIII. The Stark broadening only accounts for the electron impact contribution

It is thus possible and sometimes necessary to take into account several causes of broadening when none of them dominate. The line profile is in that case a convolution of profile functions.

The convolution of two Lorentzian L_1, L_2 is a Lorentzian L whose line width is defined by

$$\Gamma = \Gamma_1 + \Gamma_2. \tag{3.7.12}$$

The convolution of two Gaussian G_1, G_2 is a Gaussian G with a variance defined by

$$\sigma = \sqrt{\sigma_1^2 + \sigma_2^2}. \tag{3.7.13}$$

In the case of the convolution of a Gaussian and a Lorentzian, the result is a Voigt profile defined by

$$V(\omega, \Gamma, \sigma) = \frac{\Gamma}{2\pi} \int_{-\infty}^{\infty} \frac{\exp\left(-t^2\right)}{\left(\Gamma/2\right)^2 + \left(\omega - \omega_0 + \sqrt{2}\sigma t\right)^2} dt.$$

Assuming independent broadening processes, the resulting profile is given by the convolution product of individual processes.

3.8 Summary

In this work we assume that the active medium is optically thin, free electrons are thermalized, regime is stationary and plasma is uniform. Therefore, the thermodynamics of the plasma is entirely defined by the electronic temperature kT_e and density N_e. Since we are mainly interested in plasma out of thermodynamical equilibrium, the kinetic equations have to be solved. Therefore, the rates of the listed atomic process have to be calculated. In the following chapter we review the different methods used to evaluate the radiative rates and collisional cross sections.

Chapter 4

Radiative rates and electron-impact cross sections

4.1 Introduction

As mentioned in the third chapter, in order to solve the collisional-radiative equations it is necessary to obtain the radiative rates and collisional cross sections of the considered transitions. In this chapter we propose a description for the calculation hypothesis and methods which provide these cross sections. All these methods are presented in a non-relativistic framework for the sake of simplicity, but numerical work has been performed in a fully relativistic picture. This chapter also contributes to evaluate the convenient methods to calculate these rates. We are concerned here with the calculation of transition probabilities without consideration of the plasma influence, which will be analysed in the next chapter, with a special emphasis put on excitation cross sections. In the first part of this chapter we give the basic formula for radiative processes. Then in the second part, we review perturbative methods used to calculate collisional cross sections. In order to simplify the discussion we restrict the second part to the collisional excitation. The chapter ends with the classical theory used to calculate the collisional ionization cross section.

4.2 Radiative processes

Here, we describe transition processes induced by the radiation field in the discrete spectrum. To illustrate the Einstein coefficients, we consider a two-level ion, i corresponds to the lower level and j to the upper level. The kinetic equation of the level i is

$$\frac{dn_i}{dt} = -B_{ij}u_\nu n_i + \left(B_{ji}u_\nu + A_{ij}\right) n_j \tag{4.2.1}$$

where B_{ij} is the absorption coefficient, B_{ji} the stimulated emission coefficient, A_{ij} the spontaneous emission and u_ν the spectral density of energy. The coefficients are related by the Milne-Einstein relations

$$A_{ji} = \frac{8\pi h\nu^3}{c^3} B_{ji} \tag{4.2.2}$$

and

$$B_{ji} = \frac{g_i}{g_j} B_{ij}, \tag{4.2.3}$$

where c is the speed of light, h is the Planck constant, ν is the frequency, g_i and g_j correspond to the degeneracy of level i and j, respectively. It is more convenient to get the coefficient of the spontaneous emission because it does not depend on external field. To obtain the radiative decay rate, we have to calculate the probability of deexcitation of an atom due to the interaction with a radiative field. For an accurate description of the spontaneous emission A_{ji}, the field has to be quantized; called second quantization. The Hamiltonian of interaction between the particles and the field is

$$H_{int} = \frac{e}{2m_e c} \sum_{i=1}^{N} \left[\mathbf{P_i} \cdot \mathbf{A}(\mathbf{r_i}) + \mathbf{A}(\mathbf{r_i}) \cdot \mathbf{P_i} \right], \tag{4.2.4}$$

where $\mathbf{r_i}$ is the position of the electron and $\mathbf{P_i}$ is its kinetic momentum and $\mathbf{A}(r)$ is the potential vector in the Coulomb gauge. If a quantum description of the radiative field is required, the potential vector $\boldsymbol{A}(r)$ may be expressed by

$$\mathbf{A}(r) = \sum_k \sum_{\rho=1,2} \mathbf{u}_{\mathbf{k},\rho} \left(a_{k,\rho} e^{i\mathbf{k}\cdot\mathbf{r}} + a^\dagger_{k,\rho} e^{-i\mathbf{k}\cdot\mathbf{r}} \right), \tag{4.2.5}$$

where $\mathbf{u}_{\mathbf{k},\rho}$ is the polarization vector, k represents the wave vector, ρ is the polarization of the field, a and $a^\dagger$are the creation and annihilation operators, respectively. To obtain the probability of deexcitation from a state j to i, we use the Fermi golden rule

$$W_{i\to j} = \frac{2\pi}{\hbar} \left| \langle i \left| H_{int} \right| j \rangle \right|^2 \rho \left(E_i = E_j \right). \tag{4.2.6}$$

where $\rho\left(E_i = E_j\right)$ is the state density.This equation (4.2.6) means that the transition from a state j to i can only happen if the photon energy is equal to ΔE_{ij} the transition energy between level j and i.

4.2.1 Dipolar approximation

To lead the calculation of the spontaneous emission, the dipolar approximation is usually set. Under this approximation, we suppose that the wavelength of the radiative field is much larger than the dimension D of the atom $\lambda \gg D$. Therefore $\mathbf{k} \cdot \mathbf{r} \ll 1$ and the

exponential term of (4.2.5) can be expanded in series

$$e^{\mathbf{ik\cdot r}} = 1 + i\mathbf{k}\cdot\mathbf{r} - \frac{1}{2}(\mathbf{k}\cdot\mathbf{r})^{\mathbf{2}} + ... \tag{4.2.7}$$

In the dipolar approximation we only keep the first term of the series $e^{\mathbf{ik\cdot r}} \sim 1$.

The atomic size D is approximately estimated by n^2/Z, where n is the principal quantum number and Z is the nuclear charge. Meanwhile the relevant wave-lengths for our purpose are usually in the range $1 - 1000$ in a_0 unit. In the situation of hard X-ray, the dipolar approximation $\lambda \gg D$ breaks down . This will be the case in the future installations which use X-ray electron laser radiation (XFEL or LCLS). In that case we have to carry an exact calculations of the radiative rate.

By supposing the dipolar approximation true, the expression of the spontaneous emission is [14]

$$A_{ji} = \frac{4\left(\Delta E_{ij}\right)^3}{3\hbar^4 c^3 g_i}\left|\langle n_j l_j m_j \left|\mathbf{D}\right| n_i l_i m_i\rangle^2\right|. \tag{4.2.8}$$

between two mono-electronic states i and j , where $\mathbf{D} = -e\mathbf{r}$ stands for the dipolar electric momentum of the atom. The squared matrix element $\left|\langle n_j l_j \left|\mathbf{r}\right| n_i l_i\rangle^2\right|$is called the line strength S_{ji}. This line strength is related to the dimensionless oscillator strength (in absorption) by

$$f_{ij} = \frac{2m_e \Delta E_{ij}}{3\hbar^2 g_i} S_{ji}. \tag{4.2.9}$$

Finally, from the formulas (4.2.8) and (4.2.9) we obtain the spontaneous emission rates

$$A_{ji} = \frac{2e^2}{m_e \hbar^2 c^3}\frac{g_i}{g_j}\Delta E_{ij}^2 f_{ij}. \tag{4.2.10}$$

From this relation, we can deduce by using equations (4.2.2) and (4.2.3) the two other coefficients B_{ij} and B_{ji}. The spontaneous emission is calculated directly by the FAC code.

4.2.2 Photo-ionization

The calculation of the Photo-ionization cross sections is similar to the one of the spontaneous emission rate. The difference lies in the fact that the final state is not a bound orbital but an orbital of the continuum. By restricting the discussion to the dipolar approximation and considering a mono-electronic transition, it comes [52]

$$\sigma_{i,\epsilon} = \frac{8\pi^3 e^2 \nu}{3cg_i}\left(2l_i+1\right)\left(2l+1\right)\begin{pmatrix} l_i & 1 & l \\ 0 & 0 & 0 \end{pmatrix}^2\left[\int_0^\infty R_{\epsilon l}(r) r R_{n_i l_i}(r) dr\right]^2. \tag{4.2.11}$$

where i is the bound state with l_i its orbital quantum number momentum,ϵ identifies the continuum state with l its orbital quantum number momentum, $h\nu$ the energy of the incident photon, g_i the statistical weight of the initial state. The function $R_{nl}(r)$ stands

for the radial bound wave function and $R_{\epsilon l}(r)$ for the radial continuum wave function. The bound wave-functions are normalized to unity, while for the continuum wave-functions we have

$$\int_0^\infty R_{\epsilon l}(r) r^2 R_{\epsilon' l'}(r) dr = \delta\left(\epsilon - \epsilon'\right). \tag{4.2.12}$$

The main difficulty of this expression lies in the continuum wave function calculations.

In the expression of the spontaneous emission and the photo-ionization step in the radial wave functions of the bound electron. In the chapter 2 we have seen how to calculate these wave functions. But, in the photo-ionization, we also have to consider the continuum orbital. In the Flexible Atomic Code the continuum wave functions are obtained by solving the Dirac equation with the same central potential as for the bound states. The difference is that at large distance the continuum electron experienced the screening of an additional electron. By default in FAC the photo-ionization cross section is calculated using the distorted wave approximation. This method is discussed in the section (4.3.5).

4.3 Collisional excitation

In that part we consider the general problem of scattering of a particle by a spherical potential. Two methods are mainly investigated and used: the plane wave Born approximation (PWB) and the distorted wave method (DW). Both methods are implemented in the Flexible Atomic Code. A more detailed discussion about these two methods can be found in the references [53, 54, 55]. We also discuss methods which rely on the same formalism as PWB or DW. Finally, a list of semi-empirical formulas is also provided here. We point out that the discussion only concerns inelastic collisions.

4.3.1 General framework

At the moment, we only study potentials which decrease faster than $1/r$. By doing that, we exclude the Coulombian potential from this sub-section. Considering a particle of mass μ scattered by a potential $V(\boldsymbol{r})$, let the Hamiltonian H be defined as

$$H = \frac{p^2}{2\mu} + V(\boldsymbol{r}), \tag{4.3.1}$$

The corresponding Schrödinger equation can be written

$$\left[-\frac{\hbar^2}{2\mu}\triangle + V(\boldsymbol{r})\right]\Psi(\boldsymbol{r}) = E\Psi(\boldsymbol{r}), \tag{4.3.2}$$

or under another form, by introducing $E = \frac{\hbar^2 k_i^2}{2\mu}$, with k_i is the initial momentum of the particle and $V(\boldsymbol{r}) = \frac{\hbar^2}{2\mu} U(\boldsymbol{r})$:

$$\left[\triangle + k_i^2 - U(\boldsymbol{r})\right] \Psi(\boldsymbol{r}) = 0. \tag{4.3.3}$$

This equation possesses an infinite number of solution for each value of k_i. However, we know that physical conditions constrain us to only keep certain eigenstates. These eigenstates are called stationary states of scattering, labelled $\Psi_s(\boldsymbol{r})$. The physical condition is that in a given direction $\Omega = (\theta, \varphi)$ the radial dependency of an outgoing wave must be in the form $e^{ik_i r}/r$, the same condition apply to the inward wave. The amplitude of the outgoing wave depends on the considered direction $\Omega_{\boldsymbol{k_f}}$ because the scattering is usually not isotropic, defining $\boldsymbol{k_f} = k_f \boldsymbol{\Omega}$. These impose an asymptotic solution at infinity for the outward wave function of the equation (4.3.3)

$$\Psi_{s,\boldsymbol{k_i}} \underset{r\to\infty}{\sim} e^{i\mathbf{k}_i \cdot \mathbf{r}} + f_{\boldsymbol{k_i}}(\Omega_{k_f}) \frac{e^{ik_i \boldsymbol{r}}}{r}, \tag{4.3.4}$$

where the function $f_{\boldsymbol{k_i}}(\Omega_{\boldsymbol{k_f}})$ is called amplitude of diffusion. In the following we omit the subscripts k_i and k_f for the amplitude of diffusion, in order to simplify the notations. This function is linked to the differential cross section by

$$\sigma(\Omega) = \left|f(\Omega)\right|^2. \tag{4.3.5}$$

The demonstration of this relation can be found in the reference [55]. The total cross section is related to the differential cross section by

$$\sigma_{tot} = \int \sigma\left(\Omega\right) d\Omega \tag{4.3.6}$$

where $d\Omega$ is the solid angle. The solution of the scattering equation (4.3.3) may be rewritten in integral form

$$\Psi(\boldsymbol{r}) = \Phi_0(\boldsymbol{r}) + \int d^3 r' G\left(\boldsymbol{r} - \boldsymbol{r'}\right) U\left(r'\right) \Psi\left(\boldsymbol{r'}\right) \tag{4.3.7}$$

where $G(\boldsymbol{r})$ is the Green function on the operator $[\triangle + k^2]$:

$$\left[\triangle + k^2\right] G(\boldsymbol{r}) = \delta(\boldsymbol{r}). \tag{4.3.8}$$

Considering the asymptotic form (4.3.4), the solution of $\Phi_0(\boldsymbol{r})$ is a plane wave and $G(\boldsymbol{r}) = G_+(\boldsymbol{r}) = -\frac{1}{4\pi}\frac{e^{i\boldsymbol{k_f}.\boldsymbol{r}}}{r}$, therefore equation (4.3.7) becomes

$$\Psi_s(\boldsymbol{r}) = e^{i\mathbf{k}_i \cdot \mathbf{r}} + \int d^3 r' G_+\left(\boldsymbol{r} - \boldsymbol{r'}\right) U\left(\boldsymbol{r'}\right) \Psi_s\left(\boldsymbol{r'}\right), \tag{4.3.9}$$

for the scattering amplitude in the direction of the vector $\boldsymbol{k_f}$ (4.3.4), we get

$$f(\Omega) = -\frac{1}{4\pi}\int d^3r' e^{-i\boldsymbol{k_f}\cdot\boldsymbol{r}'} U(\boldsymbol{r}')\Psi_s(\boldsymbol{r}'). \tag{4.3.10}$$

We, thus, deduce from formula (4.3.5) the differential cross section

$$\sigma(\Omega) = \frac{\mu^2}{4\pi^2\hbar^4}\left|\int d^3r' e^{-i\boldsymbol{k_f}\cdot\boldsymbol{r}'} V(\boldsymbol{r}')\Psi_s(\boldsymbol{r}')\right|^2. \tag{4.3.11}$$

This expression is exact but in general the wave function Ψ_s is unknown. We can write this equation under different forms:

$$\frac{d\sigma_{a\to b}}{d\Omega} = \frac{\mu^2}{4\pi^2\hbar^4}\left|\langle\Phi_{0,a}\left|V\right|\Psi_{s,b}\rangle\right|^2 \tag{4.3.12}$$

where $\Phi_{0,a}$ is the plane wave in the direction $a \equiv \boldsymbol{k_i}$, and $\Psi_{s,b}$ the scattered wave-function in the direction $b \equiv \boldsymbol{k_f}$. Another notation is

$$\frac{d\sigma_{a\to b}}{d\Omega} = \frac{\mu^2}{4\pi^2\hbar^4}\left|T_{a\to b}\right|^2, \tag{4.3.13}$$

where $T_{a\to b}$ is the transition matrix for the scattering from $a \equiv \boldsymbol{k_i}$ to $b \equiv \boldsymbol{k_f}$, but it is not strictly the matrix element of the operator V because $\Phi_0(\boldsymbol{r})$ and $\Psi_s(\boldsymbol{r})$ do not belong to the same basis. A discussion about the Born approximation is made by Seaton in Ref.[56].

4.3.2 Plane wave Born approximation

Usually the value of the scattered wave function $\Psi_s(\boldsymbol{r})$ is unknown, nevertheless we can build step by step a solution of the integral equation (4.3.9). The differential equation is by consequence solved by iteration:

$$\Psi_s(\boldsymbol{r}') = e^{i\mathbf{k_i}\cdot\mathbf{r}'} + \int d^3r'' G_+\left(\boldsymbol{r}' - \boldsymbol{r}''\right) U\left(\boldsymbol{r}''\right)\Psi_s\left(\boldsymbol{r}''\right). \tag{4.3.14}$$

We replace (4.3.14) in equation (4.3.9), we can repeat this operation as much as necessary. Thereby we obtain the Born development, where each term of the series involves an increasing power of U. When we stop at the first order, it is commonly named the plane wave Born approximation (PWB). We thus obtain at the first order:

$$\Psi_s(\boldsymbol{r}) = e^{i\mathbf{k_i}\cdot\mathbf{r}} + \int d^3r' G_+\left(\boldsymbol{r} - \boldsymbol{r}'\right) U\left(\boldsymbol{r}'\right) e^{i\boldsymbol{k_i}\cdot\boldsymbol{r}}. \tag{4.3.15}$$

By substituting G_+ by its expression and using equation (4.3.3)we find the PWB differential cross section:

$$\sigma_{born}(\Omega) = \frac{\mu^2}{4\pi^2\hbar^4}\left|\int d^3r e^{-i\mathbf{K}\cdot\mathbf{r}} V(\boldsymbol{r})\right|^2, \tag{4.3.16}$$

where $\mathbf{K} = \mathbf{k_i} - \mathbf{k_f}$. Finally we can sum up:

$$\frac{d\sigma_{a\to b}}{d\Omega} = \frac{\mu^2}{4\pi^2\hbar^4} \left|\langle \Phi_{0,a} \left|V\right| \Psi_{s,b}\rangle\right|^2 \sim \frac{\mu^2}{4\pi^2\hbar^4} \left|\langle \Phi_{0,a} \left|V\right| \Phi_{0,b}\rangle\right|^2 . \tag{4.3.17}$$

The obtained cross section is simply linked to the squared modulus of the Fourier transform of the interaction potential. This approximation is valid if the orders superior to 1 are negligible. To fulfil this criteria the interaction potential has to be small enough so that the wave $\Psi_s(\boldsymbol{r})$ differs little from the plane wave Φ_0. We point out that such result (4.3.17) may be find using the Fermi golden rule (4.2.6). We recall that these formulas are valid for all potentials decreasing faster than $1/r$, otherwise the Fourier integral does not converge.

4.3.3 Scattering by an atom/ion

The considered problem is the inelastic scattering of a charged particle by an atom or an ion. The atomic units are use in this section. We apply to that problem the plane wave Born approximation. Therefore, the incident and scattered particle are solutions of

$$\left[\triangle + k^2\right] \phi(\boldsymbol{r}) = 0. \tag{4.3.18}$$

The outward and inward wave function write, respectively

$$\Phi_f = \frac{e^{i\mathbf{k}_f\cdot\mathbf{r}}}{(2\pi)^{3/2}} \qquad \Phi_i = \frac{e^{i\mathbf{k_i}\cdot\mathbf{r}}}{(2\pi)^{3/2}}, \tag{4.3.19}$$

where k_i, k_f are the initial and final electron momentum, respectively. The interaction potential of the target has the form:

$$V(\boldsymbol{r}) = \sum_{q=1}^{N} \frac{1}{|\boldsymbol{r} - \boldsymbol{r}_q|} - \frac{Z}{r}. \tag{4.3.20}$$

We only consider a mono-electronic transition. The matrix element $T_{a_i\to a_f}$ from a state a_i to a_f writes according to formula (4.3.17)

$$T_{a_i\to a_f} = \int \frac{\mathbf{dr} e^{-i\mathbf{K}.\mathbf{r}}}{(2\pi)^3} \left\langle n_i l_i \left| \frac{1}{|\boldsymbol{r} - \boldsymbol{r}_q|} - \frac{Z}{r} \right| n_f l_f \right\rangle, \tag{4.3.21}$$

We integrate over $\boldsymbol{r}$ knowing that

$$\int \mathbf{dr} \frac{e^{-i\mathbf{K}.\mathbf{r}}}{|\boldsymbol{r} - \boldsymbol{r}_q|} = \frac{4\pi}{\mathbf{K}^2} e^{-i\mathbf{K}.\mathbf{r_q}}. \tag{4.3.22}$$

Therefore, the square of the matrix element becomes

$$\left|T_{a_i\to a_f}\right|^2 = \frac{1}{4\pi^4\mathbf{K}^4}\left|\left\langle a_i\left|e^{-i\mathbf{K}.\mathbf{r_q}}\right|a_f\right\rangle\right|^2. \tag{4.3.23}$$

In equation (4.3.23), the contribution of the nucleus is zero due to the orthogonality of the states $a_i \equiv n_i l_i$ and $a_f \equiv n_f l_f$ (inelastic collision). To carry on the calculation, we expand the exponential term [55], in order to separate the radial and angular coordinates we also set $\boldsymbol{K}$ parallel to $\boldsymbol{z}$,

$$e^{i\boldsymbol{K}.\boldsymbol{r}_q} = 4\pi\sum_{\delta=0}^{\infty} i^\delta j_\delta\left(\boldsymbol{K}.\boldsymbol{r}_q\right)\sum_{m=-\delta}^{\delta}(-1)^m Y^*_{\delta m}\left(\boldsymbol{K}\right)\cdot Y_{\delta m}\left(\boldsymbol{r}_q\right), \tag{4.3.24}$$

where $j_\delta(x)$ is the spherical Bessel function related to the Bessel function of the first kind $J_\delta(x)$ [57] by

$$j_\delta(x) = \sqrt{\frac{\pi}{2x}}J_{\delta+1/2}(x). \tag{4.3.25}$$

Introducing this expression in equation (4.3.23), we get

$$\left|T_{a_i\to a_f}\right|^2 = \frac{1}{4\pi^4 K^4}$$
$$\left|\sum_{\delta=0}^{\infty}4\pi i^\delta\sum_{m=-\delta}^{\delta}(-1)^m Y_{\delta-m}\left(\boldsymbol{K}\right)(-1)^{l_i-m_i}\begin{pmatrix} l_i & \delta & l_f \\ -m_i & m & m_f\end{pmatrix}\left\langle l_i\left\|j_\delta\left(\boldsymbol{K}.\boldsymbol{r}_q\right)Y_\delta\left(\boldsymbol{r}_q\right)\right\|l_f\right\rangle\right|^2; \tag{4.3.26}$$

by expanding the square element, we have

$$\left|T_{a_i\to a_f}\right|^2 = \frac{1}{4\pi^4\boldsymbol{K}^4}\sum_{\delta=0}^{\infty}(2\delta+1)\left|\left\langle l_i\left\|j_\delta\left(\boldsymbol{K}.\boldsymbol{r}_q\right)Y_{\delta m}\left(\boldsymbol{r}_q\right)\right\|l_f\right\rangle\right|^2. \tag{4.3.27}$$

The bound wave functions are expressed by $\Psi_{n_i l_i,m_i} = \frac{1}{r}R_{n_i l_i}(r)\,Y_{l_i,m_i}(\theta,\varphi)$ (see chapter 2), then

$$\left|T_{a_i\to a_f}\right|^2 = \frac{1}{4\pi^4 K^4} \tag{4.3.28}$$
$$\sum_{\delta=0}^{\infty}(2\delta+1)\left[(-1)^{l_i}\left[\delta l_i l_f\right]^{1/2}\begin{pmatrix} l_i & \delta & l_f \\ 0 & 0 & 0\end{pmatrix}\int_0^\infty R_{l_i}(r)j_\delta(Kr)R_{l_f}(r)dr\right]^2,$$

where$[\delta l_i l_f] = (2\delta+1)(2l_i+1)(2l_f+1)$. The total excitation cross section from a state a_i to a_j is related to the differential cross section by

$$\sigma_{a_i,a_f} = (2\pi)^4\frac{k_f}{k_i}\int d\Omega_{k_f}\left|T_{a_i\to a_f}\right|^2, \tag{4.3.29}$$

where $d\Omega$ is the solid angle, $\boldsymbol{K}$ is related to Ω by the relation $2KdK = 2k_i k_f \sin(\theta_f)\, d\theta_{k_f}$, therefore

$$\sigma_{a_i,a_f} = (2\pi)^5 \frac{k_f}{k_i} \int_0^\pi d\theta_f \sin(\theta_f) \left|T_{a_i \to a_f}\right|^2 = \frac{(2\pi)^5}{k_i^2} \int_a^b K dK \left|T_{a_i \to a_f}\right|^2, \tag{4.3.30}$$

where $a = k_i - k_f$, $b = k_i + k_f$. By using the expression (4.3.28), the total cross section is

$$\sigma_\delta(l_i, l_f) = \frac{8\pi}{k_i^2 (2l_i + 1)} \int_a^b |R_\delta(K)|^2 \frac{dK}{K^3} \tag{4.3.31}$$

in atomic units, with$\delta = |l_i - l_f|, ..., l_i + l_f$ and with

$$R_\delta(K) = (-1)^{l_i} [\delta l_i l_f]^{1/2} \begin{pmatrix} \delta & l_i & l_f \\ 0 & 0 & 0 \end{pmatrix} \int_0^\infty R_{n_f l_f}(r) R_{n_i l_i}(r) j_\delta(Kr) dr. \tag{4.3.32}$$

Discussion

The plane wave Born approximation is not supposed to hold for V decreasing as $1/r$, as a consequence PWB gives better results for neutral targets than ions. Accordingly, we can verify that the PWB approximation gives a zero cross section at threshold. This point is due to the presence of the $1/k_i^2$ term in the formula (4.3.31). A zero cross section at threshold is acceptable for a neutral but not for an ion, because the long range target-projectile potential decreases faster than $1/r$ for a neutral target. The Born cross section is in good agreement at high energy because it assumes that the wave function is weakly perturbed, close to the nucleus; i.e that the kinetic energy is much greater than the relevant transition energy.

However, the PWB overestimates the cross section at its peak by a factor of 1.5 to 2[53]. This weakness can be explained by the fact that plane wave Born approximation does not take into account either the distortion of the incident and scattered wave function by the field of the target or the exchange. The distorted wave theory has been developed to circumvent this weakness. We also notice that the PWB does not take into account a spin exchange, therefore PWB completely fails to reproduce forbidden transitions.

To take into account the exchange with the Born approximation, we can use the Born-Oppenheimer theory. However, in that theory the initial and final wave functions are no more orthogonal. In that frame Ockur [58] and Beigman [59] have proposed a tractable formula of the Born approximation with exchange for neutral atom.

The advantage of the PWB is its computational efficiency, because only the radial wave function of the initial and final bound state are needed. We mention an interesting work by Kim [60] which improves the plane wave Born approximation and gives very good agreement for neutral atom. However, as stated by the author himself no rigorous justification of this scaling cross section has been found up to now. The scaled cross

section proposed is

$$\sigma_{ij}^{BE} = \sigma_{Born} \frac{E_i}{E_i + \Delta E_{ij} + E_{ioni}}, \tag{4.3.33}$$

where E_i is the energy of the incident particle, ΔE_{ij} is the transition energy between the initial and final state, E_{ioni} is the ionization energy of the level i.

4.3.4 Generalised Born approximation

It is highly desirable to generalize the Born approximation to any potential, including those behaving asymptotically as $1/r$. Since the interaction potential V may be too strong to be treated by a perturbative method, it is convenient to deal with a potential U close to V and treat the difference as a perturbation. We know the exact solution for the potential U. Therefore, we set

$$V(r) = U(r) + W(r). \tag{4.3.34}$$

The total Hamiltonian H writes

$$H = H_1 + W, \tag{4.3.35}$$

with

$$H_1 = \frac{p^2}{2m} + U, \tag{4.3.36}$$

where H_1 is the Hamiltonian for which a solution is supposed to be known, W is the rest of the interaction. The known eigenstates of H_1 are labelled by η. In the case of a Coulombic form potential, the asymptotic stationary state of H_1 is [55]

$$\eta_s \sim e^{i[\boldsymbol{k_i}.\boldsymbol{r} + \gamma \ln k_i (r-z)]} + f(\theta, \varphi) \frac{e^{i[k_i r - \gamma \ln 2k_i r]}}{r}. \tag{4.3.37}$$

where $\gamma = z_1 z_2 e^2/hv$, in which $v = \hbar k_i/\mu$.The evaluation of the scattering amplitude $f(\theta, \varphi)$ has to be performed with a Green-Coulomb function. We recall that the expression for the differential cross section between two states a and b for H_1 is

$$\frac{d\sigma_{a\to b}}{d\Omega} = \frac{\mu^2}{4\pi^2\hbar^4} \left| T_{a\to b}^{H_1} \right|^2, \tag{4.3.38}$$

where

$$T_{a\to b}^{H_1} = \langle \Phi_{0,a} | U | \eta_{s,b} \rangle . \tag{4.3.39}$$

To obtain the total matrix transition of the Hamiltonian H, we only need to add the perturbative contribution of W

$$T_{a\to b}^{H} = T_{a\to b}^{H_1} + \left\langle \eta_{s,b}^{-} | W | \Psi_{s,a} \right\rangle , \tag{4.3.40}$$

where $\Psi_{s,a}$ is the exact scattered wave function, the sign - indicate an outward wave and no sign an inward wave. The differential cross section is expressed as

$$\frac{d\sigma_{a\to b}}{d\Omega} = \frac{\mu^2}{4\pi^2\hbar^4}\left|T^H_{a\to b}\right|^2. \tag{4.3.41}$$

If we apply the Born approximation at first order, we can write

$$\left\langle \eta^-_{s,b}\left|W\right|\Psi_{s,a}\right\rangle \simeq \left\langle \eta^-_{s,b}\left|W\right|\eta_{s,a}\right\rangle. \tag{4.3.42}$$

Again the validity of the Born approximation at first order lies on the fact that the stationary wave $\Psi_{s,a}$ is supposed to be close to $\eta_{s,a}$.

4.3.5 Distorted wave method

The DW method has been first developed by Mott and Massey [55]. The purpose of DW is to take into account the distortion of the incident and the scattered wave functions by the field of the target. This two facts are not included in the PWB theory. In the literature, the distorted wave method may have two different meanings

- Fano and Inokuti [61] consider it as a perturbative method. We present it in 4.3.5.1.
- Mott and Massey [55] consider it as an approximation of a two level close-coupling approximation. We present it in 4.3.5.2.

Within these two approaches, various DW methods can be found. Most of the existing methods have been reviewed by Henry [62] for positive ions and Itikawa [63] for ions and atoms.

4.3.5.1 DW as a perturbative approach

In that approach the DW method may be seen as a generalization of the Born approximation, seen in 4.3.4. The eigenfunctions of the non-perturbed Hamiltonian H_1 verify

$$\left[\triangle + k^2 - 2U(r)\right]\Phi(\boldsymbol{r}) = 0. \tag{4.3.43}$$

The inward wave functions of the incident electron can be written as

$$\Phi_i = \frac{1}{\sqrt{2\pi}}\sum_{l_i m_i} i^{l_i}\frac{F^{k_i}_{l_i}(r)}{r}Y^*_{l_i m_i}(\boldsymbol{K})\cdot Y_{l_i m_i}(\boldsymbol{r_i}), \tag{4.3.44}$$

where the functions $F^k_l(r)$ are solutions of

$$\left[\frac{d^2}{dr^2} - \frac{l\,(l+1)}{r^2} - 2U(r) + k^2\right]F^k_l(r) = 0. \tag{4.3.45}$$

The scattered wave function is deduced from the same equation. It means that the same potential is experienced by the incident and scattered wave function. By using the same calculation as in equation (4.3.21), we get the differential cross section

$$\frac{d\sigma^{DW}_{a_i,a_f}}{d\Omega} = \frac{4\pi}{k_i^3 k_f} \sum_{l_f,m_f,l_i,m_i} \left| \int dr \frac{F^{k_i}_{l_i}}{r} Y^*_{l_i m_i} \left\langle n_i l_i m_i \left| W(r) \right| n_f l_f m_f \right\rangle \frac{F^{k_f}_{l_f}}{r} Y_{l_f m_f} \right|^2 . \tag{4.3.46}$$

We clearly see that for $U(r) = 0$, we retrieve the plane wave Born approximation.

4.3.5.2 DW as an approximation to a two level close-coupling system

The close-coupling method (CC) [64, 65] is a non-perturbative approach. This method proposes to treat N-integro differential equations of a given set of states. In the CC method, different processes are taken into account: the interaction between the initial and final state, the interaction between other present states and the exchange. The DW method is derived by only considering the initial and final state. The two coupled equations for the initial and final states are

$$\left[\triangle + k_i^2 - 2V_i(r)\right] \Phi_i(r) + 2V_{if}(r)\Phi_f(r) = 0, \tag{4.3.47}$$

$$\left[\triangle + k_f^2 - 2V_f(r)\right] \Phi_f(r) + 2V_{fi}(r)\Phi_i(r) = 0, \tag{4.3.48}$$

where potentials V_{if} and V_{fi} represent the interaction potential with the target. The potentials V_i and V_f correpond to the distortion potential of the initial and final state, respectively (usually the electrostatic potential of the target). In the DW approach seen as a perturbation theory, they correspond to the potential U. The assumption is made to neglect the influence of the initial state on the final state, therefore, $V_{if} = 0$. From this we conclude that the differential cross section from state i to f is

$$\frac{d\sigma^{DW}_{i\to f}}{d\Omega} = \frac{\mu^2}{4\pi^2\hbar^4} \left| \left\langle \Phi_f \left| V_{fi} \right| \Phi_i \right\rangle \right|^2 . \tag{4.3.49}$$

Discussion

We note the first important point: if the DW is seen as a perturbative theory, the initial and final potential are equal $V_i = V_f$. On the other hand, with the two level CC approximation, the potentials are different $V_i \neq V_f$. The choice of initial and final potential has been discussed by different authors [63] [66].

According to the literature [67, 68], the choice $V_i = V_f$ gives the best results compared to the experiment. However, this option could be considered as unatural due to the change of the state of the ion. Furthermore, such an assumption breaks the micro-reversibility

principles as stated by Winters [69]. Meanwhile, with a first order perturbation point of view the wave functions have to be orthogonal, therefore, the potential has to be identical.

As pointed out by Fano[61], the difference between $V_i = V_f$ and $V_i \neq V_f$ is only important at low energy where the DW method is not supposed to be accurate. The DW method is valid as soon as the interaction with the target is small, therefore, as for the PWB, we do not expect a good accuracy at low energy. However, the range of validity of DW is broader than PWB thanks to the consideration of the distortion potential and the exchange. It is generally assumed that the DW is reasonable for intermediate to high energy.

Numerically, the DW method requires more intensive effort because the Schrödinger or Dirac equations have to be solved for each incident particle, leading to a longer computing time compared to PWB.

Neutral versus ion

A point of interest for this thesis is the case of neutral targets. Indeed, for neutral species excitation cross section behaves differently than that of ions because of the absence of a long range potential. If we consider the asymptotic boundary condition of the scattered electron wave function, then for neutral target the PWB is better than DW. This is because the potential has the asymptotic behavior compatible with the hypothesis made in the PWB approximation. The long-range potential of a neutral atom is obviously not Coulombic.

Solbeman [53] mentioned that the DW method may overestimate the cross section for a neutral target. This is because at short distance the repulsion between the optical electron and the outer electron overcome the attractive field of the atom. Furthermore, DW method gives better results for highly ionized atoms [61], because the interaction between the initial and final state become weaker than the distortion potential.

We point out that atomic package codes such as FAC and HULLAC have been built to model moderately to highly ionized atoms. We conclude by asserting that DW is better than PWB in most cases except for neutral targets. But this superiority is accidental because PWB is only valid at high energy.

4.3.6 Coulomb-Born approximation

This approximation is related to the generalised Born approximation. It lies between the DW method and the PWB. The potential seen by the incident particle has a Coulombic form with an asymptotic charge of the form $Z-1$. The functions $F_l^k(r)$ are then solutions of the equation

$$\left[\frac{d^2}{dr^2} - \frac{l\,(l+1)}{r^2} + 2\frac{Z-1}{r} + k^2\right] F_l^k(r) = 0. \tag{4.3.50}$$

The cross section section is deduced by the formula (4.3.46) as for DW and PWB. We highlight that distorted wave and Coulomb-Born (CB) are different, indeed for $Z = 1$ this approximation coincide with the first Born approximation (4.3.31). Conversely, if $Z \to \infty$, DW and CB match.

4.3.7 Bethe approximation

This approximation relies on the PWB approximation. The first assumption made is to assume a small momentum transfer $K \to 0$. It leads to an expansion of the Bessel functions (4.3.25) present in the cross section expression (4.3.31):

$$j_\delta(Kr)_{K\to 0} = \frac{2^\delta \delta! K^\delta}{(2\delta+1)!} r^\delta, \tag{4.3.51}$$

The second hypothesis consists in only keeping the dipolar transition ($\delta = 1$). From (4.3.51), (4.3.31) and (4.3.32), the cross section is

$$\sigma_{a_i,a_f}^{Bethe} = \frac{8\pi}{k_i^2 \Delta E_{if}} f_{a_i a} \ln\left(\frac{K_0}{k_i - k_f}\right) \tag{4.3.52}$$

in atomic units, where $f_{a_i a_f}$ is the oscillator strength between states a_i and a_f ,$K_0 = \sqrt{\Delta E_{if}}$ and ΔE_{if} is the transition energy. Because of the small momentum transfer hypothesis ($K \to 0$) this formula is only reliable at high energy, where the PWB is expected to be physically accurate.. A detailed discussion of the Bethe approximation is made by Inokuti in Ref [70].

4.3.8 Empirical formula

Many empirical formulas have been developed to evaluate the excitation cross section. Most of those developments are based on the plane wave Born approximation.Therefore they are only reliable at relatively high energy. However, due to their simplicity those formulas are extensively used in kinetic model to obtain the collisional rates. The main motivation is linked to the large effort required by the computational time of the more accurate method such as CC, R-matrix or DW. Moreover, those formulas provide at least a rough approximation for the behaviour of the cross section.

4.3.8.1 Van Regemorter formula

The Bethe (4.3.52) cross section leads to

$$\sigma_{a_0,a} = \frac{8\pi}{k_i^2 \Delta E} f_{a_i a} g(k_i, k_f) \tag{4.3.53}$$

where $g(k_i, k_f)$ is called the Gaunt factor. In the Bethe theory, this factor is $g(k_i, k_f) = \ln\left(\frac{K_0}{k_i - k_f}\right)$. Alternate expressions for the Gaunt factor are available in the literature.

Through experimental observations done on ions and atoms, Van Regemorter [71] has tabulated the different values for the Gaunt factor. He recommends to use the Gaunt factor equal to 0.2 for ions. In this thesis we have used the Gaunt factor proposed by Mewe [72] listed in the Table 4.1, where e_i corresponds to the incident energy and $\Delta E_{ij}$to the transition energy.

Table 4.1 : Gaunt factor proposed by Mewe depending of the transition

Gaunt Factor	Transition type
$0.15 + 0.28 \log\left(\frac{e_i}{\Delta E_{ij}}\right)$	$\Delta n \neq 0$
$0.6 + 0.28 \log\left(\frac{e_i}{\Delta E_{ij}}\right)$	$\Delta n = 0$
$0.1 \times \frac{e_i}{\Delta E_{ij}} \log\left(\frac{e_i}{\Delta E_{ij}}\right)$	$\Delta S = 0$
0.15	forbidden transition

These empirical formula are not very accurate but offer a good evaluation of the behaviour of the cross section for dipolar electric transitions. Notably Sampson *et al.* [73] have carried an extensive study of the Van Regemorter formula. They show that this formula gives correct results for transition in the same shell.

4.3.9 Numerical test on cross sections calculations

We focus our attention on the quality of the excitation cross section of FAC, especially on neutral. The reason is because our goal is to study the effects of the plasma environment on collisional cross sections. When we will add the plasma potential in the FAC code, we will modify the asymptotic behavior of the potential. With the plasma potential the asymptotic behaviour is the one of a neutral atom and not the one of an ion. This point will be discussed in the chapter 6.

In the FAC code two methods are mainly used: the PWB and DW, both fully relativistic. Unfortunately neither the FAC documentation nor the article [20] give explicitly the choice of DW method $V_i = V_f$ or $V_i \neq V_f$. We do not have the possibility to assert with no doubts which DW is implemented in FAC. However, as pointed out by Fano [61] both choices will only differ at low energy, where DW is not expected to be accurate.

We study three situations: the hydrogen atom, the helium atom, the Ne-like iron. To compare the numerical results of FAC, we plot the data from the DW of Mann [74], and data of Hagelestein et al [75]. Both of those DW methods use the DW version of Mott and Massey $V_i \neq V_f$, exchange is included. We also take as the reference the First Order Many Body Theory (FOMBT) of Csanak et al. [76], this method has been successfully compared on many neutral targets[77, 78, 79]. Rescigno et al. [80]have showed that FOMBT pertained to the DW theories, where $V_i = V_f$. The DW of Mann and the FOMBT is used by the ATOMIC package [18, 81, 82], both methods are available on the Los Alamos national laboratory website.

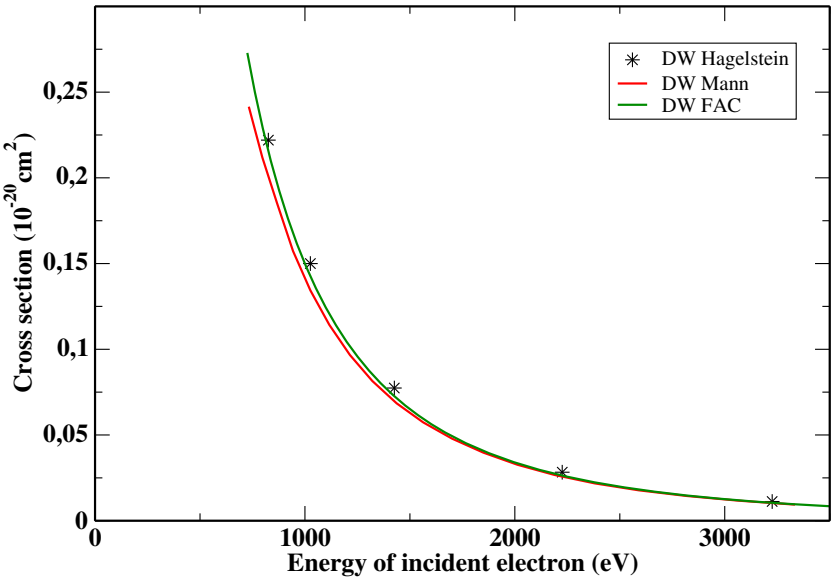

Figure 4.3.1 : Excitation cross section of Fe Neon-like, transition $1s^22s^22p^6$ to $1s^22s^22p^53s$. DW method of FAC , DW method of Mann [74], DW Hagelestein et al. [75].

In the case of the Ne-like iron, as presented in Figure 4.3.1, all DW methods agree quite well. In that situation the target is highly ionized therefore the DW approximation is relevant. The DW method of FAC is closer to the one of Hagelstein because the energy of the considered transition is closer than the transition energy given by Mann. For FAC we have $\Delta E = 725.52$ eV, from Hagelestein $\Delta E = 725.82$ eV and from Atomic $\Delta E = 725.18$eV.

In the Figure 4.3.2 and 4.3.3, we plot the excitation cross section of 1s to $2p_{1/2}$ transition in hydrogen and of $1s^2$ to $1s^12p^1$ transition in helium atom. The FOMBT theory is taken as the reference for both plots. We notice that the DW method of FAC does not have the expected behaviour near threshold for the cross section. Its behaviour is closer to the one of an ion rather than a neutral target. We point out that the PWB of FAC gives a "better" results than DW, we shall not forget that PWB is only valid at high energy. Indeed, as mentioned before the PWB considers a plane wave for the incident electron. This corresponds to the case of a fully screened potential.We may therefore considered as "accidental" the success of PWB. For many neutral cross sections the DW of FAC gives an inaccurate behaviour at low energy, this point is mentioned by the author of FAC in the user manual with no explanations. Finally, we also see that the DW of FAC and of Mann are quite different at threshold.

4.4 Collisional ionization

As for the collisional excitation, the DW and the PWB approaches may be used to evaluate the ionization cross section. However, in FAC by default another method is implemented: the Binary Encounter Dipole theory (BED) of Kim [83]. The DW method is also present

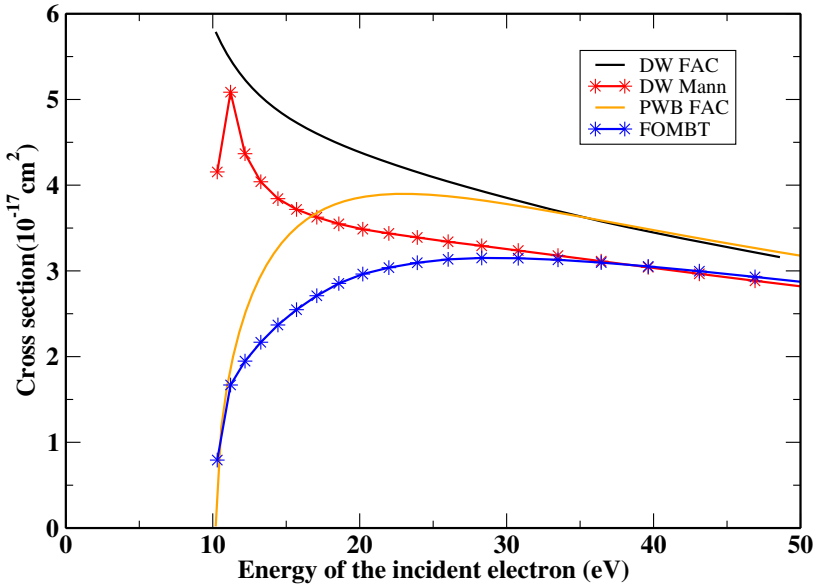

Figure 4.3.2 : Excitation cross section of Hydrogen atom, transition 1s to $2p_{1/2}$. DW method of FAC (black curve), DW method of Mann [74](red curve with stars), PWB of FAC (orange curve) and FOMBT of Csanak et al.[76].

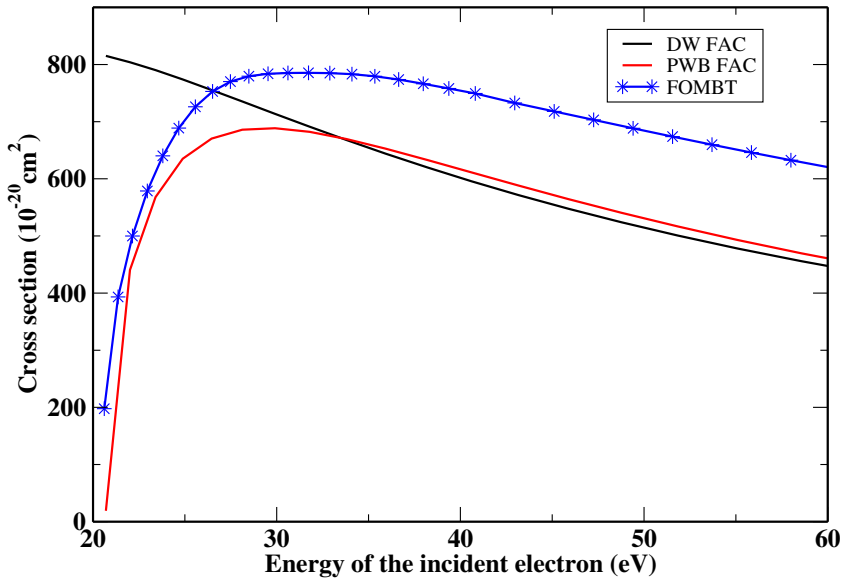

Figure 4.3.3 : Excitation cross section of Helium atom, transition $1s^2$ to $1s2p_{1/2}$ J = 1. DW method of FAC (black curve), PWB of FAC (red curve) and FOMBT of Csanak et al.[76].

in FAC for ionization cross section, but by default the BED is used. This is because the BED theory is faster than DW. This theory belongs to the class of "classical scattering theory". By classical theory, we mean theories which do not describe the structure of the atom. L.Vriens made a detail discussion of the Binary encounter theory in Ref.[84]. In the classical theory, two assumptions are made:

- The incident particle interacts with only one target
- The interaction between the atomic electron (target) and the nucleus is neglected.

The first assumption can be regarded as the Born approximation (one scattering center), the second assumption is only possible if the interaction between the "bound" electron and the atom takes place in a region smaller than the dimension of the atom. This means that binary theory should give good results for hard collision (large momentum transfer compared to the momentum of the bound electron or close collision). Under these hypotheses the considered system could be seen as scattering of two free electrons. In the following sub-section we present the classical "Rutherford " and the quantum "Mott" calculations cross section for that system.

4.4.1 Rutherford and Mott scattering

We consider two particles with masses m_1 and m_2 and charge z_1e and z_2e, respectively. In the center of the mass applies the following Schrödinger equation:

$$\left[-\frac{\hbar^2}{2\mu}\triangle + \frac{z_1 z_2 e^2}{r}\right]\Psi(r) = E\Psi(r), \tag{4.4.1}$$

where μ is the reduced mass, E is the energy in the center of mass frame. Defining $\gamma = z_1 z_2 e^2/hv$, where $v = \hbar k/\mu$, we can write

$$\left(\triangle + k^2 - \frac{2\gamma k}{r}\right)\Psi(\boldsymbol{r}) = 0. \tag{4.4.2}$$

This equation may be solved by using the parabolic coordinates, the detailed demonstration is made in [85]. The solution is

$$\Psi(\boldsymbol{r}) = \Gamma(1+i\gamma)\, F_1(-i\gamma; 1; ik(r-z)) \exp\left(-\frac{1}{2}\pi\gamma + ikz\right). \tag{4.4.3}$$

F_1 is the confluent hyper geometric function[57].We only need the asymptotic behaviour of that wave function to obtain the diffusion amplitude labelled $f_c(\theta)$ which is

$$f_c(\theta) = -\frac{\gamma}{2k\sin^2\left(\frac{\theta}{2}\right)} \exp\left(-i\gamma \ln\left(\sin^2\left(\frac{\theta}{2}\right)\right) + 2i\sigma_0\right), \tag{4.4.4}$$

where $\sigma_0 = \arg\Gamma(1+i\gamma)$. For two non-identical particles we can write

$$\sigma(\theta,\varphi) = \left| f_c(\theta,\varphi)^2 \right|, \tag{4.4.5}$$

from which we obtain the cross section

$$\sigma(\theta,\varphi) = \left[\frac{z_1 z_2 e^2}{2\mu v^2}\right]^2 \frac{1}{\sin^4\left(\frac{\theta}{2}\right)}. \tag{4.4.6}$$

This cross section coincides with the classical cross section found by Rutherford.

In the case of identical particles, the wave function has to be antisymmetric in the exchange of these two particles. This leads to

$$\sigma(\theta,\varphi) = \left| f_c(\theta,\varphi) - f_c(\pi-\theta,\varphi) \right|^2. \tag{4.4.7}$$

We finally obtain, by using equation 4.4.4, the Mott cross section[86]:

$$\sigma_{Mott}(\theta,\varphi) = \left[\frac{z_1 z_2 e^2}{2\mu v^2}\right]^2 \left[\frac{1}{\sin^4\left(\frac{\theta}{2}\right)} + \frac{1}{\cos^4\left(\frac{\theta}{2}\right)} - \frac{\cos\left(\gamma \ln\left(\tan^2\left(\frac{\theta}{2}\right)\right)\right)}{\sin^2\left(\frac{\theta}{2}\right)\cos^2\left(\frac{\theta}{2}\right)}\right]. \tag{4.4.8}$$

The terms in the Mott formula correspond respectively to the direct collision (as in Rutherford formula), the exchange collision between the two particles and the interference between exchange and direct collision. The two last terms are the consequence of the exclusion principle. In the first order Born approximation the hypothesis is to neglect the exchange between particles. Through PWB we may retrieve the Rutherford cross section but not the Mott cross section.

4.4.2 Binary encounter dipole theory

Here, we summarize the main method used in the Flexible Atomic Code to calculate ionization cross sections. This theory[83] merges two approaches. The first one is binary encounter theory valid for large momentum transfer. The second theory used is the Bethe approximation valid for small momentum transfer (4.3.52). The Bethe formula shows that the interaction between the target and the incident electron mainly takes place through the dipole terms (explaining the name of the theory). In the Mott cross section (4.4.8) the target electron is supposed to be at rest. This consideration is not realistic because the atomic electron has an orbital velocity. Therefore in the Binary encounter theory [84] a velocity distribution is given to the atomic electron. Kim et al. [83] proposed for the differential cross section :

$$\frac{d\sigma}{dW} = \frac{4\pi a_0^2 N E_H^2}{B+T+U} \left[\frac{N_i/N-2}{T+B}\left[\frac{1}{W+B}+\frac{1}{T-W}\right] + \frac{\ln(T/B)}{N(W+B)} + (2-N_i/N)\left[\frac{1}{(W+B)^2}+\frac{1}{(T-W)^2}\right]\right] \frac{df(W)}{dW}. \tag{4.4.9}$$

where T is the kinetic energy of the incident particle, W is the energy of the scattered electron, B is the binding energy, U is the average kinetic energy of the atomic electron, N is the number of electrons and E_H is Rydberg constant. The term df/dW is bound-free differential oscillator strength and $N_i = \int_0^\infty dW\ df/dW$. In that formula, the only difficulty remains in the calculation of the bound-free oscillator strength df/dW. The formula (4.4.9) can be applied for ions or neutral target as mentioned by its author.

The Binary encounter theory is not suitable for excitation cross section computation[84]. Indeed, two problems arise: we cannot define properly a quantization of the angular momentum and we cannot distinguish between different azimuthal quantum numbers.

4.5 Summary

We have reviewed a large set of methods to calculate collisional cross sections and the radiative rates. We highlight that the frame of this chapter was non-relativistic though, in FAC a relativistic version is implemented. As we have seen in this this chapter, we conclude that for neutral or near neutral atoms the DW option in FAC cannot be reasonably used, but is reliable for highly stripped ion. In the case of ions in a plasma, as in chapter 5, the PWB will be used. In table 4.2, we summarize the methods used to obtain the atomic cross sections. In FAC the auto-ionization is calculated via DW method with no other option, explaining why we did not discuss auto-ionization in this chapter.

Table 4.2 : Cross section methods used to provide our atomic data

	DW	PWB	CB	BED	Empirical-formula	Fit
Collisional Excitation	×	×	×		×(Mewe)	
Collisional ionization	×			×	×(Lotz)	
Photo-ionization	×				×(Kramers)	×
Auto-ionization	×					

Chapter 5

Plasma potential

5.1 Introduction

The developments in the previous chapters concerned an isolated ion. However our work is devoted to ions immersed in a plasma environment. Few atomic code take into account the environment of ions. Most of the time the effect of the plasma are added in the atomic code through perturbation theory or at the step of the kinetic code. This work represents a first attempt to include the plasma effect in the Flexible Atomic Code. The environment of ions plays a significant role at high density, leading to effects such as plasma polarization shifts, pressure-induced ionization, changes on the absorption and emission spectra and on the equation of state. Taking into account such effects in a consistent way is a serious task since the number of involved particles is huge, which suggests to treat free electrons statistically. As mentioned by Rosznay[8] we may distinguish two types of approaches to determine the plasma potential: the ion correlation and ion sphere theories.

In the ion correlation model, the ion is immersed into an infinite polarizable medium (also called jellium). Asymptotically, the positive and negative charges cancel out each other to form a neutral background. The mostly known and used ion-correlation model is the Debye-Hückel theory [87, 88, 89]. An other approach pertaining to the density of the functional is the atom in the jellium of Perrot [10], Blenski and Piron [11, 12].

In the ion sphere model the ion is enclosed in a cell which contains the exact number of electrons to ensure the neutrality of the sphere. The ion sphere model has been extensively used [7, 9, 12, 90], in order to get energy levels and transition rates of ions in plasmas. Such models assume a spherical symmetry and define an electron density distribution that obeys self-consistency equations. Coupling the Poisson equation and the statistical distribution of electrons, one may obtain Thomas-Fermi [91, 92] or relativistic Thomas-Fermi [7].

All these theories pertain to the group of density functional theories [93]. One must notice that they also assume thermodynamic equilibrium. Additionally some formalisms only assume cylindrical symmetry and use a molecular approach describing the inter-

action with the nearest ion [94]; this approach mainly concerns strongly correlated plasmas.When a realistic quantum description of bound electrons is required and when dealing with non-local-thermal-equilibrium (non-LTE) plasmas, only free electrons will be treated statistically. Under this assumptions (ion-sphere + statistical treatment of free electrons) we have firstly used the uniform electron gas model (UEGM) and then a Thomas-Fermi approach (TF). Both approaches are implemented in the FAC code [20]. We point out that a very popular model for level shifts which make the connection between the Debye-Hückel and the ion-sphere model has been developed by Stewart and Pyatt [95]. However this model assumes thermal equilibrium for ions as well as electrons.

In this chapter we briefly discuss the Debye-Hückel theory. Then a detailed discussion is carried on the ion sphere model for the UEGM and the TF approach. We extend previous approaches based on UEGM assumptions by deriving analytical formulas in non relativistic hydrogen-like ions. This analytical work is used to check the atomic data of the modified FAC code.

Atomic units are used throughout this chapter.

5.2 Debye-Hückel

One of the first attempt to model plasma effects was the Debye-Hückel theory [87, 88, 89]. The first assumption of this theory is to assume a Boltzmann distribution of free electrons and ions. The second hypothesis is to consider that

$$\left|\frac{V(r)}{kT_e}\right| \ll 1 \tag{5.2.1}$$

Owing to this hypothesis we can linearize the Boltzmann distribution of ions and electrons. Then, the Poisson equation is solved to obtain the potential. It comes while keeping the first order term of densities

$$V(r) = -\frac{Z}{r}e^{-\frac{r}{\lambda_D}} \tag{5.2.2}$$

with

$$\lambda_D^2 = \frac{kT_e}{4\pi N_i\left(\sum_j Z_j^2 f_j + Z_f\right)} \tag{5.2.3}$$

is the Debye length, f_j is the fraction of ion with charge $Z_j$and Z_f the number of free electrons. Of course, the assumption of linearization of the Boltzmann distribution induced strong limitation on the range of application of the Debye-Hückel potential. To fulfill the criterion $\left|\frac{V(r)}{kT_e}\right| \ll 1$, the temperature has to be high and the density low, or can only be applied if the potential of the nucleus is weak which implies a large principal quantum

number. Weisheit [96]proposed the validity condition

$$\frac{4}{3}\pi\lambda_D^3 N_e \gg 1 \tag{5.2.4}$$

For plasmas out of thermodynamical equilibrium, the assumption of the Boltzmann distribution for ionic levels is not relevant. A last argument which has been pointed out by Nguyen et al [97] is that the correlation time of the ion is much longer than the lifetime of excited atomic states. So we have estimated that this model limited to weakly correlated plasma is not relevant for our purpose.

5.3 Ion sphere model

Under the ion sphere model pertain all models which assume a neutral cell containing a central ion surrounded by its environment. Moreover, one assumes that the free electron density exactly cancels the ion density beyond the Wigner-Seitz radius. In this approach the potential is also calculated using the Poisson equation. The difference between the various ion sphere models lie in the way the density of free electrons is determined. We present two models of ion sphere type, the uniform electron gas model (UEGM) and the Thomas-Fermi approach (TF).

5.3.1 Uniform electron gas model

The uniform electron gas model supposes a uniform distribution of free electrons N_e. This hypothesis means that we neglect the polarization of free electrons due to nucleus. It has been checked [98] that theoretical estimates based on it agree with several experimental data recorded in highly stripped ions. As in every ionic sphere model (see, for instance [9]), we assume that outside the ionic sphere the free-electron density compensates the ion density, and we have to ensure neutrality of the ionic sphere

$$Z - N_b - \frac{4}{3}\pi R_0^3 N_e = 0, \tag{5.3.1}$$

where R_0 is the ionic sphere radius, Z the atomic number, N_b the number of bound electron and N_e the free electron density.

Using the uniform electronic density hypothesis, we obtain the potential

$$V_{\rm pl}(r) = \frac{Z_f}{2R_0}\left(3 - \frac{r^2}{R_0^2}\right) \qquad \text{if } r \leq R_0 \tag{5.3.2}$$

$$V_{\rm pl}(r) = \frac{Z_f}{r} \qquad \text{if } r \geq R_0. \tag{5.3.3}$$

in atomic unit and with Z_f the number of free electron defined by

$$Z_f = Z - N_b \tag{5.3.4}$$

V_{pl} is the potential energy, however we mention it in what follows by potential.

In this work, we have not imposed any cancellation property of the wave-function at $r = R_0$, at variance with other authors [99, 100]. Since we are interested in dense plasmas, R_0 is rather large as detailed below. Furthermore, canceling the wave-function on the sphere surface is equivalent to assume an infinitely repulsive potential beyond R_0 leading to possible unphysical effects. Despite its simplicity, the UEGM was compared to self-consistent approaches and turns out to be acceptable for moderate densities [101, 102, 103, 104]

5.3.1.1 Discussion

We point out that several authors [105, 106] have chosen a different condition for Z_f:

$$Z_f = Z - N_b + 1. \tag{5.3.5}$$

Massacrier *et al.* [101] choose this definition because they impose the sphere to be neutral for every bound electrons. It means that the optical electron is not bound and therefore a free electron is added to fill the hole. In that situation the optical electron experiences a zero potential when it is far from the origin. Conversely, in our case the optical electron is embedded in the potential of an hydrogen like atom. Our choice is justified by the neutrality condition (5.3.1), while the condition of (5.3.5) lies on a ad-hoc choice.

5.3.2 Thomas-Fermi approach

The self-consistent equations defining the free-electron density and the plasma potential in a semi-classical picture — Thomas-Fermi restricted to free electrons — has been discussed in a series of papers [97, 104]. In the ion-sphere theory [9], neutrality is still assumed inside the Wigner sphere with radius R_0 defined by

$$4\pi R_0^3 N_e/3 = Z_f \tag{5.3.6}$$

with the same notation as above. Free-electron and the other-ion background densities are supposed to neutralize

$$n_e(r) = 0 \text{ for } r \geq R_0. \tag{5.3.7}$$

In order to comply with the definition of the average density N_e, one imposes

$$4\pi \int_0^{R_0} dr\ r^2 n_e(r) = Z_f. \tag{5.3.8}$$

Assuming Maxwell-Boltzmann statistics, the free-electron density follows in atomic unit

$$n_e(r) \propto \int_{p_0(r)}^{\infty} dp\, p^2 \exp\left(-\left(\frac{p^2}{2} + V(r)\right)/kT_e\right) \tag{5.3.9}$$

where kT_e is the electron temperature and $p_0(r)$ is the minimal momentum value making the total electron energy positive, i.e., $p_0(r) = (-2V(r))^{1/2}$ if $V(r) \leq 0$, or 0 if $V(r) > 0$. Here we assume thermal equilibrium for electrons, but not necessarily for ions which is consistent with the assumption made in the collisional-radiative models. We note that in the work of Blancard et al. [107], the density of free electrons is calculated via a quantum description. Here, we prefer to treat the free electrons via a semi-classical description to be consistent with the hypothesis of the collisional-radiative model (Maxwell distribution of free electrons). The quantity $V(r)$ is the energy associated with the electrostatic interaction with all the charges included in the Wigner sphere, namely the nucleus, bound electrons and free electrons

$$V(r) = \begin{cases} -\frac{Z}{r} + V_b(r) + V_{\mathrm{pl}}(r). & r \leq R_0 \\ 0 & r > R_0 \end{cases} \tag{5.3.10}$$

The term $V_{\mathrm{pl}}(r)$ describing the interaction with free electrons is the so-called plasma potential. The use of Fermi-Dirac statistics is usually not necessary as discussed in subsection 5.3.5. We also assume that free electrons are not relativistic, which holds for temperatures $k_{\mathrm{B}}T_e \ll 511$ keV which is always fulfilled in the cases considered here.

The last equation required to obtain the plasma potential and the electron density is the Poisson equation which can be written in integral form

$$V_{\mathrm{pl}}(r) = 4\pi \left(\frac{1}{r}\int_0^r ds\, s^2 n_e(s) + \int_r^{R_0} ds\, s n_e(s)\right). \tag{5.3.11}$$

This expression ensures that $V_{\mathrm{pl}}(r)$ and its derivative are continuous at $r = R_0$, knowing that $V_{\mathrm{pl}}(r) = Z_f/r$ if $r \geq R_0$, according to the ion-sphere hypothesis.

Assuming an attractive potential $V(r) < 0$, the Maxwell-Boltzmann equation (5.3.9) leads to

$$n_e(r) = \frac{K}{2} e^{-V(r)/kT_e} (2kT_e)^{3/2} \Gamma\left(\frac{3}{2}, -\frac{V(r)}{kT_e}\right) \tag{5.3.12}$$

$$= \frac{K}{2}(2kT_e)^{3/2}\left[\left(-\frac{V(r)}{kT_e}\right)^{1/2} + \frac{\pi^{1/2}}{2} e^{-V(r)/k_B T_e} \mathrm{erfc}\left(\left(-\frac{V(r)}{kT_e}\right)^{1/2}\right)\right] \tag{5.3.13}$$

the constant K being derived from the neutrality condition (5.3.8). We have introduced the incomplete Gamma function $\Gamma(a,x) = \int_x^{\infty} dt\ t^{a-1}e^{-t}$ and the complementary error function $\mathrm{erfc}(x) = (2/\pi^{1/2}) \int_x^{\infty} du\ e^{-u^2}$ [57].

5.3.3 Limit of weakly coupled plasmas

In order to simplify the discussion we define a radius connected to the electron temperature (atomic are used to defined the radius)

$$R_1 = \frac{Z_f}{\pi k T_e}, \tag{5.3.14}$$

the ratio R_1/R_0 is proportional to the plasma-coupling parameter

$$R_1/R_0 = \frac{Z_f}{\pi k T_e R_0} = \frac{\Gamma}{Z_f \pi} \tag{5.3.15}$$

with a definition slightly different from the most usual one, which is based on ion-ion and not electron-ion interaction [108].

In the limit of infinite temperature or zero density $R_1/R_0 \to 0$, the electron density is constant inside the Wigner sphere and the potential is obtained straightforwardly from Poisson equation (5.3.11). This well-known Uniform Electron Gas Model (UEGM) solution may however be usefully refined by considering the first correction in a R_1/R_0 expansion. Here we consider hydrogen-like ions where the V_b term is absent in the potential (5.3.10). Starting from the Maxwell-Boltzmann equation (5.3.12), and the expansion of the incomplete Gamma function

$$\exp(X)\Gamma(3/2, X) = \frac{\sqrt{\pi}}{2} + \frac{\sqrt{\pi}X}{2} - \frac{2X^{3/2}}{3} + \frac{\sqrt{\pi}X^2}{4} + O(X^{5/2}) \tag{5.3.16}$$

where the first 2 terms are kept, one gets

$$n_e(r) = N_{\rm ht}\left\{1 + \frac{1}{kT_e}\left[\frac{Z}{r} - \frac{Z_f}{2R_0}\left(\frac{3}{2} - \frac{r^2}{R_0^2}\right)\right]\right\} \tag{5.3.17}$$

up to $(R_1/R_0)^{3/2}$ corrections. Here N_{ht} is a constant proportional to the electron density and determined from the neutrality condition (5.3.6)

$$N_{\rm ht} = \frac{3Z_f}{4\pi R_0^3}\frac{1}{1 + \dfrac{3}{2kT_eR_0}\left(Z - \frac{4}{5}Z_f\right)}. \tag{5.3.18}$$

From Poisson integral equation (5.3.11), we write the high-temperature plasma potential

$$V_{\rm pl}^{\rm ht}(r) = \frac{3Z_f/R_0^3}{1 + \dfrac{3}{2kT_eR_0}\left(Z - \dfrac{4}{5}Z_f\right)}\left[\frac{R_0^2}{2} - \frac{r^2}{6} + \frac{Z_fR_0}{kT_e}\left(\frac{Z}{Z_f} - \frac{5}{8} - \frac{Zr}{2Z_fR_0} + \frac{r^2}{4R_0^2} - \frac{r^4}{40R_0^4}\right)\right] \tag{5.3.19}$$

up to $kT_e^{-3/2}R_0^{-5/2}$ terms. Letting

$$u = 1 - r/R_0 \tag{5.3.20}$$

one gets, using the closest approach distance R_1 (5.3.14), the low-density form of the plasma potential (5.3.19)

$$R_0 V_{\rm pl}^{\rm ht}(r)/Z_f = 1+u-\frac{u^2}{2}+\frac{3\pi R_1}{10R_0}\left[\left(\frac{5Z}{2Z_f}-1\right)u^2+u^3-\frac{u^4}{4}\right]+O\left((R_1/R_0)^{3/2}\right). \quad (5.3.21)$$

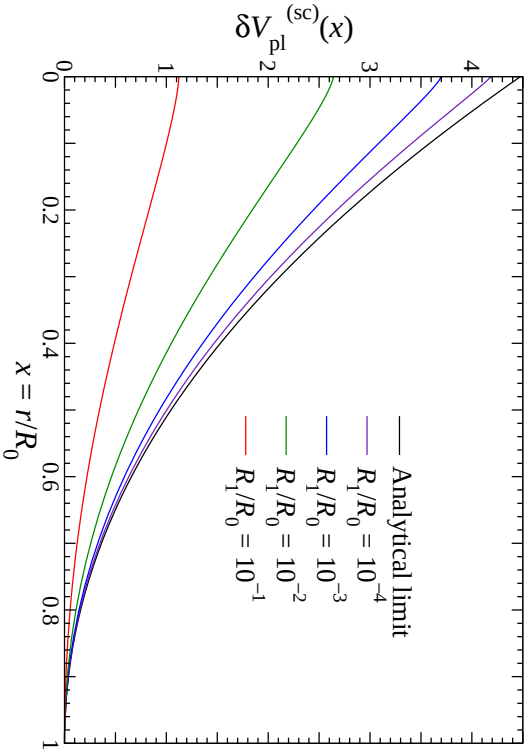

Figure 5.3.1 : Variation of the reduced plasma potential divided by the coupling parameter R_1/R_0 in H-like helium. The scaled variation $\delta V_{pl}^{(sc)}(x) = (R_0/Z_f e^2)(V_{\rm pl}(r) - V_{\rm pl}^{\rm UEGM}(r))/(R_1/R_0)$ is plotted versus $x = r/R_0$ for various R_1/R_0 and is compared to the analytical form $y = (3\pi/10)(1-x)^2[5 - x - (1-x)^2/4]$ as given by (5.3.21).

The convergence of the numerical solution towards this analytical form when the coupling parameter tends to zero is illustrated by Fig. 5.3.1 where we have plotted the radial dependence of the potential variation $(R_0/Z_f)(V_{\rm pl}(r) - V_{\rm pl}^{\rm UEGM}(r))/(R_1/R_0)$ for various small values of R_1/R_0 and its analytical limit (5.3.19). It turns out that the numerical solution does converge towards this limit but rather slowly with the parameter R_1/R_0, as expected since the first omitted term is of order $(R_1/R_0)^{3/2}$: for instance if $R_1/R_0 = 10^{-3}$ the analyzed ratio is 3.70, i.e., 17% below the analytical result equal to 4.48.

5.3.4 Scaling laws

From the neutrality, Maxwell-Boltzmann, and Poisson equations, one may easily assert that the reduced potential and free-electron density obey the scaling laws

$$n_e(R_0, R_1, Z, Z_f, r) = Z_f R_0^{-3} f(R_1/R_0, Z, Z_f, r/R_0) \tag{5.3.22}$$

$$V_{\rm pl}(R_0, R_1, Z, Z_f, r) = Z_f R_0^{-1} g(R_1/R_0, Z, Z_f, r/R_0). \tag{5.3.23}$$

If one further assumes that the potential is purely Coulombic $-Z/r$, these laws even simplify into

$$n_e(R_0, R_1, Z, Z_f, r) = Z_f R_0^{-3} f(R_1/R_0, Z/Z_f, r/R_0) \tag{5.3.24}$$

$$V_{\rm pl}(R_0, R_1, Z, Z_f, r) = Z_f R_0^{-1} g(R_1/R_0, Z/Z_f, r/R_0). \tag{5.3.25}$$

These laws may be useful when checking the calculation of the plasma potential and free-electron density at various temperatures and densities.

5.3.5 Ion sphere limitations

We discuss here the validity range of ion sphere model. First, if the spatial extension of the bound electron wave-function is larger than the ionic sphere radius, the orbitals of two neighboring ions overlap and molecular effects [109] must be accounted for. This condition is also connected to the possibility of pressure ionization. The parameter describing this overlap is

$$\beta = \frac{\langle r \rangle}{R_0}, \tag{5.3.26}$$

where $\langle r \rangle$ is the size of the outermost orbital and R_0 is a measure of the half distance between two neighboring ions.

If $\beta > 1$ the wave-functions of two neighboring ions significantly overlap. The atomic structure codes provide values for the size $\langle r \rangle$. Furthermore in hydrogen-like case, the classical extension of the wave-function is bounded by the outer turning point position $\langle r \rangle \lesssim 2n^2/Z$, where n is the principal quantum number. For multi-electron ions, a rough estimate of this dimension is obtained assuming total screening of the nucleus by $N_b - 1$ bound electrons, and this atomic size becomes $2n^2/(Z - N_b + 1)$. Since the wave-function decreases exponentially beyond the outer turning point, it is sufficient to impose the condition

$$\frac{2n^2}{Z_f + 1} < R_0 \tag{5.3.27}$$

which amounts to

$$N_e \lesssim 0.03 \frac{(Z_f + 1)^3 Z_f}{n^6} \sim 2.10^{23} \frac{Z^4}{n^6} \text{ cm}^{-3} \tag{5.3.28}$$

A similar condition has been derived by various authors [101, 103].

The preceding discussion does not take into account the dynamical response of free electrons. Indeed, when the active electron moves far away from the nucleus, free electrons neutralize the positive charge with a characteristic time equal to the inverse of plasma frequency. In this case the net charge seen by an electron far from the nucleus is zero, in contradiction with formula (5.3.3). The active electron is bounded by a potential $-(Z-N_b+1)/r$ — nucleus screened by the other bound electrons — which adds to free-electron potential $(Z-N_b)/r$ and results in a nonzero $-1/r$ Coulomb potential far from nucleus. Therefore we must impose on the electron orbital frequency (or Bohr frequency) ω_{orbital} and on the plasma frequency ω_{pe} the adiabatic condition

$$\omega_{\text{pe}} = (4\pi N_e)^{1/2} \ll \omega_{\text{orbital}} \tag{5.3.29}$$

which, in the hydrogenic case or assuming complete screening by bound electrons, writes

$$N_e \ll \frac{(Z_f+1)^4}{4\pi n^6} \sim 5.35\times 10^{23}\frac{Z^4}{n^6}\ \text{cm}^{-3}. \tag{5.3.30}$$

This condition is closely related to the non-overlap hypothesis (5.3.28). An obvious consequence of the relation (5.3.29) is that ω_{orbital} is above the cut-off frequency when condition (5.3.30) is fulfilled. We observe that both conditions (5.3.30) and (5.3.28) are very similar. In any cases, it appears difficult to take into account the ionization by pressure without the dynamic response.

The above discussion, mostly concerning UEGM does not involve the temperature kT_e which is indeed connected to Z_f through the ionization balance — given by Saha equation or any other ionization model —, we can also estimate the correlation parameter

$$\Gamma = \frac{Z_f^2}{R_0 kT_e} \tag{5.3.31}$$

where k_B is the Boltzmann constant. Numerically, one has $\Gamma \sim 1$ with parameters $k_BT_e = 650$ eV and $N_e = 10^{23}\text{cm}^{-3}$ — which give $\langle Z_f. \rangle \sim 12$ according to Saha equation in aluminum. Therefore, the present model applies to plasmas with a low or medium correlation parameter.

In order to define whether Maxwell-Boltzmann or Fermi-Dirac statistics applies to free electrons, one must estimate the degeneracy parameter

$$\gamma = \frac{T_{\text{Fermi}}}{T_e} = \frac{\left(3\pi^2 N_e\right)^{2/3}}{2kT_e} = \frac{3^{2/3}\pi^{1/3}}{4}\left(N_e\lambda_{th}^3\right)^{2/3}. \tag{5.3.32}$$

Using again $N_e = 10^{23}\text{cm}^{-3}$,one gets $kT_F \simeq 8$ eV. Therefore, the plasmas considered here are usually non-degenerate. The non-degeneracy condition may also be written

$$\gamma = N_e\lambda_{th}^3 \ll 1. \tag{5.3.33}$$

The difference between Maxwell-Boltzmann and Fermi-Dirac statistics is illustrated by Fig. 5.3.2 where we have plotted the numerical results for the free-electron density and plasma potential in the case of H-like aluminum at 1 eV and 10^{24} e/cm^3. In this case the degeneracy factor γ is 331 and the plasma coupling parameter is $\Gamma = 1461.5$ making the free electrons degenerate. However one notices on this figure that the relative variation between Maxwell-Boltzmann and Fermi-Dirac statistics is about 0.2 on density and 0.1 on the potential. If one considers the relative variation of the potential versus the UEGM limit the modification due to quantum statistics is again 0.2. That is why we only consider Maxwell-Boltzmann statistics in this work.

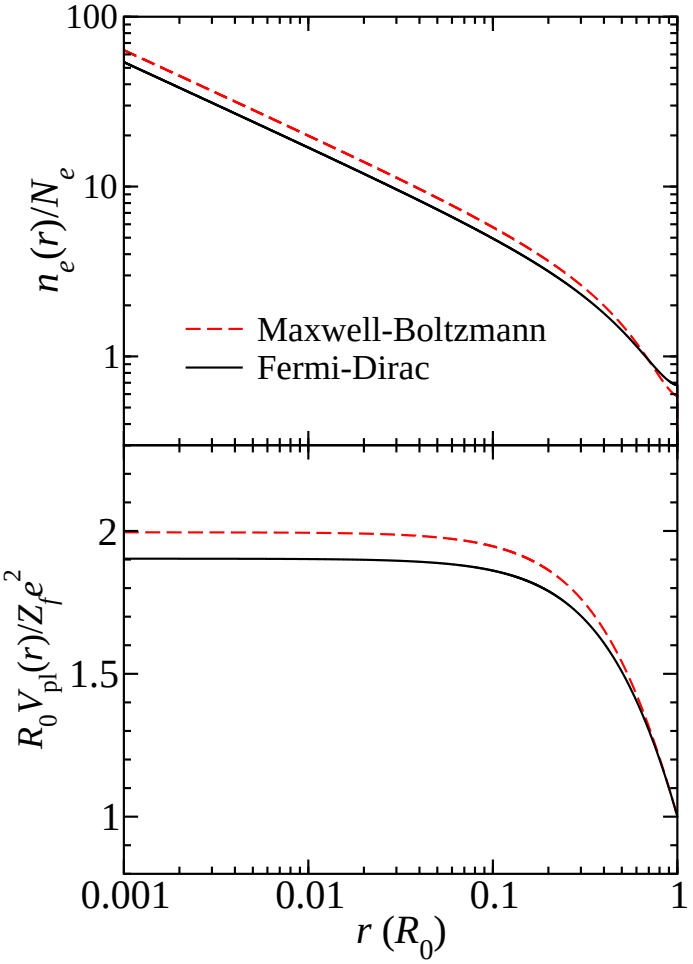

Figure 5.3.2 : Influence of statistics on the self-consistent free-electron density and plasma potential for H-like aluminum at $T_e = 1$ eV and $N_e = 10^{24}$ cm^{-3} or 0.148 a_0^{-3}. The density is in units of the average free-electron density $N_e = 3Z_f/4\pi R_0^3$, the potential energy is in units of $Z_f e^2/R_0$, and the electronic distance to nucleus r in units of the Wigner sphere radius $R_0 = 2.684\ a_0$.

5.4 Atomic structure calculations including plasma potential

We present the modifications that we made in the atomic code FAC which in its standard version does not take into account the plasma environment. Using the modified form of this code, we get energy levels, wave-functions, radiative rates, and cross sections accounting for the plasma environment within the ionic sphere model. Furthermore we have developed analytical formulas of energies and wave-functions valid for hydrogenic ions, which will be compared to FAC results.

5.4.1 Numerical approach

The atomic code FAC is fully relativistic and therefore solves the Dirac equation. Eliminating the small component as seen in chapter 3 (2.3.24), one obtains a Schrödinger-like equation

$$F\left(r\right)^{''}+\left[2\left[E-U(r)\right]-\frac{\kappa\left(\kappa+1\right)}{r^{2}}\right]F\left(r\right)=0, \tag{5.4.1}$$

where κ is the spin-orbit quantum number, equal to l (resp. $-l-1$) for $j=l-1/2$ (resp. $j=l+1/2$). The effective potential U is given by

$$U(r)=V(r)-\frac{\alpha^{2}}{2}\left\{\left(E-V\left(r\right)\right)^{2}-\frac{1}{2A(r)^{2}}\left[V^{''}-\frac{3\alpha^{2}V^{'2}}{A\left(r\right)^{2}}+\frac{\kappa V^{'}}{r}\right]\right\}, \tag{5.4.2}$$

where $A(r)=\sqrt{\left[E-V(r)+\frac{2}{\alpha^{2}}\right]}$ and $F(r)$ is the large component. The total potential acting on the electron is

$$V(r)=-\frac{Z}{r}+V_{\mathrm{pl}}+V_{ee}, \tag{5.4.3}$$

where V_{ee} accounts for all interactions between bound electrons, including nucleus screening by bound electrons, exchange interaction described by a local potential, and quantum electrodynamics corrections.

The original modification we brought to FAC code consists in including in V the contribution of the ionic sphere potential V_{pl}. Because of the presence of the first and second derivatives of the potential in (5.4.2) we need to account for $V_{\mathrm{pl}}^{'}$ and $V_{\mathrm{pl}}^{''}$.

5.4.2 Numerical implementation of TF approach

The basic equations are those of section 5.3.2 . The plasma potential and free-electron density are numerically obtained from an efficient iterative scheme. Starting from the

UEGM solution

$$n_e(r) = N_e \tag{5.4.4}$$

$$V_{\text{UEGM}} = \frac{Z_f}{2R_0}\left(3 - \frac{r^2}{R_0^2}\right) \tag{5.4.5}$$

for $r \leq R_0$, one obtains a first iteration for the density using Maxwell-Boltzmann equation (5.3.12) — where the overall constant is determined by the neutrality condition — and a first-order iterated potential using Poisson equation (5.3.11). One next obtains second-order electron density and plasma potential. The iterative scheme obtained is

$$n_e^{(i)}(r) = K\int_{p_0(r)}^{\infty} dp\, p^2 \exp\left(-\left(\frac{p^2}{2} + V^{(i-1)}(r)\right)/k_B T\right), \tag{5.4.6}$$

$$V^{(i-1)}(r) = -\frac{Z}{r} + V_b(r) + V_{pl}^{(i-1)}(r), \tag{5.4.7}$$

$$Z_f = 4\pi\int_0^{R_0} dr\, r^2 n_e^{(i)}(r), \tag{5.4.8}$$

$$V_{pl}^{(i)}(r) = 4\pi\left(\frac{1}{r}\int_0^r ds\, s^2 n_e^{(i)}(s) + \int_r^{R_0} ds\, s n_e^{(i)}(s)\right), \tag{5.4.9}$$

The convergence is controlled by monitoring the variation of the density on the Wigner sphere $|n_e^{(i+1)}(R_0) - n_e^{(i)}(R_0)|$, ending iteration when this difference falls below a given ε. We found that $\varepsilon = 10^{-8}$ in atomic units gave the self-consistent potential with a fair accuracy, and that the procedure converged in most cases in less than 12 iterations.

On Fig. 5.4.1 is plotted the free-electron density in units of the average value N_e using Maxwell-Boltzmann statistics in H-like helium $Z = 2, Z_f = 1$. From bottom to top the curves correspond to T_e = 500, 5000, 5, 0.005 and 5.10^{-4} eV, and densities 10^{12}, 10^{21}, 10^{21}, 10^{21}, and 10^{24} per cm^3 respectively. On this figure, the parameter R_1/R_0 is equal to 1.48×10^{-6}, 1.48×10^{-4}, 1.48×10^{-1}, 1.48×10^{2} and 1.48×10^{4} respectively. One notes that for $R_1/R_0 \ll 1$ density varies as $r^{-1/2}$ for small r and stays almost constant for $r \leq R_0$. This is close to the behavior predicted by Rosmej *et al* [104]. For $R_1/R_0 = 0.148$, electron density varies as $r^{-1/2}$ on almost all 0–R_0 region, though one observes a small upward deviation for $r \simeq R_0$. For $R_1/R_0 = 1.48 \times 10^2$ and 1.48×10^4 the reduced density is identical at the drawing accuracy. Its dependence is again $r^{-1/2}$ on most of the 0–R_0 interval, but for $r \simeq R_0$ there is now a downward deviation.

For R_1/R_0 as large as 1.48×10^4 one may criticize the applicability of Maxwell-Boltzmann statistics. However the criterion (5.3.32) may still be compatible with the non-degeneracy of electrons provided that R_0 and R_1 are both very large. For instance, $R_0 = 10^6 \mathrm{a}_0$ and $R_1 = 1.48 \times 10^{10} \mathrm{a}_0$ give $\gamma = 0.086$. Of course this correspond to extremely low density and temperature, but this is simply to illustrate the high R_1/R_0 limit on figure 5.4.1.

The radial dependence of the free-electron density is qualitatively similar for higher Z,

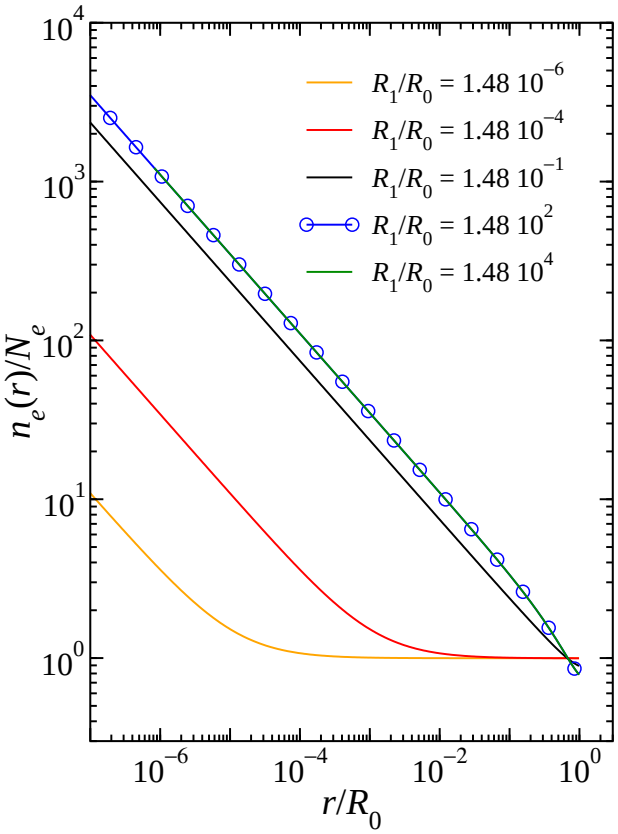

Figure 5.4.1 : Self-consistent free-electron density in H-like helium for various densities and temperatures. The local free-electron density $n_e(r)$ in units of the average density $N_e = 3Z_f/4\pi R_0^3$ is plotted versus r in units of the Wigner radius R_0 for various plasma-coupling parameters. See text for details.

the main difference being a stronger variation of $n_e(r)$ in the $r = R_0$ region.

5.4.3 Analytical development in hydrogen-like ions

Several papers [97, 102, 103] have pointed out that with the UEGM potential (5.3.2)an analytical expression can be derived for energy at first-order perturbation. Here we will extend this approach by giving also explicit expressions of wave-functions, dipolar and quadrupolar transition rates at first perturbation order, and energies at second perturbation order. To keep the approach rather tractable, relativistic effects are not considered but it will be shown later that their effect is small as long as $Z \lesssim 10$. The present work relies on standard Rayleigh-Schrödinger perturbation theory completed by Dalgarno and Lewis summation technique [110, 111]. In brief, noting H_0 the unperturbed Hamiltonian with eigen energies $E_i^{(0)}$ and eigenfunctions $\Phi_i^{(0)}$, and V the perturbing potential, this technique consists in trying to get the first order eigenfunction $\Phi_i^{(1)}$ by direct solution of the equation in $\mathbf{r}$ representation

$$\left\langle \mathbf{r} \left| H_0 - E_i^{(0)} \right| \Phi_i^{(1)} \right\rangle = \left\langle \mathbf{r} \left| E_i^{(1)} - V \right| \Phi_i^{(0)} \right\rangle, \tag{5.4.10}$$

where the first-order energy is obtained as usual from

$$E_i^{(1)} = \left\langle \Phi_i^{(0)} \right| V \left| \Phi_i^{(0)} \right\rangle. \tag{5.4.11}$$

The method can even be generalized at any perturbation order. Writing the hydrogen-like perturbed radial wave-function as $R_{nl}(r) + v_{nl}(r)$ where R_{nl} is the unperturbed wave-function at first order, n and l being the principal and orbital quantum numbers respectively, v_{nl} obeys

$$\left(\frac{d^2}{d\rho^2} + \frac{2}{\rho}\frac{d}{d\rho} - \frac{l(l+1)}{\rho^2} + \frac{2}{\rho} - \frac{1}{n^2} \right) v_{nl} = \frac{Z_f}{Z^4 R_0^3} (\left\langle \rho^2 \right\rangle - \rho^2) R_{nl}(r), \tag{5.4.12}$$

where $\rho = Zr$ is the scaled radius. To ensure neutrality, on must have $Z = Z_f + 1$. In this radial equation, the large-r dependence of the plasma potential (5.3.3) has been ignored. As studied in appendix A.1 this substitution is acceptable as soon as $R_0 > 2n^2/Z$. The average square radius is given by

$$\left\langle \rho^2 \right\rangle = \frac{1}{2} n^2 (5n^2 - 3l(l+1) + 1). \tag{5.4.13}$$

The trial resolution we have made of (5.4.12) in various cases suggests that a particular solution may be found as a sum of terms $c_j \rho^j \exp(-\rho/n)$ with j varying from l to n. The general solution is given by such a solution plus the homogeneous equation regular solution R_{nl} multiplied by a constant to be determined. To obtain the properly normalized

first-order correction, we must ensure the orthogonality condition

$$\int_0^\infty d\rho \rho^2 R_{nl} v_{nl} = 0. \tag{5.4.14}$$

Though we have been able to get analytical expressions for any n, l they are too cumbersome to be explicitly given here and we will restrain to some simple though demonstrative enough cases to show general tendencies, namely $n = l + 1$ and $n = l + 2$.

If $n = l+1$, the general solution of the radial equation (5.4.12) with proper normalization is given by

$$v_{nn-1} = \langle r \,|\widetilde{n\; n-1}\rangle = \frac{Z_f}{Z^{5/2}R_0^3}\frac{(2/n)^{n+1/2}}{(2n)!^{1/2}}\left(\frac{n}{6}\rho^3 + \frac{n^2}{4}(n+1)\rho^2 - \frac{n^4}{24}(n+1)(2n+1)(5n+6)\right)\rho^{n-1}e^{-\rho/n}. \tag{5.4.15}$$

A comparison between such analytical expression and numerical calculations will be given in the next chapter. While the first order energy shift is simply given by

$$E^{(1)}_{nn-1} = \frac{Z_f}{2R_0}\left(3 - \frac{n^2}{Z^2R_0^2}(n+1)\Big(n+\frac{1}{2}\Big)\right), \tag{5.4.16}$$

the equation (5.4.15) allows one to write the second order energy shift

$$E^{(2)}_{nn-1} = \frac{Z_f}{2Z^3R_0}\int_0^\infty d\rho\, \rho^2 R_{nn-1}\left(3 - \frac{\rho^2}{Z^2R_0^2}\right) v_{nn-1}, \tag{5.4.17}$$

which is after performing the integration

$$E^{(2)}_{nn-1} = -\frac{Z_f^2}{Z^6R_0^6}\frac{n^6}{32}(n+1)(2n+1)(8n^2+21n+14). \tag{5.4.18}$$

The ratio of the above correction to the first-order n-dependent term (5.4.16) gives a quantitative indication of the perturbation development validity

$$E^{(2)}_{nn-1}/E^{(1)}_{nn-1}(n\text{-dependent}) = \frac{Z_f}{Z^4R_0^3}n^4(n^2 + 21n/8 + 7/4). \tag{5.4.19}$$

This shows that, for large n, the characteristic parameter of the perturbation series is $Z_f n^6/Z^4R_0^3 = 4\pi N_e n^6/3Z^4$. Comparing this to the validity conditions (5.3.28), (5.3.30), one verifies that the non-overlap and the adiabatic conditions imply a second order much less than first order in the perturbation series.

The radiative rate depends on the perturbed matrix element $\widetilde{\langle nl|\, r\, |n'l'\rangle}$ given, up to first order, by

$$\widetilde{\langle nl|\, r\, |n'l'\rangle} = \langle nl|\, r\, |n'l'\rangle + \widetilde{\langle nl|} r\, |n'l'\rangle + \langle nl|\, r\widetilde{|n'l'\rangle}. \tag{5.4.20}$$

we provide explicit expressions of this element for adjacent quantum numbers $n' = n+1$, $l' = l+1$. With the additional condition $l = n-1$, the first-order perturbation involves two integrals. The first one is

$$\widetilde{\langle n\ n-1|}r\,|n+1\ n\rangle = \frac{Z_f}{Z^5R_0^3}\frac{n^{n+13/2}(n+1)^{n+3}}{2^6 3(n+1/2)^{2n+11/2}}(288n^4+1140n^3+1720n^2+1175n+306). \tag{5.4.21}$$

The second integral is

$$\langle n\ n-1|\,r\widetilde{|n+1\ n\rangle} = -\frac{Z_f}{Z^5R_0^3}\frac{n^{n+5/2}(n+1)^{n+6}}{192(n+1/2)^{2n+11/2}}(n+2)(2n+3)(48n^3+138n^2+71n+11). \tag{5.4.22}$$

For the complete matrix element defined above (5.4.20) one gets

$$\langle n\ n-\widetilde{1|}\,r\,|n+1\ n\rangle = \frac{n^{n+5/2}(n+1)^{n+2}}{Z(n+1/2)^{2n+5/2}}\left[1+\frac{Z_f}{Z^4R_0^3}\frac{(n+1)D_1(n)}{96(n+1/2)^2}\right] \tag{5.4.23}$$

with

$$D_1(n) = 96n^7+72n^6-936n^5-2678n^4-3180n^3-1916n^2-569n-66. \tag{5.4.24}$$

The polynomial $D_1(n)$ is negative for $n<5$ and positive above 5.

The derivation is similar for the $n = l+2$ case, though the result involves more terms. The perturbed wave-function obtained from radial differential equation (5.4.12) is

$$\mathrm{v}_{nn-2} = \frac{Z_f}{Z^{5/2}R_0^3}\left(\frac{n-1}{2}\right)^{1/2}\frac{(2/n)^n}{(2n-3)!^{1/2}}\left(-\frac{\rho^4}{6(n-1)}-\frac{n(n+5)}{12(n-1)}\rho^3+\frac{n^2}{4}(n+5)\rho^2 \right.$$
$$\left. -\frac{n^4}{24}(2n-1)(5n^2+n+60)\left(1-\frac{\rho}{n(n-1)}\right)\right)\rho^{n-2}e^{-\rho/n}. \tag{5.4.25}$$

The energy shift is at first order from 5.4.13

$$E^{(1)}_{nn-2} = \frac{Z_f}{2R_0}\left(3-\frac{n^2}{Z^2R_0^2}(n+5)\left(n-\frac{1}{2}\right)\right) \tag{5.4.26}$$

and at second order, a formula analogous to (5.4.16) gives after integration

$$E^{(2)}_{nn-2} = -\frac{Z_f^2}{Z^6R_0^6}\frac{n^6}{32}(2n-1)(8n^3+103n^2-7n+154). \tag{5.4.27}$$

The above expressions show once again that the ratio of the second-order correction to the n-dependent first-order correction is $Z_f n^6/Z^4R_0^3$, which is small as soon as the conditions (5.3.28) or (5.3.30) are fulfilled.

Using the wave-function (5.4.25) one may also evaluate the perturbed matrix element

(5.4.20) for $l = n - 2$. The perturbation by the plasma potential is here obtained for the first part as

$$\langle \widetilde{n\ n-2}|r\,|n+1\ n-1\rangle = \frac{Z_f}{Z^5 R_0^3}\frac{2^{2n-1}\Big(n(n-1/2)\Big)^{1/2} n^{n+6}(n+1)^{n+1}}{3(2n+1)^{2n+5}} (672n^5 + 2652n^4 + 6628n^3 + 7617n^2 + 3905n + 744) \quad (5.4.28)$$

which is always positive. The second part is

$$\langle n\ n-2|\,r|\widetilde{n+1\ n-1}\rangle = -\frac{Z_f}{Z^5 R_0^3}\frac{2^{2n-1}\Big(n(n-1/2)\Big)^{1/2} n^{n+2}(n+1)^{n+5}}{3(2n+1)^{2n+5}} (480n^5 + 1164n^4 + 1948n^3 + 1605n^2 + 539n + 66) \quad (5.4.29)$$

and turns out to be negative. Finally one gets the perturbed radial element (5.4.20) for $n = l + 2$

$$\langle n\ n-2|\widetilde{r\,|n+1\ n-1}\rangle = \frac{(n(n-1/2))^{1/2} n^{n+2}(n+1)^{n+1}}{Z(n+1/2)^{2n+2}}\left[1 + \frac{Z_f}{Z^4 R_0^3}\frac{D_2(n)}{96(n+1/2)^2}\right] \quad (5.4.30)$$

with

$$D_2(n) = 96n^8 - 264n^7 - 1296n^6 - 4694n^5 - 7592n^4 - 6236n^3 - 2815n^2 - 671n - 66. \quad (5.4.31)$$

The first-order correction to the dipolar matrix element is negative for $n \leq 6$, positive above 6.

The corresponding effect on quadrupolar matrix elements is studied on the $n_a = n + 2, l_a = n + 1 \to n_b = n, l_b = n - 1$ transition in A.2. The radiative rates corresponding to these dipolar and quadrupolar electric transitions are detailed in A.3.

5.5 Summary

We have reviewed the ion sphere model and discussed its range of application. In the following we apply the TF and the UEGM assuming the adiabatic condition (5.3.28) and the non-overlapping condition (5.3.27). Both approaches have been implemented in the Flexible Atomic Code. Moreover, using a uniform electron gas model, analytical formulas have been developed in the case of non-relativistic hydrogen-like ions, Allowing use to obtain energies and wave-functions till the second order of perturbative theory. Thanks to this developments we are able to check the atomic data of our modified version of FAC.

Chapter 6

Influence of the plasma on atomic structure and collisional cross sections

6.1 Introduction

In the previous chapter, we have discussed the ion sphere approach for describing the plasma environment effect under the UEGM hypothesis and the Thomas-Fermi formalism. In this chapter, we present the influence of such potential on the atomic structure (energies, wave-functions and radiatives rates) and collisional cross sections (excitation, ionization, photo-ionization). In the framework of the Ion sphere, other approaches available in the literature use a Multi-configurational Dirac Fock Formalism [112], a Hartree-Fock formalism [102] or, in simpler cases, a hydrogen-like framework [97, 98]. We devote a significant part of this chapter to the calculation of collisional cross sections. They deserve a special interest for at least two reasons. First, in order to describe plasmas out of local thermodynamical equilibrium, it is necessary to solve kinetic equations which involve the radiative and collisional transition rates. Second, the line shape determination, particularly important for spectral opacity calculation, requires a detailed analysis of collisional rates (see, e.g., [113]).

In addition, most of the available literature about plasma effects on excitation cross sections relies on Debye-Hückel potential [114, 115, 116, 117, 118] or for the ion sphere the UEGM [117] and a Thomas-Fermi approach [107]. Ionization impact cross sections are also dealt with in a series of papers, based on Debye-Hückel hypothesis [119, 116, 118] or Thomas-Fermi approach [120]. Concerning, the photo-ionization cross sections, a series of papers [121, 100, 122] has investigated this process with a Debye-Hückel potential and [100] with an ion sphere potential through the uniform electron gas model. To our knowledge such analysis has not been performed yet using a relativistic parametric potential code such as FAC.

The following results have been obtained thanks to the modification of the FAC code as explained in chapter 5. In that chapter we firstly focus on the effect of plasma environment

on atomic structure within the UEGM. To support this numerical calculation we use the analytical development done on hydrogen-like ions. In the same section we compare the Thomas-Fermi approach and the UEGM. To investigate the effect on collisional cross section, we only use the more realistic Thomas-Fermi approach. Some analytical expressions are proposed for hydrogen-like ions in the limit where Born or Lotz approximation apply and are compared to the numerical results from the FAC code. Concluding remarks are finally given.

6.2 Effect of density on atomic structure

This section is devoted to calculation of energies, wave functions and radiative rates with FAC code modified as explained in the previous chapter. Some comparisons with analytical formula are also provided. We choose to study some representative cases H-like, He-like, and Li-like aluminum. Here and in all what follows we consider a specific charge state without consideration of the real ionization degree that would be reached under these thermodynamic conditions.

6.2.1 Energies

UEGM

The first plasma effect is the energy shift due to the screening of nucleus by free electrons leading to a reduction of the $-Z/r$ potential. According to the formula (5.4.16) when the average squared radius $\langle r^2 \rangle$ is much smaller than the ionic sphere radius R_0^2 all levels move uniformly upward by a constant proportional to $N_e^{1/3}$. When the ratio $\langle r^2 \rangle / R_0^2$ increases, the shift involves a level-dependency contribution. This behavior is clearly observed on Figure 6.2.1 .

On this figure we have restricted the study of binding energies on the figure 6.2.1 due to the non overlapping condition: $< r > /R_0 \ll 1$ (cf discussion in chapter 5). On the Figure 6.2.2, we have plotted the evolution of the average radius $< r >$ for some orbitals present in the Figure 6.2.1 versus the electron density. The average radius is calculated as follows

$$\langle r \rangle = \int_0^\infty \left[P^2(r) + Q^2(r) \right] r dr \tag{6.2.1}$$

where $P(r)$ and $Q(r)$ are the large and the small component of the wave function, respectively. Via this plot we may define when the non-overlapping condition is respected. We point out that when $< r >$ is greater than R_0 we observe jumps in the average radius of the orbitals. This is because when $< r > /R_0 \gg 1$, the effective nucleus charge seen by the active electron is equal to 1 (as mentioned in 5.3). Therefore outside the sphere the wavefunctions are similar to those of the hydrogen atom.. For example the configuration $3p_{1/2}$ have two thresholds around 5 a.u and 12 a.u, which correspond to the orbital of $2p$

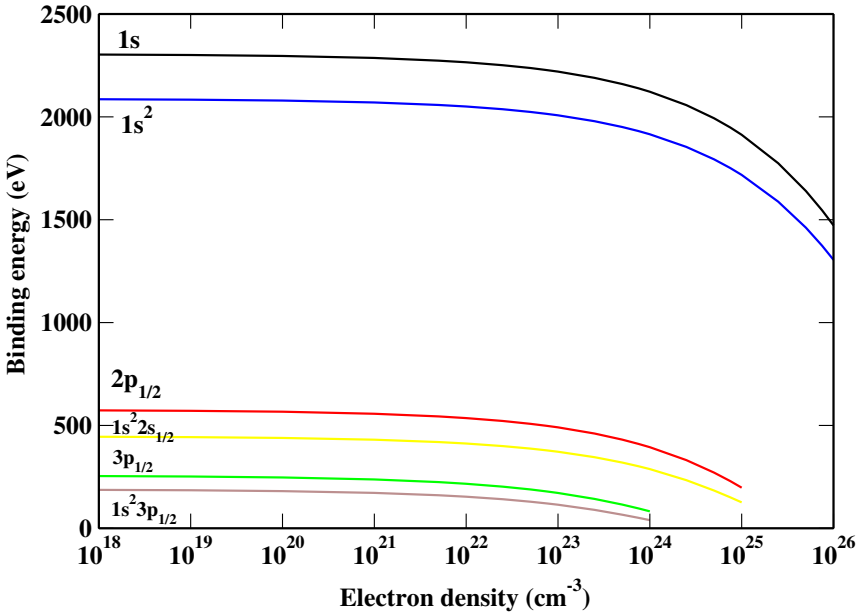

Figure 6.2.1 : Binding energy of Al XIII,XII,XI versus the average electron density N_e, calculation are realized with the UEGM

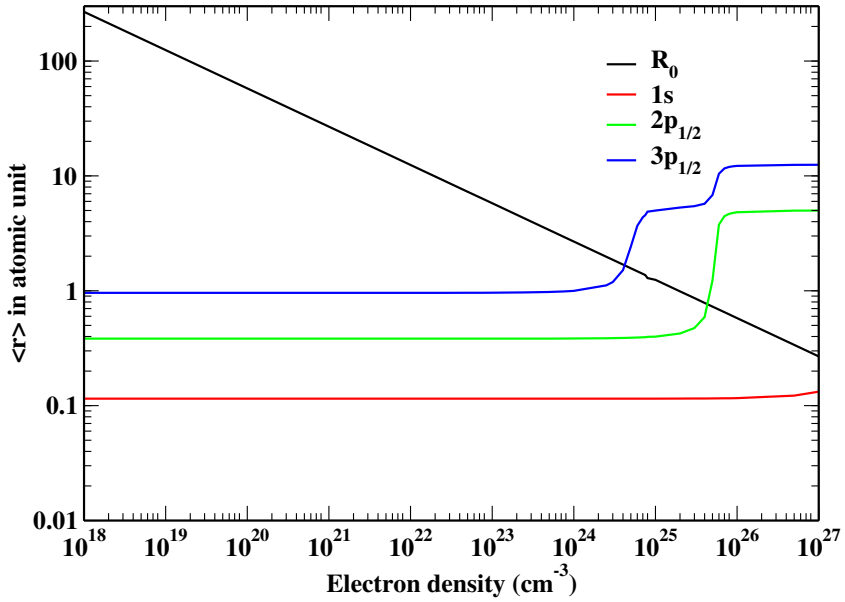

Figure 6.2.2 : Average radius of several Al XIII orbital versus the average electron density N_e, within the UEGM. The black curve represent the ion sphere radius

and $3p$ of an hydrogen atom.We will assume the non-overlapping condition.

In the hydrogen-like case, Table 6.1 compares detailed results from FAC and analytical formula (5.4.16), (5.4.18) for the energy shift.

	N_e (cm^{-3})	FAC shift (eV)		Analytical shift (eV)	Relative error %	
1s	10^{23}	84.69351		84.69342	1.06×10^{-4}	
	10^{24}	182.34969		182.348811	4.82×10^{-4}	
		$J = 1/2$	$J = 3/2$		$J = 1/2$	$J = 3/2$
2p	10^{23}	84.559455	84.55872	84.55845	1.12×10^{-3}	3.19×10^{-4}
	10^{24}	181.00462	180.99635	180.99386	5.91×10^{-3}	1.37×10^{-3}
		$J = 3/2$	$J = 5/2$		$J = 3/2$	$J = 5/2$
3d	10^{23}	84.07811	84.07723	84.07671	1.6×10^{-3}	6.1×10^{-4}
	10^{24}	175.98192	175.97250	175.995850	7.9×10^{-3}	0.013

Table 6.1 : Comparison of energy shifts obtained via FAC (UEGM) and analytical formulae for Al XIII

We notice that analytical and numerical values are very close when the density is not too high. This was expected since we have a large ionic sphere so the contribution to the energy shift is mainly due to the constant term $3Z_f/(2R_0)$ of expression (5.4.16). When the ionic sphere radius becomes smaller, the agreement between analytical expressions (5.4.16), (5.4.18) and FAC results deteriorates. Two reasons might explain this. First, the present analytical formalism is not relativistic and the expected correction is of order of $Z^2\alpha^2$ ($\sim 1/100$ for Al ion). Second, when density increases, higher orders in perturbation theory should be taken into account. To illustrate the behavior of the first contributions to the level shifts, the energy terms up to second order are detailed in Table 6.2. Nevertheless, when higher-order effects are important, we have shown that the ion-sphere model validity becomes questionable.

	N_e (cm^{-3})	$3Z_f/2R_0$ (eV)	$-Z_f \langle r^2 \rangle / 2R_0^3$ (eV)	$E^{(2)}$ (eV)
1s	10^{23}	84.707795	-0.014992	$-1.751230.10^{-7}$
	10^{24}	182.49740	-0.149915	$-1.75123.10^{-5}$
2p	10^{23}		-0.149915	$-5.73426.10^{-5}$
	10^{24}		-1.499155	-0.0057343
3d	10^{23}		-0.629645	-0.002064
	10^{24}		-6.29645	-0.206441

Table 6.2 : Comparison of the different terms in the analytical formulae for the energy shift of Al XIII

To illustrate density effects in multi-electron ions, we have plotted in Figure 6.2.3 the energy difference $E(1s4l^{2S+1}L_J) - E(1s4s^3S_1)$. In this quantity the constant term $3Z_f/2R_0$ eliminates, and its linear dependence versus density indicates that higher order perturbation effects are small. As discussed above, this means that the non-overlap condition (5.3.28) is fulfilled. As observed by Li and Rosmej [123], level crossings occur between

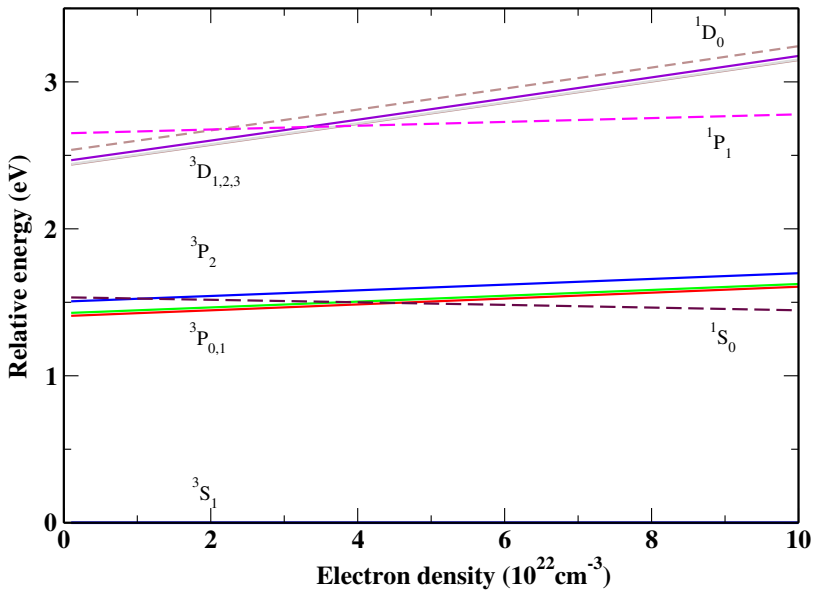

Figure 6.2.3 : Energy of helium-like Al relative to the level 1s4s $^3S_1$ versus density for various levels of the configurations 1s4l, made with the UEGM potential

triplet and singlet states, for instance $1s4p^3P$ and $1s4s^1S$, or $1s4d^3D$ and $1s4p^1P$. This effect is due to the screening of the nucleus by free electrons and, as shown in [123], results in strong variation in the radiative rates.

Thomas-Fermi

The TF model and the UEGM differ in the way to consider the temperature. The temperature is directly present for the TF via the Maxwell distribution and for the UEGM implicitly present via the assumed Z_f. In Figure 6.2.4, the evolution of the binding energy of Al XIII for $1s_{1/2}$ level is plotted versus the temperature with those two potentials. We clearly see that the binding energy increases with the temperature in the TF case. We also verify that, as expected, at high temperature, the TF approach converges to the UEGM.

As the analysis of the plasma potential has shown in chapter 5, the TF potential is always greater than the UEGM potential. Therefore one expects that the binding energy will be lower with TF than with UEGM. Indeed, Fig. 6.2.5 confirms this prediction. An important point to highlight on figures 6.2.4 and 6.2.5 is that the most important effect on level shift originates from density and not temperature. Our results are at variance with Salzmann and Szichman's [102] who obtained in some cases a UEGM shift greater than TF.

6.2.2 Wave functions

Including the plasma potential results in a screening by free electrons of the nucleus attraction and in a spreading of the wave function. This effect can be observed in Figure 6.2.6 for the $3p_{1/2}$ orbital of H-like aluminum. In order to check the numerical computa-

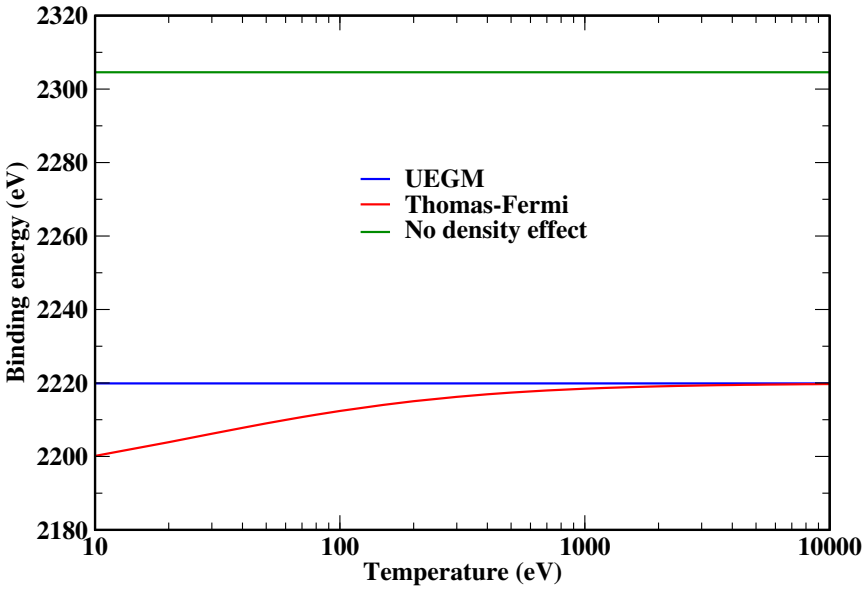

Figure 6.2.4 : Influence of temperature on binding energy of Al XIII for $1s_{1/2}$ level with an average density $N_e = 10^{23}$ cm^{-3}

tions, we present in Figure 6.2.7 a comparison of FAC and analytical wave functions given by formula (5.4.15). We notice a good agreement especially when the density is not too high as for the energy shift. As previously noticed, when the density becomes high the two computations diverge because of the perturbation theory breakdown. The effects of plasma density on wave functions observed here are moderate but visible, underlining the necessity of taking them into account, for instance when computing atomic spectra.

6.2.3 Radiative rates

With the above-analyzed perturbed wave functions, we may compute radiative rates. In the FAC code, we have computed the multipole integrals with the non-relativistic approximation. Hydrogen-like aluminum 1s-2p dipolar rate and 1s-3d quadrupolar rate are detailed in Table 6.3.

In all the listed cases FAC results are in good agreement with the analytical formulae, even though the largest considered density $N_e = 10^{24}$cm^{-3} only marginally allows one to use first-order perturbation theory. The agreement is less fair for the quadrupolar rate because i) this rate depends on the transition energy as E^5 instead of E^3 for dipolar rates, ii) the involved matrix element is more sensitive to the radial spreading of the wave function.

On Figure 6.2.8 we have plotted dipolar radiative rates of Li-like Al ion for two $3d \rightarrow 2p$ fine-structure transitions. The rates decrease almost linearly with the free-electron density. Nevertheless a small departure from this linear variation is visible at the higher densities. This indicates that second-order effects in the electron density are then present, and that the non-overlap hypothesis may become questionable. A similar variation has been

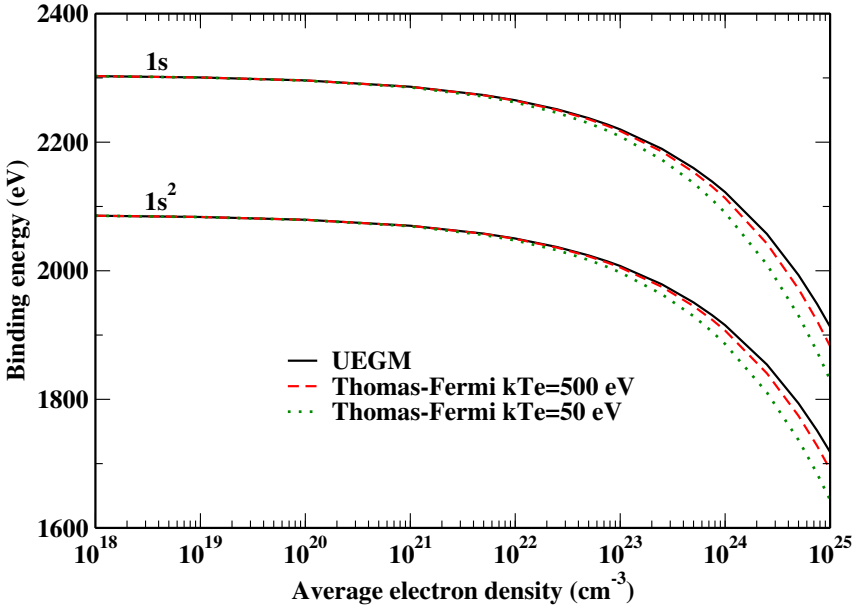

Figure 6.2.5 : Influence of density on binding energy of Al XIII and XII for $1s_{1/2}$ and $1s^2 {}^1S_0$ levels.

observed for a series of dipolar and quadrupolar rates in multi-electron ions.

However, we cannot assert that all rates are decreasing or increasing with the increase of density. Such behavior has been previously mentioned by Li and Rosmej [123]. This is because such rates depend on transition energies and dipolar matrix elements, and as may be seen for instance on Fig. 6.2.9 the transition energy may increase or decrease with the density. Specifically, the transition energy decreases with density between the triplet ${}^3P_{0,1}$ and the singlet ${}^1S_0$ and increases between the triplet ${}^3P_{0,1}$ and the triplet ${}^3S_1$. Thus radiative rates may exhibit a different behavior with respect to the density. In a similar way, Fig. 6.2.10 shows that radiative rates between the triplet ${}^3P_{0,1}$ and the singlet ${}^1S_0$ of Al XII increase with density. However as seen on Fig. 6.2.11 the $1s$–$2p_j$ rates decrease in the case of hydrogen-like Al. In both cases the UEGM leads to a qualitatively similar behavior but a smaller change in the radiative rates. As a rule most of radiative rates decrease due to plasma effect, because of the decreasing of ΔE_{ij}^3 in the probability. The case of figure 6.2.10 is specific because ΔE_{ij} is then very small.

6.3 Influence of the plasma environment on cross sections

6.3.1 Excitation cross sections

As mentioned in the introduction, there exists a wide literature about density effects on collisional cross-sections. However, a series of papers use the Debye-Hückel theory, which, as stated in the chapter 5, is not well suited for strongly coupled plasmas.

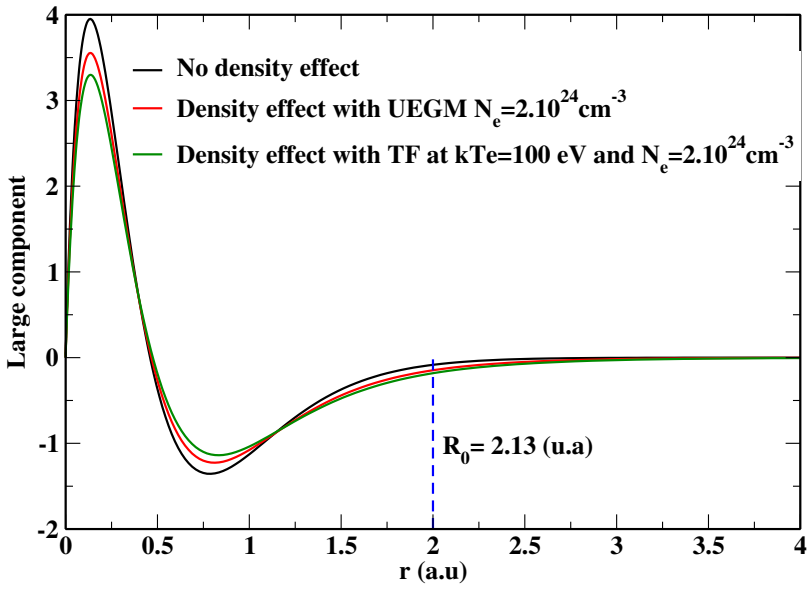

Figure 6.2.6 : Comparison of perturbed and unperturbed (solid line) large component of the wave function $3p_{1/2}$ in H-like Al obtained with FAC. The perturbed wave function has been computed assuming a $N_e = 2 \times 10^{24}$ cm^{-3} free-electron density. For the UEGM (red curve)$\langle r \rangle = 1.06$ a.u , Thomas-Fermi (green curve) $\langle r \rangle = 1.14$ a.u and for the unperturbed situation $\langle r \rangle = 0.96$ a.u. The ion-sphere radius at this density is 2.13 atomic units.

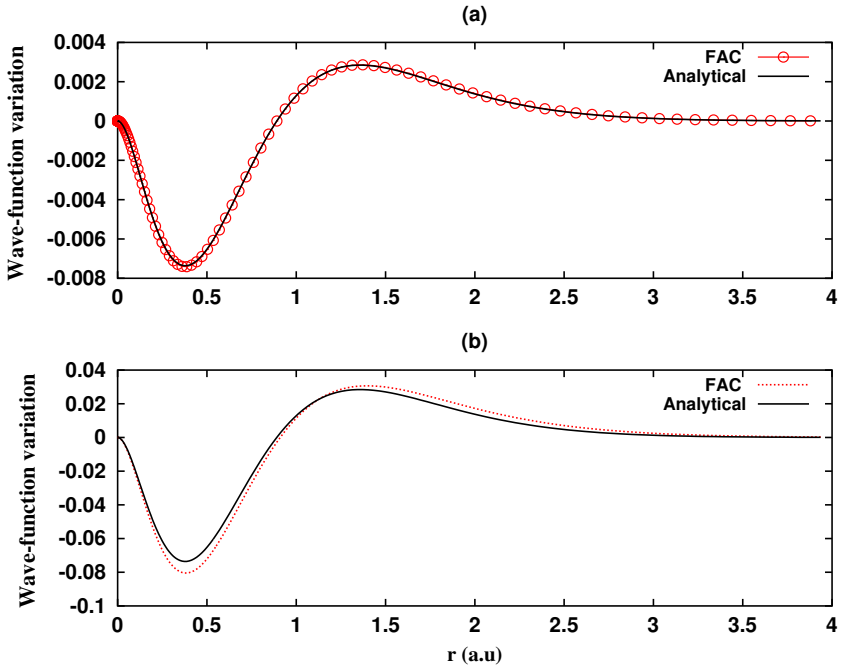

Figure 6.2.7 : Density effect on the $3d_{3/2}$ wave function of H-like aluminum. The large-component variation $P(N_e) - P(N_e = 0)$ calculated with FAC (with the UEGM) and the first-order perturbed wave function (5.4.15) are plotted as a function of the radius. The upper subfigure corresponds to $N_e = 10^{23}$ cm^{-3} and the lower subfigure to $N_e = 10^{24}$ cm^{-3}.

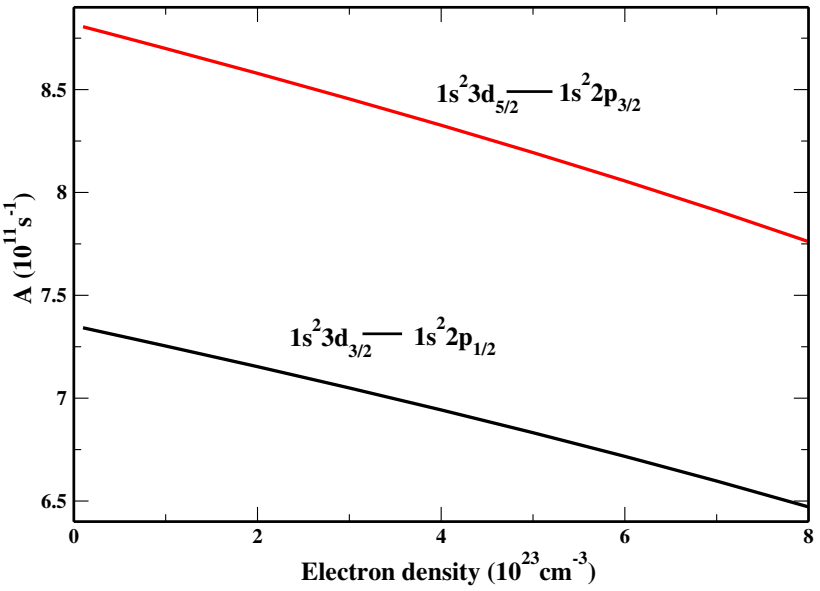

Figure 6.2.8 : Dipolar radiative rates of Li-like Al as a function of electron density.

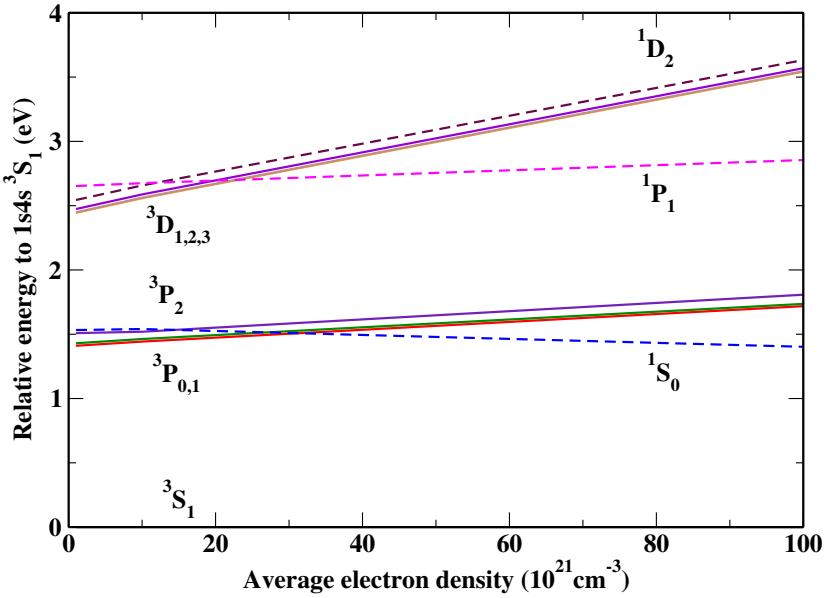

Figure 6.2.9 : Energy of helium-like Al relative to the level 1s4s $^3S_1$versus density for various levels of the configuration $1s4l$ with Thomas-Fermi potential at $kT_e = 100$ eV.

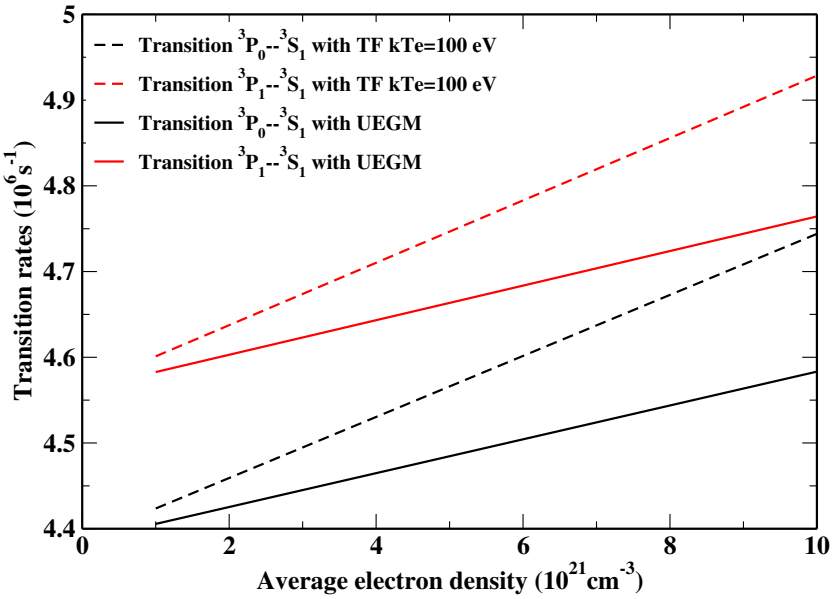

Figure 6.2.10 : Dipolar radiative rates $1s4p^3P_J$–$1s4s^3S_1$ in Al XII versus average electron density at $kT_e = 100$ eV.

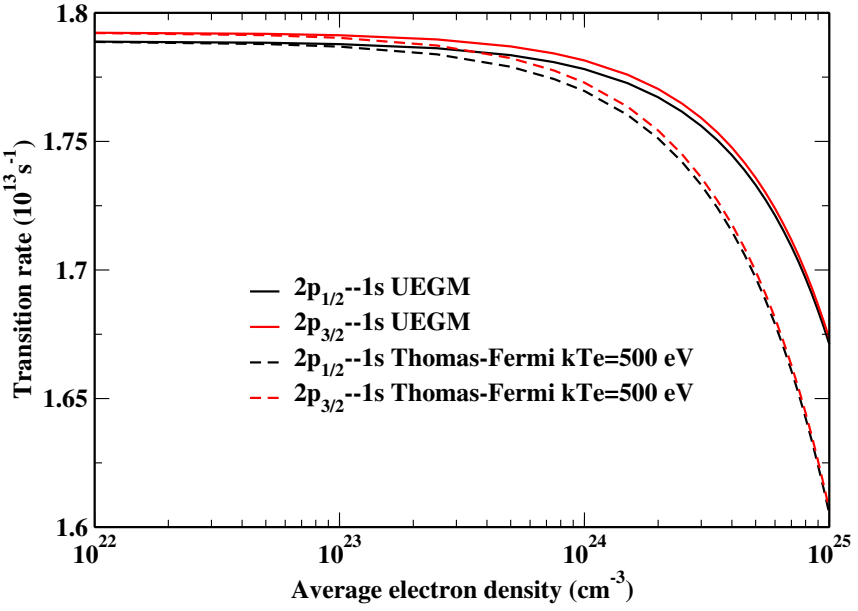

Figure 6.2.11 : Dipolar radiative rates in Al XIII versus average electron density at $kT_e = 500$ eV.

	Density (cm^{-3})	FAC		Analytical
		$j = 1/2$	$j = 3/2$	
A_{2p_j-1s}	0	1.7889×10^{13}	1.7924×10^{13}	1.7903×10^{13}
	10^{24}	1.7781×10^{13}	1.7815×10^{13}	1.7795×10^{13}
$\frac{dA_{2p_j-1s}}{dN_e}$		-1.077×10^{-13}	-1.090×10^{-13}	-1.081×10^{-13}
		$j = 3/2$	$j = 5/2$	
A_{3d_j-1s}	0	2.8624×10^{9}	2.8685×10^{9}	2.8675×10^{9}
	10^{24}	2.6137×10^{9}	2.6187×10^{9}	2.6317×10^{9}
$\frac{dA_{3d_j-1s}}{dN_e}$		-2.487×10^{-16}	-2.498×10^{-16}	-2.358×10^{-16}

Table 6.3 : Comparison of radiative rates between FAC (with UEGM) and analytical formulae (A.3) (A.3.11) for Al XIII. Rates are in s^{-1} and rate variations in cm^3/s.

We use two methods to study excitation cross sections: plane wave Born approximation (PWB) and the distorted waves approximation (DW) (see Chap. 3 of [53] and chapter 4 of this manuscript). We notify that on the plots the PWB is identified as Born.

The choice between them requires to consider which asymptotic behavior those formalisms assume for the long-range potential. Both of them are perturbative theories and valid only in the case of weak interaction potential between the target and the incident electrons. The differences, however,are important. Distorted waves method takes into account the long range form of the potential contrary to PWB approximation. The asymptotic form of the incident particle wave function is a plane wave for Born approximation and Coulombic for distorted waves. Therefore the distorted wave model is not relevant when density effects in the ion-sphere model are considered, because the asymptotic potential is not Coulombic. At the most, one might use DW approximation when the density is so low that the radius is greater than the zone where the collisional process takes place. Besides, We point out that the DW method implemented in FAC is not reliable for neutral and near neutral ions, as mentioned by the author of FAC and observed in chapter 4. As a consequence, the plane wave Born approximation is used in this work when the density effect is included.

We must emphasize a difficulty met when one tries to observe the influence of the plasma on cross sections. Indeed, the effect of plasma will change the long-range behavior of the potential. However, at high energies distorted wave and PWB approximation converge, meaning that we can then isolate the influence of plasma.

In order to compare PWB approximation to distorted-wave (DW) results we have plotted on Fig. 6.3.1 the e-impact excitation cross sections for $1s$–$2p_{1/2}$ transition in Al XIII. Since as mentioned above the DW theory is not adapted when density effects are accounted for, such effects have been included in PWB theory only.

The behavior of the cross-sections from both methods is different near threshold due to the way they treat long-range interaction. At high energy, cross sections show the

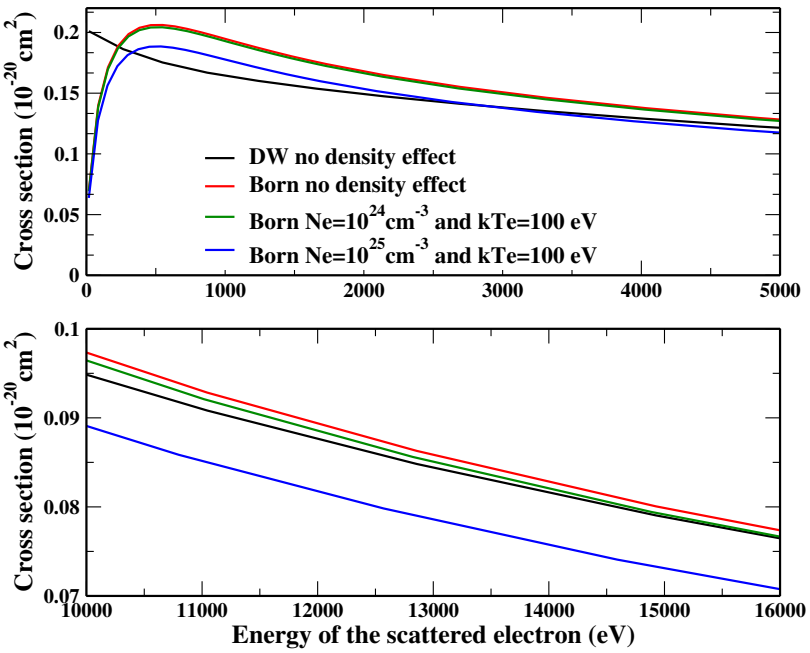

Figure 6.3.1 : Comparison of excitation cross section for transition $1s$–$2p_{1/2}$ for Al XIII at several densities and $kT_e = 100$ eV

same behavior. On Fig. 6.3.1 we notice that the plasma effect lowers this excitation cross section,though this variation is minor. To observe a significant change, we have to reach a high density such as $N_e = 10^{25}$ cm^{-3}. Then one has for the Wigner radius $R_0 = 1.25$ a$_0$, which is much greater than the wave function extension, and the plasma coupling parameter Z_f^2/kT_eR_0 is close to 1. This means that our formalism assuming non-overlap condition of ion wave functions [28] is applicable while non negligible density effects occur.

As seen in section 6.2.1, the radiative rates may increase or decrease depending of the studied transition, and the same behavior applies to excitation cross sections. Indeed excitation cross sections may increase as seen in the Al XII case presented on Fig. 6.3.2. In that case the transition energy from $1s4p\,^1P_1$ to $1s4d\,^1D_2$ first decreases with density and at the density $N_e \simeq 1.2 \times 10^{22}$ cm^{-3} those levels cross. We observe on that plot that the cross section increases until this critical density is reached. After the crossing the emission occurs from $^1D_2$ to $^1P_1$ and the cross-section decreases with the density. The increase of the cross section is stronger around the peak, but we have to keep in mind that PWB calculation overestimates the cross section in this area. Thus we must only rely on the high energy results where the cross-section shift is small. A possible explanation to this level crossing is that the electronic interaction is weak. Therefore in that situation the plasma potential has a stronger effect, which means that the bound electron interacts more with the continuum than the bound electrons.

We use Van Regemorter formula [71] to confirm our observations. This formula is valid under Born approximation and Bethe assumption (high energy and dipolar transition, see

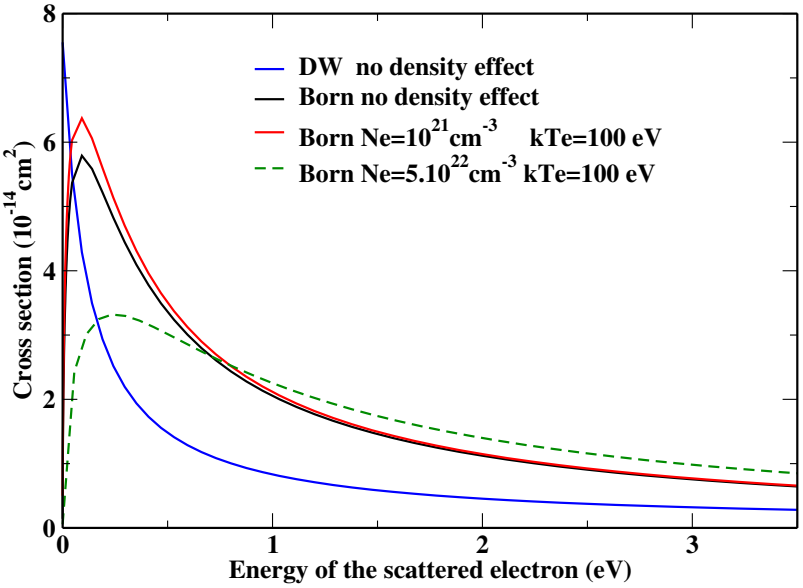

Figure 6.3.2 : Comparison of excitation cross sections for transition between 1s4d $^1D_2$ and 1s4p $^1P_1$ for Al XII at several densities

for instance chapter 4)

$$\sigma_{ij} = \frac{8\pi}{\sqrt{3}} \frac{R_y^2}{e_i} \frac{f_{ij}}{\Delta E_{ij}} \bar{g}\left(e_i/\Delta E_{ij}\right) \pi a_0^2, \tag{6.3.1}$$

where ΔE_{ij} is the transition energy from level i to j, a_0 is the Bohr radius, R_y the Rydberg energy, e_i is the energy of the incident electron, $\bar{g}$ is the Gaunt factor determined through empirical observations and f_{ij} is the oscillator strength. We choose the Gaunt factor as suggested by Mewe [72]

$$\bar{g} = 0.15 + 0.28 \log\left(\frac{e_i}{\Delta E_{ij}}\right). \tag{6.3.2}$$

We compare numerical cross sections and the Van Regemorter formula on Fig. 6.3.3. We note that the shift of cross sections is similar. In order to provide analytical expressions for the cross sections in the simplest case, we use a development based on equation (6.3.1). In that equation , the density effects modify the transition energy ΔE_{ij} and the oscillator strength f_{ij}. The Gaunt factor is also modified but we neglect it because of its slow variation with ΔE_{ij}. Thus the magnitude of the cross section mainly depends on the ratio $f_{ij}/\Delta E_{ij}$. Up to numerical constants this ratio is the square of a dipolar matrix element

$$\frac{f_{ij}}{\Delta E_{ij}} \propto \langle n_i l_i \left|r\right| n_j l_j \rangle^2 . \tag{6.3.3}$$

We now use the analytical formulas (chapter 5) for hydrogen-like ion in the UEGM framework. Thanks to this, we are able to isolate the contribution of the plasma potential by decomposing the matrix element at 0 order and first order of perturbation

$$\langle n_i l_i \left|r\right| n_j l_j \rangle = \langle n_i l_i \left|r\right| n_j l_j \rangle^0 + \langle \widetilde{n_i l_i \left|r\right| n_j l_j} \rangle. \tag{6.3.4}$$

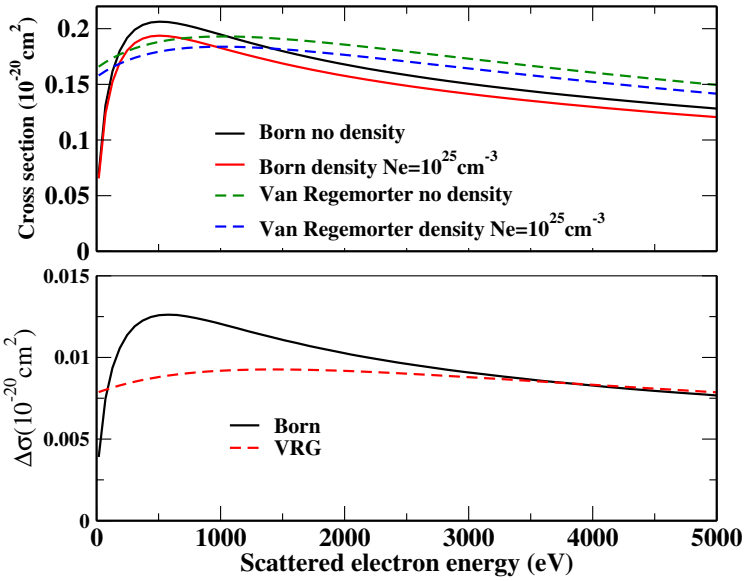

Figure 6.3.3 : Excitation cross sections for the transition $1s_{1/2}$–$2p_{1/2}$ in Al XIII: comparison between plane wave Born approximation and Van Regemorter formula. The upper figure represents the cross sections while on the lower figure are plotted the variations $\sigma(N_e = 0) - \sigma(N_e > 0)$ for both approximations.

	$\Delta\sigma/\sigma\ (N_e = 0)$			
E_f	TF $kT_e = 100$ eV	TF $kT_e = 500$ eV	TF $kT_e = 2000$ eV	UEGM
500	0.085	0.060	0.0489	0.0426
2000	0.086	0.061	0.0494	0.0430

Table 6.4 : Relative variation of excitation cross section for $1s - 2p_{1/2}$ with Thomas-Fermi and UEGM at a density of 10^{25} cm^{-3}.$\Delta\sigma = \sigma\,(N_e = 0) - \sigma\,(N_e)$

We calculate the matrix element under UEGM for the non-relativistic transition $1s$–$2p$ and obtain for an hydrogen-like ion, in atomic units

$$\langle 1s\,|r|\,2p\rangle = \frac{128}{243}\frac{\sqrt{6}}{Z}\left(1 - \frac{3059}{36}\frac{Z_f}{Z^4 R_0^3}\right). \tag{6.3.5}$$

In the case of hydrogen-like Al, we get

$$\langle 1s\,|r|\,2p\rangle^0 = 9.925 \times 10^{-2} \tag{6.3.6}$$

and for an average free-electron density $N_e = 10^{24}$ cm^{-3}

$$\widetilde{\langle 1s\,|r|\,2p\rangle} = -1.8329 \times 10^{-4}. \tag{6.3.7}$$

At such density the matrix-element perturbation is very small. Equations (6.3.6) and (6.3.7) confirm that the excitation cross section is not notably modified. In the table 6.4 we give some relative variation of the transition $1s - 2p_{1/2}$.

Forbidden and allowed transitions are differently affected by the plasma potential. This

comparison is illustrated by Fig. 6.3.4, where cross sections are calculated via the PWB approximation. The plot clearly shows that the allowed transition $1s - 2p_{1/2}$ is more sensitive to the plasma potential than the forbidden transition $1s - 2s$. This result has been first observed and explained by Hatton *et al* [115] who used a different plasma potential (Debye potential).

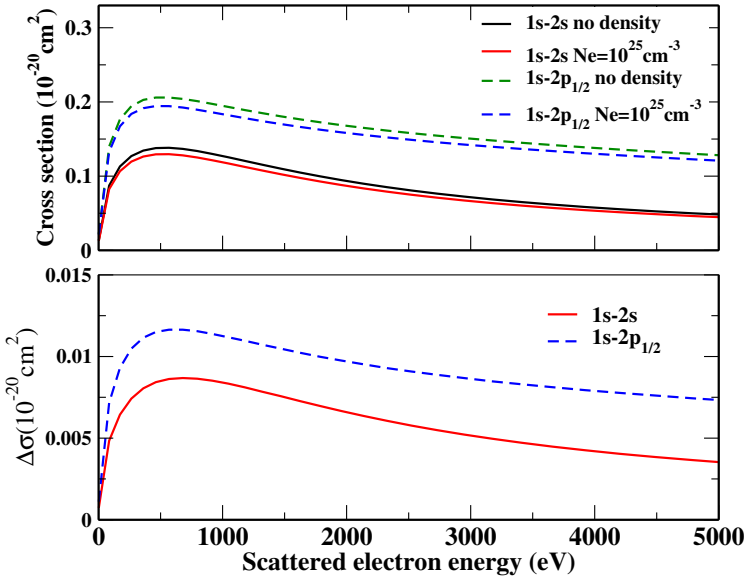

Figure 6.3.4 : Comparison of excitation cross sections for transition $1s$–$2p_{1/2}$ (dashed lines) and $1s_{1/2}$-$2s_{1/2}$ (solid line) for Al XIII using the plane wave Born approximation. When density effects are included, the temperature is 500 eV. The upper figure represents the cross sections while on the lower figure are plotted the variations $\sigma(N_e = 0) - \sigma(N_e > 0)$ for both transitions.

To be complete on the excitation cross section, we point out that articles of Whitten et al. [117] and Blancard et al.[107] mention resonances near threshold. We made the same observations, this resonances are only visible with the DW formalism and with an important amount of points (around hundreds). This resonances are explained in article [117]: this resonances correspond to the embed of a low energy outgoing electron inside the centrifugal barrier. We have chosen to not show this observation because the DW method is not supposed to be accurate in this range of energy. Moreover, the number of points used is so large that it appears cumbersome to make any computational calculations for a large set of configurations.

6.3.2 Ionization cross sections

Several works have considered the influence of plasma environment on electron-impact ionization cross-sections. Some use the Debye-Hückel theory (e.g., [116]), other the Thomas-Fermi (TF) approach [120]. Both the cited works use Hartree-Fock-Slater theory with cross-sections computed using distorted waves (DW). Here we have adopted the TF formalism for the plasma effect, but the collision formalism used, instead of DW, is the more

relevant binary encounter dipole theory (BED) [83] implemented in FAC. This method combines the Mott semi-classical calculation of cross section [86] for the scattering of two free electrons (valid for close collisions, i.e., at large momentum transfer), and the Bethe theory [124] which is the Born plane-wave approximation (valid at high energy and small momentum transfer) with only the dipolar term kept. This theory is of great interest due to its applicability both for ions and neutral atoms. Contrary to the case of excitation, we do not need to change our calculation approach when the plasma effect is included.

We plot the impact ionization cross section from state $1s^2$ to $1s$ in Al, at several densities on figure 6.3.5. A comparison is done with the empirical formula of Lotz [42]

$$\sigma_{ij} = C\pi a_0^2 Ry^2 \frac{w_n}{e_i \Delta E_{ij}} \log\left(\frac{e_i}{\Delta E_{ij}}\right), \tag{6.3.8}$$

where $C = 2.77$, w_n is the initial number of electrons concerned by the ionization process in the shell.

Our purpose is not to discuss the accuracy of Lotz formula compared to BED, but to characterize the plasma effect.

The cross section increases with density, as seen on figure 6.3.5. We can explain this increase by the decrease of the transition energy which in turn leads to larger collisional ionization. If we compare the cross-section variation due to the plasma effect at 10^{23} cm^{-3} and $kT_e = 200$ eV for BED and Lotz formula on Fig. 6.3.6, we notice that they are quite similar. We also see on this plot that the cross-section variation increases with the energy of scattered electrons and then slowly decreases after the peak. The temperature has an effect opposite to density, when it increases the cross section decreases.

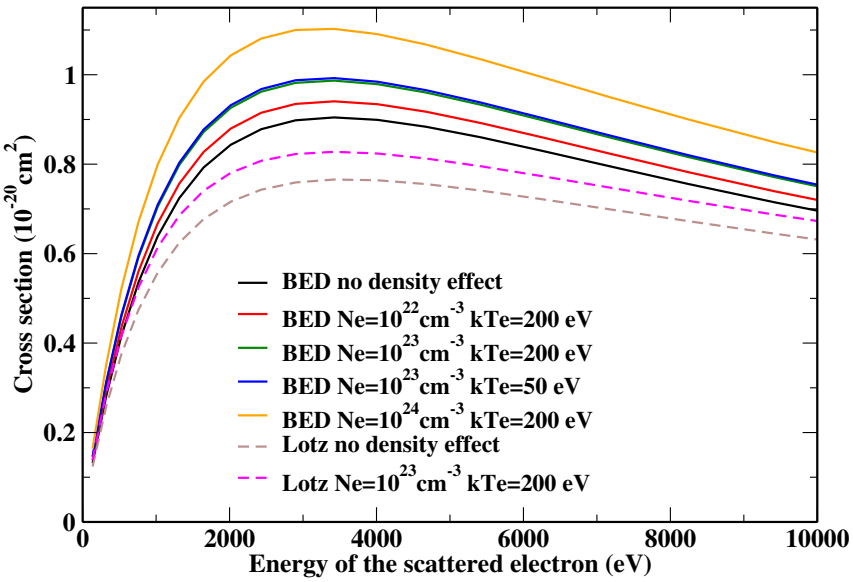

Figure 6.3.5 : Comparison of ionization cross section for the transition $1s^2$ to $1s$ for AlXII and XIII. The free-electron density is obtained from Thomas-Fermi model, and for the scattering process BED and Lotz formalisms are compared.

We may support these results using a formalism based on Lotz formula and a perturbative approach within the UEGM. As mentioned above, in UEGM, the first-order energy correction for a hydrogen-like ion is

$$E^{(1)}_{\text{plasma}} = \frac{Z_f}{R_0}\left(\frac{3}{2} - \frac{\langle r^2\rangle_{nl}}{2R_0^2}\right), \tag{6.3.9}$$

with

$$\left\langle r^2\right\rangle_{nl} = \frac{n^2}{2Z^2}\left(5n^2 - 3l\left(l+1\right)+1\right). \tag{6.3.10}$$

For example, for the ionization of a hydrogen-like ion in nl state to a fully stripped ion, the transition energy is

$$\Delta E = \frac{Z^2}{2n^2} - \frac{Z_f}{R_0}\left(\frac{3}{2} - \frac{\langle r^2\rangle_{nl}}{2R_0^2}\right), \tag{6.3.11}$$

which shows that the energy decreases with density. The cross section increases with density due to its dependency on the energy transition $1/\Delta E_{ij}$, as observed on Fig. 6.3.5. The study on other elements leads to same results.

Our results agree with Wu *et al* [120] in the increase of the ionization cross-section with density, though their work rely on DW theory. As mentioned by Pindzola *et al* [116], we checked that their cross-sections in Ge-like gold are underestimated by a factor of 2. But the cross-sections from [116] decrease with density. These authors explain that this behavior is linked to the Debye screening of inter-electronic interaction. However their work since it is based on Debye theory is applicable only at low coupling parameter while we do not believe the same restriction applies to the present work. Additional results from theory and experiment would be useful to clarify this point.

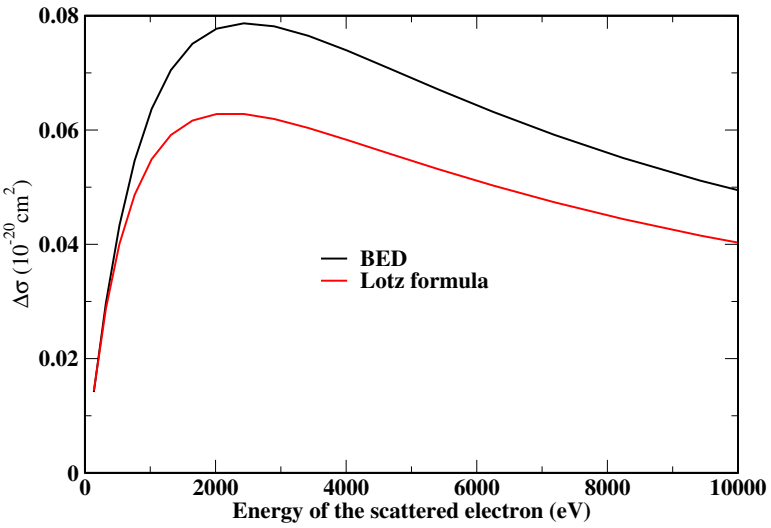

Figure 6.3.6 : Comparison of ionization cross section for transition $1s^2$ to $1s$ for AlXII and XIII at $N_e = 10^{23}$ cm^{-3}at $kT_e = 200$ eV. $\Delta\sigma$ is the cross section at $N_e = 10^{23}$cm^{-3}minus the cross section at $N_e = 0$

6.3.3 Photo-ionization cross section

The influence of the plasma environment on photo-ionization has been investigated by different authors. Chang et al.[121] in case of Hydrogen-like ion and by Sahoo et al. [122] for alkali elements have used the Debye-Hückel theory. The ion sphere model has been used by Das[100] under the UEGM with the condition of cancellation of the wave function on the ion sphere. Here we have adopted the supposedly more realistic TF formalism for the plasma effect. The evaluation of the bound-free oscillator strength is similar to the bound-bound oscillator strength. In the FAC code the continuum wave function for the photo-ionization is calculated by the DW method.

We plot the impact ionization cross section from state $1s^2$ to $1s$ in Al, at several densities on Figure 6.3.7. The cross section increases with density, as seen on figure 6.3.7. This increase is more significant at low energy. At high energy the cross section fall rapidly to zero, therefore the plasma potential has almost no impact on the photo-ionization. This increase of the the cross section is linked to continuum lowering which lead to a decrease of the transition energy as for the ionization.

A comparison is done on Figure 6.3.8 with the empirical formula of Kramers [43]

$$\sigma_{ij} = \frac{64\pi}{3\sqrt{3}} \alpha a_0^2 Ry \frac{w_i}{n_i} \frac{\Delta E_{ij}^2}{(h\nu)^3}, \tag{6.3.12}$$

where $\Delta E_{ij}$is the threshold energy for photo-ionization, w_n is the initial number of electrons concerned by the ionization process in the shell, n_i is the principal quantum number of the initial state and $h\nu$ is the energy of the incident photon.On Fig. 6.3.8 we compare at different densities 10^{23} cm^{-3}and 10^{24} cm^{-3}with a temperature $kT_e = 500$ eV the DW method of FAC and the Kramers formula. Here we notice that in both cases the cross section increase at low energy. However the upward shift of the photo-ionization is smaller with the empirical approach. We explain this by the fact that the Kramers formula only takes into account the transition energy but not the wave functions perturbation. At higher energy the agreement about the cross section behavior is worst. Indeed, with the density effect the Kramers cross section decrease faster than the DW cross section.

The increase of the cross section agrees with the observation Sahoo et al. [122] Das [100]and Chang et al [121].

The most important change in the photo-ionization cross section appear near threshold. In this range of energy and in absence of plasma effect the cross section behavior is monotonous. However with the plasma effect the shape of the cross section completely change. A minimum is present next to the threshold followed by a peak, with the increase of the density this minimum is more pronounced. This minimum is called in the litterature a Cooper minimum. The Cooper minimum has been explained by J.C Cooper [125] in case of alkali element. This minimum appears when the the amplitude of the bound and free wave function exactly canceled. Many authors [121, 100, 122] have seen the Copper

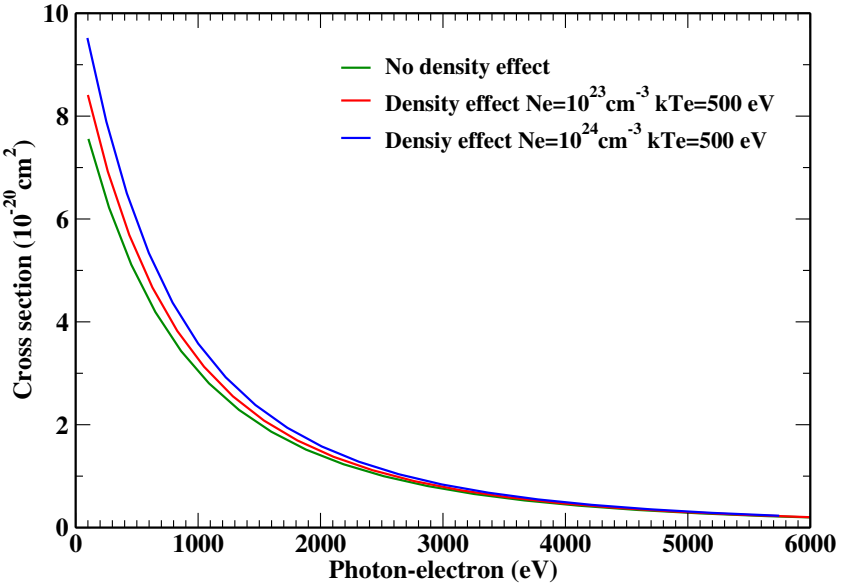

Figure 6.3.7 : Comparison of photo-ionization cross section for the transition $1s^2$ to $1s$ for AlXII and XIII at $kT_e = 500$ eV. The free-electron density is obtained from Thomas-Fermi model, and for the scattering process are calculated with the DW formalisms.

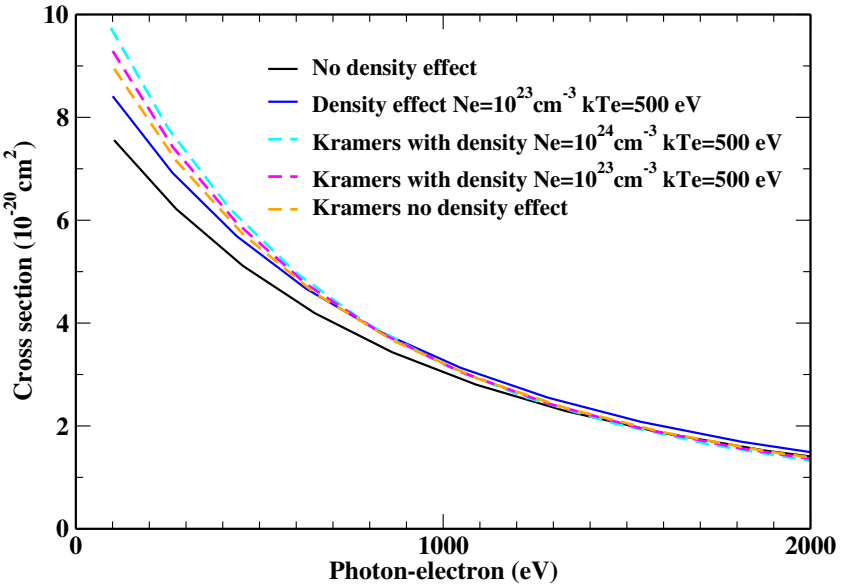

Figure 6.3.8 : Comparison of photo-ionization cross section for the transition $1s^2$ to $1s$ for AlXII and XIII at $kT_e = 500$ eV. The free-electron density is obtained from Thomas-Fermi model, and for the scattering process DW and Kramers formalisms are compared

minimum for different element than aluminum and with different plasma potential Debye-Hückel or ion sphere. In every cases the Cooper minimum is shifted to higher energy with the increase of the density.

As for the electron impact excitation, we have chosen to not show this observation on a plot, because of the presence of resonances in the same region as the Cooper minimum. We point out that in the article of Das [100] which use an ion sphere potential, additional resonances are observed. These oscillations are the consequence of the choice of the cancellation of the wave function on the Wigner-Seitz sphere. We recall that this choice has been rejected for this present work.

6.4 Summary and conclusions

Using a Thomas-Fermi (TF) approach for free electrons, we have investigated the effect of the plasma environment on the atomic structure. It has been shown that this formalism valid at finite temperature leads to a larger plasma potential than the Uniform Electron Gas Model (UEGM) previously used. In most cases the inclusion of density effects results in level shifts and change in rates which are stronger with TF model than with UEGM. This self-consistent plasma potential has been included in the FAC code allowing us to obtain an accurate atomic description for opacity calculations or collisional-radiative models. The results obtained here show that no general behavior for the perturbation of bound-bound processes can be predicted. As a spectroscopic analysis by Li and Rosmej [123] has shown, transition energies may increase or decrease with electron density. Using FAC we have been able to confirm this observation and generalized it to radiative rates and e-impact excitation rates. The situation is usually simpler for H-like ions, as stated previously [28]. Furthermore we obtained ionization cross sections increasing with density, a fact which we explained by the decrease of the transition energy. A similarly observation is made on the photo-ionization. However the cross section are less impacted by the plasma potential.

This work represent a first important step in the investigation of density effects in a collisional-radiative code. Indeed, a previous study [126] using a plasma potential based on quasi-particle energies and effective interaction claims that the plasma environment has a minor impact on rates, the main effect on population distribution coming from the allowed number of bound levels. Accordingly this work clearly shows that atomic processes are perturbed in a non-negligible way. Therefore it is highly desirable to investigate environment effects on plasma kinetics, as well as on absorption and emission spectra.

Chapter 7

Description and application of a new kinetic code

7.1 Introduction

In this last chapter we introduce a new collisional radiative code and develop several applications. One of our purposes will be to show the effect of the plasma potential within ion-sphere hypothesis on the collisional radiative model (cf chapter 3). To achieve this goal, we use a new collisional radiative code which we have named Foch. This code had been developed during the thesis in order to treat the atomic data from FAC. This chapter begins with features of the Foch kinetic code. To check the quality of the Foch code we first give an example without plasma density effect in krypton for which Bastiani et al. [127] have provided experimental data. Then we carry on with the plasma density effect on the aluminium. This case will serve to understand the impact of the ion sphere potential on a tractable situation. The last case concerns a comparison between our work and a recently published [128] experiment on Titanium.

7.2 Inclusion of density effect

First we have to recall that our plasma potential is only static, no dynamical response is included in our model. The main plasma effect present is the continuum lowering. With the static potential we have shown the shift of energy levels and spreading of wave-functions. Another effect which may be considered is the pressure ionization. This phenomenon corresponds to the transition of a bound electron into the continuum due to the screening. Of course one possible way to model this effect is to suppress the concerned configurations which pass in the continuum. This approach does not appear physically correct because a discontinuity appears in the observable [38]. This method leads to a strong increase of the ionization degree. Another approach consists of keeping all the configurations and modelling the pressure ionization by a new rate added to the kinetic equations. Such

an approach has been modelled by Vallotton et al [106][129]. The plasma potential used in his work is the ion sphere only under the UEGM form. We point out that a different choice on the neutrality condition has been made. Indeed, following Massacrier work [101] a free electron is added to the neutrality condition $Z - N_b + 1 + \frac{4}{3}\pi R_0^3 N_e = 0$. However, the results of the work shows that the inclusion of the pressure ionization reduces the ionization degree compared to the withdrawal of the configurations. In our work we have made the choice to keep the same configurations with and without plasma density effect. Unlike Vallotton, we have not implemented a pressure ionization rate .

7.3 The kinetic code Foch

7.3.1 Transition rates

This section is devoted to the method of calculating the rates included in the Foch code. By default the rates are calculated through the atomic data of FAC, but it is possible to lead the calculation with semi-empirical rates (Mewe, Lotz, Kramers). These formulas have been implemented to obtain a first idea of the plasma properties before leading a more accurate calculation of the collisional cross section. For instance, the excitation cross section computation time becomes prohibitive. Therefore the electron impact cross section for doubly excited states is often calculated by the Mewe formula (4.3.53). In what follows we will provide the calculation specificities with respect to the studied case. We only consider inelastic collisions. The influence of the elastic collisions is included in a phenomenological way via the line broadening [50].

The collisional rate from the level i to j for an incident electron is given by

$$R_{ij} = N_e \int_{\Delta E_{ij}}^{\infty} \sqrt{\frac{2E}{m_e}} \sigma_{ij}(E) f(E) dE \tag{7.3.1}$$

in cgs unit. N_e is the electron density, m_e the mass of the electron, E the energy of the incident electron, ΔE_{ij} the transition energy and $\sigma_{ij}(E)$ the inelastic cross section. The function $f(E)$ is the kinetic energy distribution of the free electrons which we assume here to follow the Maxwell law

$$f(E) = \frac{2}{\sqrt{\pi}} \frac{\sqrt{E}}{kT_e^{3/2}} e^{-E/kT_e}, \tag{7.3.2}$$

where kT_e corresponds to the electronic temperature. The normalization condition is

$$\int_0^{\infty} f(E) dE = 1. \tag{7.3.3}$$

The collision strength labeled $\Omega_{ij}(E)$ is linked to the cross section $\sigma_{ij}(E)$by the relation in atomic units

$$\sigma_{ij}(E) = \frac{\pi}{g_i k_i^2} \Omega_{ij}(E) \tag{7.3.4}$$

where g_i the degeneracy of the level i and k_i the momentum of the incident electron ($k_i^2 = 2E$ in a.u). The equation (7.3.1) can be expressed in term of the scattered electron energy E_f

$$R_{ij} = \sqrt{2\pi}\frac{\hbar^2}{m_e^{3/2}}\frac{N_e}{kT_e^{3/2}g_i}e^{-\Delta E_{ij}/kT_e}\int_0^\infty \Omega_{ij}\left(E_f\right)e^{-E_f/kT_e}dE_f, \tag{7.3.5}$$

with $E - E_f = \Delta E_{ij}$. The FAC code gives by default the cross sections and the collision strength with respect to the scattered electron energy.

In the case of an incident photon the photo-ionization rate is obtained by

$$R_{ij} = c\int_{\Delta E_{ij}}^\infty \sigma_{ij}\left(\epsilon\right)\frac{U\left(\epsilon\right)}{\epsilon}d\epsilon \tag{7.3.6}$$

with c the speed of light and $\epsilon = E_f + \Delta E_{ij}$ is the photon energy. The function $U(\epsilon)$ corresponds to the spectral energy density. If we assume a Planck distribution of the radiative field, it comes

$$U\left(\epsilon\right) = \frac{\epsilon^3}{\pi^2\hbar^3c^3}\frac{1}{e^{\epsilon/kTr}-1}, \tag{7.3.7}$$

where kT_r stands for the radiative temperature.

To calculate these rates, different approaches can be used. The rates can be calculated via semi-empirical expressions for the cross section as the ones given in chapter 4. This leads to analytical expressions for the rates, such an approach is used in the ABAKO code [130]. Of course the overall accuracy of the code relies on the accuracy of those empirical formulas. Another method consists of using fit formula for the cross section such as the Goett formula [131] for excitation cross section. In the HULLAC code [16] the photo-ionization cross section is also evaluated via a fit formula. The last way to get the rates is to compute integrals involving an "accurate" cross sections obtained from one of the methods mentioned in chapter 4 (DW, Born, classical theory or R-matrix, Close coupling...). The problem relies on the computation time, which compels us to compute only a few cross sections to get the transition rate. For the Foch code, by default, all the rates are calculated via the atomic data of FAC by performing a Gauss-Laguerre integration. Because of this method the grid depends on the electronic temperature. The Gauss-Laguerre method approximates that

$$\int_0^\infty f(x)e^{-x}dx \simeq \sum_i^N f(x_i)w_i \tag{7.3.8}$$

where x_i represents the root of the Laguerre polynomial of degree N and the w_i the statistical weights of the roots. For our calculations, we usually take 16 points to carry the integration.

Collisional excitation and deexcitation rates

The excitation rate is directly obtained from equation (7.3.5) . A semi-empirical rate can be obtained via the Van Regemorter cross section (6.3.1) with a Gaunt factor $g(\Delta E_{ij}/kT_e)$

$$R_{ij} = \frac{16\sqrt{2}R_y^2\pi^2 a^2{}_0}{\sqrt{3\pi m_e}} \frac{N_e f_{ij}}{\Delta E_{ij}\left(kT_e\right)^{1/2}} g(\Delta E_{ij}/kT_e) e^{-\Delta E_{ij}/kT_e} \tag{7.3.9}$$

where R_y represents the Rydberg constant, a_0 the Bohr radius and f_{ij} the oscillator strength from i to j. Finally, by calculating the constants, assuming N_e is in cm^{-3} and all energies in eV,

$$R_{ij}(\mathrm{s}^{-1}) = 1.58 \times 10^{-5} \frac{N_e f_{ij}}{\Delta E_{ij}\left(kT_e\right)^{1/2}} g(\Delta E_{ij}/kT_e) e^{-\Delta E_{ij}/kT_e}. \tag{7.3.10}$$

The inverse process, the deexcitation is evaluated through the detailed balance

$$R_{ji}^{dex} = \frac{g_i}{g_j} e^{\Delta E_{ij}/kT_e} R_{ij}^{ex}. \tag{7.3.11}$$

Ionization and three bodies recombination rates

The collisional ionization is exactly calculated in the same way as the excitation rates formula (7.3.5). Through the formula (6.3.8) proposed by Lotz the ionization rate is

$$R_{ij}^{Lotz} = C\sqrt{\frac{8\pi}{m_e}} R_y^2 a_0^2 \frac{N_e w_n}{\Delta E_{ij}\left(kT_e\right)^{1/2}} E_1\left(\Delta E_{ij}/kT_e\right), \tag{7.3.12}$$

where E_1 stands for the exponential integral function, defined by

$$E_1(x) = \int_x^\infty \frac{e^{-y}}{y} dy.$$

Finally, by calculating the constants

$$R_{ij}^{Lotz}\left(\mathrm{s}^{-1}\right) = 3.02 \times 10^{-6} \frac{N_e w_n}{\Delta E_{ij}\left(kT_e\right)^{1/2}} E_1\left(\Delta E_{ij}/kT_e\right). \tag{7.3.13}$$

The inverse process, the three body recombination which concerns two electrons is calculated via the Saha equation

$$R_{ji}^{3rc} = \frac{1}{2}\lambda_{th}^3 N_e \frac{g_i}{g_j} e^{\Delta E_{ij}/kT_e} R_{ij}^{ci}, \tag{7.3.14}$$

where λ_{th} is the thermal wave-length

$$\lambda_{th} = \left(\frac{h^2}{2\pi m_e k T_e} \right)^{1/2}. \tag{7.3.15}$$

Auto-ionization and dielectronic capture rates

The auto-ionization rate R_{ij}^A is directly calculated in cgs units by the FAC code. The dielectronic capture is given by the detailed balance

$$R_{ji}^{DC} = \frac{1}{2} \lambda_{th}^3 N_e \frac{g_i}{g_j} e^{\Delta E_{ij}/kT_e} R_{ij}^A. \tag{7.3.16}$$

A semi-empirical formula can be found for the dielectronic capture [130] or [132], however its accuracy is not satisfactory in our opinion.

Photo-ionization and radiative recombination rates

We first recall the Milne relation [14] between the photo-ionization and the radiative recombination cross section

$$\sigma_{ij}^{phot} = 2 \frac{g_j}{g_i} \frac{m_e c^2 \left(E - \Delta E_{ij} \right)}{E^2} \sigma_{ji}^{rr}, \tag{7.3.17}$$

where E the photon energy. In the presence of a radiative field, the photo-ionization have to be taken into account. In that case, assuming a Planck distribution (cf. equation (7.3.7)) applies for the radiative field, the photo-ionization rate is given by

$$R_{ij}^{photo} = \frac{8\pi}{h^3 c^2} \int_{\Delta E_{ij}}^{\infty} E^2 \frac{\sigma_{ij}^{photo}(E)}{e^{E/kT_r} - 1} dE, \tag{7.3.18}$$

with kT_r the radiative temperature. Furthermore, it is necessary to take into account the stimulated radiative recombination in addition to the spontaneous radiative recombination. This rate expresses

$$R_{ij}^{rrs} = \frac{4\pi}{h^3 c^2} \frac{g_i}{g_j} \lambda_{th}^3 N_e \int_{\Delta E_{ij}}^{\infty} E^2 \frac{e^{-(E - \Delta E_{ij})/kT_e}}{e^{E/kT_r} - 1} \sigma_{ij}^{photo}(E)\, dE \tag{7.3.19}$$

In all the cases presented the plasma conditions are such that we do not have to take into account the radiative field. However, these formulas are implemented in the Foch code.

In absence of an external field, the spontaneous radiative recombination is

$$R_{ji}^{rr} = \frac{4\pi}{h^3 c^2} \frac{g_i}{g_j} \lambda_{th}^3 \int_0^{\infty} \left(E_f + \Delta E_{ij} \right)^2 \sigma_{ij}^{photo}(E_f)\, e^{-E_f/kT_e} dE_f \tag{7.3.20}$$

An analytical formula is obtained thanks to the Kramers formula. The radiative recom-

bination cross section writes

$$R_{ji}^{rr} = \frac{64\sqrt{\pi}\alpha^2 a_0^2 R_y^{1/2}}{3\sqrt{3}m_e c}\frac{g_i}{g_j}\frac{w_j}{n_j}\frac{N_e}{(kT_e)^{3/2}}\Delta E_{ij}^2 E_1\left(\Delta E_{ij}/kT_e\right)e^{\Delta E_{ij}/kT_e}, \tag{7.3.21}$$

with w_j the number of electrons in the initial shell and n_j the principal quantum number of the initial level. Finally by calculating the constants, it comes

$$R_{ji}^{rr} = 7.05\times10^{-15}\frac{g_i}{g_j}\frac{w_j}{v_j}\frac{N_e}{(kT_e)^{3/2}}\Delta E_{ij}^2 E_1\left(\Delta E_{ij}/kT_e\right)e^{\Delta E_{ij}/kT_e}. \tag{7.3.22}$$

Once the rates are calculated, the kinetic equations can be solved. To achieve that objective the code possesses three solvers: a classical Gaussian elimination (gaussj from Numerical Recipe [133]), a LU method (LU from Numerical Recipe) and a LU method for band matrix (dgbsvx from lapack [134]). This latter is the fastest of them. Our computing capacity can treat a maximum of 40 000 levels. Concerning the collisional radiative code, it is able to work in Detailed Configuration Accounting (DCA) or detailed calculations. For the free electrons we assume a Maxwell distribution consistent with the Thomas-Fermi approach used for the plasma potential. In all the following situations, no radiative field is taken into consideration. However, an option is included in the Foch code.

7.3.2 Spectra

Concerning the spectra, the code only computes the emissivity for the bound-bound, bound-free and free-free processes. The line profile chosen for the bound-bound spectra is a Voigt profile (method from Drayson [135]). A Gaussian or Lorentzian profile can also be used. For the detailed, calculation we use the natural and the Doppler broadening. To deal with the electron impact broadening, the semi-empirical formula of Dimitriejic [50] is used see equation (3.7.11). If the UTA option is used, the line profile is Gaussian and the broadening is statistical and Doppler.

To calculate the bound-free emission, the photo-ionization is evaluated via the Kramers formula (6.3.12). The Gaunt factor used, corresponds to the ratio between the photo-ionization rate calculated via the DW method of FAC and the photo-ionization rate evaluated from the Kramers formula. The free-free contribution is calculated via the semi-empirical formula (3.7.5).

7.4 Applications

7.4.1 Krypton

Here, we present a NLTE case of krypton which has been treated in the NLTE7 workshop [136]. Before treating the effect of the plasma environment, this case allows us to

evaluate the quality of the kinetic code Foch. Here, we do not include the plasma environment in our calculations.This case originates from an experiment performed at LULI2000 [127]. This experiment uses krypton gas jet and provides resolved time-integrated spectra between 6 to 8 Angströms. The plasma is diagnosed by X-ray and time-resolved XUV emission spectroscopy. The plasma temperature and density are determined by a Thomson scattering method. The range of density obtained is about $N_e = 0.2 - 1.2 \times 10^{19}$ cm^{-3} and the temperature $kT_e = 160 - 500$ eV. In the article several spectra are proposed as functions of the jet pressure and the energy of the laser.

For our numerical simulations, we have used around 40 000 levels in configurations (UTA mode of FAC), the total statistical weight of our simulation is 1.8×10^7. To compute the spectra, a Gaussian profile is used with the statistical and Doppler broadening. The excitation cross sections are computed via the plane wave Born approximation and binary encounter dipole theory for the collisional ionization. The plasma parameters used are $N_e = 10^{19}$ cm^{-3} and $kT_e = 500$ eV. The calculated mean charge is ~ 24.8. On the figure 7.4.1 the result from the Foch code and the experiment are plotted. The data of the experiment correspond to the case of a jet pressure of 4 bar and laser energy of 365 J. We notice that the comparison is quite acceptable, the positions of the peaks are close to the experiment peaks. Still, for certain lines our broadening is too weak. The line broadening calculation is the major weakness of the Foch code, no refined theory is used (no opacity effects or sophisticated broadening). However, the density and temperature used in our code fit in the range of the density and temperature mentioned by the experiment. We point out that the data of the experiment has been rescaled for clarity.

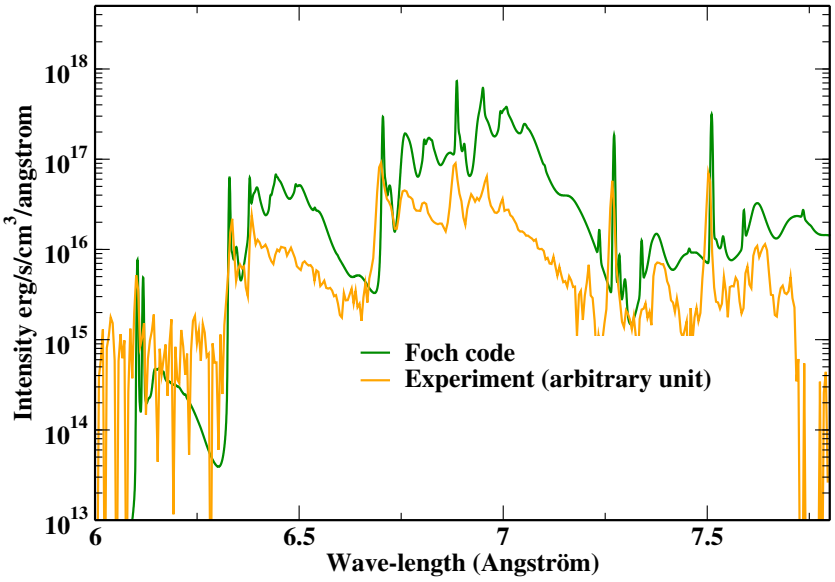

Figure 7.4.1 : Comparison of bound bound spectra for krypton between experiment [127] and Foch code for $N_e = 10^{19}$ cm^{-3} and $kT_e = 500$ eV

In Figure 7.4.2 we compare, the Foch bound-bound spectra with others collisional-radiative codes. The red colour corresponds to the code ATOMIC [18, 82] used by the Los

Alamos National Laboratory. This code uses a fully relativistic description of the atomic structure. To produce the spectra fine structure line (Doppler+natural broadening) and UTA are used. Their chosen temperature is $kT_e = 500$ eV and density is $N_e = 5 \times 10^{19}$ cm^{-3}. The mean charge is about ~ 24.15. The number of levels considered is above 40 000 with a total statistical weight of $\sim 6 \times 10^8$. The second simulated spectra is provided by the AVERROES code [22]. This code is based on the mixing of configurations and super-configurations. The atomic structure of the code is not relativistic but include relativistic corrections. This code treats the krypton case for a density of $N_e = 10^{19}$ cm^{-3} and a temperature of $kT_e = 600$ eV. The mean charge is ~ 24.6 The number of level is around 15 000 and the total statistical weight is $\sim 6 \times 10^9$. We observe that the Foch code behaves in a similar way as the two others.

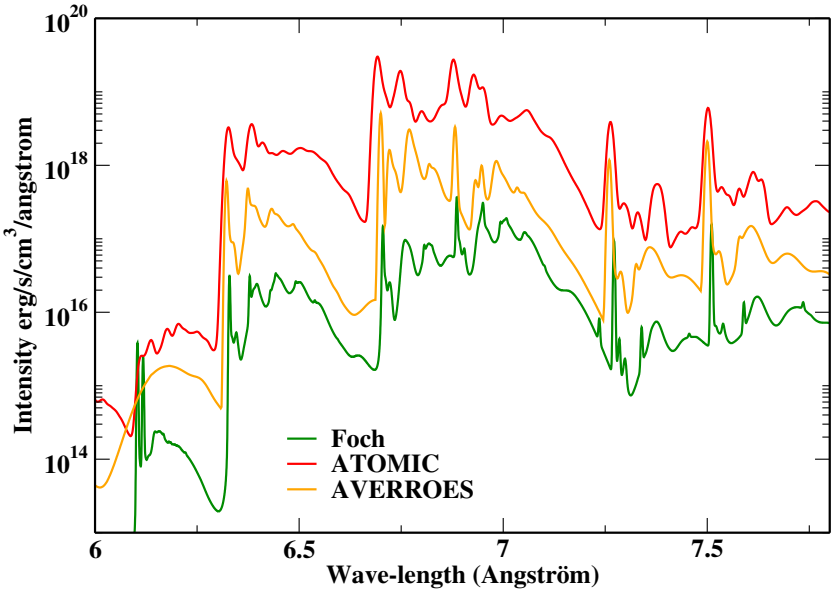

Figure 7.4.2 : Comparison of bound bound spectra for krypton between different simulations Foch code for $N_e = 10^{19}$ cm^{-3} and $kT_e = 500$ eV, ATOMIC $N_e = 5 \times 10^{19}$ cm^{-3} and $kT_e = 500$ eV, AVERROES $N_e = 6 \times 10^{19}$ cm^{-3} and $kT_e = 600$ eV.

7.4.2 Aluminum

In this section we investigate the effect of the plasma environment. The plasma potential considered is the Thomas-Fermi potential restricted to the free electrons. The temperature considered is $kT_e = 500$ eV and density is $N_e = 5 \times 10^{23}$ cm^{-3}.This case of study is simple, only 1929 detailed levels are considered with a maximum principal quantum number of $n_{max} = 3$. This allows us to respect the validity criteria of our static potential. Therefore no dynamical response has to be taken into account. Moreover, under these conditions the DW and PWB approximation for excitation cross sections give very similar results. On figure 7.4.3, the ion populations are plotted as functions of the ionic charge. We

observe that the DW and the Born calculation are very close. Under the thermodynamical conditions mentioned above, the plasma is mainly dominated by hydrogen and helium like species. The plasma coupling parameter is about $\Gamma \sim 2.2$ with an average Wigner-Seitz radius of $R_0 = 3.33\ a_0$. On the plot we can see that the effect of the plasma potential increases the ionization degree. Moreover this lead us to situation closer the LTE regime (turquoise curve).

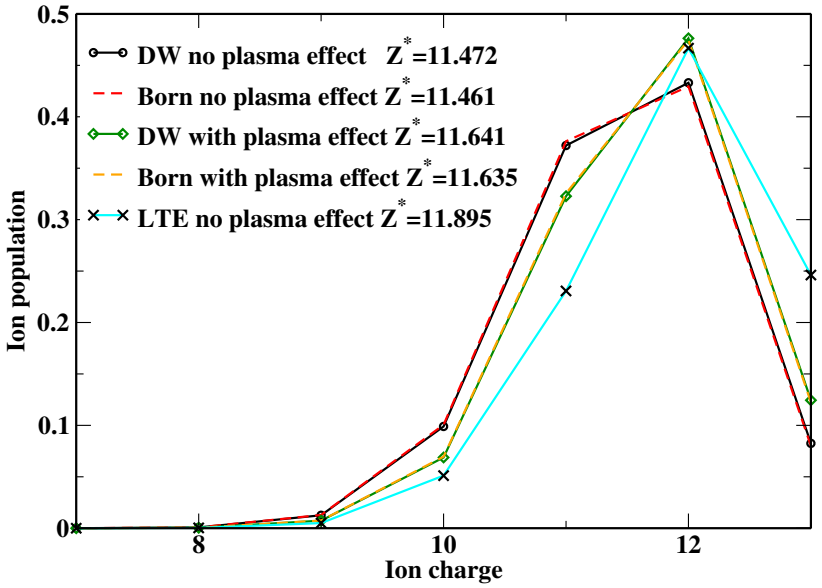

Figure 7.4.3 : Ion populations for aluminium element at $N_e = 5.10^{23}\text{cm}^{-3}$and $kT_e = 500$ eV with and without screening and with DW method (solid lines) and Born method (dashed lines).

This observation was expected because of the behaviour of collisional ionization seen in the previous chapter.

Rates

In chapter 6, we have studied the impact of the plasma environment on collisional cross sections. From those cross sections, we calculate the collisional rates involved in the claculation of atomic populations. Here, we propose to analyse the influence of the plasma environment on the collisional excitation rates. The collisional rates are proportional to

$$R_{ij} \propto e^{-\Delta E_{ij}/kT_e} \int_0^\infty \Omega_{ij}\left(E_f\right) e^{-E_f/kT_e} dE_f. \tag{7.4.1}$$

In the expression above, two terms are modified by the inclusion of the plasma environment: the transition energy ΔE_{ij} and the collision strength $\Omega_{ij}\left(E_f\right)$. In most cases ΔE_{ij} decreases with the density. As seen in the section6.3.1, the collision strengh $\Omega_{ij}\left(E_f\right)$ may decrease or increase with the density. This fact is explained by the behavior of the matrix element.

We recall that for isolated ions the distorted wave method (DW) gives good results.

However when dealing with the plasma environment we only use the plane wave Born approximation (PWB). On the Figure 7.4.4, we have plotted the ratio of PWB to DW collisional excitation rate as a function of the temperature. On the same graph we have plotted a curve showing the density effect with PWB. The considered collisional rate concerns the transition $1s - 2p_{1/2}$ for Al XIII at $N_e = 5 \times 10^{23}\text{cm}^{-3}$. This plot shows that the difference between the rates mainly lies between the two methods rather than the plasma effect. The departure of the green curve to the unit value is explained the different behaviour of the DW and the PWB at low energy. Meanwhile, at high temperature the difference shades off because both methods converge.

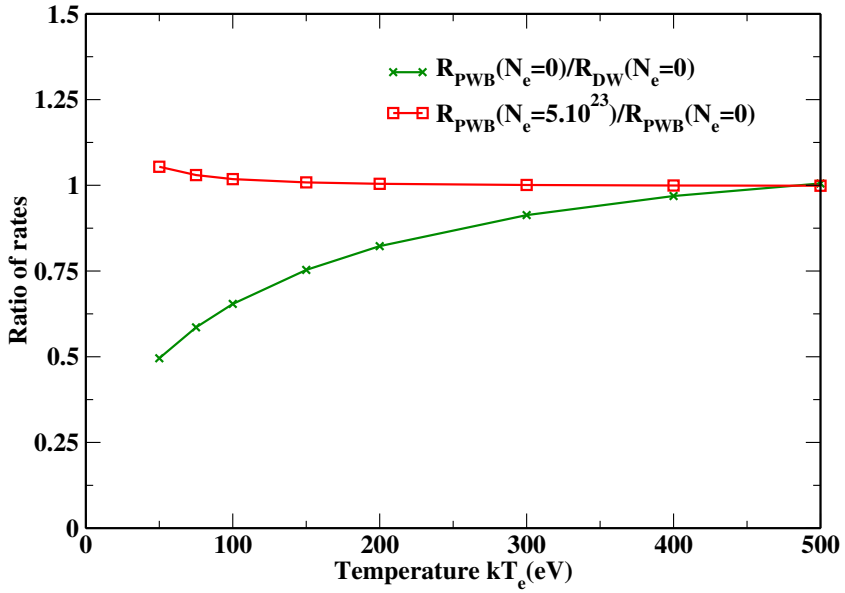

Figure 7.4.4 : Ratio of collisional excitation rates. The transition chosen is $1s - 2p_{1/2}$ for Al XIII. The considered density is $N_e = 5 \times 10^{23}\text{cm}^{-3}$.

Simple approximations can be used to analyze the plasma environment effect on these rates. For low kT_e, the integral over E_f in the rate (7.3.5) tends to $kT_e\Omega_{ij}(0)$, simply proportional to the collision strength at threshold. Therefore, the ratio of the excitation rates with and without plasma effect is

$$R_{ij}^{\text{pl}} \Big/ R_{ij}^{(0)} = \exp\left(-\frac{\Delta E_{ij}^{pl} - \Delta E_{ij}^{(0)}}{kT_e}\right) \Omega_{ij}^{pl}(0) \Big/ \Omega_{ij}^{(0)}(0) \quad \text{if } kT_e \ll \Delta E_{ij}. \tag{7.4.2}$$

where the superscript (0) stands for the case with not density effect accounted for. Since, as we have seen, the difference $\Delta E_{ij}^{pl} - \Delta E_{ij}^{(0)}$ is in most cases negative, the first factor in the ratio (7.4.2) is greater than 1 and increases with $1/kT_e$ while the ratio of the collision strengths at threshold, though less than 1, does not depend on kT_e if the UEGM is used, or weakly depends of the Temperature in the TF model. Therefore for low enough kT_e the collisional excitation rate *increases* when the plasma effect is accounted for. One should notice that the above analysis does not rely on any approximation on atomic structure or

scattering theory but on the general behavior of the plasma effect on transition energies and collision strengths. The opposite case of large kT_e can be investigated using the Van Regemorter formula (7.3.9). Since the variation of the Gaunt factor with the plasma effect can usually be neglected, the effect of the plasma environment for large kT_e is measured by the ratio

$$R_{ij}^{\rm pl} \Big/ R_{ij}^{(0)}\Big|_{\rm VR} = \exp\left(-\frac{\Delta E_{ij}^{pl} - \Delta E_{ij}^{(0)}}{kT_e}\right) \frac{f_{ij}^{pl}/\Delta E_{ij}^{pl}}{f_{ij}^{(0)}/\Delta E_{ij}^{(0)}} \quad \text{if } kT_e \gg \Delta E_{ij}. \tag{7.4.3}$$

The ratio $f_{ij}/\Delta E_{ij}$ is proportional to a squared dipolar matrix element and usually decreases when the plasma effect is accounted for — though the opposite may be true as seen in the figure 6.3.2 for an He-like ion or in equation (5.4.23) for H-like ions. Conversely, as mentioned when discussing Eq. (7.4.2), the ratio of the Boltzmann factors increases when plasma effect is accounted for. Therefore the ratio (7.4.3) may be below or above 1, and usually increases with $1/kT_e$. These considerations are illustrated by the last row of Table 7.1 where we may verify that for the $1s-2p$ transition in H-like aluminum the plasma environment effect increases the collisional excitation rates at low temperature while it lowers these rates at high temperatures. In the considered case this behavior is at variance with the plasma effect on the radiative rate.

	Thomas-Fermi		
	$T_e = 100$ eV	$T_e = 2000$ eV	UEGM
$\Delta A/A$	-0.147	-0.080	-0.066
$\Delta R/R$	$+0.324$	-0.045	$+0.095$

Table 7.1 : Relative variation $X(N_e)/X(N_e=0)-1$ of the radiative (A) and collisional-excitation rates (R) for the $1s-2p_{1/2}$ transition in Al XIII. Collisional rates are computed using Born approximation. The electronic density is $N_e = 10^{25}$ cm^{-3}. The collisional-excitation rate variation within UEGM is computed at $T_e = 100$ eV

On the Figure 7.4.5, we have selected situations where the cross sections can increase ($1s-2p_{1/2}$ and $2p_{3/2}-3d_{1/2}$) or decrease ($3p_{1/2}-3d_{3/2}$) with the electron density. We notice that changes in the rate appear at low temperature but as observed on the collisional cross section, this change of rates is below 15%. Of course, with the increase of the density the modification of the rates will be more important.

In the case of collisional ionization the rates increase when density effect is included. For example, at the density of $N_e = 5\times10^{23}$cm^{-3} and a temperature of $kT_e = 500$ eV, the transition rate of $1s^2 - 1s$ increases by 47% because of the plasma effect. This is because ΔE_{ij} decreases and the oscillator strength $\Omega_{ij}\,(E_f)$ increases.

In order to investigate the density effects on the various ionization processes, we plot

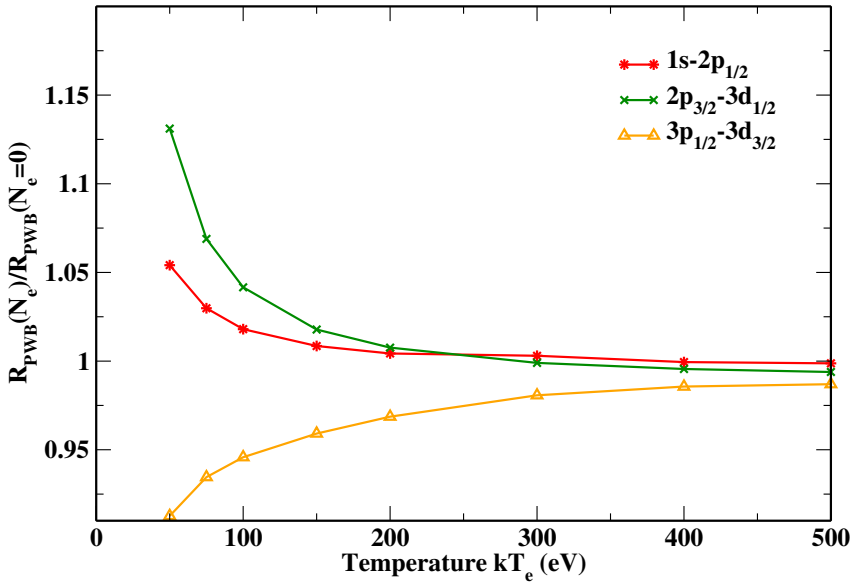

Figure 7.4.5 : Ratio of collisional excitation rates between PWB method with plasma density effect ($\mathrm{R_{PWB}}(N_e)$) and PWB without plasma density effect ($\mathrm{R_{PWB}}(N_e = 0)$) versus the temperature. The transitions plotted belong to Al XIII. The considered density is $N_e = 5 \times 10^{23}\mathrm{cm}^{-3}$.

on Figure 7.4.6 the fractional rates per ion. The fractional ionization rate is defined by

$$f_{ic} = \frac{\Gamma_{ic}}{\Gamma_{ic} + \Gamma_{ai}} \tag{7.4.4}$$

where Γ_{ic} is the collisional ionization rate and Γ_{ai} is the auto-ionization rate. We clearly see that the fractional collisional ionization increases when density effect is accounted for, of course the fractional auto-ionization rate decreases by the same amount. On Figure 7.4.7, we consider the recombination processes. On this graph the three body recombination increases, while the radiative recombination and the dielectronic capture decrease. These two plots indicate that the mechanism responsible for the increase of Z^* is the competition between the radiative recombination and the three body recombination. Indeed, the three body recombination is more sensitive to the density due to its dependence on N_e^2. We can notice that such result could have been found by leading a calculation without plasma potential, but with a higher density. This observation means that the plasma potential moves the system closer to LTE, because it increases the importance of collisional ionization.

Spectra

An important point to study is the impact of the plasma potential on the atomic spectra. This effect can be observed on Figure 7.4.8, where the bound-bound emission spectra with and without plasma potential are plotted. To calculate the spectra, a Voigt profile is used. On the upper part of the figure, the line broadening is natural and Doppler. We

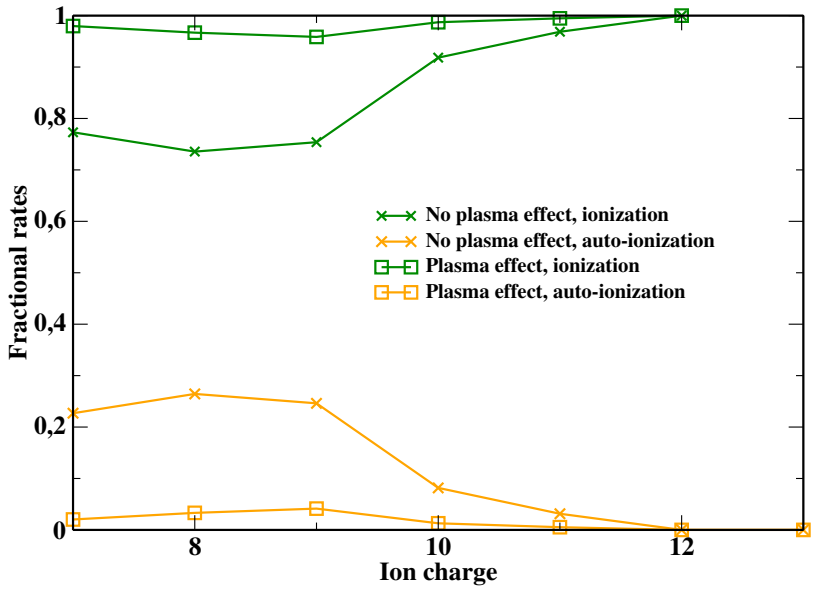

Figure 7.4.6 : Comparison of fractional rates of collisional ionization (green curves) and auto-ionization (yellow curves) with respect to the ion charge. One case in absence of screening effect (cross symbol) and second case with the plasma effect (square symbol).

observe lines shift in many cases, a red shift for example at 2020 eV which correspond to the transition from state $3p$ to $1s$. Blue shifts are also visible around 1440 eV which corresponds to the transition of the doubly excited state $2s^1 2p^1$ to the state $1s^1 3d^1$. The intensity of the lines is also modified by the plasma effect, because of the modification of the atomic population. Finally on the lower part of Figure 7.4.8, we add a Stark broadening (the electron impact) through the semi-empirical formula of Dimitrjevic [50]. In that case the difference between the case with and without plasma is less visible but still present. This point supports the idea that the plasma effect is mostly hidden by the line broadening.

A bound-free spectrum is represented in Figure 7.4.9. As mentioned in the previous chapter, the binding energies decrease because of the plasma the screening. Therefore, as observed on the spectra the ionization threshold are shifted toward lower energies.

7.4.3 Titanium

In that last case, we compare our work with an experiment published by Khattak et al. [128] on titanium. This experiment has been performed at the Rutherford Appleton Laboratory using the terawatt short pulse laser facility ASTRA. This work reports a red shift of the Ti $He-\alpha$ line which is the highest charge state $Z^* \sim 20$ measured. In that paper the titanium foil is irradiated at on optimum focus and at an offset of 100 μm from the best focus. Therefore two $He-\alpha$ line shifts are reported. The unshifted line $He-\alpha$ is taken at 4749.73 eV, this value is provided by Beiersdorfer et al [137]. We point out that the FAC code provides a value of 4749.34 eV.

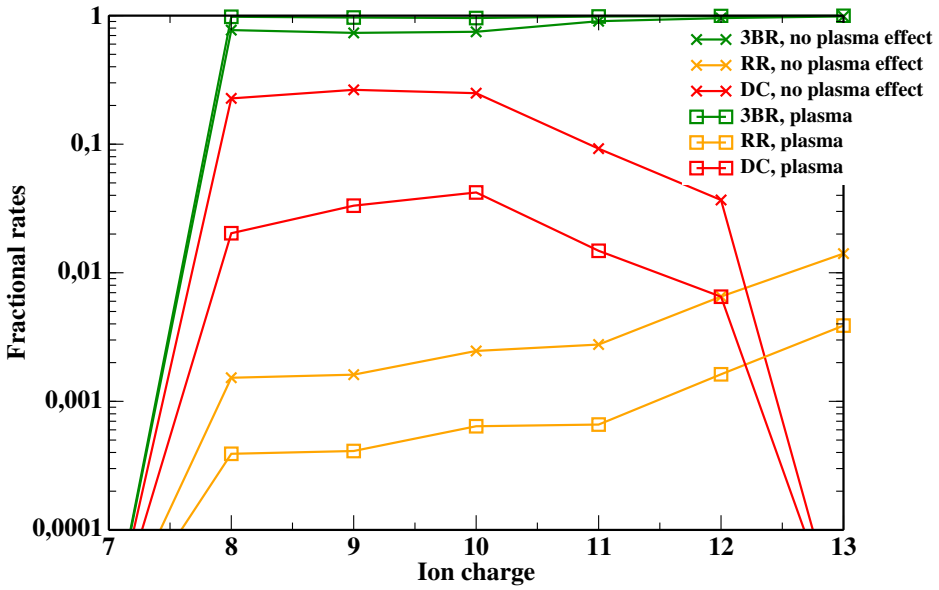

Figure 7.4.7 : Comparison of fractional rates of three bodies recombination (green curves, 3BR), radiative recombination (yellow curves, RR) and dielectronic capture (red curves, DC) with respect of the ion charge. One case in absence of screening effect (cross symbol) and second case with the plasma effect (square symbol) .

In the case of the optimum focus the reported line shift is of 3.4 eV with a Full Width at Half Maximum (FWHM) of 12.1 eV. Meanwhile in the second focus the measured line shift is of 1.8eVwith a FWHM of 5.8eV. In order to evaluate the density and the temperature, two simulations were carried out in the article. The first simulation was realized by the hydrodynamic code HYADES [138] and post processed with the Collisional radiative code SOBOLEV [139]. This simulation concludes that the plasma density exceeds 10^{24}cm^{-3}with a temperature above 3000 eV in the case of the optimum focus. In the second focus a temperature is well below 1000 eV and density lower than 10^{24} cm^{-3}. The second simulation is performed through the spectral simulation code MARIA [140]. For the optimum focus the prediction of MARIA is close to the first simulation. For the second focus, the estimate range of temperature is $500 - 1000$ eV and a density closer to 10^{23} cm^{-3} than 10^{24} cm^{-3}.

From our numerical simulation (FAC+Foch), a line shift of 3.4 eV for the $He - \alpha$ is obtained for a density of 3.7×10^{24} cm^{-3} with an electronic temperature of 3000 eV. In the Figure 7.4.10, we represent the ion population as a function of the charge state with and without plasma effect. In that case the plasma coupling parameter is about 1.94 with an average Wigner-Seitz radius of 2.098a$_0$ ($Z^* \sim 21.21$). The configurations are restricted to a maximum quantum number of 3 to comply with the condition $\omega_{pe} \ll \omega_{orbital}$ and the non-overlap condition 5.3.28.

On the Figure 7.4.11, we plot the bound-bound spectra calculated with the Foch code (Voigt profile and natural+Doppler broadening). The blue curves is the bound-bound

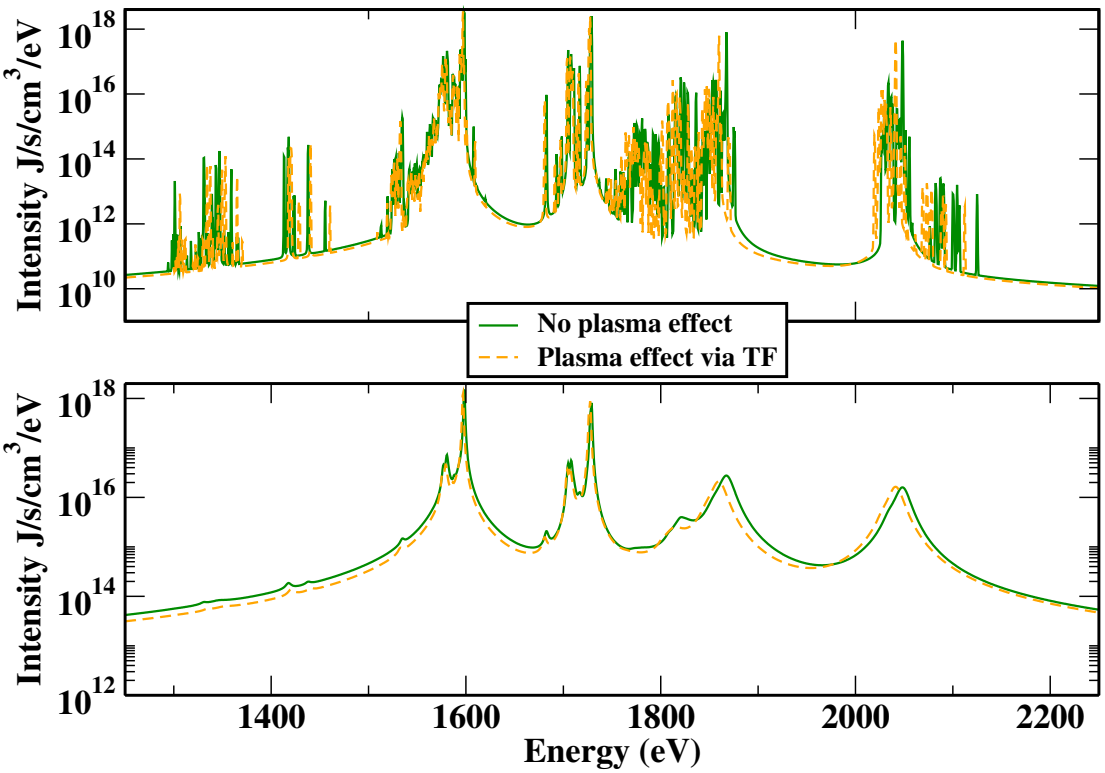

Figure 7.4.8 : Bound bound spectra of aluminium at $N_e = 5.10^{23}\text{cm}^{-3}$and $kT_e = 500$ eV with (yellow curves) and without (green curves) screening. Figure a is made with natural and Doppler broadening. Figure b is made with natural, Doppler and Stark broadening (electron impact).

spectra with the plasma effect calculated with $N_e = 3.7 \times 10^{24}$ cm^{-3} and $kT_e = 3000$ eV. This shift can be compared to the measured one [128]. But we notice that our ratio between the Li-like lines and the $He - \alpha$ line is higher than the one measured in [128]. However, the density and temperature used are in good agreement with those mentioned in the paper.

Using natural and Doppler boroadening is obviously not enough to obtain the same FWHM as in the article. Therefore, we have included a Stark broadening still with the semi-empirical formula of Dimitriejic[50]. We obtain a FWHM$\sim$ 6.03 eV which is twice less than the expected FWHM. We explain with the the absence of refined treatment of broadening by our kinetic code.

In the case of an offset of 100 μm, we reproduce the line shift for density of $N_e = 1 \times 10^{24}$ cm^{-3} and a temperature of $kT_e = 587$ eV. On the Figure 7.4.13, the $He - \alpha$ peak is at 4747.93 eV which exactly corresponds to a shift of 1.8 eV. The temperature falls in the range predicted by the code MARIA, however our density is higher than the one from code MARIA [140]. Concerning the FWHM see for instance figure (7.4.12), we find while adding the Stark broadening, a value of 2.35 eV which is a bit more than twice smaller than the experimental measurement.

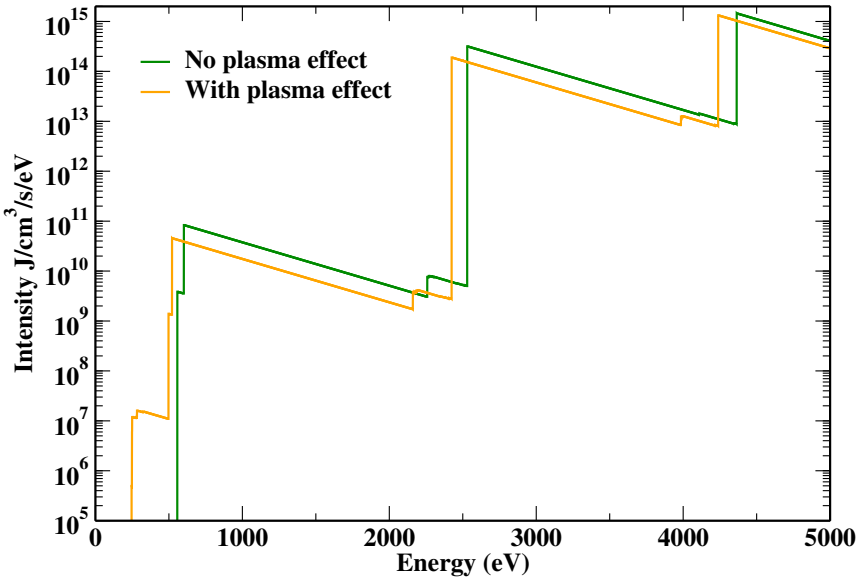

Figure 7.4.9 : Bound free spectra of Aluminium at $N_e = 5.10^{23}\text{cm}^{-3}$and $kT_e = 500$ eV with (yellow curves) and without (green curves) screening.

7.5 Summary

In this chapter we have described the major features of the Foch code. A detailed or a UTA calculation is possible, a Gauss-Laguerre quadrature with 16 points is used to calculate the rates and the kinetic equations are solved by the band diagonal Lu type routine. The bound bound spectra are computed via a Voigt profile including natural, Doppler and a Stark effect via a semi-empirical formula. An application of this kinetic code on a low density case of kyrpton show a good agreement between experiment and other kinetic codes. To emphasize the effect of the ion sphere potential, a benchmark model on aluminum has shown that the CR model is dominated by the collisional ionization. Finally, a comparison with an experiment which exhibits the density effect on spectra, shows the agreement with an alternate collisional-radiative and hydrodynamic code.

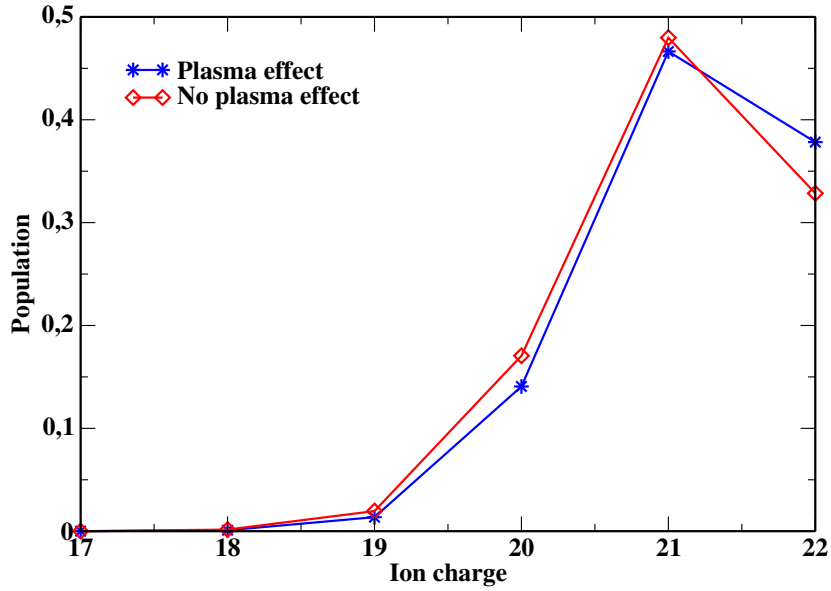

Figure 7.4.10 : Ion populations for titanium element at $N_e = 3.7 \times 10^{24}\text{cm}^{-3}$and $kT_e =$ 3000 eV with (blue curves and star symbol) and without (red curves and diamond symbol) screening .

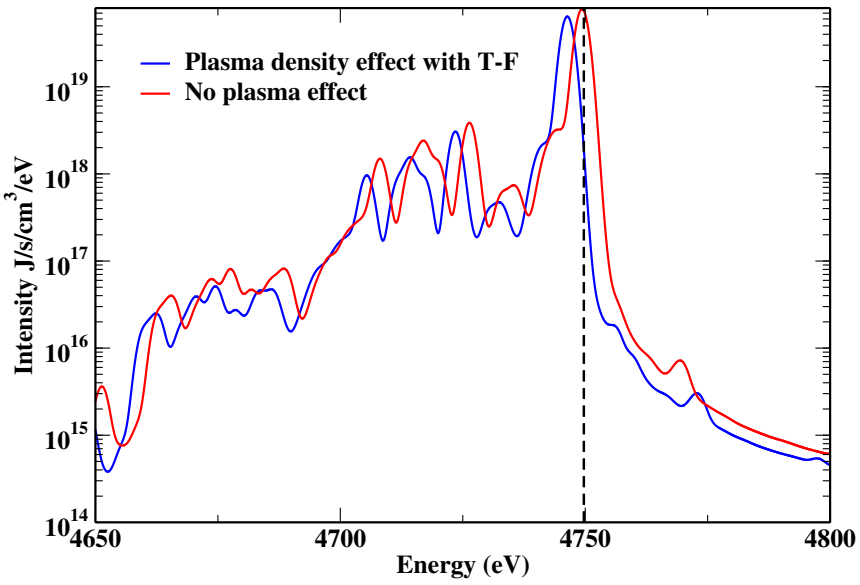

Figure 7.4.11 : Bound bound spectra of Titanium element at $N_e = 3.7 \times 10^{24}\text{cm}^{-3}$and $kT_e = 3000$ eV with (blue curves) and without (red curves) screening. Both spectra are calculated with natural and Doppler broadening. Black dashed line represent the unshifted $He - \alpha$ line .

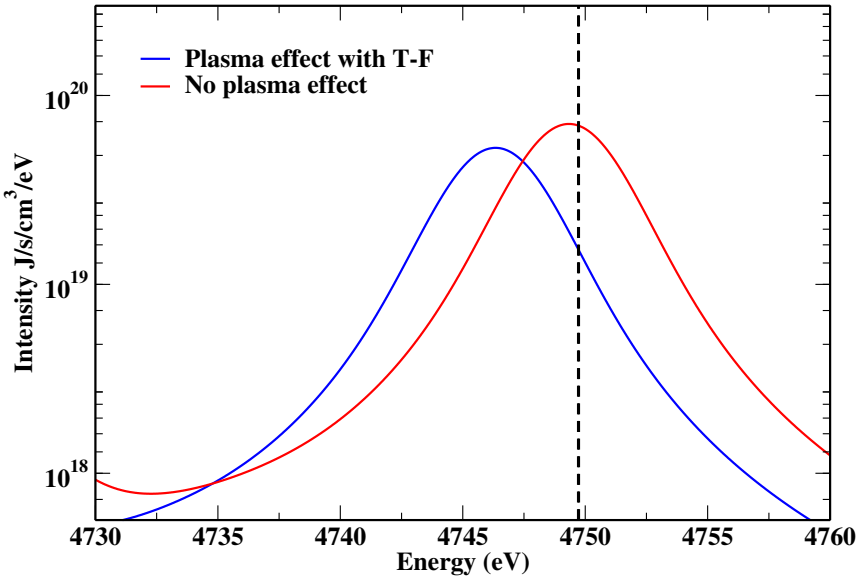

Figure 7.4.12 : Bound bound spectra of titanium element at $N_e = 3.7 \times 10^{24}\text{cm}^{-3}$and $kT_e = 3000$ eV for the $He-\alpha$ line. With (blue curves) and without (red curves) screening. Here spectra are calculated with natural Doppler and Stark broadening(electron impact). Black dashed line represent the unshifted $He-\alpha$ line.

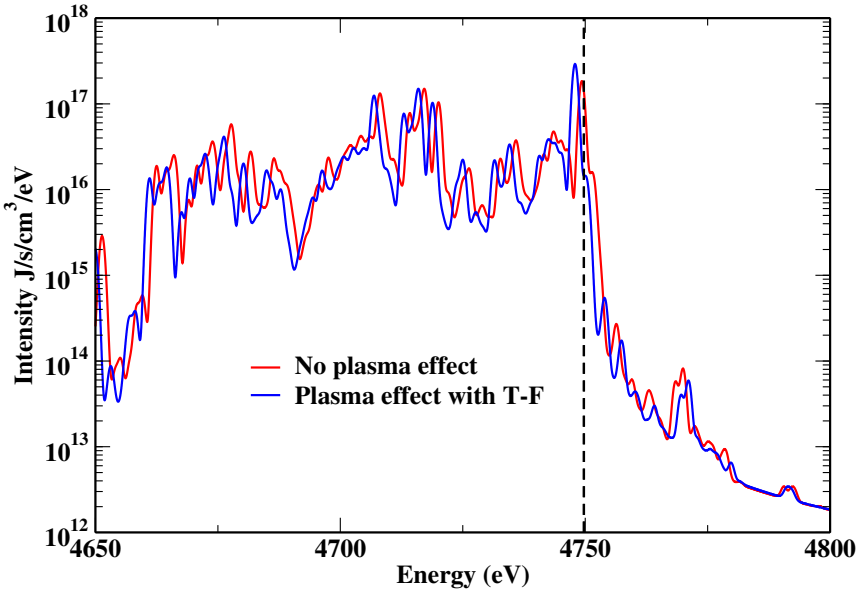

Figure 7.4.13 : Bound bound spectra of titanium element at $N_e = 10^{24}\text{cm}^{-3}$and $kT_e = 587$ eV with (blue curves) and without (red curves) screening. Black dashed line represent the unshifted $He-\alpha$ line

Chapter 8

Conclusion

8.1 Resume

In this work we have made a theoretical study of dense plasmas out of local thermodynamical equilibrium. To complete this work, a new kinetic code has been built which allows us to carry out NLTE and LTE calculations. In this work we have made the assumptions: the free electrons obey the Maxwell distribution, the plasma is optically thin and uniform. The atomic data is provided by the Flexible Atomic Code which is based on a parametric potential. This code belongs to the category of "chemical picture" description of ions, where the plasma environment is not included. We recall that this the generic term corresponds to approaches starting with isolated ion.Therefore, an important effort has been done on the inclusion of the plasma environment while keeping accurate atomic physics. The plasma environment has been modeled via the ion sphere model, under an uniform electron gas model and a Thomas-Fermi approach. This has lead us to modify the physical content of the Flexible Atomic Code. In order to support the numerical results, an analytical approach has been developed for hydrogen-like ions. An extensive study of the influence of the plasma environment has been made on the atomic structure. We have observed a non-negligible decrease of binding energies and a spreading of the wave functions. The impact of the plasma potential is also observable on the collisional cross sections. Our study highlights that it is the ionization cross section which is the most impacted. This is because of the continuum lowering. A remarkable agreement has been shown between the numerical results of FAC and the analytical formulas on hydrogen-like ions. Finally, we have investigated the density effect on the collisional radiative model. We have observed that the atomic populations are modified by the plasma effect. This fact is a logical consequence of the modification of the collisional cross section and radiative rates. This investigation reveals that the mean ion charge states increases, mainly because of the continuum lowering. On the atomic spectra, the impact is visible but not as important as on the atomic structure. This observation is mainly due to the line broadening. A successful comparison of this work has been made with other codes [139, 140]

at density where the plasma environment plays a non-significant role. This work is also in good agreement with experimental data [128].

8.2 Perspectives

- **Beyond the ion sphere potential**

The validity of the ion sphere model is limited by the non-overlap and the adiabatic conditions. To overcome the adiabatic condition, the dynamical response of the plasma has to be included in the plasma potential. Such an inclusion will only be necessary at high density. This type of development might find its application in stellar interior where the density is beyond the solid state density. Concerning the non-overlap condition, the pressure ionization must be modeled. A model based on Valloton et al.[129, 106] seems suitable, but we do believe that the dynamical response has to be taken into account at the same time. One may also consider a different symmetry for the Wigner-Seitz sphere for highly excited states. Finally, the implementation of an atom in the Jellium could be done in the Flexible Atomic Code based on the model developed by F.Perrot [10, 11] or the self-consistent approach of Blancard et al.[141].

- **Cross sections**

We have seen that because of the ion sphere neutrality, the long range behavior of the potential is modified. Moreover, resonances appear around the energy threshold. The DW method of FAC does not seem relevant in calculations of the collisional excitation cross section, especially at low energy. Furthermore, the PWB used in our work is only relevant by default. Therefore, it seems necessary to use different methods to investigate the influence of the plasma effect on collisional cross section.

- **Kinetic code**

To be totally relevant, the Foch code should be extended to time-dependent problem. It also appears desirable to include a more elaborate broadening in the spectra calculation in order to estimate the real impact of the static screening on the line broadening.

We will intend to carry out the first and second points of these perspectives during the post-doctoral activity of the present author.

Vous êtes tous les deux ténébreux et discrets :

Homme, nul n'a sondé le fond de tes abîmes ;

Ô mer, nul ne connaît tes richesses intimes,

Tant vous êtes jaloux de garder vos secrets !

Et cependant voilà des siècles innombrables

Que vous vous combattez sans pitié ni remord,

Tellement vous aimez le carnage et la mort,

Ô lutteurs éternels, ô frères implacables !

Charles Baudelaire.

extrait de l'homme et la mer dans -les fleurs du mal-

Résumé

Dans les plasmas chauds denses, l'interaction d'un ion avec les autres ions et les électrons libres peut affecter fortement la structure atomique. Pour tenir compte de ces effets, nous avons implémenté un potentiel plasma fondé sur le modèle d'un gaz d'électron uniforme et sur une approche de type Thomas-Fermi dans le Flexible Atomic Code (FAC). Ce code a été utilisé pour obtenir les énergies, les fonctions d'onde, et les taux radiatifs modifiés par l'environnement plasma. Dans des ions hydrogénoïdes, les résultats numériques ont été comparés avec succès à un calcul analytique basé sur la théorie des perturbations du premier ordre. Dans le cas les ions multi-électroniques, on observe un décalage des niveaux, en accord avec d'autres calculs récents. Diverses méthodes pour les calculs de section efficace de collision sont examinées. L'influence de la densité du plasma sur ces sections est analysée en détail. Certaines expressions analytiques sont proposées pour les ions hydrogénoïdes dans la limite où l'approximation de Born ou Lotz s'applique et sont comparés aux résultats numériques du code de FAC. Enfin, à partir de ce travail, nous étudions l'influence de l'environnement de plasma dans le cadre d'un nouveau modèle collisionnel-radiatif nommé Foch que nous avons élaboré au cours de cette thèse. En raison de cet environnement, la charge moyenne du plasma augmente, ce qui est principalement dû à l'abaissement du continuum. Nous observons également un décalage des raies sur les spectres d'émission. Un bon accord est trouvé entre notre travail et les données expérimentales sur un plasma de titane.

Keywords : Modèle collisionel-radiatif, sphère ionique, potentiel plasma, Flexible Atomic Code, Section efficace collisionnelles

Première partie

Version Française

Chapitre 9

Synthèse

9.1 Introduction

La principale information à laquelle les physiciens ont accès, est le rayonnement émis par le plasma. L'objectif du théoricien est de construire une théorie capable de retrouver ou de prédire ces informations. Les photons émis par un plasma sont le résultat de transitions d'un état atomique à un autre. Par conséquent, pour décrire les propriétés spectrales (émissivité, absorption), il est nécessaire de déterminer les niveaux d'énergie atomiques et leurs occupations. La modélisation d'un tel problème est une tâche complexe car le plasma est un problème à N-corps. Pour contourner cette difficulté, deux descriptions physiques doivent être combinées, l'approche statistique et l'approche atomique. La physique atomique est utilisée pour calculer les populations atomiques, les énergies et les fonctions d'onde, tandis que la physique statistique permet de caractériser la thermodynamique du plasma.

Deux approches se dégagent pour modéliser les plasmas. La première approche tient d'abord compte de l'environnement et de la thermodynamique d'une manière cohérente et est classé sous le terme générique de modèle de l'atome moyen. Par environnement nous entendons l'ensemble des effets des électrons libres et des ions voisins sur l'ion central. La seconde approche cherche tout d'abord à déterminer la structure atomique d'un ion isolé, puis dans un second temps détermine les populations des niveaux atomique par des lois statistiques ou des équations cinétiques. Ces théories sont nommées ici "Hartree-Fock-type" même si une autre description atomique pourrait être utilisée.

A l'équilibre thermodynamique les populations atomiques sont déterminées par les équations de Saha-Boltzmann. Dans le régime hors de l'équilibre thermodynamique aucune loi statistique ne peut plus être déduite. En conséquence chaque état atomique dépend de tous les processus atomiques qui le peuplent et le dépeuplent. Ces processus atomiques sont divisés en deux catégories, les processus de collision et radiatifs. Pour calculer ces quantités, la physique atomique associée aux théories de la diffusion doivent être considérés. Par conséquent, pour obtenir les populations atomiques, il faut rèsoudre des équations ciné-

tiques. Cette approche conduit à construire un modèle appelé modèle collisionnel-radiatif .

Le but de ce travail de thèse est de fournir une description détaillé des plasma, le plus souvent hors équilibre thermodynamique local. Pour réaliser cette tâche, une approche de type Hartree-Fock basé sur le code atomique FAC [20] a été choisie. Ce dernier fournit la structure atomique ainsi que les sections efficaces collisionnelles. Un code collisionnel-radiatif nommé Foch a été développé pour obtenir les populations atomique, l'émissivité du plasma et d'autre propriétés. Ce code est capable de réaliser des calculs détaillés ou en Unresolved Transition Array (UTA). Dans ce travail, un important effort a été fait pour inclure l'environnement plasma dans le calcul de structure atomique. En effet, dans les approches de notre domaine, les ions du plasma sont considérés comme isolés. Pour modéliser cet environnement plasma nous avons choisis le modèle dit de la sphère ionique. La thèse s'articule ainsi autour de trois objectifs :

- Construire un code cinétique utilisant les données de FAC pour obtenir les populations atomique, ainsi que les spectres d'émission.
- Prendre en compte l'environnement plasma tout en conservant une description atomique précise.
- Étudier les sections efficaces collisionnelles. Ce point a été motivé par l'inclusion de l'environnement plasma, mais également par la nécessité de réduire le temps de calcul

9.2 Définition des plasmas étudiés

Plusieurs paramètres sans dimensions caractérisent les propriétés des plasmas que nous étudions. La densité électronique N_e et ionique N_i sont liées par la condition de neutralité

$$N_e = Z^* N_i$$

Z^*étant la charge moyenne du plasma, nous exprimons dans ce travail la densité en cm^{-3}. Même si nous étude est principalement hors de l'équilibre thermodynamique, nous supposons les électrons libre thermalisés, et ainsi nous pouvons donc les décrire par une température kT_e. Le paramètre k est la constante de Boltzmann et T_e la température des électrons. Cependant par convenance kT_e désigne la température. Deux mécanismes sont en compétition dans les plasmas : l'agitation thermique et l'interaction Coulombienne entre électrons. Cette compétition est mesuré par le paramètre de couplage Γ. Cette quantité est définie [3] par

$$\Gamma = \frac{Z^{*2}}{R_0 k T_e} \tag{9.2.1}$$

en unité atomique, R_0 est défini par la condition de neutralité

$$R_0^3 = \frac{3Z^*}{4\pi N_e}. \tag{9.2.2}$$

Dans le cas d'une agitation thermique importante on a$\Gamma \ll 1$, le plasma est dit faiblement corrélé (plasmas idéaux) et le désordre domine. De tels plasmas se rencontrent en fusion magnétique et dans la couronne solaire. Au contraire pour $\Gamma \gg 1$, le plasma est fortement corrélé et il possède une structure organisée proche d'un fluide. Les intérieurs stellaires constituent un bon exemple de plasma dominé par les force Coulombienne.

Le second paramètre γ détermine si les électrons libres doivent être décrits par une approche classique ou quantique. Définissant la longueur d'onde thermique comme $\lambda_{th} = h/(2\pi mkT_e)^{1/2}$, où h est la constante de Planck et m la masse de l'électron. Nous exprimons γ par

$$\gamma = N_e \lambda_{th}^3 \tag{9.2.3}$$

Si $\gamma \ll 1$, une statistique de Maxwell-Boltzmann peut s'appliquer pour décrire les électrons libres mais si $\gamma \gg 1$ la statistique de Fermi-Dirac s'impose.

Ce travail se concentre sur les plasmas denses avec une densité comprises entre 10^{15}cm^{-3} et 10^{25}cm^{-3}, c'est à dire des densités proche de l'état solide. Concernant la température, elle se situe au-dessus de l'électron-volt, cependant, nous n'étudions pas les plasmas relativistes pour lesquels $kT_e \geq mc^2$. Ainsi, les plasmas considérés dans ce travail sont modérément à fortement corrélés $10 > \Gamma > 10^{-2}$, et la plupart du temps non-dégénérés $\gamma < 1$.

9.3 Cadre théorique

Dans le régime hors équilibre thermodynamique local (NLTE), les collisions par les électrons libres ne permettent pas d'assurer la thermalisation des niveaux ioniques à cause de l'importance des processus radiatifs. Sous cette hypothèse l'équation de Boltzmann n'est pas vérifiée, de même pour l'équation de Saha-Boltzmann. Dans le régime NLTE, nous devons tenir compte de tous les processus élémentaires qui peuplent et dépeuplent les niveaux atomiques. Ainsi pour obtenir les populations atomiques nous devons poser l'équation cinétique suivante

$$\frac{dn_j(z)}{dt} = \sum_{z'} \sum_k n_k(z) W_{kj}^{z',z} - n_j(z) \sum_{z'} \sum_i W_{ji}^{z,z'} \tag{9.3.1}$$

où $W_{ji}^{z,z'}$ est la matrice contenant tous les processus élémentaire qui contribuent à la dépopulation du niveau j de l'ion z vers le niveau i de l'ion z'. La matrice $W_{kj}^{z',z}$ représente tous les processus élémentaires qui peuplent le niveau j de l'ion z vers le niveau i de l'ion

$z^{'}$. Les populations atomiques sont contraintes par la condition :

$$\sum_{z'} \sum_{j} n_j(z^{'}) = 1. \tag{9.3.2}$$

Ces équations de taux sont difficiles à résoudre pour plusieurs raisons. Premièrement pour décrire de manière précise un ion, nous devons décrire un très grand nombre d'états (plusieurs milliers en pratique), mais également étudier plusieurs ions. Ensuite, il faut prendre en compte toutes les transitions possibles entre ces ions, ce qui atteint aisément le million de transitions. Pour simplifier notre tâche, nous effectuons les hypothèses suivantes : un environnement optiquement fin, une thermalisation des électrons libres, une étude en régime stationnaire et un plasma uniforme. Ainsi, la thermodynamique du plasma est entièrement décrite par la température électronique kT_e et la densité électronique N_e.

9.4 Modélisation de l'environnement plasma

La plupart des développements présents dans littérature, via une approche de type Hartree-Fock modélisent un ion isolé. Cependant, notre travail est consacré à des ions immergés dans un environnement plasma. Peu de codes atomiques prennent en compte cet environnement. La plupart du temps l'effet du plasma est ajouté dans le code atomique à travers la théorie de perturbation ou bien à l'étape du code cinétique. Notre travail, constitue une première tentative d'inclusion de l'effet du plasma dans le code FAC. L'environnement des ions joue un rôle important à haute densité, conduisant à des effets tels que des changements de polarisation de plasma, une ionisation induite par la pression, des changements sur les spectres d'absorption et d'émission ainsi que sur l'équation d'état. Tenir compte de ces effets de manière cohérente est une tâche difficile puisque le nombre de particules impliquées est très élevé, ce qui suggère de traiter statistiquement les électrons libres. Comme mentionné par Rosznay[8] nous distinguons deux types d'approches pour modéliser l'environnement plasma : le modéle d'ion corrélation et le modéle de sphère ionique.

Dans le modèle d'ion corrélation, l'ion est immergé dans un médium polarisé infini (aussi nommé jellium). Asymptotiquement, les charges positives et négatives s'annulent mutuellement pour former un fond neutre. Le modèle d'ions corrélation est surtout connu et utilisé par la théorie de Debye-Hückel [87, 88, 89]. Une autre approche liée à la densité de la fonctionnelle est l'atome dans le jellium de Perrot [10] et Piron [11].

Dans le modèle de la sphère ionique, l'ion est enfermé dans une cellule qui contient le nombre exact d'électrons pour assurer la neutralité de la sphère. Le modèle de la sphère d'ionique a été largement utilisé [7, 9, 12, 90], afin d'obtenir des niveaux d'énergie et les taux de transition des ions dans les plasmas. Ces modèles supposent une symétrie sphérique et définissent une répartition de densité d'électrons qui obéit à des équations d'auto-cohérence. En couplant l'équation de Poisson et la distribution statistique des

électrons, on peut obtenir le modèle de Thomas-Fermi [91, 92] ou Thomas-Fermi relativiste [7], ou hypernetted-chain [3]. Toutes ces théories appartiennent à la théorie de la fonctionnelle de la densité [93]. Il faut remarquer qu'elles supposent toutes l'équilibre thermodynamique. En outre, certains formalismes supposent une symétrie cylindrique et utilisent une approche moléculaire décrivant l'interaction avec l'ion le plus proche [94] ; cette approche concerne principalement les plasmas fortement corrélés .Lorsque qu'une description quantique réaliste des électrons liés est nécessaire et lorsqu'il s'agit de traiter des plasmas hors équilibre thermodynamique local (non-LTE), il est nécessaire de limiter le traitement statistique aux électrons libres. En vertu de cette hypothèses (ion-sphère + traitement statistique des électrons libres), nous avons tout d'abord utilisé le modèle d'un gaz uniforme d'électrons (UEGM), puis une approche de type Thomas-Fermi (TF). Les deux approches sont mises en œuvre dans le code FAC [20]. Nous rappelons qu'un modèle très populaire pour les décalage des niveaux qui effectue la connexion entre le Debye-Hückel et le modèle d'ions sphère a été développé par Stewart et Pyatt [95]. Toutefois ce modèle suppose un équilibre thermique pour les ions et les électrons, ce qui n'est donc pas directement utilisable dans l'analyse de plasmas hors de l'équilibre thermodynamique local.

Dans ce chapitre, nous abordons brièvement la théorie de Debye-Hückel. Ensuite, une discussion approfondie est effectuée sur le modèle de la sphère d'ions pour la UEGM et l'approche de type TF. Nous étendons les approches antérieures basées sur des hypothèses UEGM en dérivant des formules analytiques pour des ions hydrogènoides non relativistes. Ce travail d'analyse est utilisée pour vérifier les données atomiques du code FAC modifié.

9.5 Modèle de la sphère ionique

Tous les modèles rattachés à l'approche de la sphère ionique supposent une cellule neutre contenant un ion central plongé dans son environnement. De plus, il est supposé que la densité d'électrons libres annule exactement la densité ionique au delà de la sphère de Wigner-Seitz. Dans cette théorie le potentiel généré par cette densité de charge est calculé par l'équation de Poisson. Les différents modèles de sphère ionique se départagent sur la façon de déterminer la densité d'électrons libres. Nous présentons ici deux modèles de sphère ionique, le modèle du gaz d'électron uniforme et l'approche de type Thomas-Fermi.

9.5.1 Modèle du gaz d'électron uniforme

Le modèle du gaz d'électron uniforme (UEGM) suppose une distribution uniforme des électrons libre N_e. Cette hypothèse signifie que nous pouvons négliger la polarisation des électrons libres par le noyau. Cette hypothèse a été validé dans la référence [98], en comparant les valeurs théorique du modèle et des mesures expérimental dans le cas d'ions très chargés. Comme pour tout modèle de sphère ionique (par exemple [9]), nous

supposons qu'en dehors de la sphère, la densité d'électron libre compense la densité de l'ion. Ceci assume la condition de neutralité

$$Z - N_b - \frac{4}{3}\pi R_0^3 N_e = 0, \tag{9.5.1}$$

où R_0 est le rayon de la sphère, Z le numéro atomique, N_b le nombre d'électron lié et N_e la densité d'électron libre.

Sous l'hypothèse d'un gaz d'électron uniforme, nous obtenons le potentiel

$$V_{\text{plasma}}(r) = \frac{Z_f}{2R_0}\left(3 - \frac{r^2}{R_0^2}\right) \qquad \text{si } r \leq R_0 \tag{9.5.2}$$

$$V_{\text{plasma}}(r) = \frac{Z_f}{r} \qquad \text{si } r \geq R_0. \tag{9.5.3}$$

avec Z_f le nombre d'électrons libres défini par

$$Z_f = Z - N_b \tag{9.5.4}$$

Dans ce travail, nous n'avons pas imposé l'annulation des fonctions d'ondes à $r = R_0$, contrairement à d'autre auteurs[99, 100]. Sachant que nous nous intéressons à des plasma dense, le rayon de la sphère R_0 peut être assez large comme détaillé plus bas. De plus, l'annulation de la fonction d'onde sur la surface de la sphère implique un potentiel infiniment répulsif au-delà de la sphére, ce qui conduit à des effets non-physiques. Enfin, malgré sa simplicité le modèle UEGM a été validé contre des approches auto-consistante et s'est ainsi révélé tout à fait acceptable pour des densités modérées [101, 102, 103, 104].

9.5.2 Approche de type Thomas-Fermi

Les équations auto-consistantes définissant la densité d'électrons libres et le potentiel plasma dans une approche semi-classique — Thomas-Fermi restreint aux électrons libres — a été discutée dans une série d'articles [97, 104]. La condition de neutralité est toujours supposée dans la sphère de Wigner-Seitz de rayon R_0 définie par

$$4\pi R_0^3 N_e/3 = Z_f, \tag{9.5.5}$$

avec les même notations que précédemment. Les électrons libres et les autres ions sont supposés se neutraliser, ainsi

$$n_e(r) = 0 \text{ for } r \geq R_0. \tag{9.5.6}$$

Afin de se conformer à la définition de la densité moyenne N_e, nous devons imposer

$$4\pi \int_0^{R_0} dr\ r^2 n_e(r) = Z_f. \tag{9.5.7}$$

Nous supposons que les électrons libres se thermalisent, mais pas nécessairement les ions ce qui est consistant avec les hypothèses du modèle collisionel-radiatif. Ainsi la densité des électrons libres suit

$$n_e(r) \propto \int_{p_0(r)}^{\infty} dp\, p^2 \exp\left(-\left(\frac{p^2}{2} + V(r)\right)/k_B T_e\right) \tag{9.5.8}$$

où kT_e est la température des électrons libres et $p_0(r)$ est la valeur minimale de l'impulsion permettant à l'électron d'avoir une énergie positive i.e., $p_0(r) = (-2V(r))^{1/2}$ if $V(r) \leq 0$, or 0 if $V(r) > 0$. Le paramètre $V(r)$ est l'énergie associée à l'interaction électrostatique avec toute les charges incluse dans la sphère de Wigner-Seitz, c'est à dire le noyau, les électrons liés et libres

$$V(r) = \begin{cases} -\frac{Z}{r} + V_b(r) + V_{\text{pl}}(r). & r \leq R_0 \\ 0 & r > R_0 \end{cases} \tag{9.5.9}$$

Le terme $V_{\text{pl}}(r)$ décrit l'interaction avec les électrons libres, que nous avons nommé potentiel plasma. L'utilisation de la statistique de Fermi-Dirac n'est pas toujours nécessaire comme discuté dans la section 9.5.3. Nous avons également supposé que les électrons sont non relativistes, ce qui est vrai tant que $k_{\text{B}} T_e \ll 511$ keV.

La dernière équation, requise pour obtenir le potentiel plasma, est l'équation de Poisson. Sous forme intégrale cette dernière s'écrit

$$V_{\text{pl}}(r) = 4\pi \left(\frac{1}{r}\int_0^r ds\, s^2 n_e(s) + \int_r^{R_0} ds\, s n_e(s)\right). \tag{9.5.10}$$

Cette expression assure que $V_{\text{pl}}(r)$ ainsi que ses dérivées soient continue en $r = R_0$, sachant que $V_{\text{pl}}(r) = Z_f/r$ si $r \geq R_0$, d'après les hypothèses du modèle de sphère ionique.

En supposant le potentiel attractif $V(r) < 0$, l'équation de Maxwell-Boltzmann (9.5.8) conduit à

$$n_e(r) = \frac{K}{2} e^{-V(r)/k_B T_e} (2k_B T_e)^{3/2} \Gamma\left(\frac{3}{2}, -\frac{V(r)}{k_B T_e}\right) \tag{9.5.11}$$

$$= \frac{K}{2} (2k_B T_e)^{3/2} \left[\left(-\frac{V(r)}{k_B T_e}\right)^{1/2} + \frac{\pi^{1/2}}{2} e^{-V(r)/k_B T_e} \text{erfc}\left(\left(-\frac{V(r)}{k_B T_e}\right)^{1/2}\right)\right] \tag{9.5.12}$$

la constante K provient de la condition de neutralité (9.5.7). Dans l'expression de la densité, nous avons introduit la fonction Gamma incomplète

$$\Gamma(a, x) = \int_x^{\infty} dt\, t^{a-1} e^{-t}$$

ainsi que la fonction d'erreur complémentaire $\text{erfc}(x) = (2/\pi^{1/2}) \int_x^{\infty} du\, e^{-u^2}$ [57].

Pour l'implémentation numérique du modèle, nous initialisons avec le modèle UEGM

puis itérons avec l'équation (9.5.12) pour déterminer le potentiel plasma (9.5.10). La convergence du schéma numérique est contrôlée par la variation de densité sur la sphère de Wigner-Seitz $|n_e^{(i+1)}(R_0) - n_e^{(i)}(R_0)|$, l'itération prend fin lorsque cette valeur devient inférieur à ε. Nous trouvons qu'une valeur de $\varepsilon = 10^{-8}$ en unité atomique donne un schéma auto-consistant de bonne précision et avec une convergence couramment atteinte en moins de 12 itérations.

9.5.3 limitations du modèle

Nous discutons ici du domaine de validité du modèle de la sphère d'ions. Tout d'abord, si l'extension spatiale de la fonction d'onde de l'électron lié est plus grande que le rayon de la sphère ionique, les orbitales de deux ions voisins se chevauchent et des effets quasi-moléculaires doivent être pris en compte. Cette condition est également reliée à la possibilité d'ionisation à la pression. Le paramètre décrivant ce recouvrement est

$$\beta = \frac{\langle r \rangle}{R_0}, \tag{9.5.13}$$

où $\langle r \rangle$ est la taille moyenne de l'orbital la plus extérieur et R_0 la moitié de la distance entre deux ions voisins. Si $\beta > 1$, les fonctions d'ondes de deux ions voisins se chevauchent significativement. Le code de structure atomique permet de calculer $\langle r \rangle$. Dans le cas d'un ion hydrogénoide, l'extension classique de la fonction d'onde est liée à la position du point tournant extérieur $\langle r \rangle \lesssim 2n^2/Z$, où n est le nombre quantique principal. Pour les ions multi-électronique, une estimation grossière du rayon moyen peut être obtenue en supposant un écrantage complet par $N_b - 1$ électrons liés, ainsi la taille de l'orbitale est $2n^2/(Z - N_b + 1)$. Sachant que la fonction d'onde décroit de manière exponentielle au-delà du point tournant, il est suffisant d'imposer la condition

$$\frac{2n^2}{Z_f + 1} < R_0 \tag{9.5.14}$$

ce qui revient à

$$N_e \lesssim 0.03 \frac{(Z_f + 1)^3 Z_f}{n^6} \sim 2.10^{23} \frac{Z^4}{n^6} \text{ cm}^{-3} \tag{9.5.15}$$

Une condition similaire a été dérivée par d'autres auteurs [101, 103].

La discussion qui précède ne tient pas compte de la réponse dynamique des électrons libres. En effet, lorsque l'électron actif se déplace loin du noyau, les électrons libres neutralisent la charge positive avec un temps caractéristique égal à l'inverse de la fréquence de plasma. Dans ce cas, la charge nette vu par un électron situé loin du noyau est égal à zéro, en contradiction avec la formule (9.5.3). L'électron actif est lié par un potentiel $-(Z - N_b + 1)/r$ — le noyau étant écrantè par les autres électrons liés — ce qui ajoute à électrons libres $(Z - N_b)/r$ et se traduit par une valeur non nulle -1 / r d'un potentiel de Coulomb loin de noyau. C'est pourquoi nous devons imposer à la fréquence orbitale

d'électrons (ou fréquence de Bohr) ω_{orbital} et à la fréquence du plasma ω_{pe} la condition adiabatique

$$\omega_{\text{pe}} = (4\pi N_e)^{1/2} \ll \omega_{\text{orbital}} \tag{9.5.16}$$

ce qui dans le cas hydrogénoide ou en supposant un écrantage complet par les électrons liés s'écrit

$$N_e \ll \frac{(Z_f+1)^4}{4\pi n^4} \sim 5.35 \times 10^{23} \frac{Z^4}{n^6} \text{ cm}^{-3}. \tag{9.5.17}$$

Cette condition est reliée à l'hypothèse de non-recouvrement (9.5.15).Une condition évidente est que ω_{orbital} est au dessus de la fréquence de coupure lorsque la condition (9.5.17) est remplie. Constatant que les conditions (9.5.17) et (9.5.15) sont très proche. Il parait donc difficile de tenir compte de l'ionisation par la pression sans la réponse dynamique.

Le modèle UEGM, n'inclut pas directement la température kT_e , cependant celle-ci est relié à la quantité Z_f par l'intermédiaire de la balance d'ionisation — donnée par l'équation de Saha ou tout autre modèle d'ionisation—. On peut également estimer le paramètre de corrélation reliant kT_e et Z_f

$$\Gamma = \frac{Z_f^2}{R_0 kT_e} \tag{9.5.18}$$

Numériquement, nous avons $\Gamma \sim 1$ pour les paramètres $kT_e = 650$ eV et $N_e = 10^{23}\text{cm}^{-3}$ — ce qui donne $\langle Z_f. \rangle \sim 12$ selon la loi de Saha pour l'aluminium. Ainsi, le modèle présenté s'applique pour les plasmas avec un faible ou moyen paramètre de couplage.

Afin d'estimer si la statistique de Maxwell-Boltzmann ou de Fermi-Dirac s'applique pour les électrons libre, nous devons estimer le paramètre de dégénérescence définit par

$$\gamma = \frac{T_{\text{Fermi}}}{T_e} = \frac{(3\pi^2 N_e)^{2/3}}{2kT_e} = \frac{3^{2/3}\pi^{1/3}}{2} \left(N_e \lambda_{th}^3\right)^{2/3}. \tag{9.5.19}$$

En utilisant $N_e = 10^{23}\text{cm}^{-3}$, nous obtenons $kT \simeq 8$ eV. Ainsi, les plasmas considérés ici seront généralement non-dégenerés. La condition de non-dégenerescence s'écrit

$$N_e \lambda_{th}^3 \ll 1 \tag{9.5.20}$$

9.5.4 Développement analytique pour les ions hydrogénoides

Différent articles [97, 102, 103] ont montré qu'à partir du potentiel UEGM (9.5.2) une expression analytique peut être dérivée pour l'énergie au premier ordre de la théorie des perturbations. Nous étendons ici cette approche en donnant l'expression explicite des fonctions d'ondes, des taux radiatifs dipolaires et quadrupolaires au premier ordre des perturbations, mais également les énergies et les fonctions d'ondes au second ordre. Pour une approche simple, nous ne prenons pas en compte les effets relativistes. Ce travail repose sur la théorie perturbative standard de Rayleigh-Schrödinger et complété par la

technique de sommation de Dalgarno et Lewis [110, 111]. Nous notons, H_0 l'hamiltonien non perturbé avec les énergies propres $E_i^{(0)}$ et fonction propres $\Phi_i^{(0)}$, et V le potentiel perturbateur, Cette technique consiste à essayer de d'obtenir au premier ordre la fonction propre $\Phi_i^{(1)}$ par la résolution directe de l'équation en représentation $\mathbf{r}$

$$\left\langle \mathbf{r} \left| H_0 - E_i^{(0)} \right| \Phi_i^{(1)} \right\rangle = \left\langle \mathbf{r} \left| E_i^{(1)} - V \right| \Phi_i^{(0)} \right\rangle, \tag{9.5.21}$$

où l'énergie au premier ordre obtenue est

$$E_i^{(1)} = \left\langle \Phi_i^{(0)} \right| V \left| \Phi_i^{(0)} \right\rangle. \tag{9.5.22}$$

Cette méthode peut être généralisée à tous les ordres des perturbations. L'équation radiale de la fonction d'onde hydrogénoide perturbée s'écrit $R_{nl}(r) + \mathrm{v}_{nl}(r)$ où R_{nl} est la fonction non perturbé au premier ordre, n et l étant respectivement le nombre quantique principal et orbital, v_{nl} est solution de

$$\left(\frac{d^2}{d\rho^2} + \frac{2}{\rho}\frac{d}{d\rho} - \frac{l(l+1)}{\rho^2} + \frac{2}{\rho} - \frac{1}{n^2} \right) \mathrm{v}_{nl} = \frac{Z_f}{Z^4 R_0^3} (\left\langle \rho^2 \right\rangle - \rho^2) R_{nl}(r), \tag{9.5.23}$$

où $\rho = Zr$ est le rayon mis à l'échelle. Pour assurer la neutralité, il faut que $Z = Z_f + 1$. Dans cette équation radiale, la dépendance à grand r (9.5.3) du potentiel plasma a été ignorée . Comme étudié dans l'appendice A.1 cette oubli est acceptable tant que $R_0 > 2n^2/Z$. Le carré du rayon moyen est donné par

$$\left\langle \rho^2 \right\rangle = \frac{1}{2} n^2 (5n^2 - 3l(l+1) + 1). \tag{9.5.24}$$

L'essai de résolution que nous avons éffectué (9.5.23) dans de nombreux cas suggère qu'une solution particulière peut être trouvée comme une somme du terme $c_j \rho^j \exp(-\rho/n)$ avec j variant de l à n. La solution générale est donnée par une telle équation plus la solution homogène habituelle R_{nl} multipliée par une constante à déterminer. Pour obtenir une correction au premier ordre convenablement normalisée, nous devons suivre la condition d'orthogonalité

$$\int_0^\infty d\rho \rho^2 R_{nl} \mathrm{v}_{nl} = 0. \tag{9.5.25}$$

Nous avons été capable d'obtenir une expression analytique pour n'importe quelle valeurs de n, l , cependant leur écriture est trop lourde pour être donnée explicitement. Nous restreignons donc à des cas simples mais représentatifs, comme $n = l + 1$

Si $n = l + 1$, la solution générale de l'équation (9.5.23) avec normalisation s'écrit

$$\mathrm{v}_{nn-1} = \langle r \, |\widetilde{n \; n-1}\rangle = \frac{Z_f}{Z^{5/2}R_0^3}\frac{(2/n)^{n+1/2}}{(2n)!^{1/2}}\left(\frac{n}{6}\rho^3 + \frac{n^2}{4}(n+1)\rho^2 - \frac{n^4}{24}(n+1)(2n+1)(5n+6)\right)\rho^{n-1}e^{-\rho/n}. \tag{9.5.26}$$

Pour l'énergie correspondante, l'expression est

$$E^{(1)}_{nn-1} = \frac{Z_f}{2R_0}\left(3 - \frac{n^2}{Z^2R_0^2}(n+1)\Big(n+\frac{1}{2}\Big)\right), \tag{9.5.27}$$

Ces développements nous permettent de contrôler la qualité des résultats numériques obtenue par la version de FAC modifiée.

9.6 Effet de l'environnement plasma

Dans cette partie nous étudions l'effet du potentiel plasma sur la structure atomique, sur les sections efficaces et sur le modèle collissionel-radiatif.

9.6.1 Structure atomique

9.6.1.1 Énergies

La différence entre les modèles de TF et UEGM réside dans la façon de considérer la température. La température est directement présente pour l'approche TF à travers la distribution de Maxwell. Alors que dans UEGM la température est implicitement présente via la valeur supposée Z^*. Sur la figure 9.6.1, nous traçons l'évolution de l'énergie de liaison de Al XIII pour le niveau $1s_{1/2}$ en fonction de la température, et ceci pour les deux potentiels (TF et UEGM). Nous voyons clairement que l'énergie de liaison croit avec la température dans le cas de TF. Nous vérifions aussi qu'à haute température l'approche TF converge vers le UEGM.

Le potentiel plasma de TF est toujours plus important que celui de UEGM. Ainsi, nous pouvons attendre à ce que l'énergie de liaison soit plus basse avec TF qu'avec UEGM. La figure. 9.6.2 confirme cette prédiction. Un point important est souligné par les figures 9.6.1 et 9.6.2 . L'effet le plus important sur le décalage des niveaux provient de la densité et non pas de la température. Ce résultat est contraire à l'observation faite par Salzmann et Szichman's [102] qui obtiennent dans certain cas un décalage du à l'UEGM est supérieur à celui du à TF.

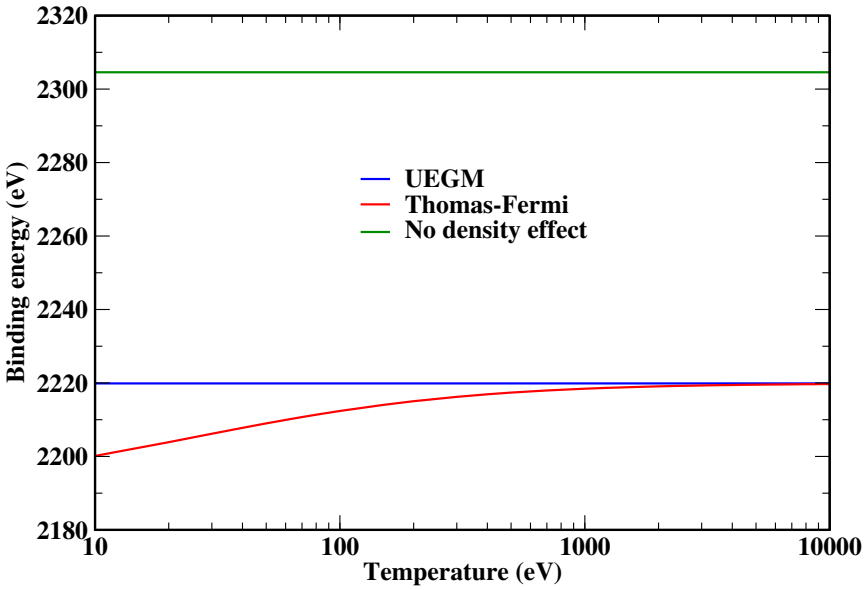

FIGURE 9.6.1 – Influence of temperature on binding energy of Al XIII for $1s_{1/2}$ level with an average density $N_e = 10^{23}$ cm^{-3}

9.6.1.2 Fonction d'ondes

L'inclusion du potentiel plasma conduit à un écrantage par les électrons libre du champ du noyau, ce qui conduit à un étalement des fonctions d'ondes. Cet effet peut s'observer sur la Figure 9.6.3 pour l'orbital $3p_{1/2}$ de l'aluminium hydrogénoide. Afin de vérifier les calculs numériques, nous présentons sur la Figure 9.6.4 une comparaison entre les fonctions d'onde obtenues par FAC et et les fonctions d'onde obtenues analytiquement via la formule (5.4.15). L'accord entre les deux approche est très bon lorsque la densité n'est pas trop forte, tout comme pour le décalage en énergie. Comme mentionné précédemment, lorsque la densité est trop élevée les deux calculs divergent car l'approche perturbative n'est plus valable. L'effet du plasma observé sur les fonctions d'onde est modéré mais visible, ce qui souligne la nécessité de les prendre en compte, comme par exemple pour les spectres atomique.

9.6.1.3 Taux radiatifs

Avec l'analyse des fonctions d'ondes perturbées par l'effet du plasma, nous pouvons calculer les taux radiatifs. Ces taux ont été calculés par le code FAC dans une approximation non-relativiste.

Nous ne pouvons pas affirmer catégoriquement que tous les taux radiatifs décroissent ou croissent avec l'augmentation de la densité. Un tel comportement a été mentionné par Li et Rosmej [123]. Ceci à cause de la dépendance des éléments de matrice dipolaire vis-à-vis de l'énergie de transition. Ce fait s'observe sur la Figure. 9.6.5, nous y voyons l'énergie de transition croitre ou décroitre en fonction de la densité.

Plus spécifiquement, la transition d'énergie entre le triplet $^3P_{0,1}$ et le singulet $^1S_0$ décroit

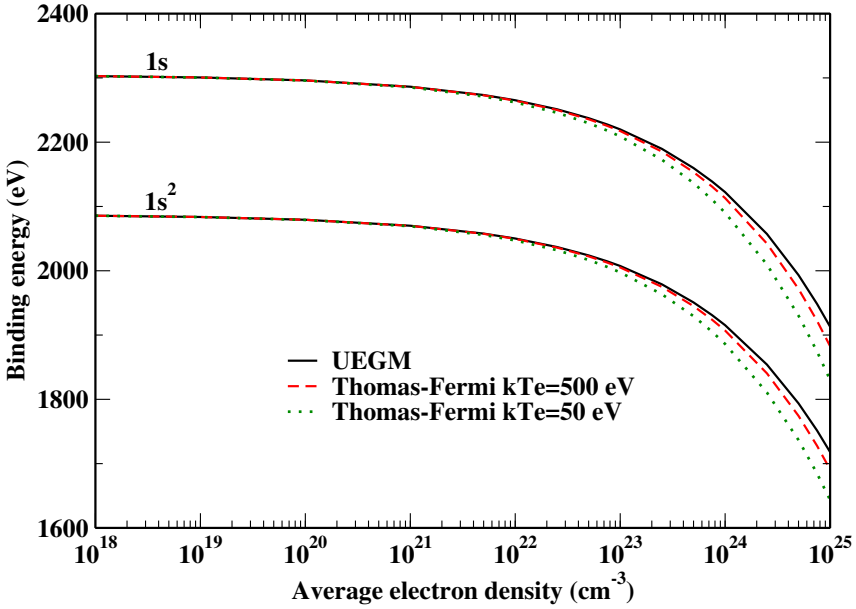

FIGURE 9.6.2 – Influence of density on binding energy of Al XIII and XII for $1s_{1/2}$ and $1s^2 {}^1S_0$ levels.

avec la densité, dans le même temps elle croit avec la densité entre le triplet $^3P_{0,1}$ et le triplet $^3S_1$. Ainsi les taux radiatifs peuvent avoir différent comportement en fonction de la densité. Comme règle, la plupart des taux radiatifs décroissent à cause de l'effet du plasma, ceci est dû à la diminution de ΔE_{ij}^3 dans la probabilité de transition. Le cas de la figure 9.6.6 est spécifique car ΔE_{ij} est très petit.

9.6.2 Sections efficaces

9.6.2.1 Excitation collisionnelle

Nous utilisons deux méthodes pour étudier les sections efficaces d'excitation collisionnelles : l'approximation en onde plane de Born (PWB) et la méthode des ondes distordues (DW) (voir chapitre 3 de [Sobelman1995] et le chapitre 4 de ce manuscrit.).

Le choix entre les deux méthodes nécessite de considérer le comportement asymptotique supposé pour le potentiel à longue portée. Toutes les deux sont des théories perturbatives et valables uniquement dans le cas d'un faible potentiel d'interaction entre la cible et les électrons incidents. Les différences sont cependant importantes. DW tient compte de la forme du potentiel à longue portée contrairement à l'approximation de Born. La forme asymptotique de la fonction d'onde pour la particule incidente est une onde plane pour PWB et de type Coulombien pour DW. Par conséquent, le modèle DW n'est pas pertinent lorsque les effets de densité sont inclus dans le cadre du modéle de sphère ionique, car le potentiel asymptotique n'est pas Coulombien. Tout au plus, on peut utiliser l'approximation DW lorsque la densité est si faible que le rayon est plus grand que la zone où le processus de collision a lieu. En outre, nous rappelons que la méthode DW mise en

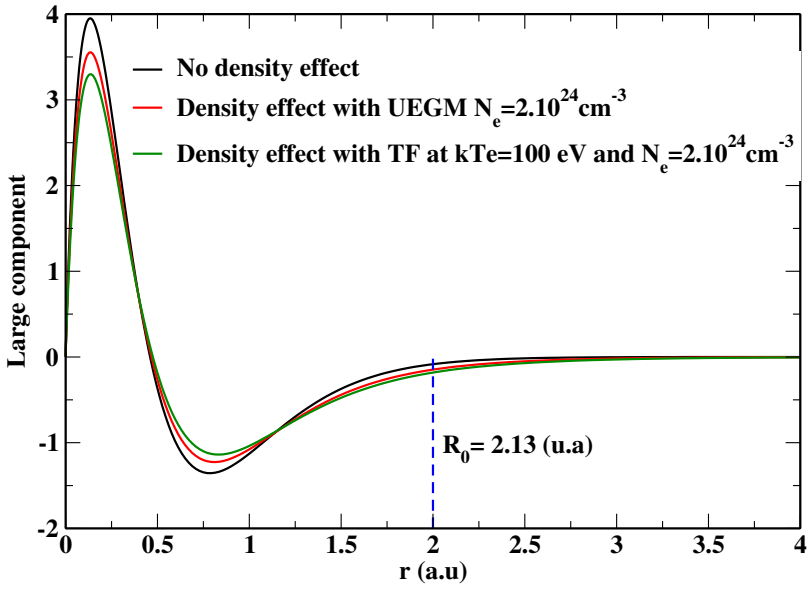

FIGURE 9.6.3 – Comparison of perturbed and unperturbed (solid line) large component of the wave-function $3p_{1/2}$ in H-like Al obtained with FAC. The perturbed wave-function has been computed assuming a $N_e = 2 \times 10^{24}$ cm^{-3} free-electron density. For the UEGM (red curve)$\langle r \rangle = 1.09$ a.u , Thomas-Fermi (green curve) $\langle r \rangle = 1.13$ a.u and for the unperturbed situation $\langle r \rangle = 0.98$ a.u. The ion-sphere radius at this density is 2.13 atomic units.

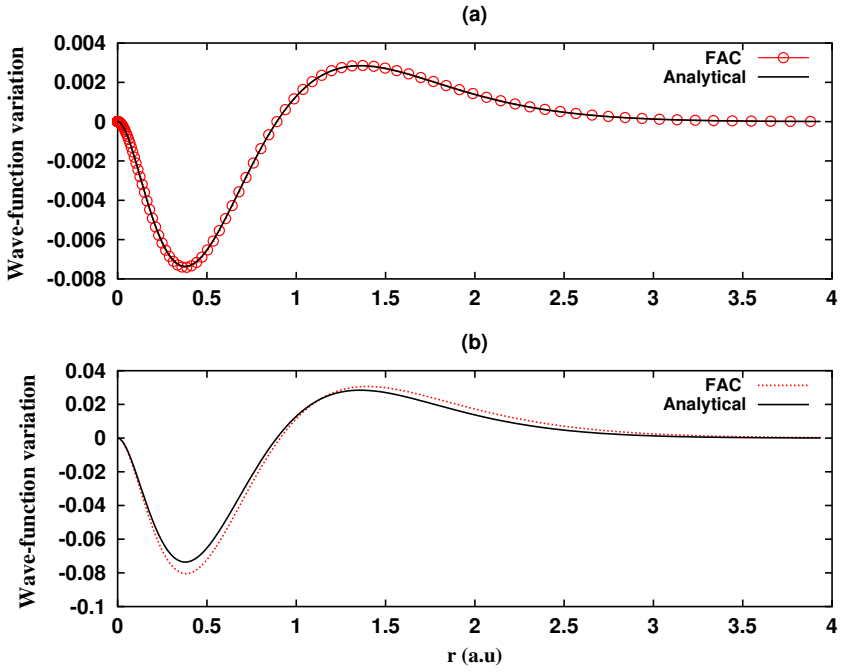

FIGURE 9.6.4 – Density effect on the $3d_{3/2}$ wave-function of H-like aluminum. The large-component variation $P(N_e) - P(N_e = 0)$ calculated with FAC and the first-order perturbed wave-function (5.4.15) are plotted as a function of the radius. The upper subfigure corresponds to $N_e = 10^{23}$ cm^{-3} and the lower subfigure to $N_e = 10^{24}$ cm^{-3}.

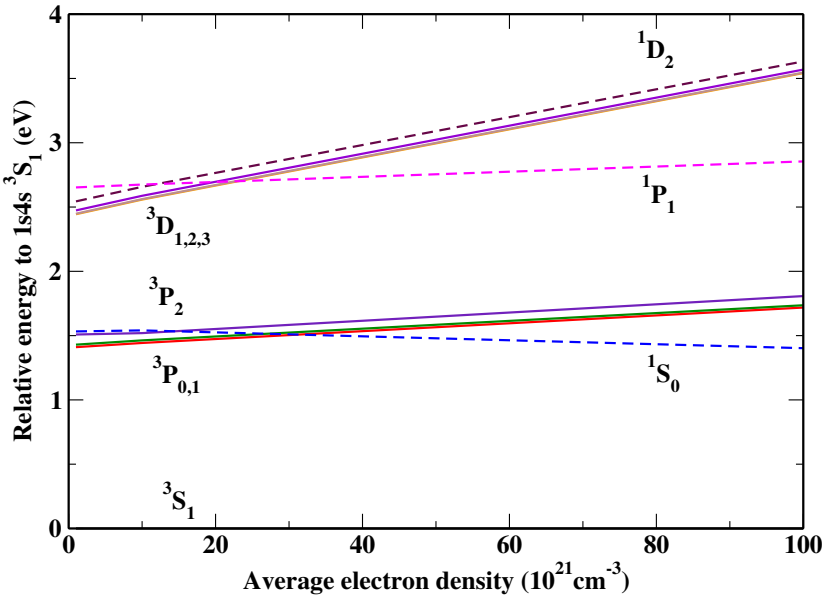

FIGURE 9.6.5 – Energy of helium-like Al relative to the level 1s4s $^3S_1$versus density for various levels of the configuration $1s4l$ with Thomas-Fermi potential at 100 eV.

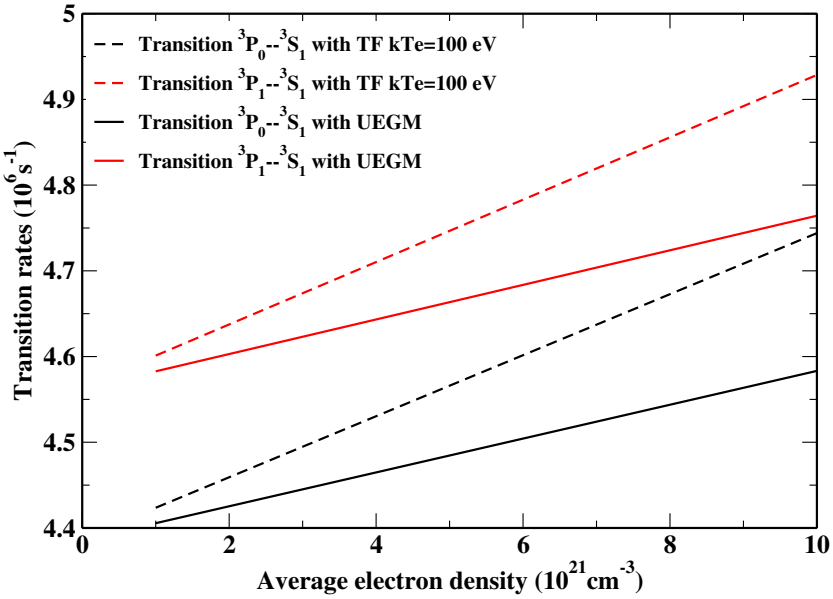

FIGURE 9.6.6 – Dipolar radiative rates $1s4p^3P_J$–$1s4s^3S_1$ in Al XII versus average electron density at $T_e = 100$ eV.

œuvre dans FAC n'est pas fiable pour les neutres et quasi-neutres comme mentionné par l'auteur de FAC et observé au chapitre 4 de cette thèse. En conséquence, l'approximation en ondes planes de Born est utilisé dans ce travail lorsque l'effet de la densité est pris en compte.

Nous devons souligner que rencontrons une difficulté pour observer l'influence du plasma sur les sections efficaces d'excitation. En effet, le potentiel plasma change le comportement à longue portée du potentiel. Cependant, à haute énergie le méthodes DW et PWB convergent, ce qui signifie que nous pouvons isoler l'influence de plasma.

Afin de comparer les résultats obtenus par PWB et DW, nous traçons sur la Figure.9.6.7 la section efficace d'excitation de la transition $1s$–$2p_{1/2}$ de Al XIII.

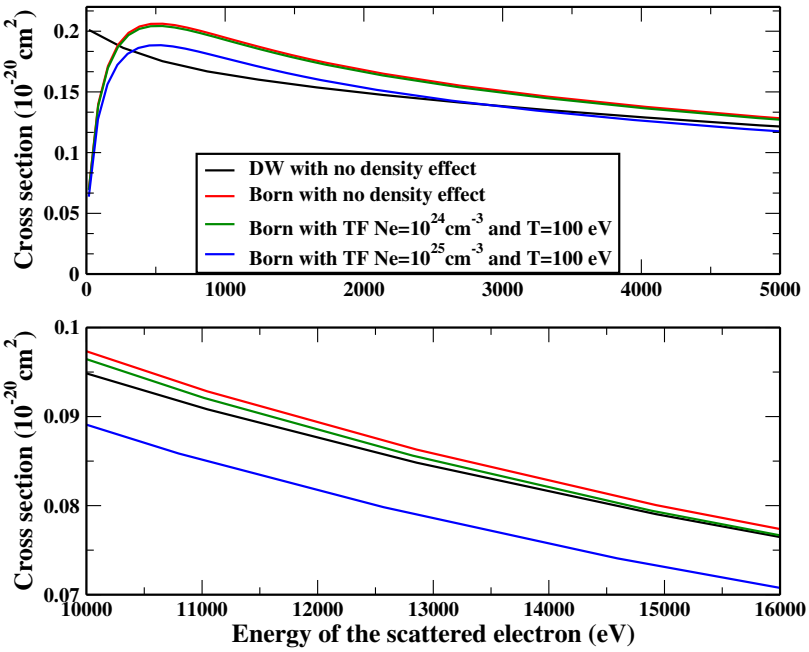

FIGURE 9.6.7 – Comparison of excitation cross section for transition $1s$–$2p_{1/2}$ for Al XIII at several densities and $T = 100$ eV

Le comportement des sections efficaces donné par les deux méthodes est différent près du seuil en raison de la façon dont elles traitent l'interaction à longue portée. A haute énergie, les sections efficaces montrent le même comportement. Sur la Figure. 9.6.7 on remarque que l'effet du plasma contribue à diminuer la section efficace, même si cela est modéré. Pour observer un changement significatif, nous devons atteindre des densité de l'ordre de $N_e = 10^{25}$ cm^{-3}. A cette densité le rayon de la sphère de Wigner-Seitz est $R_0 = 1.25$ a$_0$, ce qui est plus grand que l'extension de la fonction d'onde, dans ce cas le paramètre de couplage Z_f^2/kT_eR_0 est proche de 1. Ceci signifie que notre formalisme vérifie la condition de non-recouvrement [28] , et est applicable lorsque des effets de densité non négligeables se produisent.

Nous avons vu que les taux radiatifs peuvent croitre ou décroitre selon la transition étudiée. Le même raisonnement s'applique aux section efficace d'excitation collisionelle. Par exemple dans le cas de la transition de $1s4p\ ^1P_1$ vers $1s4d\ ^1D_2$, l'énergie diminue

avec la densité, puis à partir de $N_e \simeq 1.2 \times 10^{22}$ cm^{-3} ces deux niveaux se croissent. Pour cette transition, nous avons observons une augmentation de la section efficace jusqu'à la densité critique $N_e \simeq 1.2 \times 10^{22}$ cm^{-3}. Par la suite l'émission s'effectue de $^1D_2$ vers $^1P_1$, et ainsi la section efficace décroit avec la densité. Une possible explication du croisement de niveaux est que l'interaction électronique est faible. En conséquence, dans cette situation le potentiel plasma a un effet plus fort, ce qui signifie que l'électron lié interagit préferentiellement avec le continuum plutôt qu'avec les électrons liés.

Nous utilisons la formule de Van Regemorter [71] pour confirmer nos observations. Cette formule est valable dans le cadre de l'approximation de Born et de Bethe (haute énergie et transition dipolaire)

$$\sigma_{ij} = \frac{8\pi}{\sqrt{3}} \frac{R_y^2}{e_i} \frac{f_{ij}}{\Delta E_{ij}} \bar{g}\,(e_i/\Delta E_{ij})\,\pi a_0^2, \tag{9.6.1}$$

où ΔE_{ij} est la transition d'énergie du niveau i vers j, a_0 est le rayon de Bohr, R_y la constante de Rydberg, e_i l'énergie de l'électron incident, $\bar{g}$ le facteur de Gaunt déterminé par des observations empiriques et f_{ij} la force d'oscillateur. Nous choisissons le facteur de Gaunt suggérer par Mewe [72]

$$\bar{g} = 0.15 + 0.28 \log\left(\frac{e_i}{\Delta E_{ij}}\right). \tag{9.6.2}$$

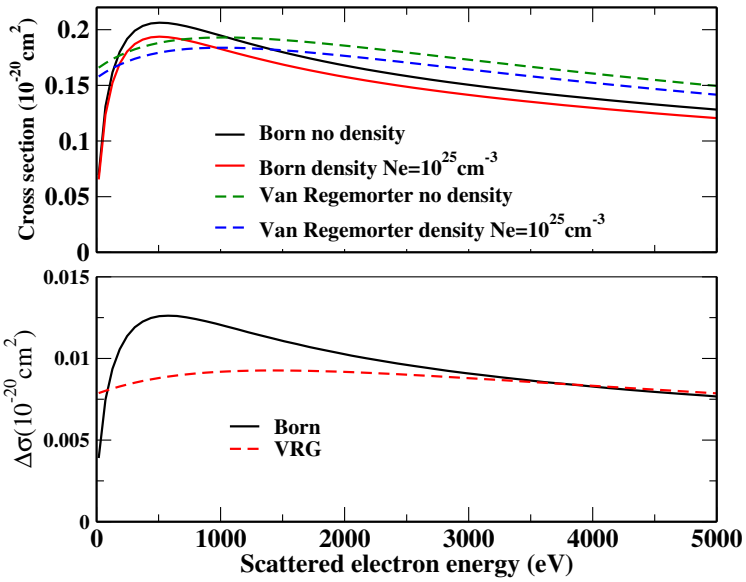

FIGURE 9.6.8 – Excitation cross sections for the transition $1s_{1/2}$–$2p_{1/2}$ in Al XIII: comparison between Born approximation and Van Regemorter formula. The upper figure represents the cross sections while on the lower figure are plotted the variations $\sigma(N_e = 0) - \sigma(N_e > 0)$ for both approximations.

Nous comparons les sections efficaces numériques et la formule de Van Regemorter sur la Figure. 9.6.8. Nous notons que le décalage de la section efficace est similaire. Afin de fournir une expression analytique nous utilisons un développement basé sur l'équation

(9.6.1). Dans cette équation, l'effet de densité modifie la transition d'énergie ΔE_{ij} et la force d'oscillateur f_{ij}. Le facteur de Gaunt est aussi modifié mais nous le négligeons car il varie lentement avec ΔE_{ij}. Ainsi l'amplitude de la section efficace dépend principalement du rappor $f_{ij}/\Delta E_{ij}$. A une constante numérique près ce ratio corresponds au carré de l'élément de matrice dipolaire :

$$\frac{f_{ij}}{\Delta E_{ij}} \propto \langle n_i l_i \left|r\right| n_j l_j \rangle^2 . \tag{9.6.3}$$

En utilisant les formules analytiques (chapitre 5) pour les ions hydrogènoide dans le cadre du potentiel UEGM, nous sommes en mesure d'isoler la contribution du potentiel du plasma par la décomposition de l'élément de matrice à l'ordre 0 et au premier ordre de la théorie des perturbations.

$$\langle n_i l_i \left|r\right| n_j l_j \rangle = \langle n_i l_i \left|r\right| n_j l_j \rangle^0 + \langle \widetilde{n_i l_i \left|r\right| n_j l_j} \rangle. \tag{9.6.4}$$

Nous calculons l'élément de matrice avec le potentiel UEGM dans un cadre non relativiste et obtenons donc, en unité atomique

$$\langle 1s \left|r\right| 2p \rangle = \frac{128}{243}\frac{\sqrt{6}}{Z}\left(1 - \frac{3059}{36}\frac{Z_f}{Z^4 R_0^3}\right). \tag{9.6.5}$$

Dans le case d'un ion aluminium hydrogénoide, nous obtenons

$$\langle 1s \left|r\right| 2p \rangle^0 = 9.925 \times 10^{-2} \tag{9.6.6}$$

et pour une densité électronique moyenne $N_e = 10^{24}$ cm^{-3}

$$\widetilde{\langle 1s \left|r\right| 2p \rangle} = -1.8329 \times 10^{-4}. \tag{9.6.7}$$

A cette densité l'élément de matrice perturbé est très petit. Les équations (9.6.6) et (9.6.7) confirment que les sections efficaces d'excitations collisionelles ne changent pas notablement.

Nous avons également constaté que les transitions interdites et permises sont affectées différemment par l'environnement plasma. Ce fait a été observé par Hatton *et al* [115] qui ont utilisé le formalisme de Debye Hückel.

9.6.2.2 Ionisation collisionelle

Ici, nous avons adopté le formalisme de TF pour inclure l'effet du plasma, pour les sections efficaces d'ionisation, à la place de DW. C'est la méthode Binary encounter dipole theory (BED) [83] qui est utilisé par FAC. Cette méthode combine le calcul des sections efficaces semi-classique de Mott [86] pour la diffusion de deux électrons libres (valable pour les grands transfert d'impulsion), et la théorie de Bethe [124] qui est fondé sur l'approxi-

mation en onde plane de Born (valable à haute énergie et petit transfert de quantité de mouvement) avec seulement le terme dipolaire retenu. Cette théorie est d'un grand intérêt en raison de son applicabilité à la fois pour les ions et les neutres. Contrairement au cas de l'excitation, nous n'avons pas besoin de changer notre approche de calcul lorsque l'effet de plasma est inclus.

Nous traçons sur la figure 9.6.9. la section efficace d'ionisation collisionnelle de l'état $1s^2$ à $1s$ pour l'aluminium, et ceci pour diverses densités. Nous y effectuons aussi une comparaison avec la formule de Lotz [42]

$$\sigma_{ij} = C\pi a_0^2 Ry^2 \frac{w_n}{e_i \Delta E_{ij}} \log\left(\frac{e_i}{\Delta E_{ij}}\right), \tag{9.6.8}$$

où $C = 2.77$, w_n est le nombre initial d'électron dans la couche concernée par l'ionisation.

Notre but n'est pas de discuter la précision de la formule de Lotz par rapport à BED, mais de caractériser l'effet du plasma.

La section efficace croit avec la densité, comme observé sur la figure 9.6.9. Nous expliquons cette augmentation par la diminution de l'énergie de transition qui ainsi conduit à faciliter l'ionisation. La variation de la section efficace due à l'effet du plasma à 10^{23} cm^{-3} et $T = 200$ eV est la quasi similaire avec BED et la formule de Lotz. L'effet de la température est opposé à celui de la densité, quand la température augmente la section efficace diminue.

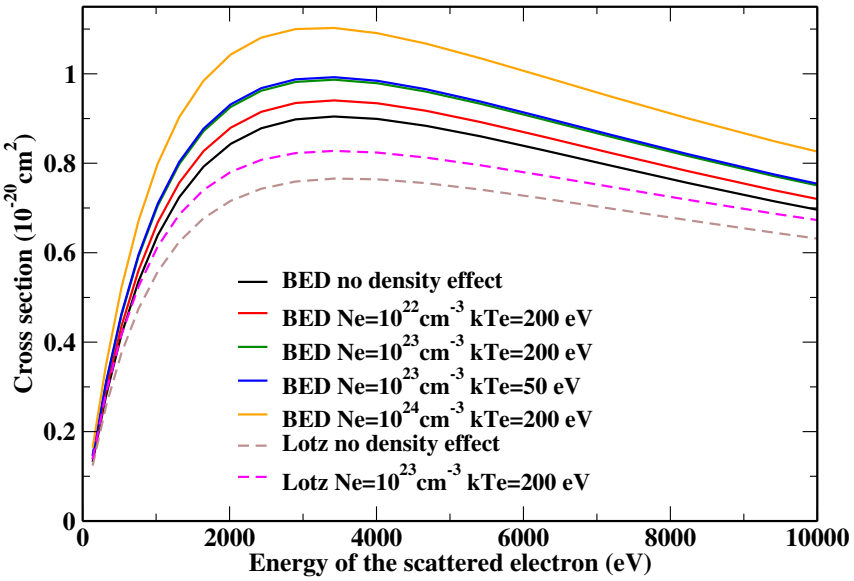

FIGURE 9.6.9 – Comparison of ionization cross section for the transition $1s^2$ to $1s$ for AlXII and XIII at $T = 200$ eV. The free-electron density is obtained from Thomas-Fermi model, and for the scattering process BED and Lotz formalisms are compared.

Nous pouvons soutenir ces résultats en utilisant un formalisme fondé sur la formule de Lotz et une approche perturbative avec le potentiel UEGM. Comme mentionné ci-dessus,

dans UEGM, la correction de l'énergie du premier ordre pour un ion hydrogénoide est

$$E^{(1)}_{\text{plasma}} = \frac{Z_f}{R_0}\left(\frac{3}{2} - \frac{\langle r^2\rangle_{nl}}{2R_0^2}\right), \tag{9.6.9}$$

avec

$$\left\langle r^2\right\rangle_{nl} = \frac{n^2}{2Z^2}\left(5n^2 - 3l\left(l+1\right) + 1\right). \tag{9.6.10}$$

Par exemple, pour l'ionisation d'un ion hydrogénoide dans un état nl vers un ion épluché, nous obtenons l'énergie de transition

$$\Delta E = \frac{Z^2}{2n^2} - \frac{Z_f}{R_0}\left(\frac{3}{2} - \frac{\langle r^2\rangle_{nl}}{2R_0^2}\right), \tag{9.6.11}$$

ce qui montre que l'énergie diminue avec la densité. La section efficace augmente à cause de sa dépendance en énergie en $1/\Delta E_{ij}$, comme observé sur la Figure. 9.6.9. L'étude sur d'autres éléments a montré les même résultats.

Nos résultats sont en accord avec ceux de Wu *et al* [120] quant à l'augmentation des sections efficaces d'ionisation avec la densité, bien que leur travaux utilisent l'approximation des ondes distordues. Comme mentionné par Pindzola *et al* [116], nous avons vérifié que leur section efficace pour l'or germaniumoide est sous-estimée d'un facteur 2. Cependant pour Pindzola et al. [116] les sections efficaces diminuent avec la densité. Les auteurs expliquent que ce comportement est lié à l'écrantage de l'interaction inter-électronique par leur modèle fondé sur Debye-Hückel. Nous notons que leur travail étant basé sur Debye-Hückel, il n'est pas applicable pour les plasmas faiblement corrélés, alors que cette restriction ne s'applique pas à notre travail.

9.6.3 Modèle collisionnel-radiatif

Nous étudions ici, l'effet de l'environnement plasma sur le code collisionel-radiatif. Le code cinétique que nous avons développé se nomme Foch. Il est fondé sur les hypothèses faites dans la section 9.3. Pour le code Foch, par défaut, tous les taux sont calculés par l'intermédiaire des données atomiques de FAC en effectuant une intégration de Gauss-Laguerre. En raison de ce procédé, la grille dépend de la température électronique. Pour nos calculs nous prenons 16 points pour réaliser l'intégration. Pour la résolution des équation cinétiques, nous utilisons un solveur fonctionnant sur le principe d'une méthode LU pour matrice à bande (dgbsvx de lapack [134]).

En ce qui concerne les spectres, le code calcule l'émissivité pour les processus, lié-libre, libre-libre et lié-lié. Le profil de raie choisi pour les spectres lié-lié est un profil de Voigt (méthode de Drayson [135]). Un profil Gaussien ou Lorentzien peut également être utilisé. Pour les calculs détaillés, nous utilisons un élargissement le naturel et Doppler. Pour inclure l'élargissement de Stark due aux collisions électroniques, nous utilisons la formule semi-empirique de Dimitriejic [50].

Pour établir l'effet de l'environnement plasma sur le code cinétique, nous nous comparons à une expérience récemment publiée par Khattak et al. [128] sur le Titane. Cette expérience a été effectueé au laboratoire Rutherford Appleton sur l'installation lasers terawatt ASTRA. Dans l'article un décalage de la raie $He-\alpha$ est rapporté. La raie $He-\alpha$ non-décalée est prise à 4749.73eV, cette valeur provient de Beiersdorfer et al [137]. Nous notons que le code FAC fournit une valeur de 4749.34eV.

Les mesures expérimentales [128] font état d'un décalage de la raie de 3.4eV avec d'une largeur à mi hauteur (FWHM) de 12.1eV. Afin d'évaluer la densité et la température, deux simulations ont été réalisées dans l'article. La première simulation a été menée par le code hydrodynamique HYADES [138] et post-traité avec le code collisionnel-radiatif SOBOLEV [139]. Cette simulation conclut que la densité du plasma excède 10^{24}cm^{-3} avec une température de 3000 eV. La seconde simulation a été faite avec le code de simulation spectrale MARIA [140]. Ce dernier fournit une densité et une température proche du premier calcul.

Pour notre simulation numérique (FAC+Foch), un décalage de la raie $He-\alpha$ de 3.4 eV est obtenu pour une densité de $3.7\times10^{24}\text{cm}^{-3}$avec un température électronique de 3000 eV. Dans ce cas le paramètre de couplage est environ 1.94 avec une sphère de Wigner-Seitz moyenne de $2.098\text{a}_0(Z^* \sim 21.21)$. Le nombre quantique principal utilisé est de 3 afin de satisfaire la condition $\omega_{pe} \ll \omega_{orbital}$ et la condition de non-recouvrement.

Sur la figure 9.6.10, nous avons tracé le spectre lié-lié calculé avec la code Foch (profil de Voigt avec élargissement naturel et Doppler). Sur le graphique, la ligne verticale en pointillé représente la raie $He-\alpha$ non décalée, la courbe rouge représente le spectre lié-lié sans effet du plasma. La courbe bleue correspond au spectre lié-lié avec l'effet du plasma et $N_e = 3.7\times10^{24}\text{cm}^{-3}$ et $kT_e = 3000$ eV. Ce graphique peut être comparé à celui mesuré[128]. Cependant, nous observons que le ratio entre la raie Li-likes et $He-\alpha$ est supérieur à celui mesuré par [128]. Malgré tout, la densité et la température sont en bon accord avec ceux mentionnés dans l'article. L'utilisation d'un élargissement naturel et Doppler n'est pas suffisant pour retrouver la largeur à mi hauteur mesuré expérimentalement. En conséquence nous avons ajouté un élargissement Stark via la formule semi-empirique de Dimitriejic[50]. Nous obtenons une largeur à mi hauteur de$\sim 6.03eV$ ce qui est deux fois plus petit que la valeur attendue. Nous expliquons ceci par l'absence de méthode sophistiquée dans notre code pour la prise en compte l'élargissement des raies.

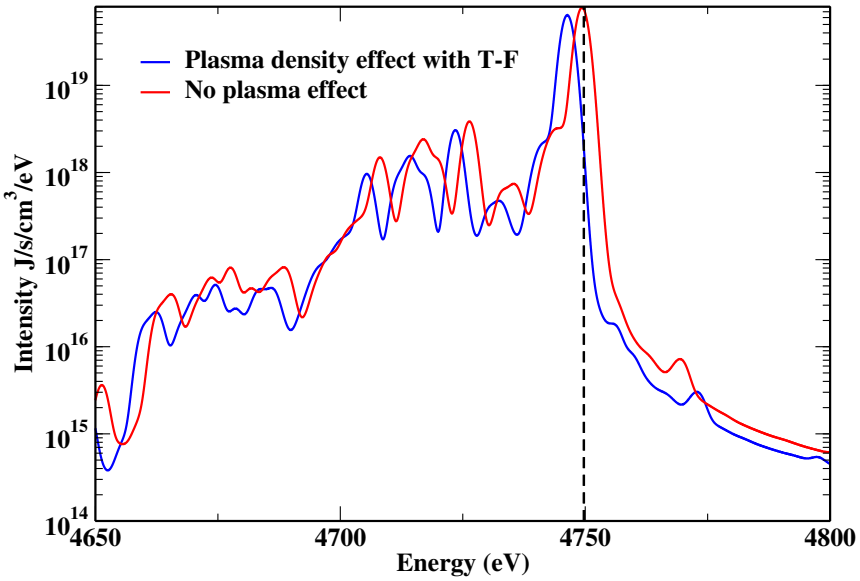

FIGURE 9.6.10 – Bound bound spectra of Titanium element at $N_e = 3.7 \times 10^{24}\text{cm}^{-3}$and $kT_e = 3000$ eV with (blue curves) and without (red curves) screening. Both spectra are calculated with natural and Doppler broadening. Black dashed line represent the unshifted $He - \alpha$ line .

Appendix

Annexe A

Chapter 5 appendix

This appendix follows closely the appendix of our first article [28]

A.1 Effect of the plasma potential out of the sphere on the hydrogen-like ion energies

In the present perturbative development, we have substituted to the ion-sphere potential (5.3.1) its inner form (5.3.2). We wish to evaluate here the influence of the correction $Z^*(r^2/2R_0^2 - 3/2 + R_0/r)/R_0$ for $r > R_0$. Since we require that the wave-functions do not significantly extend beyond R_0, it is reasonable to use their large-r form [111]

$$R_{nl}(r) \sim (-1)^{n-l-1} \frac{2Z^{3/2}}{n^2} \frac{(2Zr/n)^{n-1} e^{-Zr/n}}{[(n+l)!(n-l-1)!]^{1/2}}. \tag{A.1.1}$$

The correction to the energy at first perturbation order is

$$\delta E = \int_{R_0}^{\infty} dr\, r^2 \frac{Z^*}{R_0} \left(\frac{r^2}{2R_0^2} - \frac{3}{2} + \frac{R_0}{r} \right) R_{nl}^2(r). \tag{A.1.2}$$

Using the above asymptotic form of the radial wave-function we obtain

$$\delta E = \frac{Z^*}{2nR_0(n+l)!(n-l-1)!} \left[\frac{1}{2a^2} \Gamma(2n+3, a) - \frac{3}{2} \Gamma(2n+1, a) + a\Gamma(2n, a) \right] \tag{A.1.3}$$

where $a = 2ZR_0/n$ and $\Gamma(\nu, a)$ is the incomplete Gamma function [57]. Using the large-a limit of this function, one obtains the correction to the energy

$$\delta E \simeq \frac{3Z^*(2ZR_0/n)^{2n-2}}{2nR_0(n+l)!(n-l-1)!} e^{-2ZR_0/n} \tag{A.1.4}$$

which must be compared to both parts of the first-order energy shift

$$\delta_0 = \frac{3Z^*}{2R_0},\ \delta_1 = -\frac{Z^*}{2R_0^3}\frac{n^2}{2Z^2}\Big(5n^2 - 3l(l+1) + 1\Big). \tag{A.1.5}$$

Since we must ensure the non-overlap condition (5.3.27), we have estimated the ratios $\rho_0 = \delta E/\delta_0$ and $\rho_1 = \delta E/\delta_1$ assuming $R_0 = 2n^2/Z$. With such a choice, both ratios are small. For instance, if $n = l + 1$, ρ_0 is approximately 0.02 for $n = 1$, 0.002 for $n = 2$, and decreases exponentially with n; $\rho_1 \simeq -0.07, -0.01, -0.0008$ for $n = 1, 2$, and 3 respectively. For $n = l + 2$, $\rho_0 \simeq 0.005, 0.0002, 0.0007$, and $\rho_1 \simeq -0.025, -0.01, -0.004$ for $n = 2, 3$, and 4 respectively. These ratios are even much smaller and more rapidly decreasing with n for the larger ion-sphere radius $R_0 = 3n^2/Z$.

A.2 Quadrupolar matrix elements for hydrogenic ions including ion-sphere perturbation

Quadrupolar radial matrix elements because of the r^2 ponderation are more sensitive than dipoles to the outer region and therefore to the $-Z^*r^2/2R_0^3$ part of the ion-sphere potential. We will thus give here the first-order perturbed matrix elements.

Considering the $n = l + 1$ case, the plasma-density induced first-order perturbation to the quadrupole $\langle n\ n-1|\, r^2\, |n+2\ n+1\rangle$ is the sum of two contributions, one for each wave-function. The first one is

$$\langle \widetilde{n\ n-1}|r^2\,|n+2\ n+1\rangle = \frac{Z^*}{Z^6R_0^3}\frac{n^{n+17/2}(n+2)^{n+3}}{48(n+1)^{2n+15/2}}((2n+1)(2n+3))^{1/2} \\ (72n^5 + 558n^4 + 1816n^3 + 3093n^2 + 2747n + 1014). \tag{A.2.1}$$

and the second

$$\langle n\ n-1|\, r^2|\widetilde{n+2\ n}+1\rangle = -\frac{Z^*}{Z^6R_0^3}\frac{n^{n+9/2}(n+2)^{n+7}}{48(n+1)^{2n+15/2}}(n+3)(2n+5)((2n+1)(2n+3))^{1/2} \\ (12n^3 + 54n^2 + 53n + 16). \tag{A.2.2}$$

From this one gets the quadrupolar element up to first order

$$\langle n\ n-1|\widetilde{\,r^2\,|n}+2\ n+1\rangle = \frac{n^{n+9/2}(n+2)^{n+3}}{Z^2(n+1)^{2n+9/2}}\Big((n+1/2)(n+3/2)\Big)^{1/2}\left[1 + \frac{Z_f}{Z^4R_0^3}\frac{Q_1(n)}{12(n+1)^2}\right] \tag{A.2.3}$$

with

$$Q_1(n) = 24n^8 + 39n^7 - 819n^6 - 5131n^5 - 14273n^4 - 22324n^3 - 20128n^2 - 9688n - 1920. \tag{A.2.4}$$

This polynomial and therefore the correction in factor of $Z^*/Z^4R_0^3$ is negative for n up to 7.

In the same way, the perturbation to the quadrupolar matrix elements $\langle n\ n-2|\, r^2\, |n+2\ n\rangle$ has be obtained. The first contribution is

$$\widetilde{\langle n\ n-2|r^2\,|n+2\ n\rangle} = -\frac{Z^*}{Z^6R_0^3}\frac{n^{n+15/2}(n+2)^{n+2}}{48(n+1)^{2n+15/2}}((2n-1)(2n+1))^{1/2}$$
$$(168n^7+1194n^6+4492n^5+9055n^4+7957n^3-634n^2-5612n-2640). \quad \text{(A.2.5)}$$

The second one is

$$\langle n\ n-2|\, r^2|\widetilde{n+2\ n}\rangle = -\frac{Z^*}{Z^6R_0^3}\frac{n^{n+7/2}(n+2)^{n+6}}{48(n+1)^{2n+15/2}}(2n+3)((2n-1)(2n+1))^{1/2}$$
$$(60n^6+318n^5+515n^4-265n^3-1456n^2-1232n-328). \quad \text{(A.2.6)}$$

From which the quadrupolar matrix elements up to first perturbation order writes

$$\widetilde{\langle n\ n-2|\, r^2\,|n+2\ n\rangle} = \frac{n^{n+7/2}(n+2)^{n+2}}{Z^2(n+1)^{2n+9/2}}(n^2-1/4)^{1/2}(n^2-2n-4)$$
$$\left[1+\frac{Z_f}{Z^4R_0^3}\frac{Q_2(n)}{12(n+1)^2(n^2-2n-4)}\right] \quad \text{(A.2.7)}$$

with

$$Q_2(n) = 24n^{10}-315n^9-3135n^8-12493n^7-23559n^6-8966n^5$$
$$+48036n^4+101720n^3+93408n^2+42688n+7872. \quad \text{(A.2.8)}$$

The corrective factor $Q_2(n)/(n^2-2n-4)$ is negative for $4 \leq n \leq 20$ and positive for $n = 2, 3$, or $n > 20$.

A.3 Dipolar and Quadrupolar electric radiative rates for hydrogenic ions

The radiative rate for dipolar electric transition $n_a l_a \to n_b l_b$ is, in atomic units ($me^4/\hbar^3 \simeq 4.13 \times 10^{16}$ s^{-1}), for a spinless electron

$$A_{ab} = \frac{4\alpha^3}{3}\frac{l_>}{2l_a+1}E_{ab}^3\,\langle n_a l_a|\, r\,|n_b l_b\rangle^2 \quad \text{(A.3.1)}$$

where α is the fine-structure constant and $l_> = \max(l_a, l_b)$.

Concerning the case $n_a = n+1, l_a = n, n_b = n, l_b = n-1$, using the obtained transition energy (5.4.16) and radial matrix element (5.4.23) one gets the transition rate at zeroth

and first order

$$A_{ab}^{(0)} = \frac{2\alpha^3}{3} Z^4 \frac{n^{2n}(n+1)^{2n-2}}{(n+1/2)^{4n+3}} \tag{A.3.2}$$

$$A_{ab}^{(1)} = A_{ab}^{(0)} \left[1 - \frac{Z^*}{Z^4 R_0^3} \frac{(n+1)A_1(n)}{48(n+1/2)^2} \right]. \tag{A.3.3}$$

with

$$A_1(n) = 192n^7 + 1116n^6 + 2898n^5 + 4298n^4 + 3846n^3 + 2024n^2 + 569n + 66. \tag{A.3.4}$$

This shows that the ion-sphere potential lowers the radiative rate $n+1\ n \to n\ n-1$, whatever n. By inspection of corrections (5.4.16) and (5.4.23), it can be checked that both have the same order of magnitude, but that the energy shift dominates the radial matrix element perturbation. More precisely, for large n the dependence on the transition energy is $f_E = 3\Delta E_{ab}/E_{ab} \sim -6Z^* n^6/(Z^4 R_0^3)$, while the dependence on the matrix element $d = \langle n_a l_a | r | n_b l_b \rangle$ is $f_d = 2\Delta d/d \sim 2Z^* n^6/(Z^4 R_0^3)$. However for $n = 1$, one has $f_E/f_d \simeq 0.64$; for higher n the ratio f_E/f_d is greater than 1 in absolute value.

Concerning the case $n_a = n+1, l_a = n-1, n_b = n, l_b = n-2$, using the perturbed transition energy (5.4.16) and radial matrix element (5.4.30), one gets the zeroth- and first-order rates

$$A_{ab}^{(0)} = \frac{2Z^4\alpha^3}{3} \frac{n^{2n-1}(n+1)^{2n-4}}{(n+1/2)^{4n+1}}(n-1) \tag{A.3.5}$$

$$A_{ab}^{(1)} = A_{ab}^{(0)} \left[1 - \frac{Z^*}{Z^4 R_0^3} \frac{A_2(n)}{48(n+1/2)^2} \right] \tag{A.3.6}$$

with

$$A_2(n) = 288n^8 + 2028n^7 + 4914n^6 + 6354n^5 + 5720n^4 + 4062n^3 + 2024n^2 + 569n + 66, \tag{A.3.7}$$

which shows that in the $n = l + 2$ case, the ion-sphere potential also lowers the dipolar electric rate.

The quadrupolar electric radiative rate for the transition from level a with quantum numbers $n_a l_a$ to level b with quantum numbers $n_b l_b$ in a spinless one-electron ion is given in atomic units by ([30])

$$A_{ab} = \frac{\alpha^5}{15} E_{ab}^5 \langle n_a l_a | r^2 | n_b l_b \rangle^2 (2l_b + 1) \begin{pmatrix} l_a & 2 & l_b \\ 0 & 0 & 0 \end{pmatrix}^2 \tag{A.3.8}$$

where E_{ab} is the transition energy and the 3j symbol relevant for the present purpose can

be expressed as

$$\begin{pmatrix} l & 2 & l+2 \\ 0 & 0 & 0 \end{pmatrix} = (-1)^l \left[\frac{3(l+1)(l+2)}{2(2l+1)(2l+3)(2l+5)} \right]^{1/2}. \tag{A.3.9}$$

For $n_a = n+2, l_a = n+1, n_b = n, l_b = n-1$ the quadrupolar electric rate is given at zeroth and first order by

$$A_{ab}^{(0)} = \frac{4\alpha^5}{5} Z^6 \frac{n^{2n}(n+2)^{2n-4}}{(n+1)^{4n+3}} \tag{A.3.10}$$

$$A_{ab}^{(1)} = A_{ab}^{(0)} \left[1 - \frac{Z^*}{Z^4 R_0^3} \frac{R_1(n)}{12(n+1)^2} \right]. \tag{A.3.11}$$

with

$$R_1(n) = 72n^8 + 1017n^7 + 5853n^6 + 19052n^5 + 39016n^4 + 51368n^3 + 42056n^2 + 19376n + 3840. \tag{A.3.12}$$

Though for large n, the density correction to the matrix element (A.2.3) is positive, the density correction to the above rate is always negative. As in the dipolar-electric transition case, on notices that density corrections from energy shift as well as from matrix element variation scale as $Z^* n^6/(Z^4 R_0^3)$. More precisely, for large n the dependence on the transition energy is $f_E = 5\Delta E_{ab}/E_{ab} \sim -10 Z^* n^6/(Z^4 R_0^3)$, while the dependence on the matrix element $q = \langle n_a l_a | r^2 | n_b l_b \rangle$ is $f_q = 2\Delta q/q \sim 4 Z^* n^6/(Z^4 R_0^3)$. However for $n = 1$, one has $f_E/f_q \simeq 0.22$ and for $n = 2$, $f_E/f_q \simeq 0.67$; for higher n the ratio $|f_E/f_q|$ is greater than 1.

As a last example, using the above quadrupole (A.2.7), if $n_a = n+2, l_a = n, n_b = n, l_b = n-2$ the quadrupolar electric rate at the two lowest orders is

$$A_{ab}^{(0)} = \frac{4\alpha^5}{5} Z^6 \frac{n^{2n-2}(n+2)^{2n-6}}{(n+1)^{4n+4}} (n-1)(n^2-2n-4)^2 \tag{A.3.13}$$

$$A_{ab}^{(1)} = A_{ab}^{(0)} \left[1 - \frac{Z^*}{Z^4 R_0^3} \frac{R_2(n)}{12(n+1)^2(n^2-2n-4)} \right]. \tag{A.3.14}$$

with

$$R_2(n) = 72n^{10} + 1755n^9 + 8985n^8 + 20606n^7 + 12888n^6 - 54848n^5 - 174072n^4 - 246880n^3 - 196896n^2 - 85376n - 15744. \tag{A.3.15}$$

The scaling properties of the various corrections for large n are identical as in the above case (A.3.11). However for $n = 3$ the density-dependent corrective factor in the rate (A.3.14) is positive.

Bibliography

[1] Jeffrey P. Freidberg. *Plasma Physics and Fusion Energy.* Cambridge University Press, 2007.

[2] S. Atzeni and J. Meyer-ter Vehn. *The Physics of Inertial Fusion : BeamPlasma Interaction, Hydrodynamics, Hot Dense Matter: BeamPlasma Interaction, Hydrodynamics, Hot Dense Matter.* International Series of Monographs on Physics. Clarendon Press, 2004.

[3] Setsuo Ichimaru. Strongly coupled plasmas: high-density classical plasmas and degenerate electron liquids. *Rev. Mod. Phys.*, 54:1017–1059, 1982.

[4] Richard W. Lee, Stephen J. Moon, Hyun-Kyung Chung, Wojciech Rozmus, Hector A. Baldis, Gianluca Gregori, Robert C. Cauble, Otto L. Landen, Justin S. Wark, Andrew Ng, Steven J. Rose, Ciaran L. Lewis, Dave Riley, Jean-Claude Gauthier, and Patrick Audebert. Finite temperature dense matter studies on next-generation light sources. *J. Opt. Soc. Am. B*, 20(4):770–778, Apr 2003.

[5] P. Hohenberg and W. Kohn. Inhomogeneous electron gas. *Phys. Rev.*, 136:B864–B871, Nov 1964.

[6] W. Kohn and L. J. Sham. Self-consistent equations including exchange and correlation effects. *Phys. Rev.*, 140:A1133–A1138, Nov 1965.

[7] Balazs F. Rozsnyai. Relativistic Hartree-Fock-Slater calculations for arbitrary temperature and matter density. *Phys. Rev. A*, 5:1137–1149, Mar 1972.

[8] Balazs F. Rozsnyai. Photoabsorption in hot plasmas based on the ion-sphere and ion-correlation models. *Phys. Rev. A*, 43:3035–3042, Mar 1991.

[9] David A. Liberman. Self-consistent field model for condensed matter. *Phys. Rev. B*, 20:4981–4989, Dec 1979.

[10] F.Perrot. Atome dans le jellium de charge imposée. *C.E.A internal report.*

[11] R.Piron. *Atome moyen variationnel dans les plasmas quantiques (Variational Average-Atome in Quantum Plasmas,VAAQP).* These de doctorat, Ecole polytechnique, 2009.

[12] T. Blenski and B. Cichocki. Variational theory of average-atom and superconfigurations in quantum plasmas. *Phys. Rev. E*, 75:056402, May 2007.

[13] P. A. M. Dirac. The Quantum Theory of the Electron. *Royal Society of London Proceedings Series A*, 117:610–624, 1928.

[14] R.D.Cowan. *The Theory of Atomic Structure and Spectra*. University of California Press, Berkeley, 1981.

[15] W. Eissner, M. Jones, and H. Nussbaumer. Techniques for the calculation of atomic structures and radiative data including relativistic corrections. *Computer Physics Communications*, 8(4):270, 1974.

[16] A. Bar-Shalom, M. Klapisch, and J. Oreg. Hullac, an integrated computer package for atomic processes in plasmas. *Journal of Quantitative Spectroscopy and Radiative Transfer*, 71(2), 2001.

[17] I.P. Grant, B.J. McKenzie, P.H. Norrington, D.F. Mayers, and N.C. Pyper. An atomic multiconfigurational dirac-fock package. *Computer Physics Communications*, 21(2):207, 1980.

[18] Douglas H. Sampson, Hong Lin Zhang, and Christopher J. Fontes. A fully relativistic approach for calculating atomic data for highly charged ions. *Physics Reports*, 477(4):111, 2009.

[19] K.G. Dyall, I.P. Grant, C.T. Johnson, F.A. Parpia, and E.P. Plummer. Grasp: A general-purpose relativistic atomic structure program. *Computer Physics Communications*, 55(3):425, 1989.

[20] M F Gu. The flexible atomic code. *Can. J. Phys.*, 86(5):675–689, 2008.

[21] O Peyrusse. Atomic configuration averages and non-local thermodynamical equilibrium plasma spectroscopy calculations. *Journal of Physics B: Atomic, Molecular and Optical Physics*, 32(3):683, 1999.

[22] O Peyrusse. A superconfiguration model for broadband spectroscopy of non-lte plasmas. *Journal of Physics B: Atomic, Molecular and Optical Physics*, 33(20):4303, 2000.

[23] M. Klapisch J.Bauche, C. Bauche-Arnoult. Transition arrays in the spectra of ionized atoms. In *Advance in atomic and molecular physics*, pages 131–195. 1987.

[24] Richard M. More. Electronic energy-levels in dense plasmas. *Journal of Quantitative Spectroscopy and Radiative Transfer*, 27(3):345, 1982.

[25] H.-K. Chung, M.H. Chen, W.L. Morgan, Y. Ralchenko, and R.W. Lee. Flychk: Generalized population kinetics and spectral model for rapid spectroscopic analysis for all elements. *High Energy Density Physics*, 1(1):3, 2005.

[26] H.A. Scott and S.B. Hansen. Advances in {NLTE} modeling for integrated simulations. *High Energy Density Physics*, 6(1):39 – 47, 2010.

[27] G. Faussurier, C. Blancard, and E. Berthier. Nonlocal thermodynamic equilibrium self-consistent average-atom model for plasma physics. *Phys. Rev. E*, 63:026401, Jan 2001.

[28] M. Belkhiri and M. Poirier. Density effects in plasmas: Detailed atomic calculations and analytical expressions. *High Energy Density Phys.*, 9(3):609 – 617, 2013.

[29] M.Belkhiri and M.Poirier. Analysis of density effects in plasmas and their influence on electron-impact cross sections, Phys rev A, submitted (2014).

[30] Hans A. Bethe and Edwin E. Salpeter. *Quantum mechanics of one- and two-electron atoms*. Plenum Press, New York, USA, 1977.

[31] W.R Johnson. *Atomic Structure Theory: Lectures on Atomic Physics*. Springer Berlin, 2007.

[32] I.P. Grant. *Relativistic Quantum Theory of Atoms and Molecules: Theory and Computation*. Springer Series on Atomic, Optical, and Plasma Physics. Springer, 2007.

[33] J. C. Slater. A simplification of the hartree-fock method. *Phys. Rev.*, 81:385–390, Feb 1951.

[34] M. Klapisch. the parametric potential method. *C. R. Acad. Sci B*, 265(5):914, 1967.

[35] M. Klapisch. A program for atomic wavefunction computations by the parametric potential method. *Computer Physics Communications*, 2(5):239 – 260, 1971.

[36] Christopher J. Fontes, Douglas H. Sampson, and Hong Lin Zhang. Inclusion of the generalized breit interaction in excitation of highly charged ions by electron impact. *Phys. Rev. A*, 47:1009–1022, Feb 1993.

[37] A. M. Desiderio and W. R. Johnson. Lamb shift and binding energies of electrons in heavy atoms. *Phys. Rev. A*, 3:1267–1275, Apr 1971.

[38] Thomas Blenski and Kenichi Ishikawa. Pressure ionization in the spherical ion-cell model of dense plasmas and a pressure formula in the relativistic pauli approximation. *Phys. Rev. E*, 51:4869–4881, May 1995.

[39] Yu. Ralchenko, G. Abdallah, C. J. Fontes, M. Foster, F. de Gaufridy de Dortan, I. Golovkin, S. B. Hansen, R. W. Lee, V. Novikov, J. Oreg, O. Peyrusse, M. Poirier, A. Sasaki, H. Scott, and H. L. Zhang. Calculation of ionization distributions and radiation losses for tungsten in tokamak plasmas. *AIP Conference Proceedings*, 1161(1):242, 2009.

[40] L. Spitzer. *Physics of Fully Ionized Gases*. New York: Interscience (2nd edition), 1962.

[41] D. Salzmann. *Atomic Physics in Hot Plasmas*. The International Series of Monographs on Physics. Oxford University Press, Incorporated, 1998.

[42] Wolfgang Lotz. An empirical formula for the electron-impact ionization cross-section. *Zeit. Phys.*, 206(2):205–211, 1967.

[43] H. A. Kramers. Xciii. on the theory of x-ray absorption and of the continuous x-ray spectrum. *Philosophical Magazine Series 6*, 46(275):836–871, 1923.

[44] Hans R. Griem. *Principles of Plasma Spectroscopy*. Cambridge University Press, Cambridge, UK, 2005.

[45] Hans R. Griem. Validity of local thermal equilibrium in plasma spectroscopy. *Phys. Rev.*, 131:1170–1176, Aug 1963.

[46] McWhirter. *Plasma Diagnostic techniques*. Cambridge Monographs on Plasma Physics. Cambridge University Press, Cambridge, 1963.

[47] Arthur S. Eddington. *The Internal Constitution of the Stars*. Cambridge University Press, 1988. Cambridge Books Online.

[48] M.Baranger. Spectral line broadening in plasmas. In D.R Bates, editor, *Atomic and molecular processes*, page 493. Academic Press, New york, 1962.

[49] H.R Griem. *Spectral line broadening by plasmas*. Academic Press, New York and London, 1974.

[50] M.S. Dimitrijevic and N. Konjevic. Simple estimates for Stark broadening of ion lines in stellar plasmas. *Astron. Astrophys*, 172:345–349, January 1987.

[51] J. Holtsmark. Über die verbreiterung von spektrallinien. *Annalen der Physik*, 363(7):577–630, 1919.

[52] A. Burgess and M.J. Seaton. A general formula for the calculation of atomic photo-ionization cross-sections. *Mon. Not. Roy. Astron. Soc.*, 120:121, 1960.

[53] I. I. Sobel'man, L. A. Vainshtein, and E. A. Yukon. *Excitation of Atoms and Broadening of Spectral Lines*. Springer, Berlin, 1995.

[54] J.R. Taylor. *Scattering Theory: The Quantum Theory of Nonrelativistic Collisions*. Dover Books on Engineering. Dover Publications, 2012.

[55] N.F. Mott and H.S.W. Massey. *The theory of atomic collisions*. Number vol. 2 in International series of monographs on physics. Clarendon Press, 1965.

[56] M J Seaton. Strong coupling in optically allowed atomic transitions produced by electron impact. *Proceedings of the Physical Society*, 77(1):174, 1961.

[57] M. Abramowitz and I.A. Stegun. *Handbook of Mathematical Functions*. National Bureau of Standards, Washington DC, USA, 1972.

[58] V. I. Ochkur. The born-oppenheimer method in the theory of atomic collisions. *Sov. Phys. JETP*, 18:503, Aug 1963.

[59] I. L. Beigman and L. A. Vainshtein. Effective cross sections for the exchange excitation of atoms and ions by electron impact. *Sov. Phys. JETP*, 52:185, Jan 1967.

[60] Yong-Ki Kim. Scaling of plane-wave born cross sections for electron-impact excitation of neutral atoms. *Phys. Rev. A*, 64:032713, Aug 2001.

[61] U.Fano and M.inokuti. On the theory of ionization by electron collisions. Technical report, Argonne national laboratory, 1976.

[62] Ronald J.W. Henry. Excitation of atomic positive ions by electron impact. *Physics Reports*, 68(1):1 – 91, 1981.

[63] Yukikazu Itikawa. Distorted-wave methods in electron-impact excitation of atoms and ions. *Physics Reports*, 143(2):69 – 108, 1986.

[64] P G Burke, S Ormonde, and W Whitaker. Low-energy electron scattering by atomic hydrogen: I. the close-coupling approximation. *Proceedings of the Physical Society*, 92(2):319, 1967.

[65] M J Seaton. Computer programs for the calculation of electron-atom collision cross sections. ii. a numerical method for solving the coupled integro-differential equations. *Journal of Physics B: Atomic and Molecular Physics*, 7(14):1817, 1974.

[66] B.H. Bransden. *Atomic collision theory*. Lecture Notes and Supplements in Physics Series. Benjamin/Cummings Publishing Company, Advanced Book Program, 1983.

[67] Michael S. Pindzola and Hugh P. Kelly. Electron excitation of the 2s and 2p states of hydrogen from threshold to 50 ev. *Phys. Rev. A*, 11:221–229, Jan 1975.

[68] D. H. Madison and W. N. Shelton. Distorted-wave approximation and its application to the differential and integrated cross sections for electron-impact excitation of the 2^1p state of helium. *Phys. Rev. A*, 7:499–513, Feb 1973.

[69] K H Winter. On distorted-wave approximations for excitation. *Journal of Physics B: Atomic and Molecular Physics*, 11(1):149, 1978.

[70] Mitio Inokuti. Inelastic collisions of fast charged particles with atoms and molecules—the bethe theory revisited. *Rev. Mod. Phys.*, 43:297–347, Jul 1971.

[71] Henri Van Regemorter. Rate of collisional excitation in stellar atmospheres. *Astrophys. J.*, 136:906, nov 1962.

[72] R. Mewe. Interpolation formulae for the electron impact excitation of ions in the h-, he-, li-, and ne- sequences. *Astron. Astrophys.*, 20:215, aug 1972.

[73] Douglas H. Sampson and Hong Lin Zhang. Use of the van regemorter formula for collision strengths or cross sections. *Phys. Rev. A*, 45:1556–1561, Feb 1992.

[74] Joseph B. Mann. Excitation collision strengths for iron ions calculated with a distorted wave method. *Atomic Data and Nuclear Data Tables*, 29(3):407 – 452, 1983.

[75] Peter L. Hagelstein and Rosemary K. Jung. Relativistic distorted-wave calculations of electron collision cross sections and rate coefficients for Ne-like ions. *Atomic Data and Nuclear Data Tables*, 37(1):121 – 188, 1987.

[76] György Csanak, Howard S. Taylor, and Robert Yaris. Many-body methods applied to electron scattering from atoms and molecules. ii. inelastic processes. *Phys. Rev. A*, 3:1322–1328, Apr 1971.

[77] L D Thomas, Gy Csanak, H S Taylor, and B S Yarlagadda. The application of first order many-body theory to the calculation of the differential and integral cross sections for the electron impact excitation of the 2^1S2^1P, 2^3S, 2^3P states of helium. *Journal of Physics B: Atomic and Molecular Physics*, 7(13):1719, 1974.

[78] Luiz E. Machado, Emerson P. Leal, and George Csanak. Electron-impact excitation of some low-lying levels of neon. *Phys. Rev. A*, 29:1811–1824, Apr 1984.

[79] N. T. Padial, G. D. Meneses, F. J. da Paixao, Gy. Csanak, and David C. Cartwright. Electron-impact excitation of the lowest four excited states of argon. *Phys. Rev. A*, 23:2194–2212, May 1981.

[80] T N Rescigno, C W McCurdy Jr, and V McKoy. A relationship between the many-body theory of inelastic scattering and the distorted wave approximation. *Journal of Physics B: Atomic and Molecular Physics*, 7(17):2396, 1974.

[81] Christopher J. Fontes, Hong Lin Zhang, and Joseph Abdallah. An overview of relativistic distorted wave cross sections. *AIP Conference Proceedings*, 730(1):41–49, 2004.

[82] N. H. Magee, J. Abdallah, J. Colgan, P. Hakel, D. P. Kilcrease, S. Mazevet, M. Sherrill, C. J. Fontes, and H. L. Zhang. Los alamos opacities: Transition from ledcop to atomic. *AIP Conference Proceedings*, 730(1):168–179, 2004.

[83] Yong-Ki Kim and M. Eugene Rudd. Binary-encounter-dipole model for electron-impact ionization. *Phys. Rev. A*, 50:3954–3967, Nov 1994.

[84] L. Vriens. Binary encounte and classical collision theories. In W. McDaniel and R.C. McDowell, editors, *Case studies in atomic collision physics*, page 335. Amsterdam.

[85] L.D. Landau and E.M. Lifshits. *Quantum Mechanics: Non-relativistic Theory*. Butterworth Heinemann. Butterworth-Heinemann, 1977.

[86] N. F. Mott. The collision between two electrons. *Proc. R. Soc. London, Ser. A*, 126(801):259–267, 1930.

[87] P. Debye and E. Hückel. Zur Theorie der Elektrolyte. I Gefrierpunktserniedrigung und verwandte Erscheinungen (The theory of electrolytes. I. Lowering of freezing point and related phenomena). *Phys. Z.*, 24:185–206, 1923.

[88] Dimitri Miahalas. *Stellar atmospheres*. Series of Books in Astronomy and Astrophysics. W. H. Freeman, San Francisco, 2nd edition, 1978.

[89] P. Quarati and A. M. Scarfone. Modified Debye-Hückel electron shielding and penetration factor. *Astrophys. J.*, 666(2):1303, 2007.

[90] R. Piron and T. Blenski. Variational-average-atom-in-quantum-plasmas (vaaqp) code and virial theorem: Equation-of-state and shock-hugoniot calculations for warm dense al, fe, cu, and pb. *Phys. Rev. E*, 83:026403, Feb 2011.

[91] R. P. Feynman, N. Metropolis, and E. Teller. Equations of state of elements based on the generalized fermi-thomas theory. *Phys. Rev.*, 75:1561–1573, May 1949.

[92] R. M. More. Atomic processes in high-density plasmas. In C. J. Joachain and D. E. Post, editors, *Atomic and Molecular Physics of Controlled Thermonuclear Fusion*, number 101 in NATO Advanced Science Institutes Series, pages 399–440. Plenum Press, New York, 1983.

[93] M. W. C. Dharma-wardana and François Perrot. Density-functional theory of hydrogen plasmas. *Phys. Rev. A*, 26:2096–2104, Oct 1982.

[94] D. Salzmann, J. Stein, I. B. Goldberg, and R. H. Pratt. Effect of nearest-neighbor ions on excited ionic states, emission spectra, and line profiles in hot and dense plasmas. *Phys. Rev. A*, 44:1270–1280, Jul 1991.

[95] J. C. Stewart and K. D. Pyatt, Jr. Lowering of Ionization Potentials in Plasmas. *Astrophys. J.*, 144:1203, june 1966.

[96] Jon Weisheit. Atoms in plasmas. In Gordon W. F. Drake, editor, *Atomic, Molecular and Optical Physics Handbook*. AIP Press, Woodbury NY, 1996.

[97] Hoe Nguyen, Michel Koenig, Djamel Benredjem, Monique Caby, and Gérard Coulaud. Atomic structure and polarization line shift in dense and hot plasmas. *Phys. Rev. A*, 33:1279–1290, 1986.

[98] S. Bhattacharyya, A. N. Sil, S. Fritzsche, and P. K. Mukherjee. Effect of strongly coupled plasma on the spectra of hydrogenlike carbon, aluminium and argon. *Eur. Phys. J. D*, 46(1):1–8, 2008.

[99] A. N. Sil, J. Anton, S. Fritzsche, P. K. Mukherjee, and B. Fricke. Spectra of heliumlike carbon, aluminium and argon under strongly coupled plasma. *Eur. Phys. J. D*, 55:645–652, 2009.

[100] Madhusmita Das. Effect of strongly coupled plasma on photoionization cross section. *Physics of Plasmas*, 21(1):709, 2014.

[101] G. Massacrier. *Effets de densité et de température sur les ions des plasmas denses et chauds : structure atomique dans un modèle multiconfigurationnel ; équilibre statistique*. These de doctorat, Université de Paris VI, 1988.

[102] D. Salzmann and H. Szichman. Density dependence of the atomic transition probabilities in hot dense plasmas. *Phys. Rev. A*, 35:807–814, 1987.

[103] X. Li and F. B. Rosmej. Quantum-number dependent energy level shifts of ions in dense plasmas: A generalized analytical approach. *EPL Europhys. Lett.*, 99:33001, 2012.

[104] F. Rosmej, K. Bennadji, and V. S. Lisitsa. Effect of dense plasmas on exchange-energy shifts in highly charged ions: An alternative approach for arbitrary perturbation potentials. *Phys. Rev. A*, 84:032512, 2011.

[105] G. Massacrier and J. Dubau. A theoretical approach to N-electron ionic structure under dense plasma conditions: I. Blue and red shift. *J. Phys. B: At. Mol. Opt. Phys.*, 23(13):2459S, 1990.

[106] T. Vallotton. *Ionisation par la pression et effets de densite dans les plasmasn hors equilibre thermodynamique local*. These de doctorat, Université de Paris XI, 2009.

[107] C. Blancard and J. Dubau. Inelastic electron–ion scattering in hot and dense plasmas. *Laser and Particle Beams*, 12:401–406, 9 1994.

[108] Jon C. Weisheit. Atomic phenomena in hot dense plasmas. In H. S. W. Massey, E. W. Mc Daniel, and B. Bederson, editors, *Applied Atomic Collision Physics Vol. 2*. Academic Press, Orlando, 1984.

[109] A. Calisti, S. Ferri, M. Marciante, and B. Talin. Warm dense matter through classical molecular dynamics. *High Energy Density Physics*, 13(0):1 – 8, 2014.

[110] A. Dalgarno and J. T. Lewis. The exact calculation of long-range forces between atoms by perturbation theory. *Proc. R. Soc.*, 233(1192):70–74, 1955.

[111] Leonard I. Schiff. *Quantum mechanics*. McGraw-Hill, New York, USA, 1968.

[112] B Saha and S Fritzsche. Influence of dense plasma on the low-lying transitions in be-like ions: relativistic multiconfiguration dirac–fock calculation. *Journal of Physics B: Atomic, Molecular and Optical Physics*, 40(2):259, 2007.

[113] D. P. Kilcrease, R. C. Mancini, and C. F. Hooper. Ion broadening of dense-plasma spectral lines including field-dependent atomic physics and the ion quadrupole interaction. *Phys. Rev. E*, 48:3901–3913, Nov 1993.

[114] J. Davis and M. Blaha. Level shifts and inelastic electron scattering in dense plasmas. *J. Quant. Spectrosc. Radiat. Transfer*, 27(3):307 – 313, 1982.

[115] G J Hatton, N F Lane, and J C Weisheit. Inelastic electron-ion scattering in a dense plasma. *J. Phys. B*, 14(24):4879, 1981.

[116] M. S. Pindzola, S. D. Loch, J. Colgan, and C. J. Fontes. Electron-impact ionization of atoms in high-temperature dense plasmas. *Phys. Rev. A*, 77:062707, Jun 2008.

[117] B. L. Whitten, N. F. Lane, and J. C. Weisheit. Plasma-screening effects on electron-impact excitation of hydrogenic ions in dense plasmas. *Phys. Rev. A*, 29:945–952, Feb 1984.

[118] Mark C. Zammit, Dmitry V. Fursa, and Igor Bray. Convergent-close-coupling calculations for excitation and ionization processes of electron-hydrogen collisions in debye plasmas. *Phys. Rev. A*, 82:052705, Nov 2010.

[119] M. Schlanges and Th. Bornath. Ionization and recombination coefficients for a dense nonideal hydrogen plasma: effects of screening and degeneracy. *Physica A*, 192(2):262–279, 1993.

[120] Z Q Wu, G X Han, J Yan, and J Q Pang. Plasma effects on electron impact ionization. *J. Phys. B*, 35(10):2305, 2002.

[121] T. N. Chang and T. K. Fang. Atomic photoionization in a changing plasma environment. *Phys. Rev. A*, 88:023406, Aug 2013.

[122] Satyabrata Sahoo and Y. K. Ho. Photoionization of li and na in debye plasma environments. *Physics of Plasmas*, 13:063301, 2006.

[123] X. Li and F. B. Rosmej. Spin-dependent energy-level crossings in highly charged ions due to dense plasma environments. *Phys. Rev. A*, 82:022503, 2010.

[124] H. Bethe. Zur Theorie des Durchgangs schneller Korpuskularstrahlen durch Materie. *Ann. Phys. (Leipzig)*, 397(3):325–400, 1930.

[125] John W. Cooper. Photoionization from outer atomic subshells. a model study. *Phys. Rev.*, 128:681–693, Oct 1962.

[126] Carlos A. Iglesias and Richard W. Lee. Density effects on collisional rates and population kinetics. *J. Quant. Spectrosc. Radiat. Transfer*, 58(4):637, 1997.

[127] S. Bastiani-Ceccotti, N. Kontogiannopoulos, J.-R. Marques, S. Tzortzakis, L. Lecherbourg, F. Thais, I. Matsushima, O. Peyrusse, and C. Chenais-Popovics. Analysis of the x-ray and time-resolved xuv emission of laser produced xe and kr plasmas. *High Energy Density Physics*, 3(1):20, 2007.

[128] F Y Khattak, O A M B Percie du Sert, F B Rosmej, and D Riley. Evidence of plasma polarization shift of ti he-a resonance line in high density laser produced plasmas. *Journal of Physics: Conference Series*, 397(1):012020, 2012.

[129] T Vallotton, O Peyrusse, and D Benredjem. Density-induced continuum resonances and quasi-bound states in the collisional-radiative equilibrium of dense plasmas. *Journal of Physics B: Atomic, Molecular and Optical Physics*, 43(15):155207, 2010.

[130] R Florido, R Rodriguez, J M Gil, J G Rubiano, P Martel, D Suarez, M Mendoza, and E Minguez. ABAKO a new code for population kinetics and radiative properties of plasmas under NLTE conditions. *Journal of Physics: Conference Series*, 112(4):042008, 2008.

[131] Stephen J. Goett, Robert E.H. Clark, and Douglas H. Sampson. Intermediate coupling collision strengths for n = 0 transitions produced by electron impact on highly charged he- and be-like ions. *Atomic Data and Nuclear Data Tables*, 25(3):185 – 217, 1980.

[132] J. Bauche, C. Bauche-Arnoult, and O. Peyrusse. Role of dielectronic recombination and autoionizing states in the dynamic equilibrium of non-lte plasmas. *High Energy Density Physics*, 5:51 – 60, 2009.

[133] William H. Press, Saul A. Teukolsky, William T. Vetterling, and Brian P. Flannery. *Numerical Recipes 3rd Edition: The Art of Scientific Computing*. Cambridge University Press, New York, NY, USA, 2007.

[134] E. Anderson, Z. Bai, C. Bischof, L. S. Blackford, J. Demmel, Jack J. Dongarra, J. Du Croz, S. Hammarling, A. Greenbaum, A. McKenney, and D. Sorensen.

LAPACK Users' Guide (Third Ed.). Society for Industrial and Applied Mathematics, Philadelphia, PA, USA, 1999.

[135] S.R. Drayson. Rapid computation of the voigt profile. *Journal of Quantitative Spectroscopy and Radiative Transfer*, 16(7):611 – 614, 1976.

[136] Stephanie Hansen, G.S.J. Armstrong, S. Bastiani-Ceccotti, C. Bowen, H.-K. Chung, J.P. Colgan, F. de Dortan, C.J. Fontes, F. Gilleron, J.-R. Marquès, R. Piron, O. Peyrusse, M. Poirier, Yu. Ralchenko, A. Sasaki, E. Stambulchik, and F. Thais. Testing the reliability of non-lte spectroscopic models for complex ions. *High Energy Density Physics*, 9(3):523 – 527, 2013.

[137] P. Beiersdorfer, M. Bitter, S. von Goeler, and K. W. Hill. Experimental study of the x-ray transitions in the heliumlike isoelectronic sequence. *Phys. Rev. A*, 40:150–157, Jul 1989.

[138] Jon T. Larsen and Stephen M. Lane. Hyades, a plasma hydrodynamics code for dense plasma studies. *Journal of Quantitative Spectroscopy and Radiative Transfer*, 51(1):179, 1994.

[139] David Riley. Time dependent modelling of k-shell emission lines from laser produced plasmas. *Journal of Quantitative Spectroscopy and Radiative Transfer*, 60(2):221, 1998.

[140] F B Rosmej. Hot electron x-ray diagnostics. *Journal of Physics B: Atomic, Molecular and Optical Physics*, 30(22):L819, 1997.

[141] C. Blancard and G. Faussurier. Equation of state and transport coefficients for dense plasmas. *Phys. Rev. E*, 69:016409, Jan 2004.